CHARMED MESON AND BARYON RESONANCES IN THE HIDDEN GAUGE FORMALISM AND MESON MODIFICATIONS IN THE NUCLEAR MEDIUM

Raquel Molina

November 25, 2011

Contents

D. Eulogio Oset Báguena, Catedrático de Física Teórica de la Universidad de Valencia,

> CERTIFICA: Que la presente Memoria *Charmed meson and baryon resonances in the hidden gauge formalism and meson modifications in the nuclear medium* ha sido realizada bajo mi dirección en el Departamento de Física Teórica de la Universidad de Valencia por Raquel Molina como Tesis para obtener el grado de Doctor en Física.

Y para que así conste presenta la referida Memoria, firmando el presente certificado.

Fdo: Eulogio Oset Báguena

AGRADECIMENTOS

Resulta difícil mirar atrás y darse cuenta de que una etapa más ha concluido. Y más aún cuando esta ha estado llena de experiencias que la han hecho en todos los terrenos, intensa, y sin duda inolvidable. Recuerdo el primer día que llamé a la puerta del despacho de Eulogio como si fuera ayer. Decididamente, le dije que quería formar parte de su grupo y él aprovechó para contarme la última batalla que acababa de vivir acerca de supuestos condensados de kaones sobre los que él mismo echó tierra y me explicaba, como no podía ser de otra manera, como se generaban dinámicamente resonancias. Es obvio que en aquél entonces yo no entendía muy bien de lo que él me estaba hablando mientras se movía de un lado para otro escribiendo diagramas en la pizarra y ponía su tetera a hervir agua. Pero sí fué clave para mí, el momento en que me dijo que yo podría pedir con su grupo una de las becas. En los próximos días me presentó formalmente a aquellos que estaban allí en su día, ellos son: Alberto y Kanchan, Daniel Gamermann, Jorge Martín, Nacho, Manolo y Michael Döring. Con ellos son con los que he convivido más tiempo y guardo de todos ellos, que ya no están, un dulce y grato recuerdo de los momentos que pasé en el grupo. Sin duda, le agradezco a Alberto la paciencia y el cuidado con los que me explicaba y resolvía mis dudas, especialmente aquellas relacionadas con los temas informáticos y que hicieron más llevaderos mis primeros meses en el grupo. A Kanchan, a la que

le tengo gran admiración, por ser tanto una buena física como una bellísima persona, le agradezco sus consejos y nunca olvido las conversaciones de mujer a mujer que manteniamos y me siento orgullosa cuando digo que con ella llegué a hacer amistad. Con Michael coincidí poco tiempo, pero es de esas personas con las que resulta fácil hablar y se recuerdan con cariño. Dani siempre estuvo en disposición de ayudarme y fué con él y con Laura Tolós, con quienes realicé mi primer trabajo. No me cabe la menor duda de que resultó de lo más llevadero junto a ellos dos. Con Dani también me fuí por primera vez a Japón. Dani, Alberto y yo, eramos los tres estudiantes de doctorado de Eulogio y pasamos mucho tiempo juntos. De Dani puedo decir que sin duda siempre me ayudó y me aconsejó en todo lo que estaba al alcance de su mano, de forma sincera y desinteresada. Más tarde compartí despacho durante algún tiempo con Jorge y Nacho. No hay duda de que la picardía de Jorge amenizaba las tardes y a él le debo más que un buen puñado de risas. Debo decir que aquellos fueron tiempos de compañerismo y se respiraba un ambiente excepcional en el grupo .

Poco a poco, cada uno de ellos se fueron yendo y uno se va dando cuenta de su turno está cada vez más cerca. Pero unos se van y otros llegan. Así, no podía faltar Javi Garzón, con el que desde el primer momento tuve buen entendimiento y nos hicimos amigos. Fué con él con quien pasé mi estancia en Kyoto, en la que me reencontré con Kanchan y Alberto y nos echamos unas cuantas buenas risas. Javi resultó ser el mejor substituto de Alberto en cuanto a lo relacionado con la informática y a él le debo no sólo su disposición para ayudarme sino también el poder contar con un amigo en tu trabajo aún en los momentos difíciles.

Durante el periodo de doctorado tengo la suerte de poder decir que he viajado y conocido otros lugares que de otro modo difícilmente hubiese estado allí. Estando en Japón, conocí a Hideko y a Atsushi, Hirenzaki y Yunko, con los que presumo de tener algunos trabajos. En China colaboré con Bingsong Zou y JiaJun Wu, y aquí con Laura Tolós, Tanja Branz, Angels Ramos, Lisheng Geng y Diana Nicmorous

entre otros. A todos ellos les agradezco la paciencia y entusiasmo con la que se enfrentaron a los problemas.

En una ocasión en la que se me presentaron algunas dificultades para entender un problema, viajé a Granada y estuvé allí unos días y fué Carmen García quien me ayudó a despejar aquellas dudas. A ella, a la que tengo la suerte de conocer pues es sin duda de las personas con las que siempre puedes contar, también quiero dedicar esta tesis.

Y como no, a Juan, a Manolo y a Luis, con los que me he tomado más de un café y charlado tranquilamente unas cuantas veces. Es gracias a Manolo que converso con aquellos compañeros que más lejos están todos los días a la hora del café.

Como mencioné al principio de los agradecimientos, puedo decir que he vivido esta etapa de doctorado intensamente, pues ha sido también una etapa de cambios en el plano emocional. Durante la mayor parte del doctorado pasé bonitos años con el que fué mi compañero Roldan, al que le agradezco su apoyo siempre firme en los días más rancios.

Como no podía ser de otro modo, le quiero dedicar esta tesis a mi familia, mis hermanos, Isabel, Angeles, Rafa y Miguel, mis sobrinitos Gonzalo y Aarón, y a mis amigas, Belén Navero, Thalys, Laura, Mónica y Jessica que son de aquellas que te invitan a una cerveza cuando no tienes un chavo y están contigo no sólo en los momentos de diversión.

Ya que me considero de las personas que dejan la guinda para el final, quiero dedicar especialmente esta tesis a tres personas que son muy importantes para mí: mi madre, mi hermana Angeles y Eulogio:

A mi madre, que siempre ha estado y estará ahí y a la que gracias a sus esfuerzos, sus errores y sus sacrificios le debo sencillamente todo.

A mi hermana Angeles, mi paño de lágrimas en los momentos difíciles.

Y, por último, a Eulogio, que me ha regalado todos esos momentos

inolvidables que he vivido formando parte de su grupo, que me ha mostrado siempre su apoyo y disposición para trabajar y del que he aprendido mucho y considero como un padre.

A todos, GRACIAS.

Raquel Molina

Chapter 1

Introduction

1.1 Hadrons and Quantum Chromodynamics

The theory that studies the strong interactions is Quantum Chromodynamics. The fundamental force of the strong interaction describes the interaction between quarks and gluons which are the building blocks of Hadrons. These are divided into two groups: Mesons and baryons. The most basics mesons and baryons are made of $q\bar{q}$ and qqq respectively. The best known of the baryons is the proton ($\tau > 10^{32}$ years) and for mesons these are the pion and the kaon, discovered in the cosmic ray experiments in the 1940s. QCD emerged as a development of the Gell-Mann-Zweig model for hadrons, which was postulated to classify the hadrons in a SU(6) scheme with the spin SU(2) and flavor SU(3) symmetries. Successful as it was, it appeared, however, to have some difficulties reconciling the Fermi Statistics for quarks with the most natural assumption that all the relative angular momenta among constituent quarks in the lowest-lying hadronic states vanishes (s-wave states). Thus, baryon wave-functions should be antisymmetric in spin and flavour degrees of freedom. However,

this is not the case in the original quark model as can be immediaely seen from the $\Delta^{++}(\frac{3}{2}^+)$ wave-function which must be $u\uparrow u\uparrow u\uparrow$, where the arrow denotes $S_z = 1/2$ for each quark and u is the quark with electric charge $Q = 2/3$.

The difficulty can be resolved by postulating a new internal quantum number for quarks which has been called colour. If a quark of each flavour has three, otherwise indistinguishable, colour states, Fermi statistics is saved by using a totally antisymmetric colour wave-function $\varepsilon_{abc} u_a \uparrow u_b \uparrow u_c \uparrow$. Assuming furthermore that (i) the strong interactions are invariant under global $\mathrm{SU(3)_{colour}}$ transformations (the states may then be classified by their $\mathrm{SU(3)_{colour}}$ representation) and (ii) physical hadrons are colourless, i.e. they are singlets under $\mathrm{SU(3)_{colour}}$ (quark confinement), we can understand why only qqq and $q\bar{q}$ states, and not qq or $qqqq$ etc., exist in nature: the singlet representation appears only in the $3 \times 3 \times 3$ and $3 \times \bar{3}$ products.

The concept of colour is also supported by at least two other strong arguments. The one we explain here is based on the parton model approach (Feynman 1972) to the reaction $e^+e^- \to$ hadrons. The ratio,

$$R = \frac{\sigma(e^+e^- \to \text{hadrons})}{\sigma(e^+e^- \to \mu^+\mu^-)} \tag{1.1}$$

is predicted to be

$$\begin{aligned} R = \frac{e^2 \sum_q Q_q^2}{e^2} &= \sum_q Q_q^2 = 3 \times (\frac{4}{9} + \frac{1}{9} + \frac{4}{9} + \frac{1}{9} + \frac{1}{9} + ...) \\ &= \frac{11}{3} \qquad \text{(including quarks up to b)} \end{aligned} \tag{1.2}$$

The experimental value of R is in good agreement with this prediction and in poor agreement with the colourless prediction $\frac{11}{9}$. The other one is based on the $\pi^0 \to 2\gamma$ decay.

The concept of colour certainly underlies what we believe to be the true theory of strong interactions, namely QCD. However, the theory also has several other basic features which are partly suggested

by experimental observations and partly required by theoretical consistency. Firstly, it is assumed that strong interactions act on the colour quantum numbers and only on them. Experimentally, there is no evidence for any flavour dependence of strong forces; all flavour-dependent effects can be explained by quark mass differences and the origin of the quark masses, though not satisfactorily understood yet, is expected to be outside of QCD. In addition, only colour symmetry can be assumed to be an exact symmetry (flavour symmetry is evidently broken) and this, combined with the assumption that it is a gauge symmetry has profound implications: asymptotic freedom and presumably, though not proven, confinement of quarks. Both are welcome features. Asymptotic freedom means that the forces become negligible at short distances and consequently the interaction between quarks by the exchange of non-abelian gauge fields (gluons) is consistent with the succesful, as the first approximation, description of the parton model. It has been shown that only non-abelian gauge theories are asymptotically free (Coleman and Gross 1973). Confinement of the colour quantum numbers, i.e. of quarks and gluons, has not been yet proved to follow from QCD but it is likely to be true, reflecting strongly singular structure of the non-abelian gauge theory in the IR region. Once we assume colourful quarks as elementary objects in hadrons, confinement of colour is desirable in view of the so far unsuccessful experimental detection of free quarks and to avoid a proliferation of unwanted states.

These features of QCD make direct application of the QCD Lagrangian hardly feasible in order to solve strong interaction problems. Perturbative calculations can be done just at high energies where the strong coupling constant gets small, but for low energies, because of the running of this coupling, direct use of the QCD Lagrangian can be done just via lattice calculations which are extremely time and computer resources consuming, but still give insights into the connections between hadrons and the underlying QCD dynamics.

Exotic mesons

Apart from the ordinary $q\bar{q}$ and qqq hadrons, there are many more exotic possibilities to construct color singlets. The constituent quark model describes the observed meson spectrum as bound $q\bar{q}$ states grouped into SU(N) flavor multiplets. However, the self-coupling of gluons in QCD suggests that additional mesons made of bound gluons (glueballs), or $q\bar{q}$-pairs with an excited gluon (hybrids), may exist. Multiquark color singlet states such as $qq\bar{q}\bar{q}$ (tetraquark and "molecular" bound states of two mesons) or $qqq\bar{q}\bar{q}\bar{q}$ (six-quark and "baryonium" bound states of two baryons) have also been predicted. Here we briefly summarize these kinds of exotic mesons.

1. **Glueballs**. Lattice calculations, QCD sum rules, flux tube, and constituent glue models agree that the lightest glueballs have quantum numbers $J^{PC} = 0^{++}$ and 2^{++}. Lattice calculations predict for the ground state, a 0^{++} glueball, a mass around 1650 MeV with an uncertainty of about 100 MeV, whereas the first excited state (2^{++}) has a mass of about 2300 MeV. Thus, the low-mass glueballs lie in the same mass region as ordinary isoscalar $q\bar{q}$ states. The 0^{-+} state and exotic glueballs (with non-$q\bar{q}$ quantum numbers such as 0^{--}, 0^{+-}, 1^{-+}, 2^{+-}, etc.) are expected above 2 GeV. The lattice calculations assume that the quark masses are infinite, and therefore neglect $q\bar{q}$ loops. One meson very hard to accommodate as a $q\bar{q}$ state and most likely to be a glueball is the $f_0(1500)$. Others mesons like the $f_0(1710)$ are candidates to be mixture of $q\bar{q}$ with glueball.

2. **Tetraquark candidates and molecular bound states**. An early quark model prediction was the existence of multiquark states, specifically bound meson-antimeson molecular states [1, 2]. In the light quark sector the $f_0(980)$ and $a_0(980)$ are considered to be strong candidates for $K\bar{K}$ molecules. However, in general, it is challenging to identify unequivocously a light multiquark state in an environment of many broad and often

overlapping conventional states. The charmonium spectrum is better defined so that new types of states can potentially be more easily delineated from conventional charmonium states.

Two generic types of multiquark states have been described in the literature. The first, a molecular state, is comprised of two mesons bound together to form a molecule. These states are by nature loosely bound. In principle, molecular states can bind through two mechanisms: quark/colour exchange interactions at short distances and pion exchange at large distance [3, 4, 5] (see Fig. 1.1) although pion exchange is expected to dominate [3]. Because the mesons inside the molecule are weakly bound, they tend to decay as if they are free. Details are reviewed by Swanson in Ref. [3]. In addition, the ρ exchange plays a crucial role in some kind of molecules as will be shown in this thesis.

The second type is a tightly bound four-quark state, dubbed a tetraquark, that is predicted to have properties that are distinct from those of a molecular state. In the model of Maiani *et al* [6], the tetraquark is described as a diquark-diantiquark structure in which the quarks group into colour-triplet scalar and vector clusters and the interactions are dominated by a simple spin-spin interaction (see Fig. 1.1).

A prediction that distinguishes multiquark states containing a $c\bar{c}$ pair from conventional charmonia is the possible existence of multiplets that include members with non-zero charge (e.g. $[cu\bar{c}\bar{d}]$), strangeness (e.g. $[cd\bar{c}\bar{s}]$), or both (e.g. $[cu\bar{c}\bar{s}]$) [7].

The observation of the $X(3872)$, a strong candidate to be a $D\bar{D}^*$ molecule and the first of the XYZ particles observed, brought forward the hope that one can definitively state that multiquark states has been observed.

3. **Baryonia**. Bound states of baryon - antibaryon have been predicted, but have remained elusive. The $f_2(1565)$ which is only observed in $p\bar{p}$ annihilation is a good candidate for a 2^{++}

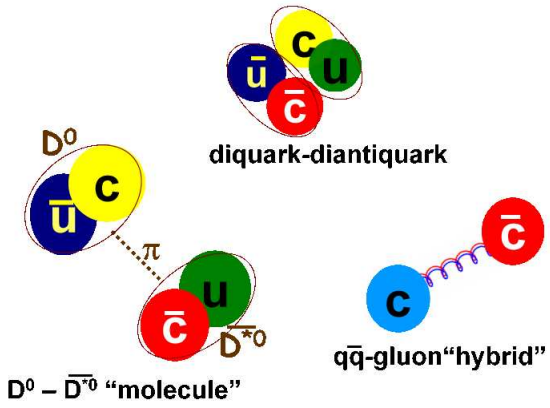

Figure 1.1: Cartoon representations of molecular states, diquark-diantiquark tetraquark mesons and quark-antiquark-gluon hybrids.

$p\bar{p}$ bound state.

4. **Hybrid mesons**. Hybrids may be viewed as $q\bar{q}$ mesons with a vibrating gluon flux tube. In contrast to glueballs, they can have isospin 0 and 1. The ground state hybrids with quantum numbers (0^{-+}, 1^{-+}, 1^{--}, and 2^{-+}) are expected around 1.7 to 1.9 GeV. Lattice calculations predict that the hybrid with exotic quantum numbers 1^{-+} lies at a mass of 1.9 ± 0.2 GeV. We now have at least two 1^{-+} exotics, $\pi_1(1400)$ and $\pi_1(1600)$, while the flux tube model and the lattice concur to predict a mass of about 1.9 GeV. The $\pi(1800)$ is in line with expectations for a 0^{-+} hybrid meson. This meson is also rather narrow if interpreted as the second radial excitation of the pion.

1.2 Heavy quark symmetries and charmed meson spectroscopy

When the mass of a quark, $m_Q >> \Lambda_{QCD}$, this is called heavy quark. The energy scale of the strong interaction, $\Lambda_{QCD} \sim 0.2$ GeV, determines the typical size of the hadrons $R_{\rm had} \sim 1/\Lambda_{QCD} \sim 1$ fm and separates the two regions of large and small coupling constant,

$$\alpha_s = \frac{g^2_{\rm eff}(Q^2)}{4\pi} = \frac{12\pi}{(33-2n_f)ln(Q^2/\Lambda^2_{QCD}} \ . \tag{1.3}$$

At large Q^2, or short distances, the strong interaction becomes weak or α_s decreases. On the other hand, the coupling α_s becomes strong at large distances or small Q^2. This lead to nonperturbative phenomena like the confinement of quark and gluons on length scales $R_{\rm had} \sim 1/\Lambda_{QCD} \sim 1$ fm. For heavy quarks, $\alpha_s(m_Q)$ is weak and this implies that at length scales $\lambda_Q \sim 1/m_Q$ the strong interactions are perturbative and much like the electromagnetic interactions. In fact, the quarkonium systems $Q\bar{Q}$, with a size around $\lambda_Q/\alpha_s << R_{\rm had}$ behave very similar to hydrogen atoms. However $Q\bar{q}$ systems are more complicated because the typical momenta exchanged between these two constituents is of the order of Λ_{QCD}. The heavy quark is surrounded by a very complicated strongly interacting cloud of light quarks, antiquarks and gluons. Nevertheless, it is the fact that $m_Q >> \Lambda_{QCD}$ or $\lambda_Q << R_{\rm had}$ which leads to considerable simplifications. In such systems, the heavy quark moves nearly with the same velocity of the hadron and it is on-shell in the heavy quark limit. The off-shell part of its momentum due to its interaction with the light degrees of freedom is of the order of $\Lambda_{QCD} << m_Q$ and as $m_Q \to \infty$, the change in the velocity of the heavy quark goes to zero. The theory that describes the interactions of a heavy quark with gluons at low energies is HQET. The lagrangian in this theory shows two symmetries: heavy quark flavor and spin symmetries. Heavy quark flavor symmetry means that the dynamics is unchanged under the exchange of heavy quark flavors, i.e. the mass of the heavy quark is completely

irrelevant in the limit $m_Q \to \infty$. There are $1/m_Q$ corrections and lead to heavy quark flavor symmetry breaking effects proportional to $(1/m_{Q_i} - 1/m_{Q_j})$, with Q_i, Q_j any two heavy flavours. On the other hand, as there are not quark-quark interactions in the QCD lagrangian, the only strong interaction of a heavy quark is with gluons, but the spin dependent part of this interaction goes like $1/m_Q$, what means that, in the heavy quark limit, the static heavy quark can only interact with gluons via its chromoelectric charge, which leads to heavy quark symmetry: the dynamics is unchanged under arbitrary transformations on the spin of the heavy quark. The heavy quark SU(2) spin symmetry and $U(N_h)$ flavour symmetries (for N_h) heavy flavours) are embedded into a U($2N_h$) spin-flavour symmetry in the $m_Q \to \infty$ limit. In this limit the spin of the heavy quark, $\vec{S}_Q$, is preserved, and as the total angular momentum of the hadron $\vec{J}$ is a conserved operator, the spin of the light degrees of freedom, $\vec{s}_l$, are also preserved. Thus, heavy mesons come into doublets with $j_\pm = s_l \pm 1/2$ degenerated in mass in the heavy quark limit, (D, D^*) or well (η_c, J/ψ) in the hidden charm sector. Here we briefly summarize the $Q\bar{q}$ and the $Q\bar{Q}$ spectrums.

1. **The $Q\bar{q}$ spectrum.** In the ground state of $Q\bar{q}$, for $l = 0$, $s_l = 1/2$, we have a doublet of mesons with $J^P = 0^-, 1^-$. For $Q = c$, the doublet is formed for the mesons $D(1865)$ and $D^*(2007)$, while for $Q = b$, the mesons are $B(5279)$ and $B^*(5325)$ which have been observed. The predictions of HQET at the lowest order that these doublets are degenerated in mass is fullfilled to a good approximation. For $l = 1$ we have two multiplets for each $s_l = 1/2$ or $3/2$, with quantum numbers $0^+, 1^+$ and $1^+, 2^+$. The doublet with $1^+, 2^+$ can be identified in this model with the experimentally confirmed mesons $D_1(2420)$ and $D_2^*(2460)$. For $Q = b$ and $q = u, d$ we have the states $B_1(5721)$ and $B_2^*(5747)$ experimentally oberved where $m_{B_2}^{*0} - m_{B_1}^0 = 19 \pm 6$ MeV consistent with the predictions of HQET. In the HQET, the two $J^P = 1^+$ states are mixtures of the $j = 1/2$ and $3/2$ states and they decay via s or D wave. The $j = 1/2$ states with

$L = 1$ decay through an s-wave and are expected to be wide while the $j = 3/2$ states decay through a D wave and are expected to be narrow. This is in fact the experimental situation, $\Gamma(D_1) = 18.9 \pm 4$ MeV, $\Gamma(D_2^*) = 23 \pm 5$, $\Gamma(D_0^*) = 261 \pm 50$ and $\Gamma(D_1') = 284^{+130}_{-150}$, although the theoretical masses are around $30 - 60$ MeV above the experimental values. The situation for the D_s spectrum is rather more complicated. The doublet with $J^P = 1^+, 2^+$ has been observed, the $D_{s1}^*(2536)$ and $D_{s2}^*(2573)$ with widths $\Gamma < 2.3$ MeV and $\Gamma = 20 \pm 5$ MeV are compatible with their theoretical predictions, however the doublet with $J^P = 0^+, 1^+$ has masses that lie around 100 MeV over the experimental states, the $D_{s0}^*(2317)$ and $D_{s1}(2460)$, and these states are very narrow, which is in disagreement with the theoretical widths $\sim 200 - 300$ MeV. The key to understand the disagreement would be the strong s-wave coupling to DK and D^*K, with the consideration of meson loop effects close to threshold [8, 9, 10] being very important.

2. The $Q\bar{Q}$ spectrum. The proper theory to study the $Q\bar{Q}$ system is NRQCD (the kinetic energy is needed to stabilize the $Q\bar{Q}$ meson). The properties of quarkonia are usually predicted as a power series in v/c, being v the relative $Q\bar{Q}$ velocity and c the speed of light. The appropriate limit of QCD to examine is $c \to \infty$. Quarkonium states are described by a potential dominated by single gluon exchange at short distances and it is Coulombic. At large distances a linear confining potential dominates. The spins of the quark and antiquark couple to give the total spin $S = 0$ (singlet) or $S = 1$ (triplet), then, the angular momentum between the quark and antiquark L couple to give the full angular momentum of the state, J. Quarkonium states are generally denoted by $^{2S+1}L_J$. For $L = 0$, we have the $^1S_0$ and $^3S_1$ states with $J^{PC} = 0^{-+}$, 1^{--}, whereas for $L = 1$ we have the states $^1P_1$ and $^3P_{0,1,2}$ with $J^{PC} = 1^{+-}, 0^{++}, 1^{++}$ and 2^{++}. The interactions are spin independent up to order $(v/c)^2$.

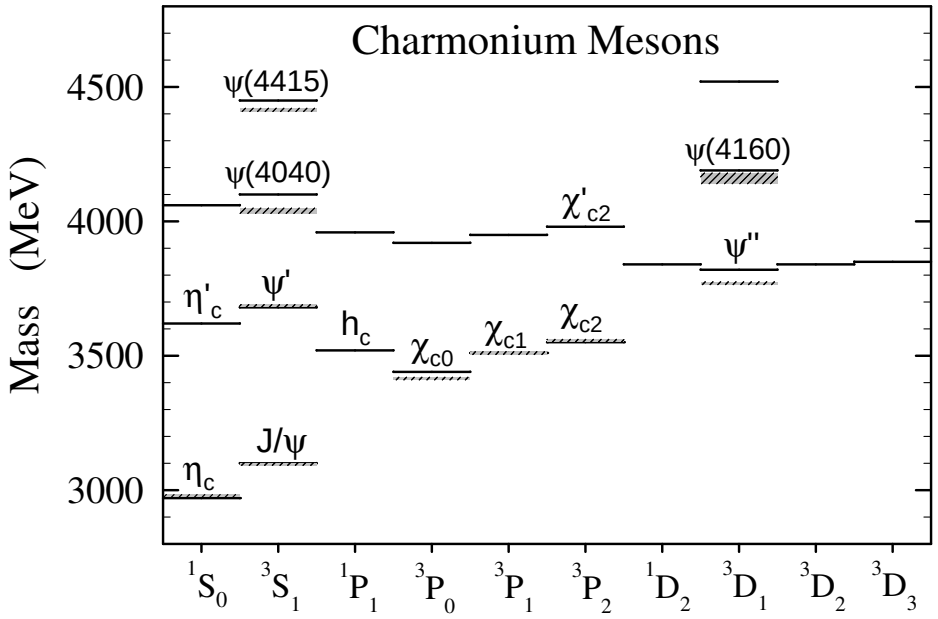

Figure 1.2: The charmonium level diagram. The commonly used names for the mesons associated with assigned states are indicated.

This is consistent with the experiment that finds mass splittings for each doublet small. The spin dependent interactions give rise to splittings within multiplets. The current status of this approach is shown in Fig. 1.2, where the charmonium levels are shown. All the charmonium states below the $D\bar{D}$ threshold have been observed and identified in the $c\bar{c}$ spectrum. However, this effective theory is not consistent for states close to the open meson thresholds. This is the case of the X(3872) that has particular characteristics due to its proximity to $D^{*0}\bar{D}^0$ threshold, and the new particles XYZ around the $D^*\bar{D}^*$ threshold.

The concept of heavy quark symmetry in HQET can be extended to heavy meson molecules. In [11], the authors show that the bind-

ing energies of the $D_{s0}^*(2317)$, being like a DK molecule, have the same value than for the $D_{s1}(2460)$ interpreted like a D^*K bound state which is a natural consequence from the fact that the leading interactions of light mesons with D and D^* mesons are independents of the heavy quark spin and the light meson-D^* meson Green functions are approximately independent close to threshold. Therefore, hadronic molecules also fall in spin multiplets and the splitting in one multiplet is the same as the splitting between heavy mesons. In [11] the authors predict in this way a new $\eta_c' f_0(980)$ bound state as the spin-doublet partner of the $Y(4660)$ (proposed as a $\psi' f_0(980)$ bound state in [12]).

Chapter 2

Formalism

2.1 Inclusion of spin-1 fields

In order to include vector fields in effective Lagrangians there are mainly three different considerations that can be taken into account regarding the kinds of field used, the transformation properties under chiral symmetry and the consideration of the gauge origin (see the summary in Table 2.1 and [13, 14, 15]):

1. Firstly, there are two different kind of fields that can be assigned to the vector mesons:

   1.1 Assign a vector field V_μ (the most widely used)

   1.2 Assign an antisymmetric tensor field $V_{\mu\nu} = V_{\nu\mu}$ [14, 16]

   These two choices can be done since what one needs is a field with only three degrees of freedom. The antisymmetric tensor field apparently has six degrees of freedom, but can be reduced to three with a suitable choice of the equation of motion (see Appendix A of [14]). We will comment later on the advantages, in some cases, of using the antisymmetric tensor field.

2. Second, there is the difference in how the fields are transformed under a realization of chiral symmetry: linear or non-linear, and in the latter case the transformation can be homogeneous or not.

   2.1 Linear means that under a transformation of the chiral group $G = SU(3)_L \otimes SU(3)_R$ the fields transform linearly in the group elements g: $V \to gVg^\dagger$

   2.2 Non-linear means that the transformation is not directly done with g but with a function h(g). Within this kind of transformation, there are two different ways to do it:
   - homogeneously: $V_\mu \to hV_\mu h^\dagger$
   - non-homogeneously: $V_\mu \to hV_\mu h^\dagger + \mathrm{cte}\, h\partial_\mu h^\dagger$

3. Finally there is also the classification due to the consideration of the gauge origin of the vector mesons:

   3.1 Not gauge bosons

   3.2 Gauge bosons of a certain symmetry:
   - Yang-Mills: usual gauge bosons in the Yang-Mills theory
   - Hidden symmetry: the Goldstone bosons matrix U(x) is decomposed in two factors, $U(x) = \xi_L(x)\xi_R^\dagger(x)$. This factorization introduces an "artificial" symmetry under SU(3) rotations and then the vector mesons appear, in the covariant derivatives, as gauge bosons of this "hidden" symmetry.

The majority of these approaches are motivated by the phenomenologically successful ideas of vector-meson dominance and universal coupling [17, 18] which lead to kinetic terms and couplings for the spin-1 mesons that have the same forms as in a gauge theory, reflecting the assumed universal coupling of these mesons to conserved currents. Some of them are the "massive Yang-Mills" [13, 19, 20] and

	Yang-Mills	Hidden symmetry	WCCWZ	EGPdR
field formalism	vector			tensor
origin	gauge boson		not gauge boson	
chiral realization	linear	non-linear and homogeneus		

Table 2.1: Essential features of different models to account for vector meson fields

"hidden-gauge" theories [21]. In these approaches, low energy theorems of chiral symmetry place important constraints on the gauge-type coupling of the ρ meson to two pions, being essential that such Lagrangians respect chiral symmetry or otherwise they can lead to unrealistic results.

Let us explain in some more detail the two different not gauge bosons models. The WCCWZ [15, 22, 23, 24] (from Weinberg, Callan, Coleman, Wess and Zumino) and the EGPdR [14] (from Ecker, Gasser, Pich and de Rafael). In both models the philosophy is the same but they differ in that in WCCWZ the formalism for the fields is vectorial while in EGPdR the antisymmetric tensor field is used. They both use non-linear and homogeneous transformation under chiral symmetry. The philosophy is, as used in the construction of the meson chiral Lagrangian, to build all the possible objects chirally invariant up to a certain order, containing the fields of the theory (note that since the vector-mesons in these two approaches are not gauge bosons, they cannot be included explicitly in covariant derivatives). One of the advantages of using the antisymmetric tensor formalism is

that there are less possible ways to contract Lorentz indices an then the number of allowed pieces in the Lagrangian is smaller. Therefore, the appearance of the Lagrangian is much more compact. The difference essentially comes in the form of the vector-meson propagator in the presence of certain local terms in the vector field formalism. By introducing local terms and with basic assumptions of vector meson dominance, the two formalisms were shown to be equivalent up to $O(p^4)$ [25] and with only one vector field. Further work on the equivalence of the two formalisms, up to local terms, for general Lagrangians, based on dual transformations of gauge theories, using path integral techniques, was done in [26]. The same kind of equivalence exploring the baryon sector was seen in [27]. In contrast to the gauge-type theories, these formalisms have $\rho\pi\pi$ couplings that involve higher powers of momentum and are not directly constrained by chiral symmetry.

In massive Yang-Mills theories [13, 19], the vector and axial fields transform under a linear realization of chiral symmetry. Three- and four-point couplings among these fields are included and, together with the kinetic terms, form a Yang-Mills Lagrangian with a local chiral symmetry. The full theory does not possess this gauge symmetry since it includes mass terms which have only global symmetry. By changing variables to spin-1 fields that transform under the nonlinear realisation of chiral symmetry, any massive Yang-Mills theory can be converted into an equivalent WCCWZ one and its relations to other theories, such as hidden-gauge ones, can be explored. The use of a linear realisation of chiral symmetry means that both the ρ meson and its chiral partner, the a_1 must be treated on the same footing. One cannot simply omit the a1 from a massive Yang-Mills theory without violating chiral symmetry. Nonetheless it is possible to write down Lagrangians with a Yang-Mills form for the ρ meson alone, provided that one takes care to include additional terms that ensure satisfaction of the chiral low energy theorems [28]. As described here a convenient way to generate these terms is to take a hidden-gauge theory and make a change of variables that brings it

into a Yang-Mills-like form.

Despite the rather different forms of their Lagrangians, and the different types of coupling contained in them, all of these approaches are in principle equivalent. Each corresponds to a different choice of fields for the spin-1 mesons. This is illustrated rather well in extended Nambu-Jona-Lasinio models [29, 30], where there is considerable freedom in the choice of auxiliary fields in the vector and axial channels. To some extent the choice of scheme must be based on the simplicity of the resulting Lagrangian. In making comparisons between the approaches it is important not to confuse features that arise from the choice of field with those that arise from requiring, for instance, universal coupling of the vector mesons. The former are not physical, controlling merely the off-shell behaviour of scattering amplitudes. The latter do have physical consequences, such as relations between on-shell amplitudes for different processes. In the hidden-gauge approach [21] an artificial local symmetry is introduced into the nonlinear sigma model by the choice of field variables. The ρ meson is then introduced as a gauge boson for this symmetry. As stressed by Georgi [31], the additional local symmetry has no physics associated with it, and it can be removed by fixing the gauge. In the unitary gauge the symmetry reduces to a nonlinear realization of chiral symmetry, under which the vector fields transform inhomogeneously, in contrast to those of WCCWZ. However, with a further change of variable any vector-meson Lagrangian of the hidden-gauge form can be converted into an equivalent WCCWZ one [31]. The rules for transforming a Lagrangian from hidden-gauge to WCCWZ form have also been noted by Ecker et al. [25]. By changing variables from the hidden-gauge to WCCWZ scheme, the gauge coupling constant of the former is really a parameter in the choice of vector field. This coupling constant does not appear in the equivalent WCCWZ Lagrangian and so hidden gauge theories with different gauge couplings, together with different higher-order couplings, can be equivalent. The conventional choice is shown to be one that eliminates any $O(p^3)$ $\rho\pi\pi$ coupling from the hidden-gauge Lagrangian, so

that the leading corrections to the O(p) coupling are of order p^5. If the $\gamma\rho$ mixing strengths satisfy a particular relation [25], then this choice of field also eliminates the leading momentum-dependent corrections, of order p^2, to the mixing. This reduction of the momentum dependence of the couplings thus allows the hidden-gauge approach to embody the empirical observation that the KSFR relation [32, 33] is well satisfied by the $\rho\pi\pi$ and $\gamma\rho$ couplings determined from the decay of on-shell ρ mesons.

2.1.1 The Hidden Gauge formalism

The HGS formalism to deal with vector mesons [21, 34] is a useful and internally consistent scheme which preserves chiral symmetry. In this formalism the vector meson fields are gauge bosons of a hidden local symmetry transforming inhomogeneously. After taking the unitary gauge, the vector meson fields transform exactly in the manner as in the non linear realization of chiral symmetry [22]. In [25] this formalism is found equivalent to the use of the tensor formalism of [14], where the vectors transform homogeneously under a non-linear realization of chiral symmetry, with the use of couplings implied in the vector meson dominance formalism (VMD) of [17]. (For a review on the different ways to implement vector mesons into effective chiral Lagrangians see [15]).

Following [25] the Lagrangian involving pseudoscalar mesons, photons and vector mesons can be written as

$$\mathcal{L} = \mathcal{L}^{(2)} + \mathcal{L}_{III} \tag{2.1}$$

with

$$\mathcal{L}^{(2)} = \frac{1}{4} f^2 \langle D_\mu U D^\mu U^\dagger + \chi U^\dagger + \chi^\dagger U \rangle \tag{2.2}$$

$$\mathcal{L}_{III} = -\frac{1}{4}\langle V_{\mu\nu} V^{\mu\nu} \rangle + \frac{1}{2} M_V^2 \langle [V_\mu - \frac{i}{g}\Gamma_\mu]^2 \rangle, \tag{2.3}$$

where $\langle ... \rangle$ represents a trace over $SU(3)$ matrices. The covariant

derivative is defined by

$$D_\mu U = \partial_\mu U - ieQA_\mu U + ieUQA_\mu, \tag{2.4}$$

with $Q = diag(2,-1,-1)/3$, $e = -|e|$ the electron charge, and A_μ the photon field. The chiral matrix U is given by

$$U = e^{i\sqrt{2}P/f} \tag{2.5}$$

with f the pion decay constant ($f = 93$ MeV). The P and V_μ matrices are the usual $SU(3)$ matrices containing the pseudoscalar mesons and vector mesons respectively

$$\begin{aligned} P &\equiv \begin{pmatrix} \frac{1}{\sqrt{2}}\pi^0 + \frac{1}{\sqrt{6}}\eta_8 & \pi^+ & K^+ \\ \pi^- & -\frac{1}{\sqrt{2}}\pi^0 + \frac{1}{\sqrt{6}}\eta_8 & K^0 \\ K^- & \bar{K}^0 & -\frac{2}{\sqrt{6}}\eta_8 \end{pmatrix}, \\ V_\mu &\equiv \begin{pmatrix} \frac{1}{\sqrt{2}}\rho^0 + \frac{1}{\sqrt{2}}\omega & \rho^+ & K^{*+} \\ \rho^- & -\frac{1}{\sqrt{2}}\rho^0 + \frac{1}{\sqrt{2}}\omega & K^{*0} \\ K^{*-} & \bar{K}^{*0} & \phi \end{pmatrix}_\mu . \end{aligned} \tag{2.6}$$

The terms with χ in $\mathcal{L}^{(2)}$ provide the mass term for the pseudoscalars. For four pseudoscalar meson fields the $\mathcal{L}^{(2)}$ Lagrangian provides the well known chiral Lagrangian at lowest order

$$\widetilde{\mathcal{L}}^{(2)} = \frac{1}{12f^2}\langle [P,\partial_\mu P]^2 + MP^4 \rangle \tag{2.7}$$

with $M = diag(m_\pi^2, m_\pi^2, 2m_K^2 - m_\pi^2)$. For the coupling between two pseudoscalars and one photon the Lagrangian $\mathcal{L}^{(2)}$ provides

$$\mathcal{L}_{\gamma PP} = -ieA^\mu \langle Q[P,\partial_\mu P]\rangle, \tag{2.8}$$

which in this formalism will get canceled with an extra term coming from $\mathcal{L}_{III}$, such that ultimately the photon couples to the pseudoscalars via vector meson exchange, the basic feature of VMD.

In $\mathcal{L}_{III}$, $V_{\mu\nu}$ is defined as

$$V_{\mu\nu} = \partial_\mu V_\nu - \partial_\nu V_\mu - ig[V_\mu, V_\nu] \tag{2.9}$$

and

$$\Gamma_\mu = \frac{1}{2}[u^\dagger(\partial_\mu - ieQA_\mu)u + u(\partial_\mu - ieQA_\mu)u^\dagger] \tag{2.10}$$

with $u^2 = U$. The hidden gauge coupling constant g is related to f and the vector meson mass (M_V) through

$$g = \frac{M_V}{2f}, \tag{2.11}$$

which is one of the forms of the KSFR relation [33]. Other properties of g inherent to the VMD formalism, relating to the tensor formalism of [25] are

$$\frac{F_V}{M_V} = \frac{1}{\sqrt{2}g}, \qquad \frac{G_V}{M_V} = \frac{1}{2\sqrt{2}g}, \qquad F_V = \sqrt{2}f, \qquad G_V = \frac{f}{\sqrt{2}}. \tag{2.12}$$

Upon expansion of $[V_\mu - \frac{i}{g}\Gamma_\mu]^2$ up to two pseudoscalar fields, we find

$$\begin{aligned}[V_\mu - \frac{i}{g}\Gamma_\mu]^2 &= \left(V_\mu - \frac{e}{g}QA_\mu - \frac{1}{g}\frac{1}{2f^2}PeQA_\mu P + \frac{1}{g}\frac{1}{4f^2}P^2eQA_\mu \right. \\ &\left. + \frac{1}{g}\frac{1}{4f^2}eQA_\mu P^2 - \frac{i}{g}\frac{1}{4f^2}[P, \partial_\mu P]\right)^2 \end{aligned} \tag{2.13}$$

from where we obtain the following interaction Lagrangians among pseudoscalars (P), photons (γ) and vector mesons (V):

$$\mathcal{L}_{V\gamma} = -M_V^2\frac{e}{g}A_\mu\langle V^\mu Q\rangle \tag{2.14}$$

$$\mathcal{L}_{V\gamma PP} = egA_\mu\langle V^\mu(QP^2 + P^2Q - 2PQP)\rangle \tag{2.15}$$

$$\mathcal{L}_{VPP} = -ig\langle V^\mu[P, \partial_\mu P]\rangle \tag{2.16}$$

$$\mathcal{L}_{\gamma PP} = ieA_\mu\langle Q[P, \partial_\mu P]\rangle \tag{2.17}$$

$$\widetilde{\mathcal{L}}_{PPPP} = -\frac{1}{8f^2}\langle[P, \partial_\mu P]^2\rangle. \tag{2.18}$$

The term in Eq. (2.17) cancels exactly the term in Eq. (2.8), as mentioned above. On the other hand, the term of Eq. (2.18) has the same structure as the derivative term of Eq. (2.7) and it is a most unpleasant term, since added to $\widetilde{\mathcal{L}}^{(2)}$ of Eq. (2.7) would break the chiral symmetry of the chiral Lagrangian. However, this term is canceled by the exchange of vector mesons between the pseudoscalars that result from the Lagrangian of Eq. (2.16), $\mathcal{L}_{VPP}$, in the limit of $q^2/M_V^2 \to 0$, where q is the momentum carried by the exchanged vector meson. This was already noticed in [22].

2.2 Unitary extension of χPT

Because of the difficulties presented by QCD, hadron problems can be tackled by different approaches, namely effective theories. The underlying idea is to use QCD Lagrangian's symmetries to construct Lagrangians for the interaction of hadrons (color singlets) instead of quarks. In this direction, one of the most successful theories is chiral perturbation theory (χPT), which is based on the approximate chiral symmetry of QCD. In this approach, the pseudoscalar mesons are Goldstone bosons coming from the spontaneous breakdown of the chiral symmetry and one constructs Lagrangians for the interaction of pseudoscalar mesons expanded in a power series of the boson's momenta [16, 35]. This theory has overwhelming success in describing scattering of hadrons at low energies [14, 25, 36, 37, 38] or hadron production [39] and unitarization in coupled channels has extended the energy region of its applicability [40, 41, 42, 43, 44, 45, 46, 47, 48, 49, 50].

Chiral perturbation theory, as its name says, is a perturbation theory, where the amplitudes are expanded in power series of the particle's momenta. It is possible to improve the results by going to higher orders in the momentum expansion but one has to pay the price of a huge number of free parameters appearing in the higher order Lagrangians. Therefore χPT has many limitations since the the-

ory eventually breaks down, once the energy is sufficiently large. The absolute limit of applicability in meson-meson interaction is where the first singularity of the T-matrix appears which happens for the σ meson, this means around 450 MeV for $\pi\pi$ interactions.

Unitarization in coupled channels allows one to study inelasticity among channels and the decays of resonances. It uses the chiral amplitudes as a kernel to solve a scattering equation respecting the analytical properties of the scattering matrix (S-matrix), in particular that it should be unitary. This is a non-perturbative method and hence has a wider energy range of applicability. It allows also the study of the formation of resonances which is a non-perturbative phenomenon.

The resonances that appear within this method are called dynamically generated resonances, since they appear from the dynamical interaction of the particles included explicitly as building blocks. One example is the study of the interaction of the light pseudoscalar mesons in s-wave or the interaction of pseudoscalars with vector mesons, one obtains the low lying scalar and axial vector particles as dynamically generated resonances [51, 52, 53, 54, 55]. In these works, one includes pseudoscalar and vector mesons as degrees of freedom in the Lagrangians and the unitary S-matrix has poles that can be associated with the axial and scalar mesons. In addition, nucleon resonances can be studied in this framework [41, 42, 43, 44, 56, 57].

There are different ways to implement the ideas of unitarity and analyticity of the T matrix: the Inverse Amplitude Method (IAM) [53, 58], the N/D method [52] and the Bethe- Salpeter equation [51, 59, 61], although very similar results are obtained between these approaches. All these methods, which are now known as unitarized chiral perturbation theory ($U\chi PT$), give rise basically to the same results and reproduce very well the data on meson-meson scattering up to 1.2 GeV, leading to poles in the T matrix for many of the different resonances appearing up to that energy. Among these resonances, the low-lying scalar ones ($\sigma(500)$, κ, $f_0(980)$ and $a_0(980)$ [51, 52, 53, 62, 63]) are generated dynamically, meaning that the use

of the strong interaction provided by the lowest order meson chiral Lagrangian, together with the unitarity constraints which generate multiple scattering of the mesons, leads automatically to these resonances without the need to introduce them explicitly in the formalism. As an example, in the rest of this section I will sketch the essential ideas using the N/D method, (which are taken from [43, 52, 60]). It is well known that probability conservation implies necessarily the scattering amplitude ($S = 1 - i\alpha T$) to be unitary (α containing normalization factors of the fields). We can define the transition T_{ij}-matrix between the i and j channels which couple to certain quantum numbers. Unitarity in coupled channels can be written, using Mandl and Shaw normalization of states and T matrix, as

$$\mathrm{Im}T_{ij} = T_{il}\rho_l T^*_{lj} \tag{2.19}$$

where $\rho_i \equiv (2M_i q_i)/(8\pi W)$ for meson-baryon interaction and $\rho_i \equiv q_i/(8\pi W)$ for meson-meson interaction, with q_i the modulus of the c.m. three-momentum, W the c.m. energy, M_i the baryon mass and the subscripts i and j refer to the physical channels. This equation is most efficiently written in terms of the inverse amplitude as

$$\mathrm{Im}T^{-1}(W)_{ij} = -\rho(W)_i\delta_{ij} \tag{2.20}$$

From Eq. (2.19) or (2.20) we see that the amplitude is real for W below the lowest threshold and complex above it. This implies the existence of a cut in the T-matrix of partial wave amplitudes from energies above the lowest threshold to infinity, which is usually called the unitarity or right-hand cut. Hence one can write down a dispersion relation for $T^{-1}(W)$

$$\begin{aligned} T^{-1}(W)_{ij} &= -\delta_{ij}\{\tilde{a}_i(s_0) + \frac{s-s_0}{\pi}\int_{s_i}^{\infty} ds' \frac{\rho(s')_i}{(s'-s)(s'-s_0)}\} \\ &\quad + \mathcal{T}^{-1}(W)_{ij} \end{aligned} \tag{2.21}$$

where s_i is the value of the $s(W^2)$ variable at the threshold of channel i and $\mathcal{T}^{-1}(W)_{ij}$ indicates other contributions coming from local

and pole terms, as well as crossed channel dynamics but without right-hand cut. These extra terms are taken directly from χPT after requiring the matching of the general result to the χPT expressions. Notice also that

$$g(s)_i = \tilde{a}_i(s_0) + \frac{s-s_0}{\pi}\int_{s_i}^{\infty} ds' \frac{\rho(s')_i}{(s'-s)(s'-s_0)} \tag{2.22}$$

is the familiar scalar loop integral, which for the meson-meson case is given by

$$\begin{aligned} g(s)_i = & \int \frac{d^4q}{(2\pi)^4}\frac{1}{(q^2-M_i^2+i\epsilon)((P-q)^2-m_i^2+i\epsilon)} \\ = & \frac{1}{16\pi^2}\{a_i(\mu)+\mathrm{Log}\frac{m_i^2}{\mu^2}+\frac{M_i^2-m_i^2+s}{2s}\mathrm{Log}\frac{M_i^2}{m_i^2} \\ & +\frac{q_i}{\sqrt{s}}\mathrm{Log}\frac{m_i^2+M_i^2-s-2\sqrt{s}q_i}{m_i^2+M_i^2-s+2\sqrt{s}q_i}\} \end{aligned} \tag{2.23}$$

where M_i and m_i are, respectively, the meson masses in the state i. In order to calculate $g(s)_i$ one uses the physical masses both for mesons and baryons and, hence, Eq. (2.20) holds. In the case of meson-baryon $g(s)_i$ has the same expression multiplying it by $2M_i$, where M_i is the baryon mass and m_i the meson mass. One can further simplify the notation by employing a matrix formalism. Introducing the matrices $g(s) = diag(g(s)_i)$, T and $\mathcal{T}$, the latter defined in terms of the matrix elements T_{ij} and $\mathcal{T}_{ij}$, the T-matrix can be written as:

$$T(W) = [I - \mathcal{T}(\mathcal{W})g(s)]^{-1}\cdot\mathcal{T}(W) \tag{2.24}$$

which can be recast in a more familiar form as

$$T(W) = \mathcal{T}(W) + \mathcal{T}(W)g(s)T(W) \tag{2.25}$$

Now suppose one is taking the lowest order chiral amplitude for the kernel as done in [43]. Then the former equation is nothing but

the Bethe-Salpeter equation with the kernel, $\mathcal{T}(W)$, taken from the lowest order Lagrangian and factorized on shell, the same approach followed in [44] where different arguments were used to justify the on shell factorization of the kernel. Furthermore in [43] a simple relationship is found between the cut off used in [44] and the subtraction constants used in [43]

$$a_i(\mu) = -2\text{Log}\left(1 + \sqrt{1 + \frac{m_i^2}{\mu^2}} + ..., \right) \tag{2.26}$$

where μ plays the role of the cutoff. Then taking values of μ around 650 MeV to 1 GeV one would find subtraction constants of the order of -2, which we call of natural size. The unitary extensions of chiral perturbation theory, $U\chi PT$, have brought new light in the study of the meson-meson and meson-baryon interaction and have shown that some well known resonances qualify as dynamically generated, or in simpler words, they are quasibound states of meson-meson or meson-baryon. Another case of successful application of these chiral unitary techniques is the interaction of mesons with baryons [42, 43, 44, 59, 64, 65] showing that the $\Lambda(1405)$ and the $N^*(1535)$ were dynamically generated resonances. A more systematic study of these latter interaction has shown that there are two octets and one singlet of resonances from the interaction of the octet of pseudoscalar mesons with the octet of stable baryons [46, 50]. Work along these lines has continued by studying the interaction of the octet of pseudoscalar mesons with the decuplet of baryons [66, 67] which has also led to the generation of many known resonances, like the $N^*(1520)$ and the $\Lambda(1520)$. Of course, from these successful studies one cannot extrapolate the idea that the rest of mesons and baryons are also dynamically generated. In fact, some of these studies of the meson-meson and meson-baryon interaction have also shown that some mesons or baryons are not dynamically generated, i.e., they are not consequence of the interaction between the meson or baryon components and they qualify better as genuine, or preexistent states,

a word that can be substantiated starting that they would remain in the limit of large N_c limit where the loops of intermediate states vanish. This is the case of the vector mesons of the ρ octet [52, 68]. The N_c behavior of the scalar and vector resonances studied within unitary techniques has been discussed in [69].

Chapter 3

The $\rho\rho$ interaction and its extension to SU(3)

We apply the methods explained in the previous pages that describe the interaction between vectors mesons within the Hidden Gauge Formalism to the system of two ρ's. Then this study will be extended to SU(3). We will find that the use of the set of Lagrangians of the hidden gauge formalism together with unitary technics for the scattering amplitudes lead to the generation of resonances in the complex plane that can be described as vector-vector molecular states. Particularly, the $\rho\rho$ bound states found will be identified with the $f_2(1270)$ and $f_0(1370)$. In addition, the decay of these to two or four pseudoscalars will be studied.

3.1 Introduction

The $f_2(1270)$ and $f_0(1370)$ are intriguinly close to the $\rho\rho$ threshold. In [70], the $f_2(1270)$ is assumed to be predominantly a $q\bar{q}$ state. Within the formalism of the IAM, the $f_2(1270)$ is obtained starting from the $\pi\pi$ interaction [71]. However, this does not mean the $f_2(1270)$ is

a resonance built up from $\pi\pi$. In fact, the addition of some counterterms was needed to produce this resonance. This also happened before in the familiar case of the ρ meson, obtained in a similar way within the IAM from the $\pi\pi$ interaction. Indeed, a careful study of the large N_c behaviour of the ρ meson shows that the state remains as N_c goes to infinity, as corresponds to genuine $q\bar{q}$ states, unlike the dynamically generated scalar mesons that fade away in that limit. Some counterterms are needed in the IAM to produce this state and the information on the $f_2(1270)$ nature is buried in these terms.

The nature of the $f_0(1370)$ has been also controversial and there are many alternative explanations from $q\bar{q}$ to glueball. In [72] the $f_0(1370)$ is assumed to be dominantly a $q\bar{q}$ state, unlike the lighter scalars that are assumed to be largely four quark states. In [73] the $f_0(1370)$ is studied within the improved ladder approximation of QCD and it is assumed to be mostly $q\bar{q}$, however, the meson-meson or four quark components are supposed to be important. In addition, mixtures of $q\bar{q}$ and four quarks [74], $q\bar{q}$ with glueballs [75] or $q\bar{q}$ with quarks of nonstrange nature [76] are also considered for this resonance.

In the following we explain that by means of the lagrangians of the Hidden Gauge Formalism for the vector-vector interaction one generates the $f_2(1270)$ and $f_0(1370)$ states as bound states with practically no freedom.

3.2 Vector - Vector scattering

The Hidden Gauge Lagrangian is given by

$$\mathcal{L}_{III} = -\frac{1}{4}\langle V_{\mu\nu}V^{\mu\nu}\rangle \ , \tag{3.1}$$

where the symbol $\langle\rangle$ stands for the trace in the $SU(3)$ space and $V_{\mu\nu}$ is given by

$$V_{\mu\nu} = \partial_\mu V_\nu - \partial_\nu V_\mu - ig[V_\mu, V_\nu] \ , \tag{3.2}$$

with g given by

$$g = \frac{M_V}{2f} \ , \tag{3.3}$$

We can extract the four- and three-vector contact terms,

$$\mathcal{L}_{III}^{(c)} = \frac{g^2}{2}\langle V_\mu V_\nu V^\mu V^\nu - V_\nu V_\mu V^\mu V^\nu \rangle \ , \tag{3.4}$$

and

$$\mathcal{L}_{III}^{(3V)} = ig\langle (\partial_\mu V_\nu - \partial_\nu V_\mu) V^\mu V^\nu \rangle \ , \tag{3.5}$$

where V_μ is given by

$$V_\mu = \begin{pmatrix} \frac{\rho^0}{\sqrt{2}} + \frac{\omega}{\sqrt{2}} & \rho^+ & K^{*+} \\ \rho^- & -\frac{\rho^0}{\sqrt{2}} + \frac{\omega}{\sqrt{2}} & K^{*0} \\ K^{*-} & \bar{K}^{*0} & \phi \end{pmatrix}_\mu \ . \tag{3.6}$$

Eq. (3.4) gives rise to the diagram of Fig. 3.1 a), and the three-vector term of Eq. (3.5) is needed in the vector-exchange diagram of Fig. 3.1 b) and c). In addition, we have the diagrams involving pseudoscalar mesons, as it is shown in Fig. 3.1 d). The diagrams a)-d) in Fig. 3.1 are the mechanisms that contribute to the s-wave potential of the vector-vector scattering and the input (V) of the Bethe-Salpeter equation. As we will show, the diagrams a) and b) are the strong part of the potential and produce bound states by themselves. The diagram of Fig. 3.1 d) gives essentially the imaginary part of the potential and thus, the decay width of the states. The diagram 3.1 c) is p-wave repulsive for equal particles and very weakly attractive potential in s-wave for different ones.

The vector-pseudoscalar-pseudoscalar vertex involved in the box diagram of Fig. 3.1 d) is provided by the same formalism given by the Lagrangian of Eq. (2.3) and is given by Eq. (2.16).

3.3 Spin and Isospin projection

In the way that we unitarize amplitudes, a resumation of loops is called for. This is implicit in the Bethe-Salpeter equation, Eq. (3.22).

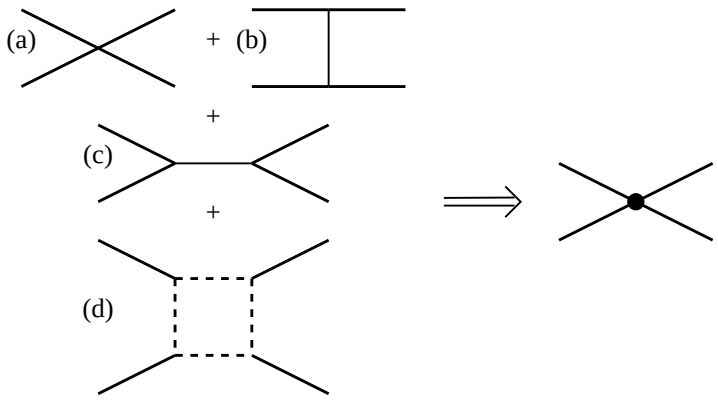

Figure 3.1: The mechanisms contributing to the tree-level vertex of vector-vector scattering, which appears as V in the Bethe-Salpeter equation, Eq. (3.22).

The problem that is treated here is the factorization of the spin structure in the loop series.

The structure of spin of the amplitude for $VV \to VV$ is a combination of the three possible contractions of the polarization vectors, $\epsilon_1^\mu \epsilon_{2\mu} \epsilon_3^\nu \epsilon_{4\nu}$, $\epsilon_1^\mu \epsilon_2^\nu \epsilon_{\mu 3} \epsilon_{4\nu}$ and $\epsilon_1^\mu \epsilon_{2\nu} \epsilon_3^\nu \epsilon_{4\mu}$. As all possible states have definite spin, we need to project the amplitudes into spin. To do so, one builds tensors of spin $= 0, 1, 2$. These are

$$\begin{aligned}
\mathcal{T}^{\mu\nu}_{(J=0)} &= \frac{1}{\sqrt{3}} \epsilon^\alpha \epsilon_\alpha g^{\mu\nu} \\
\mathcal{T}^{\mu\nu}_{(J=1)} &= \frac{1}{2}(\epsilon^\mu \epsilon^\nu - \epsilon^\nu \epsilon^\mu) \\
\mathcal{T}^{\mu\nu}_{(J=2)} &= \frac{1}{2}(\epsilon^\mu \epsilon^\nu + \epsilon^\nu \epsilon^\mu) - \frac{1}{3} \epsilon_l \epsilon^l g^{\mu\nu} \ ,
\end{aligned} \tag{3.7}$$

Under the approximation of neglecting the momentum of the external particles compared to the mass of the vector meson, i. e. $|\vec{q}|/M \sim 0$ we can neglect the ϵ^0 component, $\epsilon^0 \simeq 0$ and work with spatial components. With this approximation, the squared of these

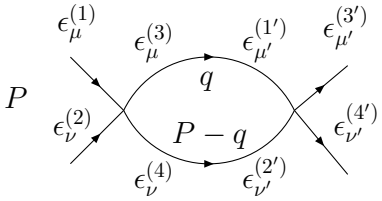

Figure 3.2: Loop function for two mesons.

spin tensors behave like projectors of spin $= 0, 1, 2$ that can be factorized in the loop series implicit in the Bethe Salpeter equation. In order to show this, let us take the loop diagram of Fig. 3.2 and treat the possible structures of contractions between polarization vectors. First, we have the combination

$$\epsilon_1^\alpha \epsilon_{2\beta} \epsilon_3^\alpha \epsilon_{4\beta} \epsilon_{1'}^{\alpha'} \epsilon_{2'\beta'} \epsilon_{3'}^{\alpha'} \epsilon_{4'\beta'} \ , \tag{3.8}$$

which can be simplified in our approximation since the indices α, β, α', β' are spatial and that makes all the indices are spatial. Thus, we have the factor

$$(\delta_{ii'} + \frac{q_i q_{i'}}{M_V^2})(\delta_{jj'} + \frac{q_j q'_j}{M_V^2}) \ . \tag{3.9}$$

In a renormalization scheme where the loop function can be expressed as a function of q, $f(q)$, multiplied by the two meson propagators, we can divide $f(q)$ into two terms, $f(q_{\rm on-shell})$ and $f(q) - f(q_{\rm on-shell})$. Obviously, the last term vanishes for $q = q_{\rm on-shell}$, and it cancels the singularity by tadpoles or otherwise renormalize the $\rho\rho$ potential. This implies that we can take only $f(q_{\rm on-shell})$ neglecting $\frac{q_i q_{i'}}{M_V^2}$.

Another different contribution to the diagram of Fig. 3.2 is

$$\epsilon_1^\alpha \epsilon_{2\alpha} \epsilon_3^\beta \epsilon_{4\beta} \epsilon_{1'}^{\alpha'} \epsilon_{2'\alpha'} \epsilon_{3'}^{\beta'} \epsilon_{4'\beta'} \ . \tag{3.10}$$

The argument to manipulate it is slightly different. We can distinguish three cases

i) $\beta = i, \alpha' = j'$ space like. The same argument done above leads to take only $\delta_{ij'}\delta_{ij'}$ and neglect $O(\vec{q}^2/M_V^2)$.

ii) $\beta = 0$, $\alpha' = i$ or vice versa. The remaining terms, $q^0(P-q)^0\vec{q}^2/M_V^4$, are of the order of $\vec{q}^2/M_V^2$ and therefore can be neglected.

iii) $\beta = 0, \alpha' = 0$. The factor

$$(-g_{00} + \frac{q_0 q_0}{M_V^2})(-g_{00} + \frac{(P-q)_0(P-q)_0}{M_V^2}) \ , \tag{3.11}$$

vanishes on shell up to terms of $\vec{q}^2/M_V^2$ which we also neglect.

From the above discussion, it follows that these structures in the series implicit in the Bethe Salpeter equation, result into three subseries where the following projectors factorize,

$$\begin{aligned}
\mathcal{P}^{(0)} &= \frac{1}{3}\epsilon_i^{(1)}\epsilon_i^{(2)}\epsilon_j^{(3)}\epsilon_j^{(4)} \\
\mathcal{P}^{(1)} &= \frac{1}{2}(\epsilon_i^{(1)}\epsilon_j^{(2)} - \epsilon_j^{(1)}\epsilon_i^{(2)})\frac{1}{2}(\epsilon_i^{(3)}\epsilon_j^{(4)} - \epsilon_j^{(3)}\epsilon_i^{(4)}) \\
\mathcal{P}^{(2)} &= \{\frac{1}{2}(\epsilon_i^{(1)}\epsilon_j^{(2)} + \epsilon_j^{(1)}\epsilon_i^{(2)}) - \frac{1}{3}\epsilon_l^{(1)}\epsilon_l^{(2)}\delta_{ij}\} \\
&\quad \times\{\frac{1}{2}(\epsilon_i^{(3)}\epsilon_j^{(4)} + \epsilon_j^{(3)}\epsilon_i^{(4)}) - \frac{1}{3}\epsilon_m^{(3)}\epsilon_m^{(4)}\delta_{ij}\} \ .
\end{aligned} \tag{3.12}$$

They correspond to spin projectors over spin $= 0, 1, 2$. Indeed, one can take states with a certain third component of the spin, write them in terms of spherical vectors $\pm\frac{1}{\sqrt{2}}(\epsilon_1 \pm i\epsilon_2)$ and ϵ_3 and see that these structures project over the three different states of spin spin $= 0, 1, 2$. It is convenient to write these projectors in covariant form although we keep in mind that we are dealing with spatial components. These

are:

$$\begin{aligned}
\mathcal{P}^{(0)} &= \frac{1}{3}\epsilon_\mu\epsilon^\mu\epsilon_\nu\epsilon^\nu \\
\mathcal{P}^{(1)} &= \frac{1}{2}(\epsilon_\mu\epsilon_\nu\epsilon^\mu\epsilon^\nu - \epsilon_\mu\epsilon_\nu\epsilon^\nu\epsilon^\mu) \\
\mathcal{P}^{(2)} &= \{\frac{1}{2}(\epsilon_\mu\epsilon_\nu\epsilon^\mu\epsilon^\nu + \epsilon_\mu\epsilon_\nu\epsilon^\nu\epsilon^\mu) - \frac{1}{3}\epsilon_\alpha\epsilon^\alpha\epsilon_\beta\epsilon^\beta\} \ . \qquad (3.13)
\end{aligned}$$

For the isospin projection we use the unitary normalization [51]. This implies that we add an extra factor $\frac{1}{\sqrt{2}}$ for each isospin state when identical particles are involved. Thus the isospin states for isospin $= 0, 1, 2$ are:

$$\begin{aligned}
|\rho\rho, I=0\rangle &= -\frac{1}{\sqrt{6}}|\rho^+(k_1\epsilon_1)\rho^-(k_2\epsilon_2) + \rho^-(k_1\epsilon_1)\rho^+(k_2\epsilon_2) \\
&\quad +\rho^0(k_1\epsilon_1)\rho^0(k_2\epsilon_2)\rangle \\
|\rho\rho, I=1, I_3=0\rangle &= -\frac{1}{2}|\rho^+(k_1\epsilon_1)\rho^-(k_2\epsilon_2) - \rho^-(k_1\epsilon_1)\rho^+(k_2\epsilon_2)\rangle \\
|\rho\rho, I=2, I_3=0\rangle &= -\frac{1}{\sqrt{2}}|\frac{1}{\sqrt{6}}(\rho^+(k_1\epsilon_1)\rho^-(k_2\epsilon_2) + \rho^-(k_1\epsilon_1)\rho^+(k_2\epsilon_2)) \\
&\quad -\sqrt{\frac{2}{3}}\rho^0(k_1\epsilon_1)\rho^0(k_2\epsilon_2)\rangle \ . \qquad (3.14)
\end{aligned}$$

Where we have have taken the normal phase convention $|\rho^+\rangle = -|1,1\rangle$.

3.4 S-wave scattering amplitudes

In this section we will evaluate the amplitudes of the diagrams of Fig. 3.1 a), b) and c) and project them into s-wave, spin and isospin. For the vector exchange diagram depicted in Fig. 3.1 b), particularly for

the $\rho^+\rho^- \to \rho^+\rho^-$ reaction shown in Fig. 3.3 we get

$$\begin{aligned} -it^{(ex)} &= -\sqrt{2}g\{(i(k_1-k_3)_\mu\epsilon_\nu^{(0)} - i(k_1-k_3)_\nu\epsilon_\mu^{(0)})\epsilon^{(1)\mu}\epsilon^{(3)\nu} \\ &+(-ik_{1\mu}\epsilon_\nu^{(1)} + ik_{1\nu}\epsilon_\mu^{(1)})\epsilon^{(3)\mu}\epsilon^{(0)\nu} \\ &+(ik_{3\mu}\epsilon_\nu^{(3)} - ik_{3\nu}\epsilon_\mu^{(3)})\epsilon^{(0)\mu}\epsilon^{(1)\nu}\} \times \frac{i}{(k_1-k_3)^2 - M_\rho^2 + i\epsilon} \\ &\times(-\sqrt{2})g\{(-i(k_2-k_4)_{\mu'}\epsilon_{\nu'}^{(0)} + i(k_2-k_4)_{\nu'}\epsilon_{\mu'}^{(0)})\epsilon^{(4)\mu'}\epsilon^{(2)\nu'} \\ &+(ik_{4\mu'}\epsilon_{\nu'}^{(4)} - ik_{4\nu'}\epsilon_{\mu'}^{(4)})\epsilon^{(2)\mu'}\epsilon^{(0)\nu'} + (ik_{2\mu'}\epsilon_{\nu'}^{(2)} \\ &+ik_{2\nu'}\epsilon_{\mu'}^{(2)})\epsilon^{(0)\mu'}\epsilon^{(4)\nu'}\} \ . \end{aligned} \tag{3.15}$$

where the form of the three-vector term is shown explicitly, $-it^{(3V)} = -\sqrt{2}g\{...\}$. In our approximation, the three momentum of the external particles is small and neglected, and we keep only spatial components of the polarization vectors for external legs. This means that all the terms involving $k_{i\mu}\epsilon_j^\mu$, being i,j the indices for the particles i,j = 1-4 are neglected and those terms involving the polarization vector of the internal meson $k_{i\mu}\epsilon^{(0)\mu}$ remain (note that these approximations are the same that one would do for the interaction of a vector with a pseudoscalar meson and lead to the local chiral Lagrangians of [15, 54, 55] used to generate the axial vector mesons in [54, 55]). As a consequence, our amplitude gets much more simplified and we obtain

$$-it^{(ex)} = \frac{2ig^2}{M_\rho^2}(k_1+k_3)\cdot(k_2+k_4)\epsilon_\mu\epsilon_\nu\epsilon^\mu\epsilon^\nu \ , \tag{3.16}$$

or, in terms of Lorentz invariant variables,

$$-it^{(ex)} = \frac{2ig^2}{M_\rho^2}(s-u)\epsilon_\mu\epsilon_\nu\epsilon^\mu\epsilon^\nu \ . \tag{3.17}$$

In order to project the amplitude into s-wave, we shall do a partial wave expansion of the amplitude

$$T = \sum_l (2l+1) f_l(s) P_l(x) \ , \tag{3.18}$$

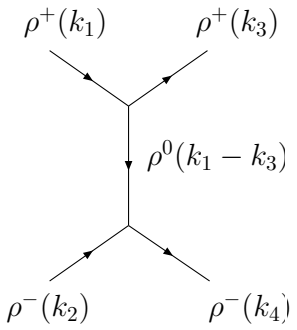

Figure 3.3: Vector exchange diagram for $\rho^+\rho^- \to \rho^+\rho^-$.

where $x = cos\theta$, being θ the center of mass scattering angle, and P_l the Legendre polynomials. Hence, the s-wave projection of the scattering amplitude is

$$f_{l=0}(s) = \frac{1}{2}\int_{-1}^{1} T(s, t(x'), u(x'))P_{l=0}(x')dx' \ . \tag{3.19}$$

The $l = 0$ partial wave is what we will call potential V_{ij}. The kinematical variable u in Eq. (3.17) can be expressed as $u = 2(m_\rho^2 - E_1E_4 + |\vec{k}_1||\vec{k}_4|x)$ with $x = cos\theta$. When performing the integral, the term proportional to x vanishes, and $E_1 = E_4 = \sqrt{s}/2$. Altogether, the three-level on-shell an s-wave amplitude is

$$V_{ij}(s) = -\frac{4g^2}{m_\rho^2}(\frac{3}{4}s - m_\rho^2)\epsilon_\mu\epsilon_\nu\epsilon^\mu\epsilon^\nu \ . \tag{3.20}$$

Once we have calculated the potential, one proceeds to calculate its projection in isospin and spin following the explanations given in the previous section. These spin-isospin projected amplitudes are listed in Table 3.1.

For the cases $(I, S) = (0, 1), (1, 0), (1, 2)$ and $(2, 1)$, not listed in the table, the potential is zero, which is consistent with the rule

I	J	Contact	Exchange	$\sim$ Total$[I^G(J^{PG})]$
1	1	$6g^2$	$-4g^2(\frac{3s}{4M_\rho^2}-1)$	$-2g^2[1^+(1^{+-})]$
0	0	$8g^2$	$-8g^2(\frac{3s}{4M_\rho^2}-1)$	$-8g^2[0^+(0^{++})]$
0	2	$-4g^2$	$-8g^2(\frac{3s}{4M_\rho^2}-1)$	$-20g^2[0^+(2^{++})]$
2	0	$-4g^2$	$4g^2(\frac{3s}{4M_\rho^2}-1)$	$4g^2[0^+(2^{++})]$
2	2	$2g^2$	$4g^2(\frac{3s}{4M_\rho^2}-1)$	$10g^2[0^+(2^{++})]$

Table 3.1: V for the different spin isospin channels. The approximate total is calculated at threshold.

for identical particles $L+S+I=$ even. From the table we observe that there is attraction for the cases $(I,S)=(1,1);(0,0)$; and $(0,2)$, whereas for $(I,S)=(2,0)$ and $(2,2)$ the potential is repulsive. We observe that the attraction obtained in the $(I,S)=(1,1)$ is much smaller than for $(I,S)=(0,0)$ and $(0,2)$. This case is special because the quantum numbers of a possible resonance obtained here, $I^G(J^{PC})=1^+(1^{+-})$, are exactly the quantum numbers of the $b_1(1235)$. This state is generated dynamically from the interaction of vector mesons with pseudoscalar ones, being the $K\bar{K}^*$ channel the dominant channel. The fact that the $\rho\rho$ attraction for these quantum numbers is small tell us that this channel would have a small effect in the dynamics of the $b_1(1235)$ resonance, dominated by the $K\bar{K}^*$ interaction. Nevertheless, this weak attraction can lead to a broad resonance at higher energies as we will see at the end of this Chapter when we extend this study to the nonet of vector mesons.

It is interesting to see that we cannot generate $I=2$ low lying states since the $\rho\rho$ interaction is repulsive there. On the contrary, we find a large attraction for $(I,S)=(0,2)$ and a smaller one for $(I,S)=(0,0)$, which anticipates that a possible bound $\rho\rho$ state from this interaction will be much deeper bound for $(I,S)=(0,2)$ than for

$(I,S)=(0,0)$. The same trend is actually followed by the $f_0(1370)$ and $f_2(1270)$ resonances. It is also worth mentioning that the exchange diagrams are mostly responsible of the final attraction found but due to the contact term these states are not degenerate in mass.

Regarding the influence of the $\omega\rho$ or $\omega\omega$ channels in the calculations, it is easy to see that there is no $\omega-\rho$ mixing in this picture. This is the fact that three-vector vertices mixing ω and ρ like $\rho\omega\omega$ and $\rho\rho\omega$ violate isospin and $G-$parity respectively, and as a consequaence, there are no three-vector contact term involving the ω meson. Besides that, the four-vector contact term with ω is also zero.

We can also build s-channel ρ-exchange diagrams like in Fig. 3.4. We obtain an amplitude for $(I,S)=(1,0)$ of the type

$$V^{(s)}=24g^2\frac{1}{(k_1+k_2)^2-M_\rho^2}\vec{k}_1\cdot\vec{k}_3\ . \tag{3.21}$$

However, this is a p-wave amplitude and repulsive which is also consistent with the rule $L+S+I=$ even.

The results obtained for the $\rho\rho$ potential (contact + exchange terms, see Table 3.1) provide the kernel (V) of the Bethe-Salpeter equation, that in its on-shell factorized form becomes [43, 52, 77]

$$T=V+VGT=[1-VG]^{-1}V\ , \tag{3.22}$$

where G is the two-ρ loop function:

$$G=\int_0^{q_{max}}\frac{q^2dq}{(2\pi)^2}\frac{\omega_1+\omega_2}{\omega_1\omega_2[(P^0)^2-(\omega_1+\omega_2)^2+i\epsilon]}\ , \tag{3.23}$$

where q_{max} stands for the cutoff, $\omega_i=(\vec{q}_i^{\,2}+m_i^2)^{1/2}$ and the center-of-mass energy $(P^0)^2=s$. In the present case of the $\rho\rho$ interaction we use the formula Eq. (3.23) with two different values of the cutoff, 875 and 1000 MeV/c but in Section 3.10 the formula of Eq. (3.45) will be used instead of this.

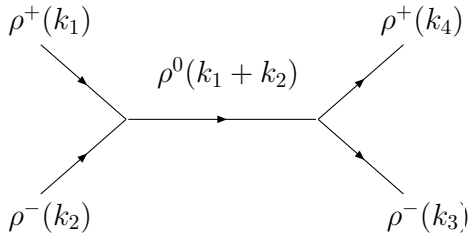

Figure 3.4: S-channel ρ exchange diagram.

The positions of the poles found when we implement the potential V of Table 3.1 as input of Eq. (3.22) are shown in Table 3.2. We want to stress that only one parameter, the cutoff of the integral, $q_{\max}$, which is around 1 GeV, was needed to get these states. We find two $\rho\rho$ bound states with masses 1255 and 1512 and zero width. Thus, as the strength of the potential for spin = 2 is bigger than for spin = 0, the state with spin = 2 is more bound. Additionally, we observe that the binding of the tensor state is more sensitive to the cutoff than the scalar state. Yet, reasonable changes of $q_{\max}$ around 1 GeV revert into changes of about 50 MeV in the binding for the tensor state and 20 MeV for the scalar one.

		$\sqrt{s}$ [MeV]	
I	J	$[q_{max} = 875\,\mathrm{MeV}/c]$	$[q_{max} = 1000\,\mathrm{MeV}/c]$
0	0	1512	1491
0	2	1255	1195

Table 3.2: Pole positions for the two different channels

3.5 Convolution of the two-meson loop function

We have seen that the use of only the potential of Table 3.1 in Eq. (3.22) leads to bound states (below threshold) with zero width. However, the widths of the $f_0(1370)$ and $f_2(1270)$ quoted in the PDG [78] are large (around 200 MeV) and they come mainly from decays to pseudoscalar mesons like two or four pions. Thus, the consideration of pions is crucial to describe adequately the properties of these states. One of the mechanisms that takes into consideration the decay to pseudoscalars is to convolute the G-function, in this way, one includes the large width of the ρ-meson in the calculation. The fact that the ρ-meson has a large width, $\Gamma_\rho = 146.2$ MeV, implies that this meson has a mass distribution, and thus, the states obtained decay in $2\rho's$ for the low mass components of the ρ mass distribution. To do so, one replaces G by $\tilde{G}$ given by

$$\begin{aligned}\tilde{G}(s) &= \frac{1}{N^2}\int_{(m_\rho-2\Gamma_\rho)^2}^{(m_\rho+2\Gamma_\rho)^2} d\tilde{m}_1^2(-\frac{1}{\pi})\mathcal{I}m\frac{1}{\tilde{m}_1^2 - m_\rho^2 + i\Gamma\tilde{m}_1} \\ &\times\int_{(m_\rho-2\Gamma_\rho)^2}^{(m_\rho+2\Gamma_\rho)^2} d\tilde{m}_2^2(-\frac{1}{\pi})\mathcal{I}m\frac{1}{\tilde{m}_2^2 - m_\rho^2 + i\Gamma\tilde{m}_2} \\ &\times G(s,\tilde{m}_1^2,\tilde{m}_2^2)\ , \end{aligned} \tag{3.24}$$

with

$$N = \int_{(m_\rho-2\Gamma_\rho)^2}^{(m_\rho+2\Gamma_\rho)^2} d\tilde{m}_1^2(-\frac{1}{\pi})\mathcal{I}m\frac{1}{\tilde{m}_1^2 - m_\rho^2 + i\Gamma\tilde{m}_1}\ , \tag{3.25}$$

where $\Gamma_\rho = 146.2\,MeV$ and for $\Gamma \equiv \Gamma(\tilde{m})$ we take the ρ width for the decay into the pions in p-wave

$$\Gamma(\tilde{m}) = \Gamma_\rho(\frac{\tilde{m}^2 - 4m_\pi^2}{m_\rho^2 - 4m_\pi^2})^{3/2}\theta(\tilde{m} - 2m_\pi) \tag{3.26}$$

The use of $\tilde{G}$ in Eq. (3.22) provides some width to the states. In Fig. 3.5 we show the results for $|T|^2$ obtained by considering the ρ

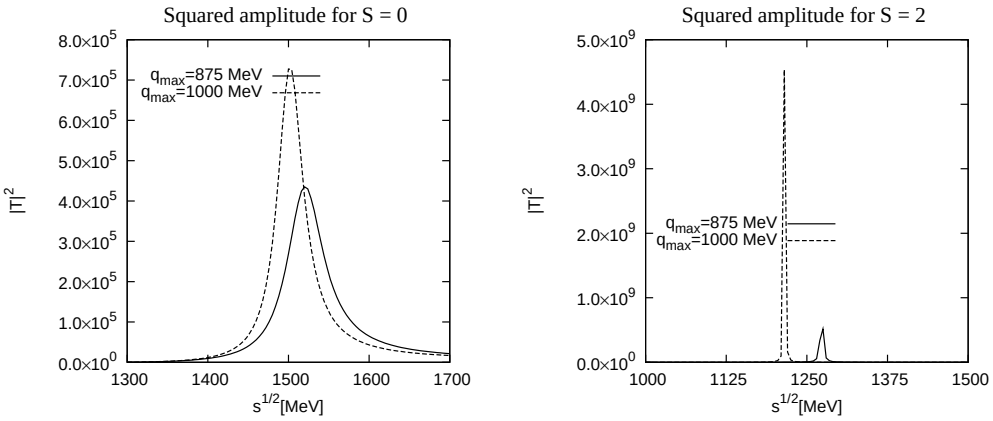

Figure 3.5: $|T|^2$ taking into account the ρ mass distribution for $S = 0$ and $S = 2$.

mass distribution. We show the results for the two cut offs of Table 3.2. As we can see in the figure, the matching of the mass of the $f_2(1270)$ is obtained with a cut off $q_{max} = 875\, MeV/c$. Then we obtain 1532 MeV for the energy of the $S = 0$ state that we would like to associate to the $f_0(1370)$. Given, large dispersion of masses of the $f_0(1370)$, the results obtained by us would be consistent with the present experimental observation. We see that $|T|^2$ has a good Breit Wigner distribution in both cases, with a peak around the masses shown in Table 3.2, but changed slightly. However, the widths are relatively small. For the tensor state one finds a width of about $2 - 3\, MeV$ and for the scalar state the width is about $50 - 75\, MeV$, depending on the cut off.

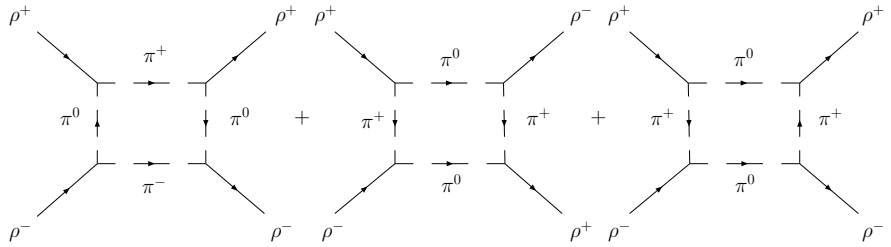

Figure 3.6: Diagrams considered for $\rho\rho \to \pi\pi$.

3.6 Consideration of the two pion decay mode

As we will see in the results section, the convolution of the G function provide some width to the states. Nevertheless, it is still very small compared to the large width of the $f_0(1370)$ and $f_2(1270)$. Therefore, one should consider more different decay mechanisms with pions. For the $\rho\rho$ states that we are concern with, the diagrams of Fig. 3.6 provide such mechanisms and, indeed, the $\rho\pi\pi$ vertex is provided by the Lagrangian of Eq. (2.3),

$$\mathcal{L}_{VPP} = -ig\langle V^\mu [P, \partial_\mu P]\rangle \ . \tag{3.27}$$

For the diagram of Fig. 3.7, we have

$$\begin{aligned} -it^{(\pi\pi)} \ = \ & \int \frac{d^4q}{(2\pi)^4}(-i)(\sqrt{2}g)^4 (q-k_1+q)^\mu \, \epsilon_{1\mu} \\ & \times i(k_1 - q + P - q)_\nu \, \epsilon_2^\nu i(k_3 - q - q)_\alpha \, \epsilon_3^\alpha \\ & \times (-i)(q - k_3 - P + q)_\beta \, \epsilon_4^\beta \\ & \times \frac{i}{q^2 - m_\pi^2 + i\epsilon} \, \frac{i}{(k_1 - q)^2 - m_\pi^2 + i\epsilon} \\ & \times \frac{i}{(P-q)^2 - m_\pi^2 + i\epsilon} \, \frac{i}{(k_3 - q)^2 - m_\pi^2 + i\epsilon} \ . \end{aligned} \tag{3.28}$$

Under the approximation of neglecting the momentum respect to the vector-meson mass, all the polarization vectors are spatial and we

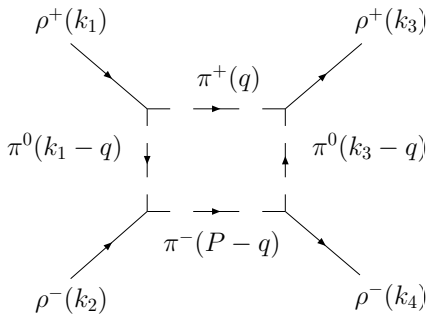

Figure 3.7: Detail of one of the diagrams of fig. 3.6.

can rewrite the amplitude as

$$\begin{aligned} -it^{(\pi\pi)} &= (\sqrt{2}g)^4 \int \frac{d^4q}{(2\pi)^4} 16\, q_i q_j q_l q_m\, \epsilon_{1i}\epsilon_{2j}\epsilon_{3l}\epsilon_{4m} \\ &\times \frac{1}{q^2-m_\pi^2+i\epsilon}\,\frac{1}{(k_1-q)^2-m_\pi^2+i\epsilon} \\ &\times \frac{1}{(P-q)^2-m_\pi^2+i\epsilon}\,\frac{1}{(k_3-q)^2-m_\pi^2+i\epsilon}\ , \end{aligned} \tag{3.29}$$

this integral is logarithmically divergent, and in the absence of data to fit the subtraction constant if using dimensional regularization, we regularise it with a cutoff in the three momentum, that should be of the order of the basic scale at the energies that we work in, 1 GeV. For this purpose, we perform the q^0 integral analytically performing exactly the divisions by factors with undefined polarity ($\pm i\epsilon$ in the denominators). By doing some algebraic manipulations, we obtain

$$\begin{aligned} V^{(\pi\pi)} &= (\sqrt{2}g)^4\ (\epsilon_{1i}\epsilon_{2i}\epsilon_{3j}\epsilon_{4j}+\epsilon_{1i}\epsilon_{2j}\epsilon_{3i}\epsilon_{4j}+\epsilon_{1i}\epsilon_{2j}\epsilon_{3j}\epsilon_{4i}) \\ &\times \frac{8}{15\pi^2}\int_0^{q_{max}} dq\,\vec{q}^{\,6}\,\{10\omega^2-(k_3^0)^2\}\frac{1}{\omega^3}\left(\frac{1}{k_1^0+2\omega}\right)^2 \\ &\times \frac{1}{P^0+2\omega}\,(\frac{1}{k_1^0-2\omega+i\epsilon})^2\frac{1}{P^0-2\omega+i\epsilon}\ , \end{aligned} \tag{3.30}$$

with $\omega = \sqrt{\vec{q}^2 + m_\pi^2}$. This expression shows explicitly the two sources of imaginary part in the cuts $k_1^0 - 2\omega = 0$ and $P^0 - 2\omega = 0$, corresponding to $\rho \to \pi\pi$ and $\rho\rho \to \pi\pi$. The double pole of Eq. (3.30) can be easily removed by taking into account the mass distribution of the ρ meson. A simpler approach, and accurate enough for our purposes is to substitute the double pole, $(k_1^0 - 2\omega + i\epsilon)^2$, by $(k_1^0 - 2\omega + \Gamma/4 + i\epsilon)(k_1^0 - 2\omega - \Gamma/4 + i\epsilon)$. In practice, the results barely change if we put $\Gamma/2$ instead of $\Gamma/4$ or some reasonable number of the size of the ρ width. The potential of Eq. (3.30) is easily extended to other charges of ρ and π mesons and must be projected in isospin and spin, and we are only interested in $I = 0$, for which the $\rho\rho$ potential of the former sections is attractive. Thus, the isospin-spin projected amplitude of the $\rho\rho$-box diagram is

$$\begin{aligned} t^{(2\pi, I=0, S=0)} &= 20\, \tilde{V}^{(\pi\pi)} \\ t^{(2\pi, I=0, S=2)} &= 8\, \tilde{V}^{(\pi\pi)} \end{aligned} \tag{3.31}$$

where $\tilde{V}^{(\pi\pi)}$ is given by the Eq. (3.30) but removing the polarization vectors. The diagrams like in Fig. 3.6 do not have spin one. This is because the ρ meson is in s-wave and thus the parity of the $\rho\rho$ system is positive, this forces the two pions to be in $L = 0, 2$, and then, since the pions have no spin, $J = L$ and only the quantum numbers $0^+, 2^+$ are possible.

We will see in the next section that the real part of this potential is much smaller than the $\rho\rho$ potential of Table 3.1 coming from the contact + exchange terms and can be neglected.

In the computation of Eq. (3.31) for the box diagrams we consider that the π exchange between two ρ mesons in the t-channel is mostly off shell and implement empirical form factors for the $\rho\pi\pi$ vertex [79, 80] like

$$F(q) = \frac{\Lambda^2 - m_\pi^2}{\Lambda^2 - (k-q)^2} \tag{3.32}$$

in each $\rho \to \pi\pi$ vertex with

$$k^0 = \frac{\sqrt{s}}{2}\ , \quad \vec{k} = 0\ , \quad q^0 = \frac{\sqrt{s}}{2}\ , \tag{3.33}$$

and $\vec{q}$ the running variable in the integral. We use several values of Λ in Eq. (3.32) between $1200 - 1300$ MeV [79, 80] and a cutoff of $q_{\rm max} = 1.2$ GeV in the integral of Eq. (3.30) which does not affect the imaginary part of the potential, that plays the important role in our calculation.

3.7 Decays to 4π's and 2ω's

There are also other contributions to the widths of the $\rho\rho$ states (but we anticipate they are smaller) apart from decays into two pions. One of them is the decay to four pions that can be considered by means of crossed box diagrams like in Fig. 3.8. The evaluation of the diagram in Fig. 3.8 can be done similarly to the box diagram with two pions in the intermediate state discussed in the previous section. As a result, the amplitude of the diagram in Fig. 3.8 obtained is

$$\begin{aligned} t^{(2\pi(c),I=0,S=0)} &= 5\,\tilde{V}^{(c,\,\pi\pi)} \\ t^{(2\pi(c),I=0,S=2)} &= 2\,\tilde{V}^{(c,\,\pi\pi)}\ , \end{aligned} \tag{3.34}$$

with

$$\begin{aligned} \tilde{V}^{(c,\,\pi\pi)} &= \frac{16\,g^4}{15\pi^2}\int_0^{q_{max}} dq\,\vec{q}^{\,6}\,\{20\omega^2-(k_1^0)^2\}\frac{1}{\omega^3} \\ &\times\left(\frac{1}{k_1^0+2\omega}\right)^3\frac{1}{k_1^0+\frac{\Gamma}{4}-2\omega+i\epsilon} \\ &\times\frac{1}{k_1^0-\frac{\Gamma}{4}-2\omega+i\epsilon}\frac{1}{k_1^0-2\omega+i\epsilon}\ . \end{aligned} \tag{3.35}$$

Furthermore, diagrams with 2ω's in the intermediate state are also possible and they are depicted in Fig. (3.9). The vertex $\rho\omega\pi$ involved in these diagrams is anomalous and with the renormalization that we use [81] is given by

$$\mathcal{L}_{VVP} = \frac{G'}{\sqrt{2}}\epsilon^{\mu\nu\alpha\beta}\langle\partial_\mu V_\nu\partial_\alpha V_\beta\,P\rangle \tag{3.36}$$

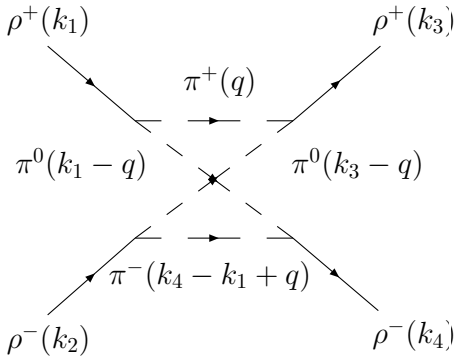

Figure 3.8: Crossed-box diagram for the four pion decay mode.

with

$$G' = \frac{3g'^2}{4\pi^2 f}, \qquad g' = -\frac{G_V M_\rho}{\sqrt{2} f^2} \ , \tag{3.37}$$

where $G_V \simeq 55\, MeV$ and $f_\pi = 93\, MeV$. Assuming $\vec{k}_{i,j} \simeq 0$ one obtains:

$$-it_{\rho\omega\pi} = iG' M_\rho \, \epsilon_{ijk} \, q_i \, \epsilon_j(\omega) \, \epsilon_k(\rho^+) \ . \tag{3.38}$$

The final expression of the amplitude of the diagrams in Fig. 3.9 is given by

$$\begin{aligned} t^{(\omega\omega, I=0, S=0)} &= 30\, \tilde{V}^{(\omega\omega)} \\ t^{(\omega\omega, I=0, S=2)} &= 21\, \tilde{V}^{(\omega\omega)} \ . \end{aligned} \tag{3.39}$$

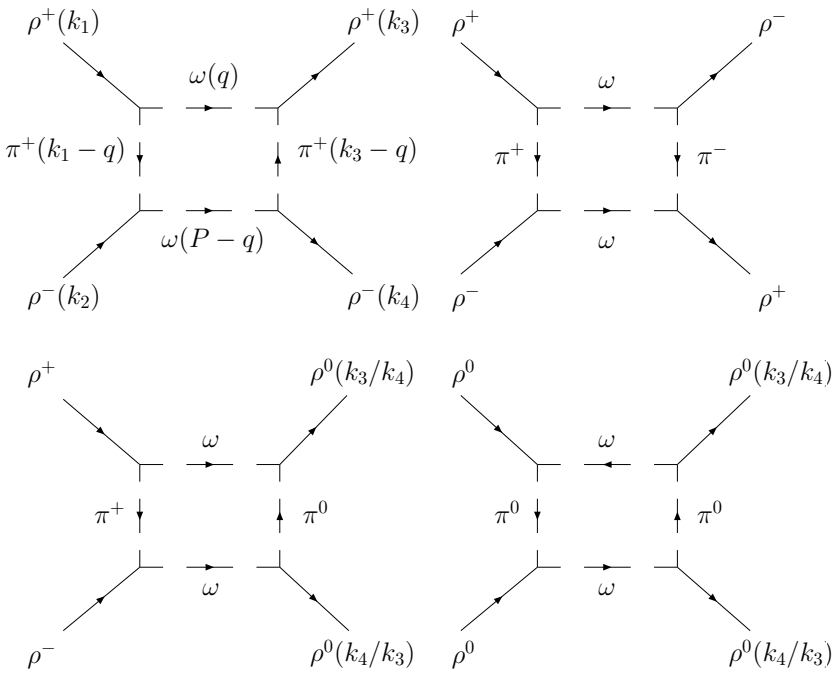

Figure 3.9: Anomalous-box diagrams for the two omega intermediate state.

with

$$\begin{aligned}\tilde{V}^{(\omega\omega)} &= -\frac{1}{30\,\pi^2}\,M_\rho^4\,G'^4\int_0^{q_{max}} dq\,\vec{q}^{\,4} \\ &\times(-\omega_\pi^3+k_3^{0^2}\omega_\omega-4\,\omega_\pi^2\omega_\omega-4\,\omega\omega_\omega^2-\omega_\omega^3) \\ &\times\frac{1}{(k_1^0+\omega_\omega+\omega)^2}\,\frac{1}{(k_1^0+\frac{\Gamma}{4}-\omega_\omega-\omega+i\epsilon)} \\ &\times\frac{1}{(k_3^0-\frac{\Gamma}{4}-\omega_\omega-\omega+i\epsilon)} \\ &\times\frac{1}{\omega_\pi^3}\,\frac{1}{(P^0-2\omega_\omega+i\epsilon)}\,\frac{1}{(P^0+2\omega_\omega)}\,\frac{1}{\omega_\omega} \end{aligned} \tag{3.40}$$

with $\omega_\omega=\sqrt{\vec{q}^{\,2}+m_\omega^2}$. The different contributions, contact + ρ exchange, $\pi\pi$ box, 4π- crossed box and $\omega\omega$ are shown in Fig. 3.10 for (isospin $=0$; spin $=0$) and (isospin $=0$, spin $=2$). In the evaluation of the integrals of Eqs. (3.30), (3.35) and (3.40), we use $q_{\rm max}=1200$ MeV and we omit the use of the form factors in the pictures for the sake of simplicity. For spin $=2$, we see that the most important contribution comes from the contact + ρ-exchange terms whereas the real parts of the $\pi\pi$, 2ω, 4π-crossed box and 2ω potentials turns out to be negligible. The case of spin $=0$ is slightly more complicated. We observe that the individual contributions of the $\pi\pi$-box, 4π-crossed box and 2ω diagrams are comparatively larger than in the case of spin $=2$. Despite of this, we find a good cancellation of the $\pi\pi$ box plus 4π-crossed box and the anomalous 2ω box term, and, finally, the interaction is dominated by the conctact plus ρ-exchange terms. Although, due to the relatively large contribution of the separate terms we admit larger uncertainties in the position of the $f_0(1370)$ state than for the $f_2(1270)$. Concerning the imaginary parts, we observe that the imaginary part for the $\pi\pi$ box is considerably larger than for the 4π-crossed and 2ω boxes, and we obtain that the 4π-crossed box only accounts for the 20% of the $\pi\pi$ box, while the anomalous-$\omega\omega$ box does not contribute in the region of interest.

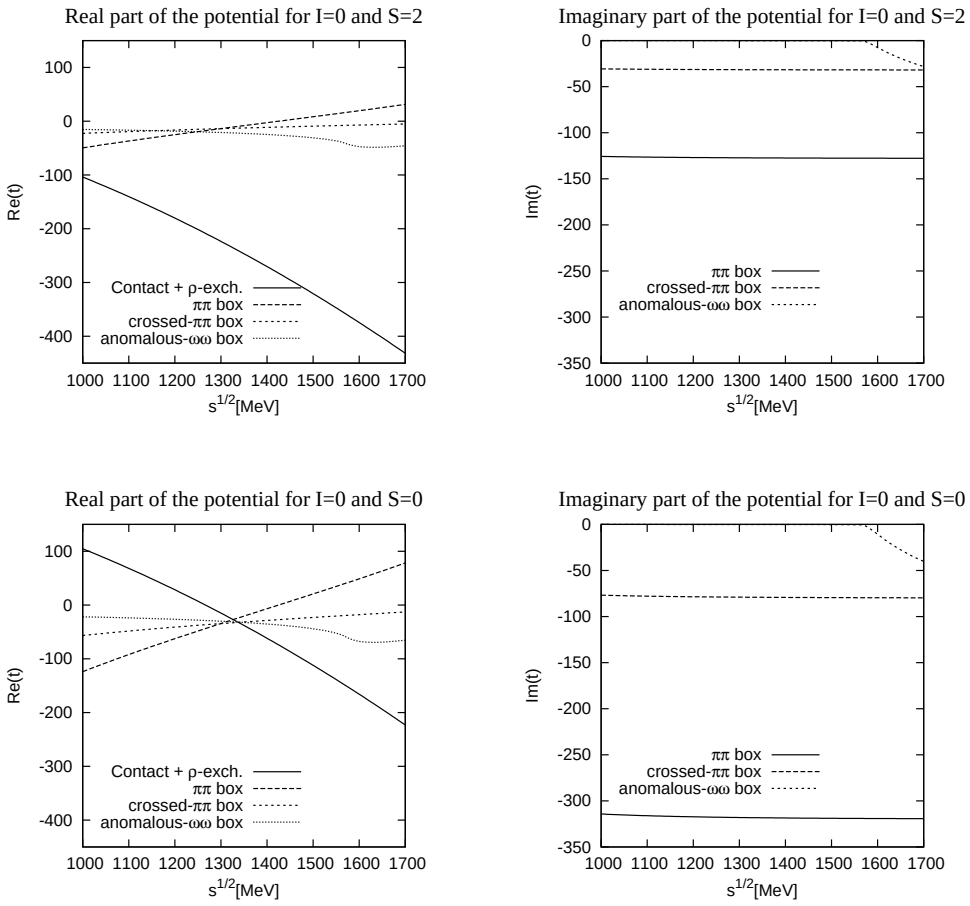

Figure 3.10: Comparison of the real and imaginary parts of the different potentials for $I = 0$, $S = 2$ and $I = 0$, $S = 0$.

3.8 Results

In Sections 3.4 and 3.5 we obtained the pole positions after including the potential of Table 3.1 in Eq. (3.22) using G or $\tilde{G}$ respectively (Eqs. (3.23) and (3.24)) for two different cutoffs, $q_{\rm max} = 875$ and 1000 MeV. Experimentally, we have $\Gamma(f_2(1270)) = 184.4^{+3.9}_{-2.5}$ MeV and $\Gamma(f_0(1370)) = 200 - 500$ MeV. These widths come 84.7% and 20% respectively from decays into two pions. In what follows we include the additional mechanisms studied in Section 3.6 which give rise to the broadening of the theoretical states of Sections 3.4 and 3.5. We saw that the diagrams of Fig. 3.9 did not account for imaginary part and the 4π-crossed box diagram in Fig. 3.8 turns out to be 20% of the $\pi\pi$-box diagram and we have some uncertainties due to the use of the form factor of the pseudoscalar-pseudoscalar-vector vertex which can reabsorb the small contribution varying the Λ parameter. Thus, we show the final $|T|^2$ matrix without including the 4π-crossed and 2ω boxes for Λ's$= 1200 - 1400$ MeV in Fig. (3.11). We observe that as Λ grows, the widths of the states becomes larger. This give us an idea of the theretical uncertainties. Yet, both states, the $f_2(1270)$ and the $f_2(1370)$ are reproduced with a reasonable agreement with the experimental data for the width and mass. In Fig. 3.12 we show the amplitudes for two different values of the cutoff used in Eq. (3.23), $q_{\rm max} = 875$ and 1000 MeV for the middle option, $\Lambda = 1300$ MeV in Eq. (3.32). In Table 3.3 we summarize the theoretical results compared to the experiment extracted from Fig. 3.12.

Experimentally, 85% of the $f_2(1270)$ width comes from $\pi\pi$ decay, this means $\Gamma_{\pi\pi} = 156$ MeV, which is in fair agreement with our findings. On the other hand, we said that the 4π-crossed box diagram accounted for the 20% of the $\pi\pi$ box diagram, this gives $\Gamma(f_0(1370) \to 4\pi)/\Gamma(f_0(1370) \to 2\pi) = 0.20$, which is in good agreement with the interval $0.10 - 0.25$ given in the recent reference [82]. Even though the PDG gives the averaged mass around 1370 MeV, the Belle Collaboration suggest that the peak appears around 1470 MeV [83]. Notice also that this state cannot be associated to the

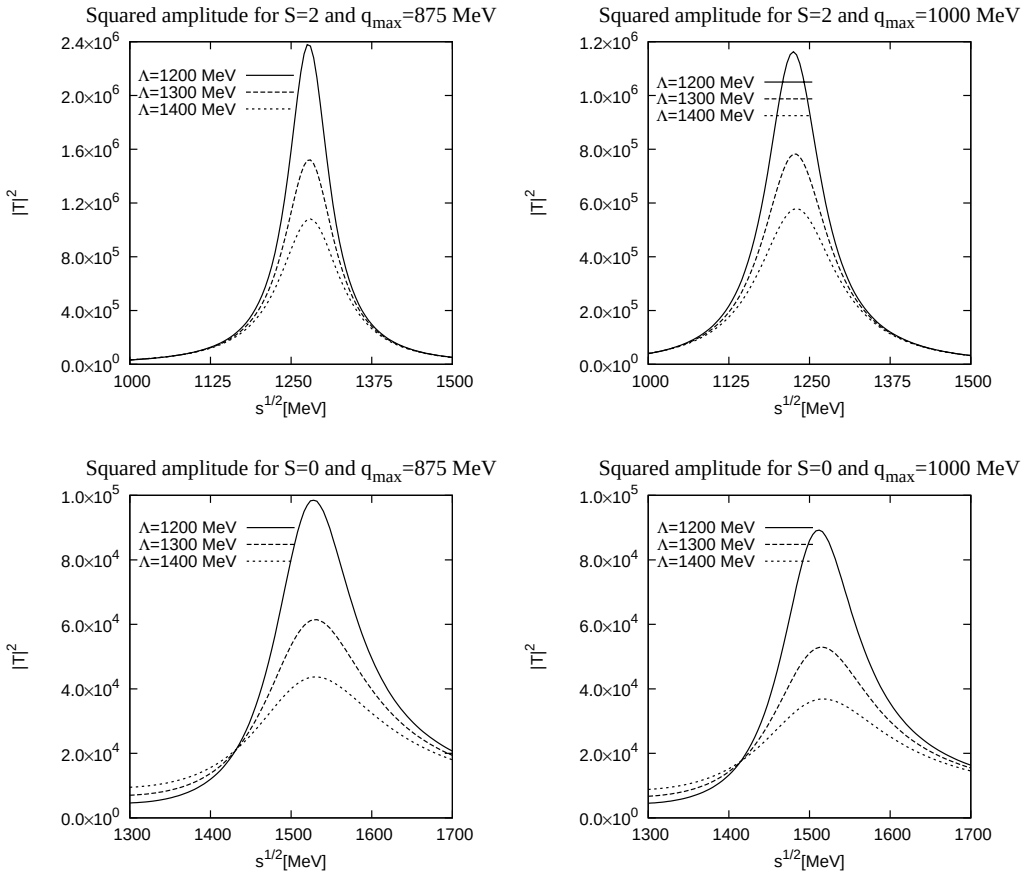

Figure 3.11: $|T|^2$ taking into account the $\pi\pi$ box for different values of $\Lambda = 1200, 1300, 1400\, MeV$ and $q_{max} = 875, 1000\, MeV$ for $S = 0$ and $S = 2$

	Theory		Experiment	
(I, J)	M[MeV]	Γ[MeV]	M[MeV]	Γ[MeV]
$(0, 0)$	1532	212	1200 to 1500	200 to 500
$(0, 2)$	1275	100	1275.1 ± 1.2	$185.1^{+2.9}_{-2.4}$

Table 3.3: Comparison to the experiment (mass and width measured from the line "$q_{\max} = 875$ MeV" in Fig. 3.12).

$f_0(1500)$ since although its width is around 100 MeV, only the 35% corresponds to $\pi\pi$. The $f_0(1500)$ is identified with a glueball in [84].

3.9 Conclusions

We have seen that the study of the $\rho\rho$ interaction using the hidden gauge formalism leads to a strong attraction, enough to bind the system, in the isospin $= 0$; spin $= 0$ and isospin $= 0$; spin $= 2$ sectors. We have also found that in the case of isospin $= 0$, spin $= 2$ the interaction was more attractive, giving rise to a tensor state more bound than the scalar. The consideration of the ρ mass distribution provides little width to the two states (decay into four pseudoscalars), much smaller for the tensor state due to its large binding. The biggest source of width comes from the decay into $\pi\pi$ by means of the box diagrams like in Fig. (3.6) that we have also studied within the same formalism. The agreement with the mass and width for the $f_0(1370)$ and $f_2(1270)$ is good and therefore the assignment to these states is done. The findings of the paper give a strong support to the idea that these two resonances are dynamically generated from the $\rho\rho$ interaction, or in other words, that they qualify largely as $\rho\rho$ molecules.

In the following we extend this study to the nonet of vector mesons and thus, the interaction can provide $K^*\bar{K}^*$ or ρK^* bound states or

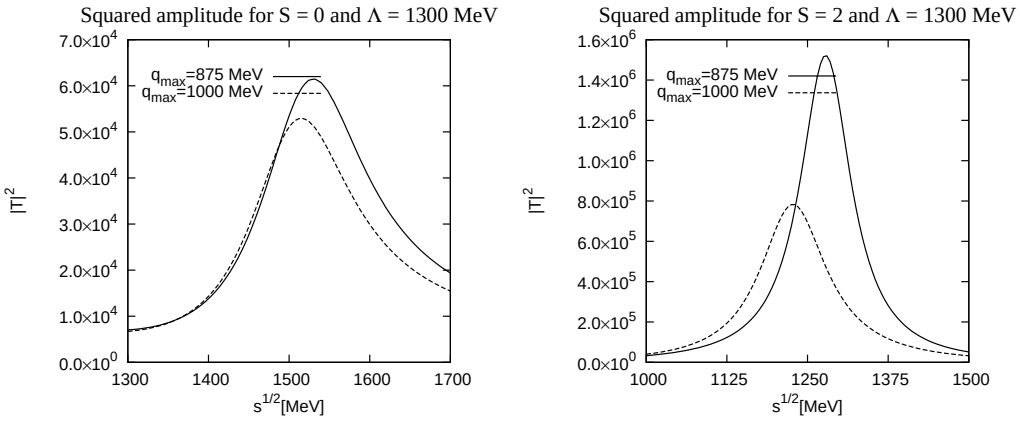

Figure 3.12: $|T|^2$ taking into account the $\pi\pi$ box with $\Lambda = 1300\,MeV$, $q_{max} = 875, 1000\,MeV$ for $S = 0$ and $S = 2$.

resonances, as we will see.

3.10 The vector-vector interaction for the nonet of vector mesons

In this section we extend the study made for two ρ's interacting to the nonet of vector mesons. Thus we treat the interaction not only between ρ mesons but also between ρ and K^* mesons, K^* and $\bar{K}^*$ for instance. The use of real masses breaks the chiral symmetry which is implicit in the Lagrangian for vector mesons. An important feature of the formalism used is also manifest here: only a few free parameters (the subtraction constants) are needed, which are fine-tuned to some well established masses of resonances and once one adjust them, predictions for others particles are obtained, some of them find experimental counterpart while others remain for future experiments. Furthermore, the branching ratios to two pseudoscalars

have not been adjusted and therefore, they are genuine predictions of the approach.

The study of the $\rho\rho$ interaction was done in Ref. [85]. Its natural extension to SU(3) which we report in this section was done in Ref. [86]. The results have been reproduced by myself taking the same values of the subtraction constants in Eq. (3.45) and are included in the thesis for completeness. Besides, they are very useful for next chapters. Thus, we do a brief summary of the procedure and the results of Ref. [86] and refer the interested reader to Ref. [86].

All the channels according to different (strangeness, isospin, spin) channels are classified. These are $(0,0,0)$, $(0,0,1)$, $(0,0,2)$, $(0,1,0)$, $(0,1,1)$, $(0,1,2)$, $(0,2,0)$, $(0,2,1)$, $(0,2,2)$, $(1,\frac{1}{2},0)$, $(1,\frac{1}{2},1)$, $(1,\frac{1}{2},2)$, $(1,\frac{3}{2},0)$, $(1,\frac{3}{2},1)$, $(1,\frac{3}{2},2)$, $(2,0,0)$, $(2,0,1)$, $(2,0,2)$, $(2,1,0)$, $(2,1,1)$, and $(2,1,2)$. One should calculate the four contact and vector exchange diagrams of Fig. 3.1 following Eqs. (3.4) and (3.5). The amplitudes are given in the Appendix of [86]. We observe that the general structure of the exchange term in the t-channel for the amplitude $(1+2\to 3+4)$, is

$$b_{ij}(k_1+k_3)\cdot(k_2+k_4)\epsilon_1\cdot\epsilon_3\epsilon_2\cdot\epsilon_4 \tag{3.41}$$

while for the u-channel diagrams, the structure is

$$c_{ij}(k_1+k_4)\cdot(k_2+k_3)\epsilon_1\cdot\epsilon_4\epsilon_2\cdot\epsilon_3 \tag{3.42}$$

where b_{ij}, c_{ij} are the coefficients (constants for the channel "i" $=$ $(1+2)\to$ channel "j" $=(3+4)$. It is interesting to see that the structure of spin of Eq. (3.41) has equal components of spin$=0,1$ and 2, while the one of Eq. (3.42) has the same projection for spin$=0$ and 2 and it has opposite sign for spin$=1$.

3.11 Unitarization procedure and search for poles

In the calculations we will always make use of the Bethe-Salpeter equation as a method to unitarize the T-matrix,

$$T = [I - VG]^{-1}V \ . \tag{3.43}$$

The two meson loop function G can be written as

$$G = i \int \frac{d^4q}{(2\pi)^4} \frac{1}{q^2 - m_\rho^2 + i\epsilon} \frac{1}{(P-q)^2 - m_\rho^2 + i\epsilon} \ , \tag{3.44}$$

which upon using dimensional regularization can be recast as

$$\begin{aligned} G &= \frac{1}{16\pi^2}\left(a + \mathrm{Log}\frac{m_1^2}{\mu^2} + \frac{m_2^2 - m_1^2 + s}{2s}\mathrm{Log}\frac{m_2^2}{m_1^2} \right. \\ &+ \frac{p}{\sqrt{s}}\left(\mathrm{Log}\frac{s - m_2^2 + m_1^2 + 2p\sqrt{s}}{-s + m_2^2 - m_1^2 + 2p\sqrt{s}} \right. \\ &\left. \left. + \mathrm{Log}\frac{s + m_2^2 - m_1^2 + 2p\sqrt{s}}{-s - m_2^2 + m_1^2 + 2p\sqrt{s}} \right) \right) \ , \end{aligned} \tag{3.45}$$

where P is the total four-momentum of the two mesons, p is the three-momentum of the mesons in the center of mass frame

$$p = \frac{1}{2\sqrt{s}} \sqrt{(s - (m_1 + m_2)^2)(s - (m_1 - m_2))^2} \tag{3.46}$$

and $m_1 = m_2 = m_\rho$, or using a cutoff as Eq. (3.23). The magnitude μ is a renormalization scale and a is called the subtraction constant. The poles appear in the first Riemann sheet for real values of $\sqrt{s}$ below threshold. For resonances, appearing above threshold and must go to the second Riemann sheet with the procedure discussed below. If these poles are not very far from the real axis they occur in $\sqrt{s} = (M \pm i\Gamma/2) \equiv \sqrt{s_p}$ with M and Γ the mass and width of the resonance respectively. Of course the only meaningful physical quantity is the

value of the amplitude for real $\sqrt{s}$, i.e., the reflexion of the pole on the real axis. Therefore, only poles not very far from the real axis would be easily identified experimentally as a resonance. The effect of passing s to the second Riemann sheet R2 has consequences only for the G functions. To evaluate G in R2 we can use the Schwartz reflexion theorem which states that if a function $f(z)$ is analytic in a region of the complex plane including a portion of the real axis in which f is real, then $[f(z^*)]^* = f(z)$. The loop function G_l satisfies these conditions, therefore, for $\mathrm{Re}(\sqrt{s}) > m_l + M_l$ we have

$$G_l(\sqrt{s}-i\epsilon) = [G_l(\sqrt{s}+i\epsilon)]^* = G_l(\sqrt{s}+i\epsilon) - i2\mathrm{Im}G_l(\sqrt{s}+i\epsilon)\ . \quad (3.47)$$

Since the beginning of R2 is equal to the end of R1 we have

$$G_l^{II}(\sqrt{s}+i\epsilon) = G_l^I(\sqrt{s}-i\epsilon) = G_l^I(\sqrt{s}+i\epsilon) - i2\mathrm{Im}G_l^I(\sqrt{s}+i\epsilon)\ , \quad (3.48)$$

where the subindices I and II refer to R1 and R2 respectively. The imaginary part of the loop function can be very easily evaluated from Eq. (3.44), for instance with Cutkosky rules, giving $\mathrm{Im}G_l^I(\sqrt{s}+i\epsilon) = -\frac{q}{8\pi\sqrt{s}}$. In principle Eqs. (3.47 and 3.48) are true only very close to the real axis but, since the analytic continuation to general complex plane is unique we can write for a general $\sqrt{s}$

$$G_l^{II}(\sqrt{s}) = G_l^I(\sqrt{s}) + i\frac{q}{4\pi\sqrt{s}}\ , \quad (3.49)$$

with $Im(q) > 0$. In Eq. (3.49) one can use for G_l^I either Eq. (3.45) or the result of the cutoff method. One could also have gone to R2 by using Eq. (3.45) but with the solution of q_l with $\mathrm{Im}(q_l) < 0$, but again one finds the problem of multivaluedness of the ln functions. We have checked, by comparing with the result obtained from Eq. (3.49), that one can use Eq. (3.45) as it is written with the prescription of the ln explained below Eq. (3.45) and using $\sqrt{s}$ in the form $a + ib$, a and b real. When looking for poles we will use $G_l^I(\sqrt{s})$ for $\mathrm{Re}(\sqrt{s}) < m_l + M_l$ and $G_l^{II}(\sqrt{s})$ for $\mathrm{Re}(\sqrt{s}) > m_l + M_l$. This prescription gives the pole positions for the real axis and the total width. In this way, when

being below the lowest threshold, we could also obtain possible pure bound states. Close to a pole, the amplitude in Eq. (3.22) can be approximated by

$$T_{ij} = \frac{g_i g_j}{s - s_{\rm pole}} \ , \tag{3.50}$$

thus, the coupling $g_{i(j)}$ to the different $i(j)$ channels are calculated by means of the residues of the amplitudes.

3.12 Results

To regularize the loop functions, the method used is the following: In Eq. (3.44) the function loop can be regularized either with a cutoff $\Lambda \sim 1$ GeV or with a subtraction constant, $a \sim -2$ for meson-baryon scattering [43]. Using $q_{\rm max} \sim 1$ GeV in Eq. (3.23) the basic physics should be reproduced, and thus, we first evaluate the amplitudes in the real axis using the formula of Eq. (3.23) with $q_{\rm max} \sim 1$ GeV. The peaks and bumps obtained should be stable with reasonable changes of the value of the cutoff Λ. Once these peaks are identified, we proceed to search the a in Eq. (3.45) that reproduces the real part of the function loop. The use of the formula (3.45) is very useful in the sense that allows to go to the general complex plane, to reach the second riemann sheet and calculate the residues of the amplitudes, and thus the coupling constants to the different channels, Eq. (3.50). Particularly, the a is adjusted to reproduce the real part of the two-meson loop function at the two ρ's threshold. This results in $a = -1.65$. Then, a fine tuning of the $a's$ for other two-meson channels is done to reproduce some well established resonances. They are the $f_2(1270)$, the $f_2'(1525)$ and the $K_2^*(1430)$. This leads to three different values of the $a's$ in the different sectors, $a_{\rho\rho} = -1.636$, $a_{\rho K^*} = -1.636$, $a_{K^*\bar{K}^*} = -1.726$ and $a_{\rho K^*} = -1.85$. In the channels that involve ω or ϕ we put $a_i = a_{\rho\rho} = -1.65$, for strangeness$= -1$, the value $a_i = a_{\rho K^*} = -1.85$ is used, whereas, similarly, we put $a_i = K^*\bar{K}^* = -1.726$ for strangeness $= -2$. Even though, we notice that qualitatively the results do not change if one puts either $a = -1.65$

or $a = -1.85$ in all the channels. For instance, using $a = -1.85$ one gets a mass for the $f_2(1270)$ pole of $(1206, -i0)$ MeV (without including the box diagram) to be compared to $(1275, -i1)$ MeV with $a = -1.636$. We only find enough attraction in the potential that leads to the generation of poles in the sectors: strangeness $= 0$, isospin $= 0$; strangeness $= 0$, isospin $= 1$ and strangeness $= 1$, isospin $= 1/2$. We find eleven poles or dynamical generated states. In Tables 3.4, 3.5, 3.6 the couplings to the different channels calculated by means of Eq. (3.50) are given (we notice that they were calculated without including the box diagram but since the real part of the box diagram is small, little effect in these couplings is expected. In Table 3.7 the positions of the poles and widths are shown for two different values of the Λ parameter in the form factor, Eq. (3.32), $\Lambda = 1.4$ and 1.5 GeV and the comparison to the PDG data. Since we have obtained eleven dynamically generated states and we have fine tuned three parameters, eight of the eleven resonances are predictions of the model. The value chosen for Λ_b is close to the one from the study made for the $f_2(1270)$ and $f_0(1370)$ in Section 3.8. However, we can invoke the same fine-tuning strategy discussed for the subtraction constant. This is, we can adjust Λ_b to get the total width of one of the resonances, and the widths of the others are predictions. Indeed, the variations of the width with the Λ parameter give us an idea of the uncertainties involved in the computation of the box diagram, which is the mechanism to decay in two pseudoscalar mesons. We also noticed that the couplings of the resonances are rather independent of the Λ parameter, which was already found in [87].

Let us also mention that in our approach we can also obtain predictions for the branching ratios to different pairs of pseudoscalars. Indeed, as the free parameters have not been fine tuned to the branching ratios, they are genuine predictions of the model. Of the eleven states obtained, five of them are associated to data in the PDG because of the proximity of the mass, width and quantum numbers, while the other six have the quantum numbers of one h_1, a_0, b_1, a_2 or K^{*0}, however, the association if possible remains with doubts and

thus more experimental data are demanded to extract some conclusions. In what follows we discuss the experimental data one by one.

$(1512, -i26)$ [spin=0]				
$K^*\bar{K}^*$	$\rho\rho$	$\omega\omega$	$\omega\phi$	$\phi\phi$
$(1208, -i419)$	$(7920, -i1071)$	$(-39, i31)$	$(33, -i43)$	$(12, i24)$
$(1726, -i14)$ [spin=0]				
$K^*\bar{K}^*$	$\rho\rho$	$\omega\omega$	$\omega\phi$	$\phi\phi$
$(7124, i96)$	$(-1030, i1086)$	$(-1763, i108)$	$(3010, -i210)$	$(-2493, -i204)$
$(1802, -i39)$ [spin=1]				
$K^*\bar{K}^*$	$\rho\rho$	$\omega\omega$	$\omega\phi$	$\phi\phi$
$(8034, -i2542)$	0	0	0	0
$(1275, -i1)$ [spin=2]				
$K^*\bar{K}^*$	$\rho\rho$	$\omega\omega$	$\omega\phi$	$\phi\phi$
$(4733, -i53)$	$(10889, -i99)$	$(-440, i7)$	$(777, -i13)$	$(-675, i11)$
$(1525, -i3)$ [spin=2]				
$K^*\bar{K}^*$	$\rho\rho$	$\omega\omega$	$\omega\phi$	$\phi\phi$
$(10121, i101)$	$(-2443, i649)$	$(-2709, i8)$	$(5016, -i17)$	$(-4615, i17)$

Table 3.4: Pole positions and residues in the strangeness=0 and isospin=0 channel. All quantities are in units of MeV.

- The $f_0(1370)$ and the $f_2(1270)$. These states were discussed in detail in Section 3.8. Yet, the present study allows compare to measured decay ratios to different pairs of pseudoscalars. In the PDG, the branching ratios of the $f_2(1270)$ are 84.8% for $\pi\pi$, 4.6% for KK and $< 1\%$ for $\eta\eta$ [78] to be compared with

$(1780, -i66)$ [spin=0]			
$K^*\bar{K}^*$	$\rho\rho$	$\rho\omega$	$\rho\phi$
$(7525, -i1529)$	0	$(-4042, i1391)$	$(4998, -i1872)$
$(1679, -i118)$ [spin=1]			
$K^*\bar{K}^*$	$\rho\rho$	$\rho\omega$	$\rho\phi$
$(1040, -i1989)$	$(6961, -i4585)$	0	0
$(1569, -i16)$ [spin=2]			
$K^*\bar{K}^*$	$\rho\rho$	$\rho\omega$	$\rho\phi$
$(10208, -i337)$	0	$(-4598, i451)$	$(6052, -i604)$

Table 3.5: The same as Table 3.4, but for the strangeness=0 and isospin=1 channel.

our values, that are $\sim 88\%$ for $\pi\pi$, $\sim 10\%$ for $K\bar{K}$ and $< 1\%$ for $\eta\eta$ which is in very good agreement with the experiment.

- The $f_0(1710)$ has a mass quoted in the PDG of 1724 ± 7 MeV and a width of $\Gamma = 137 \pm 8$ MeV. This resonance decay to $K\bar{K}$, $\eta\eta$ and $\pi\pi$ (mainly, whereas others like $\omega\omega$ has been observed). The PDG gives the following averages: $\Gamma(\pi\pi)/\Gamma(K\bar{K}) = 0.41^{+0.11}_{-0.17}$ and $\Gamma(\eta\eta)/\Gamma(K\bar{K}) = 0.48 \pm 0.15$ [78]. Our calculated branching ratios are $\sim 55\%$ for $K\bar{K}$, $\sim 27\%$ for $\eta\eta < 1\%$ for $\pi\pi$ and $\sim 18\%$ for the vector-vector component. The agreement with the mass and width obtained is very good as we can see in Table 3.7. The branching ratio $\Gamma(\eta\eta)/\Gamma(K\bar{K})$ is also fulfilled. Some problem is found for the $\Gamma(\pi\pi)/\Gamma(K\bar{K})$ branching ratio, which we get much smaller. However, when we look at the different experiments, we see that there is a BES experiment, $J/\psi \to \omega K^+K^-$ which gives $\Gamma(\pi\pi)/\Gamma(K\bar{K}) < 11\%$ at the 95% confidence level.

$(1643, -i24)$ [spin=0]		
ρK^*	$K^*\omega$	$K^*\phi$
$(8102, -i959)$	$(1370, -i146)$	$(-1518, i209)$
$(1737, -i82)$ [spin=1]		
ρK^*	$K^*\omega$	$K^*\phi$
$(7261, -i3284)$	$(1529, -i1307)$	$(-1388, i1721)$
$(1431, -i1)$ [spin=2]		
ρK^*	$K^*\omega$	$K^*\phi$
$(10901, -i71)$	$(2267, -i13)$	$(-2898, i17)$

Table 3.6: The same as Table 3.4, but for the strangeness=1 and isospin=1/2 channel.

We claim more experimental analysis is needed to clarify this issue.

- The $f_2'(1525)$. The mass and width are 1525 ± 5 and 73^{+6}_{-5}. And the PDG gives 88.7% to $K\bar{K}$, 10.4% for $\eta\eta$ and 0.8% for $\pi\pi$. We get mass and width $(1525, 45)$ MeV very close the PDG value. The theoretical state also decays mainly to $K\bar{K}$, $\sim 66\%$ and the other ratios are $\sim 21\%$ for $\eta\eta$, $\sim 1\%$ for $\pi\pi$ and 13% for the vector-vector component, which is in good agreement with the experiment.

- The $K_2^*(1430)$. The PDG values for the mass and width of this resonance are 1429 ± 1.4 and 104 ± 4 respectively. The $K\pi$ mode accounts for $(49.9 \pm 1.2)\%$ and the $K^*\pi\pi$ $(13.4 \pm 2.2)\%$. The mass and width found in the real axis are $(1431, 56)$ MeV. Therefore, the agreement with the data is reasonable.

$I^G(J^{PC})$	Theory			PDG data		
	Pole position	Real axis		Name	Mass	Width
		$\Lambda_b = 1.4$ GeV	$\Lambda_b = 1.5$ GeV			
$0^+(0^{++})$	$(1512, 51)$	$(1523, 257)$	$(1517, 396)$	$f_0(1370)$	$1200 \sim 1500$	$200 \sim 500$
$0^+(0^{++})$	$(1726, 28)$	$(1721, 133)$	$(1717, 151)$	$f_0(1710)$	1724 ± 7	137 ± 8
$0^-(1^{+-})$	$(1802, 78)$	$(1802,49)$		h_1		
$0^+(2^{++})$	$(1275, 2)$	$(1276, 97)$	$(1275, 111)$	$f_2(1270)$	1275.1 ± 1.2	$185.0^{+2.9}_{-2.4}$
$0^+(2^{++})$	$(1525, 6)$	$(1525, 45)$	$(1525, 51)$	$f_2'(1525)$	1525 ± 5	73^{+6}_{-5}
$1^-(0^{++})$	$(1780, 133)$	$(1777, 148)$	$(1777, 172)$	a_0		
$1^+(1^{+-})$	$(1679, 235)$	$(1703, 188)$		b_1		
$1^-(2^{++})$	$(1569, 32)$	$(1567, 47)$	$(1566, 51)$	$a_2(1700)$??		
$1/2(0^+)$	$(1643, 47)$	$(1639, 139)$	$(1637, 162)$	K_0^*		
$1/2(1^+)$	$(1737, 165)$	$(1743, 126)$		$K_1(1650)$?		
$1/2(2^+)$	$(1431, 1)$	$(1431, 56)$	$(1431, 63)$	$K_2^*(1430)$	1429 ± 1.4	104 ± 4

Table 3.7: The properties, (mass, width) [in units of MeV], of the eleven dynamically generated states and, if existing, of those of their PDG counterparts. Theoretical masses and widths are obtained from two different ways: "pole position" denotes the numbers obtained from the pole position on the complex plane, where the mass corresponds to the real part of the pole position and the width corresponds to two times the imaginary part of the pole position (the box diagrams corresponding to decays into two pseudoscalars are not included); "real axis" denotes the results obtained from real axis amplitudes squared, where the mass corresponds to the energy at which the amplitude squared has a maximum and the width corresponds to the difference between the two energies, where the amplitude squared is half of the maximum value. (In this case, the box amplitudes corresponding to decays into two pseudoscalars are included). The two entries under "real axis" are obtained with different Λ_b as explained in the main text.

Chapter 4

Testing the nature of the $f_0(1370)$ and the $f_2(1270)$ through radiative decays into $\gamma\gamma$

4.1 Introduction

In the previous Chapter we generated the $f_0(1370)$ and the $f_2(1270)$ using a set of hidden gauge lagrangians together with unitarization technics for the T matrix. These resonances can be interpreted as coming from the $\rho\rho$ interaction, the state for spin $= 2$ being more bound than the spin $= 0$ state. Although the $\rho\rho$ molecular nature of the $f_0(1370)$ was also suggested in [88, 89], the $f_2(1270)$ is, however, generally believed to belong to a p-wave nonet of $q\bar{q}$ states [88, 89]. Thus, the work of [85] introduce a new interpretation of the $f_2(1270)$ and give support to the $\rho\rho$ molecular interpretation of the $f_0(1370)$ suggested in [88, 89].

The experimental situation regarding the mass, width and radiative decay width of the $f_2(1270)$ is much clearer than for the $f_0(1370)$, which is rather confuse when comparing the different experiments in the PDG. In particular, the Belle Collaboration quotes a central value

for the mass of the $f_0(1370)$, $m = 1470^{+6+72}_{-7-255}$ [83], which large uncertainties and $\Gamma_{\rm tot}(\pi^0\pi^0) = 90^{+2+50}_{-1-22}$ MeV, $\Gamma_{\gamma\gamma}B(\pi^0\pi^0) = 11^{+4+603}_{-2-7}$, whereas the Crystal Ball Collaboration gives completely different numbers, $m = 1250$ MeV, $\Gamma_{\rm tot} = (268 \pm 70)$ MeV, $\Gamma_{\gamma\gamma}B(\pi^0\pi^0) = 430 \pm 80$ eV.

From the theoretical side, the values obtained for the mass and width in Chapter 3 are $m(f_2(1270)) = 1275$ MeV (from fitting the subtraction constant), $\Gamma(f_2(1270)) = 100$ MeV, $m(f_0(1370)) = 1532$ MeV and $\Gamma(f_0(1370)) = 212$ MeV, using $q_{\rm max} = 875$ MeV and $\Lambda = 1300$ MeV. This favors the Belle experiment but then the theoretical width remains bigger that that of this experiment, but closer to the Crystal Ball value. However, one must take into account the theoretical uncertainties from adjusting the subtraction constant and there could be some other channels as $\sigma\sigma$ that can affect (in a small amount) this result.

There are previous theoretical studies on the radiative decays into $\gamma\gamma$ of the $f_2(1270)$ and $f_0(1370)$. In [70], the authors assumed that the $f_2(1270)$ together with the $f_2(1525)$ are $q\bar{q}$ and a good description of the decay rates is obtained by adjusting two free parameters. In [74], an evaluation of the radiative decay width of the $f_0(1370)$ into $\gamma\gamma$ is done supposing that this resonance is a mixture of $q\bar{q}$ and $qq\bar{q}\bar{q}$, and the authors obtain values between 0 and 0.22 KeV, whereas in [75], using a model where this resonance is basically a $q\bar{q}$ with quarks of nonstrange nature, values much bigger around 4 KeV are obtained.

In the next subsection we evaluate the decay rates of the $f_0(1370)$ and the $f_2(1270)$ into $\gamma\gamma$ in the $\rho\rho$ molecular picture. The details can be seen in [87].

4.2 Evaluation of the radiative decays of the $\rho\rho$ molecules into $\gamma\gamma$

Within the Hidden Gauge formalism, photons always come out through their conversion into ρ, ω and ϕ. The diagrams for the radiative

decays of $\rho\rho$ molecules into $\gamma\gamma$ are given in Fig. 4.1. These diagrams can be separated in one strong part, $R \to \rho^0\rho^0$ and depicted in Fig. 4.2, and the direct conversion of the two ρ's into photons. Thus, the strong part contains both the vector-exchange and contact terms. The amplitude of Fig. 4.3 a) can be parametrized as a Breit Wigner amplitude, and using the spin projection operators given in Eq. (3.13), one obtain

$$
\begin{aligned}
&J = 0 \\
&\quad t^{(0)} = \frac{g_S^2}{s - M_R^2 + iM_R\Gamma} \times \frac{1}{\sqrt{3}}\epsilon_i^{(1)}\epsilon_i^{(2)}\frac{1}{\sqrt{3}}\epsilon_j^{(3)}\epsilon_j^{(4)} \qquad (4.1) \\
&J = 2 \\
&\quad t^{(2)} = \frac{g_T^2}{s - M_R^2 + iM_R\Gamma}\{\frac{1}{2}(\epsilon_i^{(1)}\epsilon_j^{(2)} + \epsilon_j^{(1)}\epsilon_i^{(2)}) - \frac{1}{3}\epsilon_l^{(1)}\epsilon_l^{(2)}\delta_{ij}\} \\
&\qquad \times\{\frac{1}{2}(\epsilon_i^{(3)}\epsilon_j^{(4)} + \epsilon_j^{(3)}\epsilon_i^{(4)}) - \frac{1}{3}\epsilon_m^{(3)}\epsilon_m^{(4)}\delta_{ij}\} \qquad (4.2)
\end{aligned}
$$

Since, indeed we are interested in the diagram of Fig. 4.3 b), the

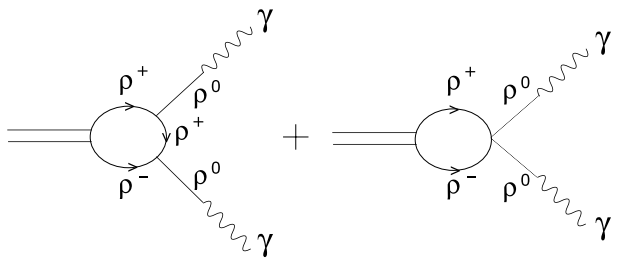

Figure 4.1: Feynman diagrams to evaluate the radiative decay width of $f_0(1370)$ and $f_2(1270)$.

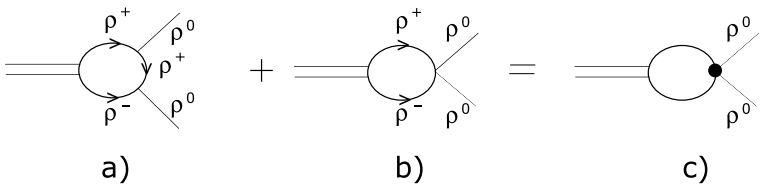

Figure 4.2: Strong part of feynman diagrams to evaluate the radiative decay width of $f_0(1370)$ and $f_2(1270)$.

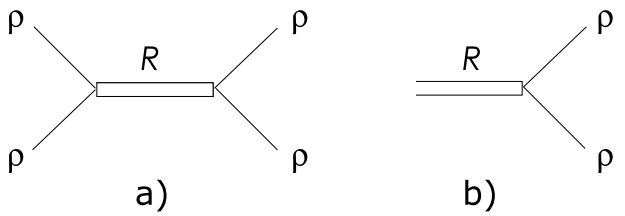

Figure 4.3: a) Resonance pole representation of the amplitude of [85]. b) Diagram depicting the coupling of the resonance to $\rho\rho$.

coupling of the resonance to the $\rho\rho$ system is given by

$J = 0$

$$P^{(0)} \equiv g_S \frac{1}{\sqrt{3}} \epsilon_i^{(3)} \epsilon_i^{(4)} \quad , \tag{4.3}$$

$J = 2$

$$P^{(2)} \equiv g_T [\frac{1}{2}(\epsilon_i^{(3)} \epsilon_j^{(4)} + \epsilon_j^{(3)} \epsilon_i^{(4)}) - \frac{1}{3} \epsilon_m^{(3)} \epsilon_m^{(4)} \delta_{ij}] \tag{4.4}$$

When dealing with identical particles one must take into account the factor 1/2 of symmetry, but this is implicit in the use of the unitary normalization. On the other hand, in order to consider only the $\rho^0\rho^0$ component of the $I = 0$ state, we only need to multiply Eqs. (4.3) and (4.4) by $-1/\sqrt{3}$. Thus, the sum of the two diagrams a) and b) of Fig. 4.2 can be written as

$$t_{R\rho^0\rho^0} = (-\frac{1}{\sqrt{3}}) g^{(i)} G(M_R) V P^{(i)} \quad , \tag{4.5}$$

where $g^{(i)}$ stands for $g^{(S)}$ or $g^{(T)}$, $P^{(i)}$ are the corresponding spin operators of Eqs. (4.3) and (4.4) and $G(M_R)$ stands for the loop function defined in Eq. (3.44) evaluated at $\sqrt{s} = M_R$.

Nevertheless, as we are at the pole of the amplitude, we have $GV = 1$, according to Eq. (3.22), and we obtain,

$$t_{R\rho^0\rho^0} = -\frac{1}{\sqrt{3}} g^{(i)} P^{(i)} \ . \tag{4.6}$$

This result was expected since the addition of an extra bubble to the diagramatic series implicit in the Bethe Salpeter equation leads to the same amplitude at the pole of the resonance.

The couplings g_s and g_T involved in Eqs. (4.3) and (4.4) can be obtained from

$$g_{S,T}^2 = M_R \Gamma_R (|T|^2_{\max})^{1/2} \tag{4.7}$$

In Tables 4.1 and 4.2, we give different values of g_S, g_T for different Λ's. As we can observe, these values are rather stable, and we use

average values

$$g_S^2 = 76 \times 10^6 \ \ \text{MeV}^2, \quad g_T^2 = 160 \times 10^6 \ \ \text{MeV}^2 \tag{4.8}$$

which involve uncertainties of the 10 %.

$J = 0$	Λ [MeV]	$\lvert T\rvert^2_{\max}$	Γ_R [MeV]	g_S^2 [MeV^2]
	1200	1.0×10^5	144	70×10^6
$M_R = 1532$ [MeV]	1300	6.0×10^4	212	80×10^6
	1400	4.2×10^4	244	77×10^6

Table 4.1: Resonance parameters and coupling constants obtained by fitting the results shown in Fig. 3.11 for $J = 0$ state with $q_{\max} = 875$ MeV.

$J = 2$	Λ [MeV]	$\lvert T\rvert^2_{\max}$	Γ_R [MeV]	g_T^2 [MeV^2]
	1200	2.4×10^6	78	154×10^6
$M_R = 1275$ [MeV]	1300	1.5×10^6	100	156×10^6
	1400	1.1×10^6	125	167×10^6

Table 4.2: Resonance parameters and coupling constants obtained by fitting the results shown in Fig. 3.11 for $J = 2$ state with $q_{\max} = 875$ MeV.

On the other hand, the vertex that involves the conversion of one vector into one photon is given by the Lagrangian

$$\mathcal{L}_{V\gamma} = -M_V^2 \frac{e}{g} A_\mu \langle V^\mu Q \rangle \ , \tag{4.9}$$

with $Q = \mathrm{diag}(2,-1,-1)/3$, $e = -|e|$ the electron charge, and A_μ the photon field. From this lagrangian we get the amplitude

$$-it_{\rho^0\gamma} = (-i)\frac{1}{\sqrt{2}}M_V^2\frac{e}{g}\epsilon_\mu(\rho)\epsilon^\mu(\gamma) \quad (e<0) \ , \tag{4.10}$$

Finally, in the Coulomb gauge for photons ($\epsilon^0 = 0$, $\vec{\epsilon}\cdot\vec{k} = 0$), the sum over the final polarization is

$$\sum_\lambda \epsilon_i(\gamma)\epsilon_j(\gamma) = \delta_{ij} - \frac{k_i k_j}{\vec{k}^2} \tag{4.11}$$

Thus, at the end one finds the amplitudes

$$\begin{aligned} &J=0 \\ &t_{R\to\gamma\gamma} = -\frac{1}{3}\frac{e^2}{2}\frac{g_S}{g^2}\epsilon_i(\gamma_1)\epsilon_i(\gamma_2) \ . \qquad (4.12) \\ &J=2 \\ &t_{R\to\gamma\gamma} = -\frac{1}{\sqrt{3}}\frac{e^2}{2}\frac{g_T}{g^2}[\frac{1}{2}(\epsilon_i(\gamma_1)\epsilon_j(\gamma_2)+\epsilon_j(\gamma_1)\epsilon_i(\gamma_2)) \\ &\qquad -\frac{1}{3}\epsilon_m(\gamma_1)\epsilon_m(\gamma_2)\delta_{ij}] \qquad (4.13) \end{aligned}$$

and the final partial decay widths are given by

$$\begin{aligned} &J=0 \\ &\qquad \Gamma = \frac{1}{16\pi}\frac{1}{M_R}g_S^2\frac{2}{3}\frac{1}{12}e^4(\frac{2f}{M_\rho})^4 \ . \qquad (4.14) \\ &J=2 \\ &\qquad \Gamma = \frac{1}{5}\frac{1}{16\pi}\frac{1}{M_R}g_T^2\frac{7}{3}\frac{1}{12}e^4(\frac{2f}{M_\rho})^4 \qquad (4.15) \end{aligned}$$

Thus, using the couplings g_S^2, g_T^2 of Eq. (4.8) one finds:

$$\begin{aligned} \Gamma(f_0(1370)\to\gamma\gamma) &= 1.6 \ \text{keV} \\ \Gamma(f_2(1270)\to\gamma\gamma) &= 2.8 \ \text{keV} \end{aligned} \tag{4.16}$$

with estimated errors of the 10 %.

As we can see, the final result for the $f_2(1270)$ is in perfect agreement with the experimental data, $\Gamma(f_2(1270) \to \gamma\gamma) = 3.03 \pm 0.35$ KeV. Concerning on the $f_0(1370)$, one needs also the branching ratio $B(\pi^0\pi^0)$ which is provided also by the theory [85]. In [85], one gets that the total width of the $f_0(1370)$ comes around $1/4$ from $\rho\rho$ and $3/4$ from $\pi\pi$, out of which $1/3$ corresponds to the $\rho^0\rho^0$ component. Then one gets $\Gamma_{\gamma\gamma}B(\pi^0\pi^0) = 405$ eV which is in perfect agreement with the experimental value given by the Crystall Ball Collaboration, $\Gamma_{\gamma\gamma}B(\pi^0\pi^0) = (430 \pm 80)$ eV.

Chapter 5

Decay of vector - vector resonances into a pseudoscalar meson and a photon

We study the possible decays into a pseudoscalar meson and a photon of the resonances generated from the vector - vector interaction up to now. Within the HGS formalism photons are tied to the vector meson fields through the Lagrangian providing direct conversion of photons into neutral vector mesons. In addition, the decay mechanism will involve loops containing anomalous couplings that using the appropiate Lagrangian. The radiative decays has shown to be an essential tool to determine the nature of the resonances [90, 91, 92, 93, 94, 95, 96, 97], and evaluating these observables with the new perspective for the vector - vector resonances is particularly challenging since some of these resonances have traditionally been accomodated within quark models [88, 89, 98, 99, 100, 101, 102].

5.1 Introduction

First of all, we consider all the possible cases of spin-parity of the initial meson in Table 3.7: In case we had an initial resonance with $J^P = 0^+$, the angular momentum between the pseudoscalar meson and photon should be $L = 1$, which implies negative final parity, and is not allowed. In the language of photon multipoles this corresponds to an M0 transition, which does not exist. The rest of the resonances in Table 3.7 are either with or without strangeness. The resonances without strangeness in the table except those with $J = 1$ have positive C-parity and the decay into $\pi^0(\eta)\gamma$ is forbidden. This leaves non vanishing decay rates only for the h_1, b_1, K_1 and $K_2^*(1430)$, and only the $K_2^*(1430)$ has a clear experimental counterpart. In the present work we concentrate on this case, where there are also experimental data in the PDG for its decay into $K\gamma$:

$$\begin{aligned} \Gamma(K_2^{*+}(1430) \to K^+\gamma)/\Gamma &= (2.4 \pm 0.5) \times 10^{-3} \\ \Gamma(K_2^{*0}(1430) \to K^0\gamma)/\Gamma &< 9 \times 10^{-4} \end{aligned} \tag{5.1}$$

In [86] there was also one a_2 resonance found at around 1560 MeV, which was compared with the $a_2(1700)$ for the proximity of the masses, but serious problems with the widths were observed. Here we shall assume that the $a_2(1560)$ found in [86] corresponds to the experimental $a_2(1320)$ and we will also evaluate the radiative width into $\pi^+\gamma$. Experimentally we have

$$\Gamma(a_2(1320) \to \pi^+\gamma)/\Gamma = (2.68 \pm 0.31) \times 10^{-3} \, . \tag{5.2}$$

The difference of the masses between the $a_2(1560)$ found and the experimental $a_2(1320)$ could be reduced in [86] with some fine tuning of the subtraction constants, but we shall not do it here.

From Tables 3.5 and 3.6 we take the channels and coupling constants, g_i, of the $a_2(1320)$ ($a_2(1569)$ in [86]) and $K_2^*(1430)$. As we see in Table 3.6, the $K_2^*(1430)$ couples to three channels: ρK^*, $K^*\omega$ and $K^*\phi$, the ρK^* being the most important one. Two different decay

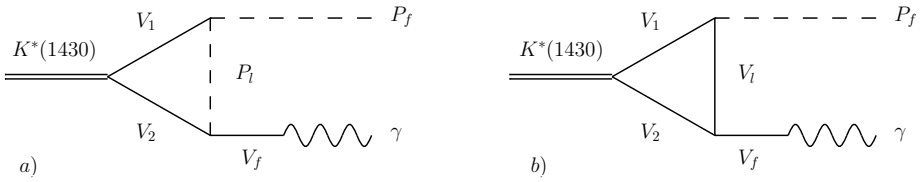

Figure 5.1: The two different diagrams that contribute to the $K_2^*(1430) \to K\gamma$ decay.

mechanisms are responsible for the decay of the $K^*(1430)$ into $K\gamma$, which are shown in Fig. 5.1. On the other hand, the $a_2(1320)$ couples to $K^*\bar{K}^*$, $\rho\omega$ and $\rho\phi$, the largest coupling corresponding to $K^*\bar{K}^*$.

Both diagrams contain an anomalous VVP coupling, whereas one has an anomalous VVP coupling, exchanging a pseudoscalar meson, P_l, Fig. 5.1 a), in the other one, Fig. 5.1 b) a vector meson is exchanged having a 3V vertex. These diagrams lead to four possible configurations, as shown in Fig. 5.2 for the ρK^* channel, depending on whether a non-strange meson is exchanged or not. At the end, all possible VV channels are taken into account.

For the $a_2(1320)$ we show the possible diagrams in Fig. 5.3). In this case, only a few diagrams contribute so we show all the possibilities.

From the Hidden Gauge Lagrangian, Eq. (2.3), we get the term that couples the vector to the photon, which is given by Eq. (4.9).

In principle, both diagrams in Fig. 5.1 containing an anomalous VVP vertex, are expected to be small due to the higher order nature of the anomalous term in the chiral expansion. This anomalous VVP interaction accounts for a process that does not preserve intrinsic parity, and can be obtained from the gauged Wess-Zumino term (see e.g. [13, 103]). Nonetheless, as the relevant energy becomes larger, the role of the anomalous contribution becomes more important since it contains momentum factors (see Eq. (3.36)). This has also been seen in works on the radiative decays of scalar mesons [92, 104]. The

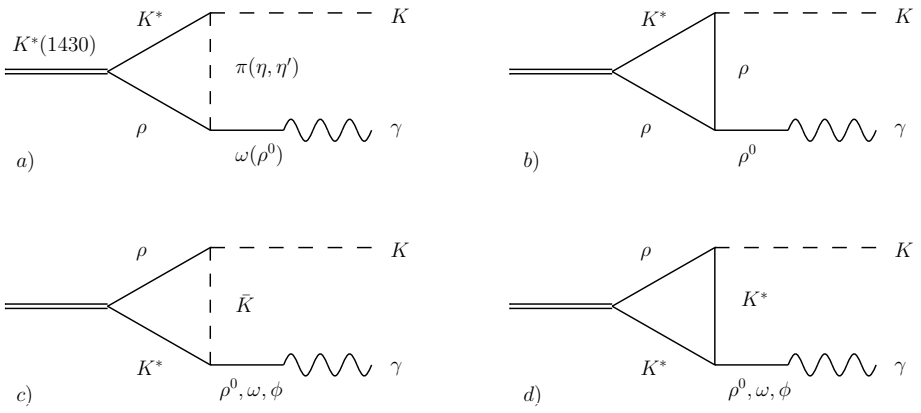

Figure 5.2: Possible Feynman diagrams contributing to the $K_2^*(1430) \to K\gamma$ decay in the ρK^* channel.

VVP Lagrangian is given by Eq. (3.36). In the following subsections we evaluate the two different kinds of diagrams shown in Fig. 5.1. See also [105] for a detailed evaluation.

5.2 Diagram of the $K^*(1430) \to K\gamma$ decay containing the PPV vertex

In Fig. 5.5 we show the first diagram to compute in charge basis with explicit momentum. In what follows, we shall consider the $K_2^{*+}(1430)$ at rest. Firstly, we need the coupling of the resonance $K_2^{*+}(1430)$ to $K^{*0}\rho^+$. This coupling is given in Table 3.5. Close to a pole, the amplitude of Fig. 5.4 can be expressed as:

$$\begin{aligned} t_{rs}^{(J=2)ij} &= \frac{g_r g_s}{s - s_{\rm pole}} \{\frac{1}{2}(\epsilon^{(1)i}\epsilon^{(2)j} + \epsilon^{(1)j}\epsilon^{(2)i}) - \frac{1}{3}\epsilon^{(1)l}\epsilon^{(2)l}\delta^{ij}\} \\ &\times \{\frac{1}{2}(\epsilon^{(1)i}\epsilon^{(2)j} + \epsilon^{(1)j}\epsilon^{(2)i}) - \frac{1}{3}\epsilon^{(1)m}\epsilon^{(2)m}\delta^{ij}\} \ , \end{aligned} \tag{5.3}$$

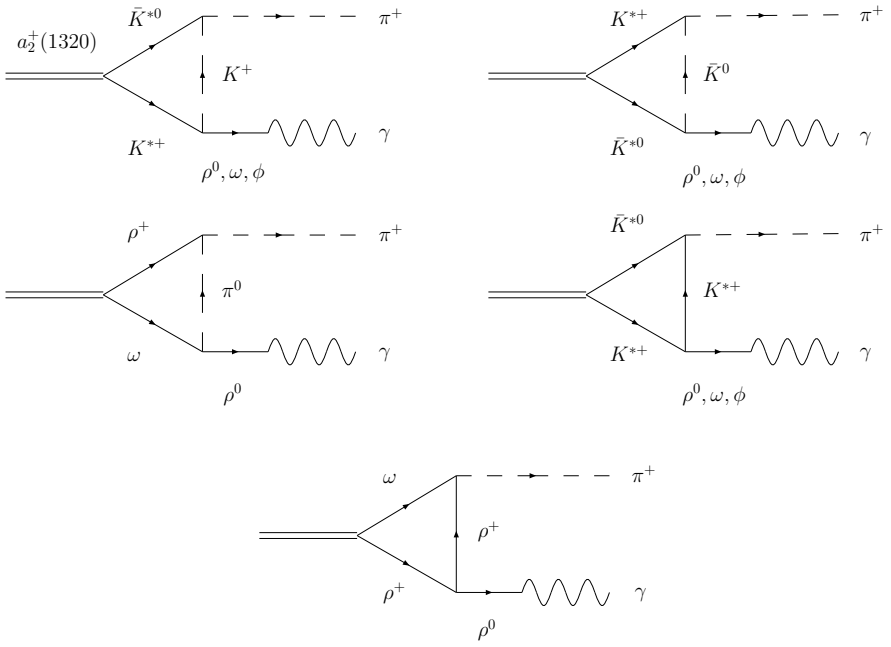

Figure 5.3: Possible Feynman diagrams contributing to the $a_2^{*+}(1320) \to \pi^+\gamma$ decay.

with $s_{\rm pole} = (M - i\Gamma/2)^2$. The coupling of the resonance to a vector - vector channel is given by $\tilde{g_r} = g_r\{\frac{1}{2}(\epsilon^{(1)i}\epsilon^{(2)j} + \epsilon^{(1)j}\epsilon^{(2)i}) - \frac{1}{3}\epsilon^{(1)l}\epsilon^{(2)l}\delta^{ij}\}$, r or s corresponding to one of the channels ρK^*, ωK^* or ϕK^* but multiplying by the correspondent Clesch-Gordan coefficient since the couplings are in the isospin basis.

$$\begin{aligned} |\rho\, K^*, 1/2, 1/2\rangle &= -\sqrt{\frac{2}{3}}\,\rho^+ K^{*0} - \frac{1}{\sqrt{3}}\,\rho^0 K^{*+} \\ |\rho\, K^*, 1/2, -1/2\rangle &= -\sqrt{\frac{2}{3}}\,\rho^- K^{*+} + \frac{1}{\sqrt{3}}\,\rho^0 K^{*0}\ . \end{aligned} \tag{5.4}$$

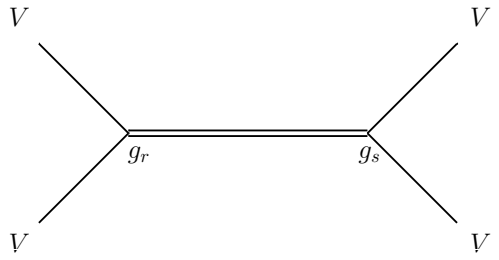

Figure 5.4: Dynamically generated resonance from the VV interaction

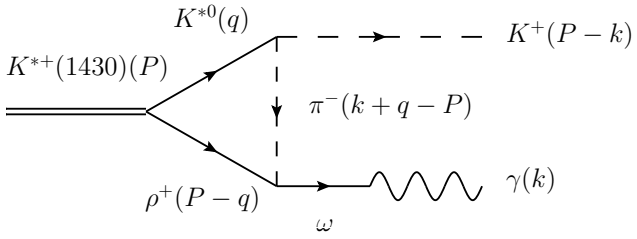

Figure 5.5: Feynman diagram of the $K_2^{*+}(1430) \to K^+\gamma$ decay in the $\rho^+ K^{*0}$ channel with a PPV vertex.

The isospin coefficient is denoted as g_I. Thus, the RVV, Vγ, PPV and VVP vertices involved in Fig. 5.5 are

$$\begin{aligned}
t^{ij}_{RV_1V_2} &= g_I g_r \{\frac{1}{2}(\epsilon^{(1)i}\epsilon^{(2)j} + \epsilon^{(1)j}\epsilon^{(2)i}) - \frac{1}{3}\epsilon^{(1)l}\epsilon^{(2)l}\delta^{ij}\} \\
t_{V_f\gamma} &= \lambda \frac{e}{g} M^2_{V_f} \epsilon^{(\gamma)}_\mu \epsilon^{(f)\mu} \\
t_{P_lP_fV_1} &= Ag(p_{\rm in} + p_{\rm fin})_\mu \epsilon^{(1)\mu} = -Ag(2(P-k)-q)_\mu \epsilon^{(1)\mu} \\
t_{V_2V_fP_l} &= -B\frac{G'}{\sqrt{2}}\epsilon^{\alpha\beta\gamma\delta}(P-q)_\alpha \epsilon^{(2)}_\beta k_\gamma \epsilon^{(f)}_\delta \ , \qquad (5.5)
\end{aligned}$$

being $V_1 = K^{*0}$, $V_2 = \rho^+$, $V_f = \omega$, $P_l = \pi^-$, $P_f = K^+$, and the coefficients g_I, g_r, A, B and λ are: $-\sqrt{\frac{2}{3}}$, $(10901, -i71)$ MeV, -1, $\sqrt{2}$ and $\frac{1}{3\sqrt{2}}$ respectively. The $V_f \to \gamma$ conversion essentially replaces, up to a constant, $\epsilon_\delta^{(f)}$ by $\epsilon_\delta^{(\gamma)}$. Therefore, we can write the amplitude of the diagram depicted in Fig. 5.5 can be expressed as

$$\begin{aligned} -it^{ij}_{K_2^{*+}(1430)\to K^+\gamma} &= eg_r G' \mathrm{F_I} \int \frac{d^4q}{(2\pi)^4} \{ \frac{1}{2}(\epsilon^{(1)i}\epsilon^{(2)j} + \epsilon^{(1)j}\epsilon^{(2)i}) \\ &\quad -\frac{1}{3}\epsilon_l^{(1)}\epsilon_l^{(2)}\delta^{ij}\}\epsilon^{(1)\mu}(2(P-k)-q)_\mu \epsilon^{\alpha\beta\gamma\delta} \\ &\quad \times (P-q)_\alpha \epsilon_\beta^{(2)} k_\gamma \epsilon_\delta^{(\gamma)} \\ &\quad \times \frac{1}{q^2 - M_1^2 + i\epsilon} \frac{1}{(k+q-P)^2 - m_l^2 + i\epsilon} \\ &\quad \times \frac{1}{(P-q)^2 - M_2^2 + i\epsilon} \ , \end{aligned} \tag{5.6}$$

with $M_1 = m_{K^*}$, $M_2 = m_\rho$, $m_l = m_\pi$ and $\mathrm{F_I} = \frac{1}{\sqrt{2}} AB\lambda g_I = \frac{1}{3\sqrt{3}}$. We should be consistent with the approximation done in Chapter 3, where $|\vec{q}|/M_1 \simeq 0$, which implies that $\epsilon^{(1)0} \simeq 0$. This means that the μ and β indices should be spatial and also that the $q^i q^j / M_V^2$ terms in the sum over vector polarizations should be neglected. For convenience, we will keep them as covariant indices and will consider them as spatial indices at the end. Thus, after summing over polarizations

$$\begin{aligned} \sum_\lambda \epsilon^{(1)i}\epsilon^{(1)\mu} &= -g^{i\mu} \\ \sum_\lambda \epsilon^{(2)j}\epsilon_\beta^{(2)} &= -g^j{}_\beta \ , \end{aligned} \tag{5.7}$$

we obtain

$$
\begin{aligned}
-it^{ij}_{K_2^{*+}(1430)\to K^+\gamma} &= eg_r G' \mathrm{F_I} \int \frac{d^4q}{(2\pi)^4} \{ \frac{1}{2} \epsilon^{\alpha j \gamma \delta} (2(P-k)-q)^i \\
&\times (P-q)_\alpha k_\gamma \epsilon_\delta^{(\gamma)} \\
&+ \frac{1}{2} \epsilon^{\alpha i \gamma \delta} (2(P-k)-q)^j (P-q)_\alpha k_\gamma \epsilon_\delta^{(\gamma)} \\
&- \frac{1}{3} \epsilon^{\alpha m \gamma \delta} (2(P-k)-q)^m (P-q)_\alpha k_\gamma \epsilon_\delta^{(\gamma)} \delta^{ij} \} \\
&\times \frac{1}{q^2 - M_1^2 + i\epsilon} \frac{1}{(k+q-P)^2 - m_l^2 + i\epsilon} \\
&\times \frac{1}{(P-q)^2 - M_2^2 + i\epsilon} \ . \qquad (5.8)
\end{aligned}
$$

All the terms of Eq. (5.8) are proportional to an integral like

$$
\begin{aligned}
&\int \frac{d^4q}{(2\pi)^4} (2(P-k)-q)^i (P-q)_\alpha \frac{1}{q^2 - M_1^2 + i\epsilon} \\
&\times \frac{1}{(k+q-P)^2 - m_l^2 + i\epsilon} \frac{1}{(P-q)^2 - M_2^2 + i\epsilon} \ , \qquad (5.9)
\end{aligned}
$$

which, from Lorentz covariance, must be a tensor built from P and k,

$$
a g^i{}_\alpha + b P^i P_\alpha + c k^i P_\alpha + d P^i k_\alpha + e k^i k_\alpha \ . \qquad (5.10)
$$

The second and fourth terms in Eq. (5.10) vanish directly because $P^i = 0$. Thus, the first term in Eq. (5.10) leads to a term proportional to

$$
\frac{1}{2} k_\gamma \epsilon_\delta^{(\gamma)} a (\epsilon^{ij\gamma\delta} + \epsilon^{ji\gamma\delta}) - \frac{1}{3} \epsilon^{\alpha m \gamma \delta} k_\gamma \epsilon_\delta^{(\gamma)} \delta^{ij} a g^m{}_\alpha \ , \qquad (5.11)
$$

which vanishes by the contraction of this antisymmetric operator with a symmetric one, $g^m{}_\alpha$. This is a welcome feature since this term was the only one that is divergent in the integral of Eq. (5.9). The fifth

term, $ek^i k_\alpha$, leads to terms proportional to $k_\gamma k_\alpha \epsilon^{\alpha l \gamma \delta}$, and therefore it also vanishes. Thus, only the third term, $ck^i P_\alpha$, remains, but we can still simplify it. With these simplifications, the integral in Eq. (5.8) is proportional to

$$\frac{1}{2} c P_\alpha k_\gamma \epsilon_\delta^{(\gamma)} (k^i \epsilon^{\alpha j \gamma \delta} + k^j \epsilon^{\alpha i \gamma \delta}) - \frac{1}{3} c \epsilon^{\alpha m \gamma \delta} k_\gamma \delta^{ij} \epsilon_\delta^{(\gamma)} k^m P_\alpha \ . \qquad (5.12)$$

and the last term in the above equation vanishes for $P^i = 0$. To see it, let us split the factor $\epsilon^{\alpha m \gamma \delta} k_\gamma k^m P_\alpha$ in two terms

$$\sum_{m=1,3} \epsilon^{\alpha m 0 \delta} k_0 k^m P_\alpha + \sum_{m=1,3} \sum_{l=1,3} \epsilon^{\alpha m l \delta} k_l k^m P_\alpha \ , \qquad (5.13)$$

the last term is zero since it is a product of an antisymmetric operator by a symmetric one. Also, the presence of P_α forces $\alpha = 0$, which makes the first term disappear.

Now we must evaluate the c coefficient in Eq. (5.12). Let us use the formula of the Feynman parametrization for $n = 3$

$$\frac{1}{\alpha\beta\gamma} = 2 \int_0^1 dx \int_0^x dy \frac{1}{[\alpha + (\beta - \alpha)x + (\gamma - \beta)y]^3} \ . \qquad (5.14)$$

For the integral of Eq. (5.9), we can use the above parametrization with

$$\begin{aligned} \alpha &= q^2 - M_1^2 \\ \beta &= (P - q)^2 - M_2^2 \\ \gamma &= (P - q - k)^2 - m_l^2 \ . \end{aligned} \qquad (5.15)$$

Besides that, we define a new variable $q' = q - Px + ky$, such that the integral of Eq. (5.9) can be expressed as

$$2 \int \frac{d^4 q'}{(2\pi)^4} \int_0^1 dx \int_0^x dy (2(P - k) - q)^i (P - q)_\alpha \frac{1}{(q'^2 + s)^3} \ , \qquad (5.16)$$

with

$$\begin{aligned} s &= -(P^0)^2x^2 + 2P^0k^0xy + ((P^0)^2 - M_2^2 + M_1^2)x \\ &\quad +(-2P^0k^0 + M_2^2 - m_l^2)y - M_1^2 \ . \end{aligned} \tag{5.17}$$

From Eq. (5.16), we should take the k^iP_α term with accompanies the c coefficient. Therefore, we obtain

$$c = 2\int \frac{d^4q'}{(2\pi)^4}\int_0^1 dx \int_0^x dy \frac{(1-x)(y-2)}{(q'^2+s)^3} \ . \tag{5.18}$$

And the integral in the q' variable can be performed analytically:

$$\int d^4q' \frac{1}{(q'^2+s)^3} = \frac{i\pi^2}{2s} \ . \tag{5.19}$$

Finally, we get

$$c = \frac{i}{16\pi^2}\int_0^1 dx \int_0^x dy \frac{(1-x)(y-2)}{s} \ , \tag{5.20}$$

and the amplitude of the diagram of Fig. 5.5 is

$$-it^{ij}_{K_2^{*+}(1430)\to K^+\gamma} = \frac{1}{2}\mathrm{F_I}\, e g_r G' c P_\alpha k_\gamma \epsilon_\delta^{(\gamma)}(k^i\epsilon^{\alpha j\gamma\delta} + k^j\epsilon^{\alpha i\gamma\delta}) \ . \tag{5.21}$$

5.3 Diagram of the $K^*(1430) \to K\gamma$ decay containing the 3V vertex

In order to compute the second diagram for the $K^*(1430) \to K\gamma$ decay depicted in Fig. 5.1, we show it in Fig. 5.6 with the explicit momenta in the case of the $K^{*0}\rho^+$ intermediate state. The difference with the diagram calculated in the previous section is the presence of the 3V vertex. The corresponding 3V and VVP vertices are

$$\begin{aligned} t_{V_2V_lV_f} &= gD\{(2k+q-P)_\mu \epsilon_\nu^{(l)}\epsilon^{(2)\mu}\epsilon^{(f)\nu} \\ &\quad -(k+P-q)_\mu \epsilon_\nu^{(2)}\epsilon^{(l)\mu}\epsilon^{(f)\nu} \\ &\quad +(2(P-q)-k)_\mu \epsilon_\nu^{(l)}\epsilon^{(f)\mu}\epsilon^{(2)\nu}\} \\ t_{V_1V_lP_f} &= -B\frac{G'}{\sqrt{2}}\epsilon^{\alpha\beta\gamma\delta}q_\alpha \epsilon_\beta^{(1)}(k+q-P)_\gamma \epsilon_\delta^{(l)} \ , \end{aligned} \tag{5.22}$$

with $D = \sqrt{2}$, $B = 1$, and g_I, g_r, λ in Eqs. (5.5) are $-\sqrt{\frac{2}{3}}$, $(10901, -i71)$ MeV, $\frac{1}{\sqrt{2}}$ respectively. Thus, the amplitude of the diagram in Fig. 5.6 can be written as

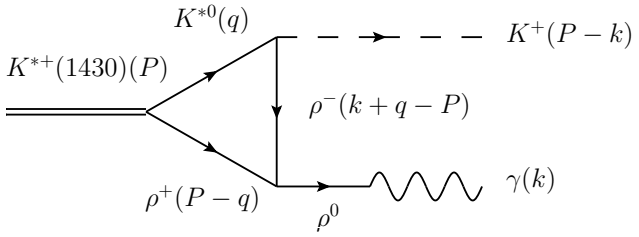

Figure 5.6: Feynman diagram of the $K_2^{*+}(1430) \to K^+\gamma$ decay in the $\rho^+ K^{*0}$ channel with a 3V vertex.

$$
\begin{aligned}
-it^{ij}_{K_2^{*+}(1430)\to K^+\gamma} \;=\; & \mathrm{F}'_{\mathrm{I}}\, e g_r G' \int \frac{d^4q}{(2\pi)^4} \{ \frac{1}{2}(\epsilon^{(1)i}\epsilon^{(2)j} + \epsilon^{(1)j}\epsilon^{(2)i}) \\
& -\frac{1}{3}\epsilon_l^{(1)}\epsilon_l^{(2)}\delta^{ij}\}\epsilon^{\alpha\beta\gamma\delta} q_\alpha \epsilon_\beta^{(1)} (k+q-P)_\gamma \epsilon_\delta^{(l)} \\
& \times \{ (2k+q-P)_\mu \epsilon_\nu^{(l)} \epsilon^{(2)\mu}\epsilon^{(\gamma)\nu} \\
& -(k+P-q)_\mu \epsilon_\nu^{(2)} \epsilon^{(l)\mu}\epsilon^{(\gamma)\nu} \\
& +(2(P-q)-k)_\mu \epsilon_\nu^{(l)} \epsilon^{(\gamma)\mu}\epsilon^{(2)\nu}\} \\
& \times \frac{1}{q^2 - M_1^2 + i\epsilon} \frac{1}{(k+q-P)^2 - M_l^2 + i\epsilon} \\
& \times \frac{1}{(P-q)^2 - M_2^2 + i\epsilon}
\end{aligned}
\tag{5.23}
$$

with $\mathrm{F}'_{\mathrm{I}} = -\frac{1}{\sqrt{2}} g_I B D \lambda$. The way to proceed is very similar to that of the previous subsection, with the only difference of the use of the Lorentz condition, $k_\mu \epsilon^{(\gamma)\mu} = 0$. Now, there are two kinds of integrals.

The first one, is

$$\int \frac{d^4q}{(2\pi)^4} q_\alpha \frac{1}{q^2 - M_1^2 + i\epsilon} \frac{1}{(k+q-P)^2 - M_l^2 + i\epsilon} \times \frac{1}{(P-q)^2 - M_2^2 + i\epsilon} \ , \tag{5.24}$$

which from Lorentz covariance takes the form

$$a_1 P_\alpha + b_1 k_\alpha \ . \tag{5.25}$$

When contracting with the term $k_\gamma P_\delta \epsilon^{\alpha i \gamma \delta}$, this integral becomes zero. The second integral is

$$\int \frac{d^4q}{(2\pi)^4} q_\alpha (2k+q-P)^j \frac{1}{q^2 - M_1^2 + i\epsilon} \times \frac{1}{(k+q-P)^2 - M_l^2 + i\epsilon} \frac{1}{(P-q)^2 - M_2^2 + i\epsilon} \tag{5.26}$$

and takes the form

$$a_2 g^j{}_\alpha + b_2 k_\alpha k^j + c_2 k^j P_\alpha + d_2 P^j k_\alpha + e_2 P^j P_\alpha \ . \tag{5.27}$$

The first term disappears due to the factor $g^j{}_\alpha \epsilon^{\alpha i \gamma \delta} + g^i{}_\alpha \epsilon^{\alpha j \gamma \delta} = 0$ and the last two terms are zero since $P^j = 0$. The final amplitude is a function of the b_2 and c_2 coefficients, and it can be expressed as

$$\begin{aligned} -it^{ij}_{K_2^{*+}(1430)\to K^+\gamma} &= -\frac{1}{2} \mathrm{F_I'} e g_r G' \left(k^j \epsilon^{\alpha i \gamma \delta} + k^i \epsilon^{\alpha j \gamma \delta}\right) \\ &\quad \times \epsilon^{(\gamma)}_\delta (-b_2 k_\alpha P_\gamma + c_2 P_\alpha k_\gamma) \ , \end{aligned} \tag{5.28}$$

with

$$\begin{aligned} b_2 &= \frac{i}{16\pi^2} \int_0^1 dx \int_0^x dy \frac{y(y-2)}{s'} \\ c_2 &= \frac{i}{16\pi^2} \int_0^1 dx \int_0^x dy \frac{x(2-y)}{s'} \end{aligned} \tag{5.29}$$

and

$$\begin{aligned} s' &= -(P^0)^2x^2 + 2P^0k^0xy + ((P^0)^2 - M_2^2 + M_1^2)x \\ &\quad +(-2P^0k^0 + M_2^2 - M_l^2)y - M_1^2 \ . \end{aligned} \tag{5.30}$$

Finally, the sum of the diagrams in Fig. 5.2, from Eqs. (5.20), (5.21), (5.28) and (5.29), lead to the amplitude:

$$\begin{aligned} -it^{ij}_{K_2^{*+}(1430)\to K^+\gamma} &= \frac{1}{2}eG'(b_2'k_\alpha P_\gamma + (c' - c_2')P_\alpha k_\gamma) \\ &\quad (k^j\epsilon^{\alpha i\gamma\delta} + k^i\epsilon^{\alpha j\gamma\delta})\epsilon_\delta^{(\gamma)} \ , \end{aligned} \tag{5.31}$$

with

$$\begin{aligned} b_2' &= g_r\,\mathrm{F_I'}\,b_2 \\ c' &= g_r\,\mathrm{F_I}\,c \\ c_2' &= g_r\,\mathrm{F_I'}\,c_2 \ . \end{aligned} \tag{5.32}$$

In order to compute the decay width of the process $K_2^{*+}(1430) \to K^+\gamma$, we still need to evaluate the squared amplitude summing over polarizations, i. e., $\frac{1}{2J+1}\sum_{\lambda_f}\sum_{\lambda_i} t_{ij}(t^{ij})^*$. The sum over the polarizations of the photon $\sum_{\lambda_f}\epsilon_\delta^{(\gamma)}\epsilon_{\delta'}^{(\gamma)}$ leads to a factor $-g_{\delta\delta'}$. In addition, products of the antisymmetric $\epsilon^{\alpha\beta\gamma\delta}$ operators appear, for what one can use the rule

$$\epsilon^{\alpha\beta\gamma\delta}\epsilon^{\alpha'}{}_{\beta'}{}^{\gamma'}{}_{\delta} = -\begin{vmatrix} g^{\alpha\alpha'} & g^{\alpha}{}_{\beta'} & g^{\alpha\gamma'} \\ g^{\beta\alpha'} & g^{\beta}{}_{\beta'} & g^{\beta\gamma'} \\ g^{\gamma\alpha'} & g^{\gamma}{}_{\beta'} & g^{\gamma\gamma'} \end{vmatrix} \ , \tag{5.33}$$

with β, β' spatial indices. Thus, we obtain

$$\frac{1}{2J+1}\sum_{\lambda_f}\sum_{\lambda_i}|t|^2 = \frac{1}{2J+1}|\vec{k}|^4P_0^2|b_2' + c_2' - c'|^2(eG')^2 \ . \tag{5.34}$$

And finally, the $K_2^{*+}(1430) \to K^+\gamma$ decay width is given by

$$\Gamma(K_2^{*+}(1430) \to K^+\gamma) = \frac{1}{8\pi}\frac{1}{2J+1}|\vec{k}|^5|b_2' + c_2' - c'|^2(eG')^2 \ . \quad (5.35)$$

In order to include all the possible channels, ρK^*, ωK^* and ϕK^* we list the different $\mathrm{F_I}$, $\mathrm{F_I'}$ for each channel r in Tables A.1 - A.8 in the Appendix A. Thus,

$$\begin{aligned} c' &= \frac{1}{16\pi^2}\int_0^1 dx \int_0^x dy\,(1-x)(y-2)\sum_r \frac{\mathrm{F_I}(r)g_r}{s(r)} \\ b_2' &= \frac{1}{16\pi^2}\int_0^1 dx \int_0^x dy\,y(y-2)\sum_r \frac{\mathrm{F_I'}(r)g_r}{s'(r)} \\ c_2' &= \frac{1}{16\pi^2}\int_0^1 dx \int_0^x dy\,x(2-y)\sum_r \frac{\mathrm{F_I'}(r)g_r}{s'(r)} \ . \end{aligned} \quad (5.36)$$

We show s, s', $\mathrm{F_I}$ and $\mathrm{F_I'}$ again for completeness.

$$\begin{aligned} s &= -(P^0)^2x^2 + 2P^0k^0xy + ((P^0)^2 - M_2^2 + M_1^2)x \\ &\quad +(-2P^0k^0 + M_2^2 - m_l^2)y - M_1^2 \\ s' &= -(P^0)^2x^2 + 2P^0k^0xy + ((P^0)^2 - M_2^2 + M_1^2)x \\ &\quad +(-2P^0k^0 + M_2^2 - M_l^2)y - M_1^2 \\ \mathrm{F_I} &= +\frac{1}{\sqrt{2}}AB\lambda g_I \\ \mathrm{F_I'} &= -\frac{1}{\sqrt{2}}g_I BD\lambda \end{aligned} \quad (5.37)$$

5.4 The decay of the $a_2^+(1320) \to \pi^+\gamma$

This case is identical to the former one with the only difference in the couplings of Table 3.6. The coefficients F_I, F_I' for the different diagrams of Fig. 5.3 are shown in Tables A.7, A.8 in the Appendix A.

5.5 Results

In Tables A.1 - A.8 in the Appendix A we show the partial widths for loops containing different particles. We observe that the total sum of all the contributions of these diagrams is mostly constructive for the $K_2^{*+}(1430)$. In contrast, the interference is very destructive in the case of the $K_2^{*0}(1430)$. In order to evaluate the uncertainties in the theoretical decay widths we take errors in the coupling constants Δg of order 15% in Ref. [86] and generate random numbers of the couplings g_i weighted by the Normal (Gaussian) distribution:

$$f(x) = \frac{1}{\sigma\sqrt{2\pi}} e^{\frac{(x-g)^2}{2\sigma^2}} \ , \tag{5.38}$$

by means of the von Newmann rejection method. Thus, we obtain the errors in Γ. We evaluate the average value and its standard deviation from a sample of thirty results.

In the first place we evaluate separately the contribution of the diagram with two vectors (Fig. 5.1 a)) and three vectors (Fig. 5.1 b)). Before showing the results, let us see the partial widths of each different decay mechanism as indicated in Table 5.1. We observe from this table that the contributions of the two mechanisms are of the same order of magnitude, and therefore, both must be taken into account. Finally, the results obtained from the sum of the two differ-

Contribution	$\Gamma_{(K_2^{*+}(1430)\to K^+\gamma)}$	$\Gamma_{(K_2^{*0}(1430)\to K^0\gamma)}$	$\Gamma_{(a^+(1320)\to\pi^+\gamma)}$
PPV	46.6	0.19	65.7
3V	28.2	0.29	34.8

Table 5.1: Partial decay widths to pseudoscalar-photon of the different contributions shown in Fig. 5.1 for some of the resonances in Table 3.7 in units of KeV.

ent kinds of amplitudes, are shown in Table 5.2 where we also include

	$\Gamma_{(K_2^{*+}\to K^+\gamma)}$	$\Gamma_{(K_2^{*0}\to K^0\gamma)}$	$\Gamma_{(a_2(1320)\to\pi^+\gamma)}$
Theory	150 ± 50	$(1.0 \pm 0.8) \times 10^{-2}$	196 ± 30
Experiment	236 ± 50	< 98	281 ± 34

Table 5.2: Total decay width to pseudoscalar-photon for some of the resonances in Table 3.7 in units of KeV.

the experimental data available. We see that the result obtained for the charged K_2^{*+} is compatible with the data in the error interval established. We see that the interference of these two mechanisms is constructive for the K_2^{*+} and a_2^+, whereas it is destructive in the case of the K_2^{*0}. Thus, the decay width for $K_2^{*0} \to K^0\gamma$ is much smaller than the $K_2^{*+} \to K^+\gamma$, in both the theoretical and experimental results. We have noticed that there is a complete cancellation of the amplitudes of the K_2^{*0} when the masses of the pseudoscalar mesons are made equal and also those of the nonet of vectors. This result seems to be tied to the neutral charge of the K_2^{*0}, providing the same result as quark models. Hence, the small finite results obtained are due to the use of the physical masses within the SU(3) multiplets and the upper bound is fulfilled. It would be interesting to have this upper bound improved experimentally, since we predict such a small number for the width.

In the case of the $a_2(1320)$ the agreement with data can be considered qualitatively. Considering errors the maximum theoretical value would be 226 KeV and the minimum experimental one 247 KeV. But if we look at the ratio of $\Gamma(K_2^{*+} \to K^+\gamma)/\Gamma(a_2^+ \to \pi^+\gamma)$, we get 0.77 ± 0.30, which is in good agreement with the experiment, 0.84 ± 0.20. Let us mention that we have not changed the values of the coupling constants of [86]. Should one redo the evaluation of these couplings with an improved mass for this resonance we would expect small variations, adding to our present error estimates. Yet, the large mass difference between the state obtained in [86] and the experimen-

tal one should be taken as an indication that extra components to those of VV considered in the present approach should be present in the physical state $a_2(1320)$, so there is no point in demanding a more accurate agreement with data.

Chapter 6

Resonances from the ρD^*, ωD^* interaction

We have studied the $\rho\rho$ interaction in the framework of the hidden gauge formalism. Two bound states have appeared from this interaction: the $f_0(1370)$ was identified with a pole just at the $\rho\rho$ threshold with mass ~ 1500 MeV in the real axis, and the $f_2(1270)$, a $\rho\rho$ state bound by 280 MeV. Afterwards, this study has been extended to the nonet of vector mesons and eleven states have been dynamically generated from the vector-vector interaction, five of them that could be identified with particles in the PDG: The $f_0(1370)$, $f_2(1270)$, $f_0(1710)$, $f_2'(1525)$ and the $K_2^*(1430)$.

Here we extend this study to include charm mesons, but we deal with some difficulties, since the heavy mass of the D^* suggests that it should be treated in a different way. Being aware of that we follow this strategy: Starting from the same kinematical structure for the vertex than for the other vector mesons, we break the symmetry. This is done by setting the masses of the particles as realistic masses and suppressing those terms where a heavy meson is exchanged. This was already done in the previous studies of the pseudoscalar-pseudoscalar and pseudoscalar-vector interaction [108, 109] with charmed mesons.

The results were compared from those using a chiral Lagrangian in SU(4) and they led to the same results quantitatively. In that way, unitarity is fulfilled and thresholds are respected. Then, we look at the possible sources of uncertainties and move "g^2" from $(m_\rho/2f_\pi)^2$ to $g_D^2 = (m_{D^*}/2f_D)^2$.

6.1 Introduction

In [108] the authors studied the coupled channels of two pseudoscalar mesons of the 16-plet by using two different modes. One is a chiral Lagrangian for the pseudoscalar-pseudoscalar interaction, while the other is a phenomenological model that starts from a SU(4) symmetric Lagrangian. Then, it is broken into pieces that separate the heavy-meson currents from the light ones. The diagrams where a heavy vector meson is exchanged are suppressed in terms of a breaking symmetry parameter. When comparing the results of the two different models, the chiral Lagrangian and the phenomenological one, they lead to the same conclusions (and numerically very close results): The $D_{s0}(2317)$ is found to be essentially a $DK(D_s\eta)$ bound state. In the pheomenological model the chiral symmetry can be restored by setting the SU(4) symmetry breaking parameters to zero and using a unique f_π parameter [110]. In [111, 112, 113], the $D_{s0}(2317)$ is obtained from an effective Lagrangian approach as a pure DK bound state. The study of [108] is extended to the pseudoscalar-vector interaction [109], and in a very similar procedure, the $D_{s1}(2460)$ and the $D_{s1}(2536)$ are explained in terms of $KD^*(\eta D_s^*)$ and $DK^*(D_s(\omega(\phi))$ molecules respectively. Very similar results were achieve for the $D_{s1}(2460)$ using different approaches in [114, 115, 117]. In [117], the interaction is provided by a chiral Lagrangian based on heavy quark symmetry and the authors neglect the exchange of heavy vector mesons. Thus, the phenomenological model of [108] leads to similar results concerning the $D_{s0}(2317)$ and the $D_{s1}(2460)$ than the chiral model used in this work and the heavy

quark lagrangians built in [111, 112, 113, 115]. Here we follow the strategy of the phenomenological model of [108] and keep in mind the possible sources of uncertainties to evaluate them as an essential part of the work. See [116] for further details.

6.2 Potential

Now we are concerned on the sector with charm= 1 and strangeness= 0. There are four channels in this sector: The ρD^*, ωD^*, ϕD^* and $\bar{K}^* D_s^*$. However, the channels ϕD^* does not give any contribution for the contact neither the exchange term because the $\omega\omega\phi$, $\phi\phi\phi$, $\phi\phi\omega$ violate G-parity. The mass of the $D_2^*(2460)$ is 315 MeV below of the ρD^* and ωD^* thresholds. By now we have seen that the formalism of vector - vector interaction generates resonances with spin= 2 bound by around $200-300$ MeV. For instance, the $f_2(1270)$ is a $\rho\rho$ state bound by 280 MeV. The $f_2'(1525)$ is mostly bound in the $K^*\bar{K}^*$ channel by 165 MeV, and the $K_2^*(1430)$ by 230 MeV. One could expect to get similar bindings for possible ρD^* and ωD^* bound states. The $\bar{K}^* D_s^*$ channel is too far away from the ρD^* and ωD^* thresholds, so it can be discarded.

Even though we are dealing with heavy mesons (D^*) with a very different mass from the nonet of vector mesons, we assume that the structure of the vertices is the same and make a straightforward extension of the V matrix in the Lagrangian of Eq. (2.3) in order to include the heavy mesons,

$$V_\mu = \begin{pmatrix} \frac{\rho^0}{\sqrt{2}} + \frac{\omega}{\sqrt{2}} & \rho^+ & K^{*+} & \bar{D}^{*0} \\ \rho^- & -\frac{\rho^0}{\sqrt{2}} + \frac{\omega}{\sqrt{2}} & K^{*0} & D^{*-} \\ K^{*-} & \bar{K}^{*0} & \phi & D_s^{*-} \\ D^{*0} & D^{*+} & D_s^{*+} & J/\psi \end{pmatrix}_\mu , \qquad (6.1)$$

The diagrams for the exchange of one vector meson in the t and u channels are shown in Figs. 6.1 and 6.2. The difference with the light sectors come when one puts real masses of the particles. This must be

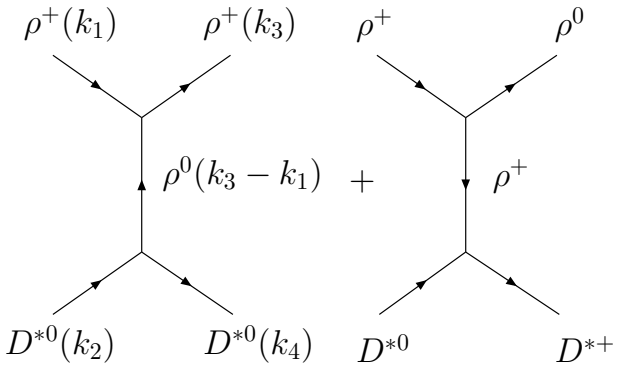

Figure 6.1: Vector exchange diagrams for $\rho D^* \to \rho D^*$.

done in order to respect thresholds and fulfill unitarity. Then, one can see that the diagrams of Fig. 6.2 have a rather different contribution than if one puts, for instance, a $\bar{K}^*$ instead of a D^* meson. Due to the heavy vector exchange, the diagrams of Fig. 6.2 will be proportional to $\kappa \sim m_\rho^2/m_{D^*}^2 = 0.15$ which makes them small. In addition, the "g^2" parameter will be moved from $m_\rho^2/(2f_\pi)^2$ to $m_{D^*}^2/2f_D^2$. We have seen that the important role is played by the vector exchange term, which means that the main source of interaction would come mostly from the two diagrams in Fig. 6.1. Note that in Fig. 6.1 there are not any ω meson, the $\omega\omega\omega$, $\rho\rho\omega$ and $\rho\omega\omega$ vertices are forbidden due to G-parity or isospin. This, added to the fact that the diagrams of Fig. 6.2 are suppressed by the factor $\kappa \simeq 0.15$ tell us that the ωD^* channel would not have an important place in the dynamics as will be shown when calculating the couplings to the different channels. It is easy to construct the isospin combinations that in our convention

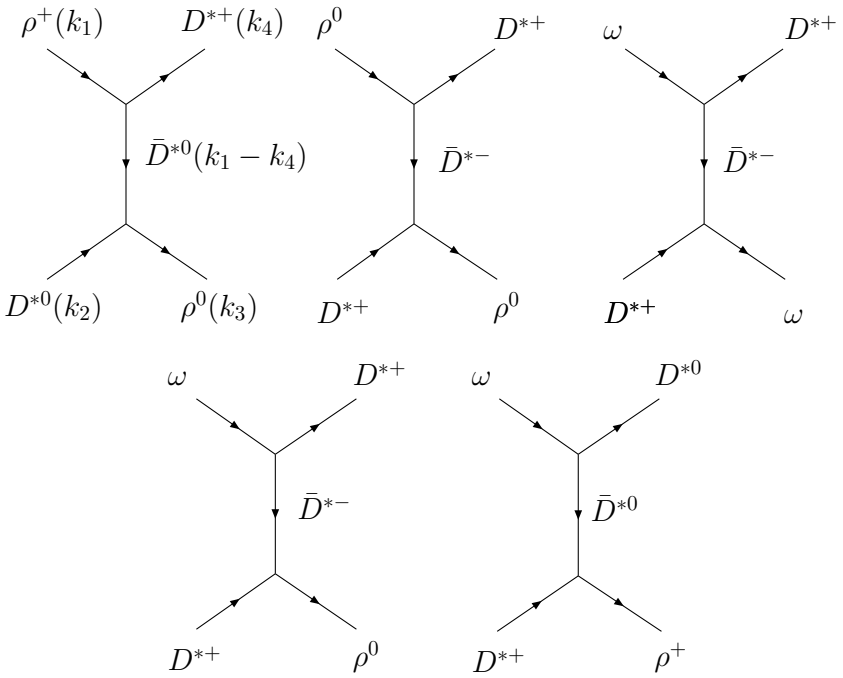

Figure 6.2: Diagrams including the exchange of one heavy vector meson.

is $D^{*0} = -|1/2, 1/2\rangle$ and $\rho^+ = -|1, 1\rangle$.

$$\begin{aligned} |\rho D^*, I = 1/2, I_3 = 1/2\rangle &= \sqrt{\frac{2}{3}}|\rho^+ D^{*0}\rangle - \frac{1}{\sqrt{3}}|\rho^0 D^{*+}\rangle, \\ |\rho D^*, I = 1/2, I_3 = 3/2\rangle &= \frac{1}{\sqrt{3}}|\rho^+ D^{*0}\rangle + \sqrt{\frac{2}{3}}|\rho^0 D^{*+}\rangle \ . \end{aligned} \quad (6.2)$$

We could also have s-channel D^*-exchange diagram but we found in [85] that this leads to a p-wave interaction for equal masses of the vectors, and only to a minor component of s-wave in the case of different masses [86].

The s-wave potential obtained once one has projected the amplitude into spin and isospin is written in Tables 6.1, 6.2 and 6.3 for the different possibilites: $\rho D^* \to \rho D^*$, $\rho D^* \to \omega D^*$ and $\omega D^* \to \omega D^*$ respectively. Where the $(k_1 + k_3) \cdot (k_2 + k_4)$ and $(k_2 + k_4) \cdot (k_2 + k_3)$ terms are expressed in terms of the invariant s:

$$\begin{aligned} (k_1 + k_3) \cdot (k_2 + k_4) &= \frac{3}{2}s - m_\rho^2 - m_{D^*}^2 - \frac{(m_\rho^2 - m_{D^*}^2)^2}{2s} \ , \\ (k_1 + k_4) \cdot (k_2 + k_3) &= \frac{3}{2}s - m_\rho^2 - m_{D^*}^2 + \frac{(m_\rho^2 - m_{D^*}^2)^2}{2s} \ . \end{aligned} \quad (6.3)$$

The factor κ is the suppressing factor of the D^* exchange terms, $\kappa = m_\rho^2/m_{D^*}^2 \sim 0.15$. We have calculated that these terms represent corrections of the order of 10% of the ρ exchange ones.

From the approximate total potential in these tables we can extract some conclusions: There is attraction in the $I = 1/2$ sector whereas the $I = 3/2$ sector is repulsive. Since the $I = 3/2$ quantum numbers is exotic, this is a welcome feature that seems to be rather universal in other studies [86, 118, 119] since the elusive exotic states do not show up in the approach due to dynamical reasons. The $\rho D^* \to \omega D^*$ and $\omega D^* \to \omega D^*$ potentials are repulsive and small. Finally, we can see in the Tables that the ρ-exchange term dominates.

I	J	Contact	ρ-exchange	D^*-exchange	$\sim$ Total$[I(J^P)]$
$1/2$	0	$+5g^2$	$-2\frac{g^2}{M_\rho^2}\,(k_1+k_3)\cdot(k_2+k_4)$	$-\frac{1}{2}\frac{\kappa\, g^2}{M_\rho^2}\,(k_1+k_4)\cdot(k_2+k_3)$	$-16g^2[1/2(0^+)]$
$1/2$	1	$+\frac{9}{2}g^2$	$-2\frac{g^2}{M_\rho^2}\,(k_1+k_3)\cdot(k_2+k_4)$	$+\frac{1}{2}\frac{\kappa\, g^2}{M_\rho^2}\,(k_1+k_4)\cdot(k_2+k_3)$	$-14.5g^2[1/2(1^+)]$
$1/2$	2	$-\frac{5}{2}g^2$	$-2\frac{g^2}{M_\rho^2}\,(k_1+k_3)\cdot(k_2+k_4)$	$-\frac{1}{2}\frac{\kappa\, g^2}{M_\rho^2}\,(k_1+k_4)\cdot(k_2+k_3)$	$-23.5g^2[1/2(2^+)]$
$3/2$	0	$-4g^2$	$+\frac{g^2}{M_\rho^2}\,(k_1+k_3)\cdot(k_2+k_4)$	$+\frac{\kappa\, g^2}{M_\rho^2}\,(k_1+k_4)\cdot(k_2+k_3)$	$+8g^2[3/2(0^+)]$
$3/2$	1	0	$+\frac{g^2}{M_\rho^2}\,(k_1+k_3)\cdot(k_2+k_4)$	$-\frac{\kappa\, g^2}{M_\rho^2}\,(k_1+k_4)\cdot(k_2+k_3)$	$+8g^2[3/2(1^+)]$
$3/2$	2	$+2g^2$	$+\frac{g^2}{M_\rho^2}\,(k_1+k_3)\cdot(k_2+k_4)$	$+\frac{\kappa\, g^2}{M_\rho^2}\,(k_1+k_4)\cdot(k_2+k_3)$	$+14g^2[3/2(2^+)]$

Table 6.1: $V(\rho D^* \to \rho D^*)$ for the different spin-isospin channels including the exchange of one heavy vector meson. The approximate Total is obtained at the threshold of ρD^*.

I	J	Contact	ρ-exchange	D^*-exchange	$\sim$ Total$[I(J^P)]$
$1/2$	0	$-\sqrt{3}g^2$	-	$+\frac{\sqrt{3}}{2}\frac{\kappa\, g^2}{M_\rho^2}\,(k_1+k_4)\cdot(k_2+k_3)$	$0[1/2(0^+)]$
$1/2$	1	$+\frac{3\sqrt{3}}{2}g^2$	-	$-\frac{\sqrt{3}}{2}\frac{\kappa\, g^2}{M_\rho^2}\,(k_1+k_4)\cdot(k_2+k_3)$	$\frac{\sqrt{3}}{2}g^2[1/2(1^+)]$
$1/2$	2	$+\frac{\sqrt{3}}{2}g^2$	-	$+\frac{\sqrt{3}}{2}\frac{\kappa\, g^2}{M_\rho^2}\,(k_1+k_4)\cdot(k_2+k_3)$	$\frac{3\sqrt{3}}{2}g^2[1/2(2^+)]$

Table 6.2: $V(\rho D^* \to \omega D^*)$ for the different spin-isospin channels including the exchange of one heavy vector meson. The approximate Total is obtained at the threshold of ρD^*.

I	J	Contact	ρ-exchange	D^*-exchange	$\sim$ Total$[I(J^P)]$
$1/2$	0	$-g^2$	-	$+\frac{1}{2}\frac{\kappa\, g^2}{M_\rho^2}\,(k_1+k_4)\cdot(k_2+k_3)$	$0[1/2(0^+)]$
$1/2$	1	$+\frac{3}{2}g^2$	-	$-\frac{1}{2}\frac{\kappa\, g^2}{M_\rho^2}\,(k_1+k_4)\cdot(k_2+k_3)$	$\frac{1}{2}g^2[1/2(1^+)]$
$1/2$	2	$+\frac{1}{2}g^2$	-	$+\frac{1}{2}\frac{\kappa\, g^2}{M_\rho^2}\,(k_1+k_4)\cdot(k_2+k_3)$	$\frac{3}{2}g^2[1/2(2^+)]$

Table 6.3: $V(\omega D^* \to \omega D^*)$ for the different spin-isospin channels including the exchange of one heavy vector meson. The approximate Total is obtained at the threshold of ρD^*.

6.3 Results with the four-vector-contact + vector exchange potentials

When dealing with D mesons we follow the works of D. Gamermann [108] and [109]. This means that we take similar parameters. We take $\mu = 1500$ MeV in the formula of Eq. (3.45) and fine-tune α (which must be ~ -2) to get the mass of the $D_2^*(2460)$, this gives $\alpha = -1.74$. When we put $\alpha = -2$ we get the position of the spin= 2 state at 2346 MeV. The pole positions with $\mu = 1500$ MeV and $\alpha = -1.74$ can be seen in Table 6.4. We find three states, one for each spin= $0, 1, 2$ and like for the $\rho\rho$ interaction we also obtain a more bound state with spin= 2 than for spin= $0, 1$. In the PDG there is one state listed, the $D^*(2640)$ with $I(J^P) = 1/2(?^?)$. In principle, we do not have reasons to identify it with the state found at 2611 MeV for spin= 1 instead of the state found for spin= 0. But we identify this state of the PDG with our state with spin= 1 and the reasons will be given later. In Table 6.5 we give the modules of the couplings g_i

I	J	$\sqrt{s}$ (MeV)
1/2	0	2592
1/2	1	2611
1/2	2	2450

Table 6.4: Pole positions for the three different cases

in units of GeV to the different channels that have been calculated as the residues of the amplitudes, Eq. (3.50). We have also used the formula of the cutoff for G, Eq. (3.23), instead of the formula of dimensional regularization, Eq. (3.45), and we have tested the results with a cutoff of natural size $q_{\max} = 1 - 1.2$ GeV. The differences are around 10%, which is an indication of the stability of the results.

According to the PDG, the widths of the $D_2^*(2460)$ and $D^*(2640)$

Channel	$D_0^*(2600)$	$D_1^*(2640)$	$D_2^*(2460)$
ρD^*	14.32	14.04	17.89
ωD^*	0.53	1.40	2.35

Table 6.5: Modules of the couplings g_i in units of GeV for the poles in the $J = 0,\ 1,\ 2;\ I = 1/2$ sector with the channel ρD^* and ωD^*.

are 43 ± 4 MeV (for the D_2^{*0}, and 37 ± 6 MeV for the $D_2^{*\pm}$) and < 15 MeV respectively. This is not compatible with the width that we obtain here, zero, and different decay mechanisms will be introduced. This will be done in Section 6.5.

6.4 Uncertainties related to SU(4) breaking

Until now the results have been obtained from a potential which is proportional to g^2, being $g = m_\rho/2f_\pi$. However, we have heavy particles, D^*, in the vertices. We have set $g = m_\rho/2f_\pi$ since it is the ρ meson that is exchanged in the most important terms. But, it is important to test how stable are the result by taking different values of g^2. To do so, we estimate uncertainties, following two strategies:

1) We vary g^2 taking $g^2 = (m_\rho/2f_\pi)^2$, gg_D, with $g_D = m_{D^*}/2f_D = 160$ MeV, and g_D^2, and make a small readjustement of the subtraction constant, α, in order to get the D_2^* state mass at its value when using $g = m_\rho/2f_\pi$. This option of looking at the uncertainties is realistic in the sense that the fine tuning of the parameter α to get the precise position of one resonance is always done. The pole positions and coupling constants obtained are shown in Tables 6.6 and 6.7 respectively.

2) We observe the problem from a more extreme point of view, which is taking $\alpha = -1.53$ and evaluate the changes in the results when varying $g^2 \to g^2, gg_D, g_D^2$. The results are shown in Tables 6.8 and 6.9.

Constant & α	$J=0$	$J=1$	$J=2$
g^2 & -1.74	2592	2611	2450
gg_D & -1.53	2571	2587	2450
g_D^2 & -1.39	2551	2565	2450

Table 6.6: Pole positions and subtraction constant obtained for the three different cases, g^2, gg_D and g_D^2, when one fixes the mass of the pole with $J = 2$.

When performing the strategy 1), we observe moderate changes in the pole positions of around 20 MeV and small variations in the ρD^* coupling constant of 8%. The ωD^* couplings experience larger variations of 25% but we can see from Table 6.7 that this channel, due to the heavy-vector exchange terms, plays essentially no role in the problem.

The strategy 2) leads to larger changes in the pole positions shown in Table 6.8. We see that this strategy leads to larger changes than the former one. The changes in the mass of the resonances are of the order of $70-90\%$ MeV. Even though, these variations are usual in any hadron model upon reasonable changes in the parameters. Regarding the coupling constants, Table 6.9, we observe that those of the most important channel are rather stable and we can say the variations are of around 8%, definitely very similar to those obtained from 1).

To sum up, we have seen that the results are rather stable upon breaking the SU(4) symmetry and do not depend so much of the use of g or g_D if the correct readjustment of the subtraction constant is

Channel	$D_0(2600)$			$D_1^*(2640)$			$D_2^*(2460)$		
Cases:	1)	2)	3)	1)	2)	3)	1)	2)	3)
ρD^*	14.32	15.69	17.05	14.04	15.37	16.69	17.89	19.58	21.01
ωD^*	0.53	0.68	0.84	1.40	1.69	1.99	2.35	2.60	2.78

Table 6.7: Modules of the couplings g_i in units of GeV for the poles in the $J = 0$, 1, 2; $I = 1/2$ sector and the channels ρD^* and ωD^*, in the cases 1) using g^2 and $\alpha = -1.74$, 2) using gg_D and $\alpha = -1.53$ and 3) using g_D^2 and $\alpha = -1.39$.

$\alpha = -1.53$	$D_0(2600)$			$D_1^*(2640)$			$D_2^*(2460)$		
Cases:	g^2	gg_D	g_D^2	g^2	gg_D	g_D^2	g^2	gg_D	g_D^2
$\sqrt{s}\,(MeV)$	2645	2571	2502	2661	2587	2517	2539	2450	2370

Table 6.8: Pole positions for the three states using $\alpha = -1.53$ in the different cases g^2, gg_D and g_D^2.

Channel	$D_0(2600)$			$D_1^*(2640)$			$D_2^*(2460)$		
$\alpha = -1.53$	g^2	gg_D	g_D^2	g^2	gg_D	g_D^2	g^2	gg_D	g_D^2
ρD^*	14.51	15.69	16.32	14.08	15.37	16.06	18.15	19.58	20.67
ωD^*	0.37	0.68	1.12	1.19	1.69	2.28	2.20	2.60	3.03

Table 6.9: Modules of the couplings g_i in units of GeV for the poles in the $J = 0$, 1, 2; $I = 1/2$ sector and the channels ρD^* and ωD^*.

done. Even fixing α, and varying g^2 the changes are not very large and the results remain qualitatively the same. This is a wellcome feature that makes the strategy when dealing with heavy mesons more reliable. In the following, we take the g^2 option, but keeping in mind the uncertainties obtained.

6.5 Convolution of the G function and the πD decay mode

Here we study different mechanisms that allow the states obtained to decay into pseudoscalar mesons. Due to the large width of the ρ mesons, the states decay to $D^*\pi\pi$. This can be implemented in the calculations via the convolution of the G function with the ρ mass distribution, that, in the case where we have only one ρ-meson correspond to use the formulas:

$$\begin{aligned}\tilde{G}(s) &= \frac{1}{N}\int_{(m_\rho-2\Gamma_\rho)^2}^{(m_\rho+2\Gamma_\rho)^2} d\tilde{m}_1^2(-\frac{1}{\pi})\mathcal{I}m\frac{1}{\tilde{m}_1^2-m_\rho^2+i\Gamma\tilde{m}_1} \\ &\quad \times G(s,\tilde{m}_1^2,m_{D^*}^2)\ , \end{aligned} \tag{6.4}$$

with

$$N=\int_{(m_\rho-2\Gamma_\rho)^2}^{(m_\rho+2\Gamma_\rho)^2} d\tilde{m}_1^2(-\frac{1}{\pi})\mathcal{I}m\frac{1}{\tilde{m}_1^2-m_\rho^2+i\Gamma\tilde{m}_1}\ , \tag{6.5}$$

where $\Gamma_\rho = 146.2$ MeV and for $\Gamma\equiv\Gamma(\tilde{m})$ we take the ρ width for the decay into the pions in p-wave

$$\Gamma(\tilde{m})=\Gamma_\rho(\frac{\tilde{m}^2-4m_\pi^2}{m_\rho^2-4m_\pi^2})^{3/2}\theta(\tilde{m}-2m_\pi)\ . \tag{6.6}$$

Now, the states appear at masses 2602, 2620 and 2465 with widths $\sim$ 5, 4 and 0 for spin$=0,1$ and 2 respectively. The widths obtained are small compared to the data in the PDG and other mechanisms should be included. The box-diagrams for decaying into πD are shown in

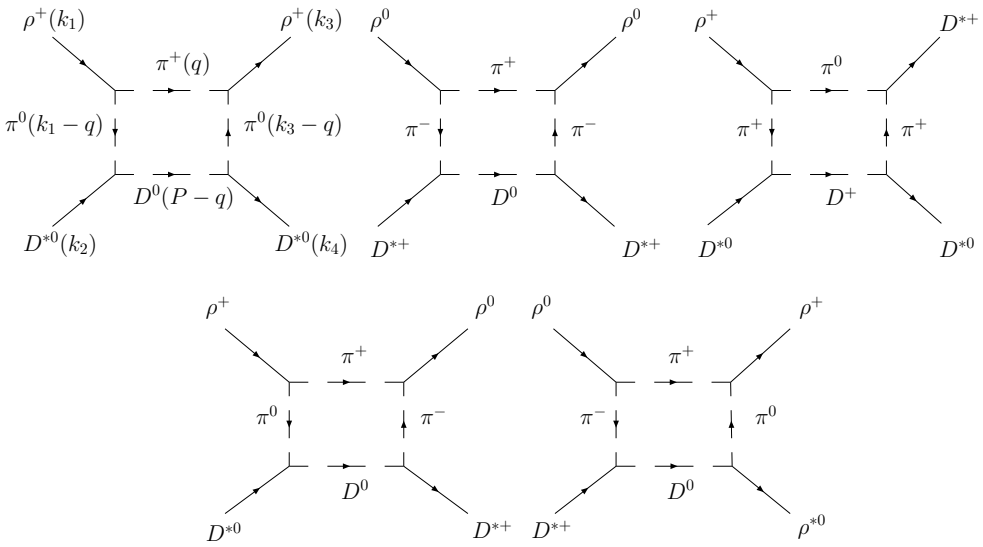

Figure 6.3: πD-box diagrams

Fig. 6.3. The evaluation of those amplitudes is similar to that made for the $\pi\pi$-box in Chapter 3 and we simply show the final formula.

$$\begin{aligned} t^{(2\pi,I=1/2,J=0)} &= 20\,\tilde{V}^{(\pi D)}\,, \\ t^{(2\pi,I=1/2,J=2)} &= 8\,\tilde{V}^{(\pi D)}\,, \end{aligned} \tag{6.7}$$

where $\tilde{V}^{(\pi D)}$ is given by

$$\begin{aligned} \tilde{V}^{(\pi D)} &= \frac{8\,g^4}{15\pi^2}\int_0^{q_{max}} dq\,\vec{q}^{\,6}\,\left(\frac{1}{2\omega}\right)^3\left(\frac{1}{k_1^0+2\omega}\right)^2\frac{1}{2\omega_D}\,f(P^0) \\ &\times\frac{1}{k_4^0-\omega-\omega_D+i\epsilon}\,\frac{1}{k_1^0-2\omega+i\epsilon}\,\frac{1}{k_3^0-2\omega+i\epsilon} \\ &\times\frac{1}{P^0-\omega-\omega_D+i\epsilon}\frac{1}{P^0+\omega+\omega_D} \\ &\times\left(\frac{1}{k_2^0+\omega+\omega_D}\right)^2\frac{1}{k_2^0-\omega-\omega_D+i\epsilon} \end{aligned} \tag{6.8}$$

where

$$\begin{aligned} f(P^0) &= 4\{-32k_3^0P^0\omega^2\omega_D((P^0)^2-2\omega^2-3\omega\omega_D-\omega_D^2) \\ &\quad +2(k_3^0)^3P^0\omega_D((P^0)^2-5\omega_D^2-2\omega\omega_D-\omega_D^2) \\ &\quad +(k_3^0)^4(2\omega^3-(P^0)^2\omega_D+3\omega^2\omega_D+2\omega\omega_D^2+\omega_D^3) \\ &\quad +4\omega^2(8\omega^5+33\omega^4\omega_D+54\omega^3\omega_D^2+3\omega_D((P^0)^2-\omega_D^2)^2 \\ &\quad +18\omega\omega_D^2(-(P^0)^2+\omega_D^2)+\omega^2(-12\ (P^0)^2\omega_D+44\omega_D^3)) \\ &\quad -(k_3^0)^2(16\omega^5+63\omega^4\omega_D+74\omega^3\omega_D^2+\omega_D((P^0)^2-\omega_D^2)^2 \\ &+ \quad 32\omega^2\omega_D(-(P^0)^2+\omega_D^2)+\omega(-6(P^0)^2\ \omega_D^2+6\omega_D^4))\} \end{aligned} \tag{6.9}$$

and $\omega=\sqrt{\vec{q}^2+m_\pi^2}$, $\omega_D=\sqrt{\vec{q}^2+m_D^2}$, $P^0=k_1^0+k_2^0$. Due to the presence of heavy particles, we have more uncertainties when using form factors. Concretely, the measurement of the CLEO Collaboration [120] gives a strong coupling for the $D^*D\pi$ vertex. The experimental value turns out to be almost a factor two larger than the value obtained from some theoretical predictions using different approaches of the QCD sum rule [121, 122]. In the Hidden Gauge formalism, we have:

$$\langle D^{*+}(p)\pi^-(q)|D^0(p+q)\rangle=-2\,g'_{D^*D\pi}q_\mu\epsilon^\mu\ , \tag{6.10}$$

with $g'_{D^*D\pi}=m_{D^*}/2f_D=6.3$. This is also smaller than the experimental value, $g^{exp}_{D^*D\pi}=8.95\pm0.15\pm0.95$. In view of this, we implement two different form factors in order to obtain the final results:

1) We use a form factor for an off-shell π in each vertex like in Chapter 3, which is

$$F(q)=\frac{\Lambda^2-m_\pi^2}{\Lambda^2+\vec{q}^2}\ , \tag{6.11}$$

with $\Lambda=1400,1500$ MeV and we put $g=m_\rho/2f_\pi$ in the formula Eq. (6.8). The results for the real and imaginary part of the box diagram of Fig. 6.3 can be seen in Figs. 6.4 and 6.5 for different Λ values and compared to the contact + exchange terms. We observe that the real parts are much smaller

than that of the contact + exchange terms and we simply neglect them in the calculations. The imaginary part obtained is larger for spin= 2 than for spin= 0, which is consistent with the formula of Eq. (6.7) .

2) We use a form factor for the $D^*D\pi$ vertex that comes from QCD sum rules [123] for a π offshell, which is:

$$F'(q^2) = g_{D^*D\pi} e^{q^2/\Lambda^2} \quad \text{with } \Lambda = 1\, GeV \ , \tag{6.12}$$

together with the use of the experimental value of the $D^*D\pi$ coupling measured by the CLEO Collaboration, $g^{\rm exp}_{D^*D\pi} = 8.95$. In Eq. (6.12), we must change $q \to k_1 - q$, with $q_0 \sim 769.4$ MeV and $k_1 - q^0 \sim 6$ MeV which leads to $(k^0 - q^0)^2/\Lambda^2 \sim 10^{-5}$. Therefore, the zero component in the pion cuadrimomentum can be neglected. Thus, we replace the factor g^4 in Eq. (6.8) by

$$g^2_{\rho\pi\pi}\, (g^{exp}_{D^*D\pi})^2\, (e^{-\vec{q}^{\,2}/\Lambda^2})^4 \ , \tag{6.13}$$

with $g_{\rho\pi\pi} = m_\rho/2\, f_\pi = 4.2$ and $g^{exp}_{D^*D\pi} = 8.95$ MeV (the experimental value), $\Lambda \sim 1$ GeV and $\vec{q}$ running in the integral.

The real and imaginary part of the potential are shown in Figs. 6.6 and 6.7 respectively. Again, the real part of the πD box diagram is much smaller than the contact + exchange terms and can be neglected.

The final squared amplitudes for spin= 0 and 2 are shown in Figs. 6.8 and 6.9, for the two kinds of form factors, Eqs. (6.11) and (6.12) respectively. In Table 6.10 the masses and widths taken from these plots are shown. We observe that the two form factors, provide widths of the same order of magnitude, but, the closest value to the PDG data gives preference to the second option.

One remarkable point is that now we are able to predict the quantum numbers of the $D^*(2640)$ to be 1^{++} since the box diagrams have only $J = 0$ and 2, and $J = 1$ is forbidden, what makes the state with 1^{++} to be narrow and the ones with 0^{++} and 2^{++}, the $D_0(2600)$ and

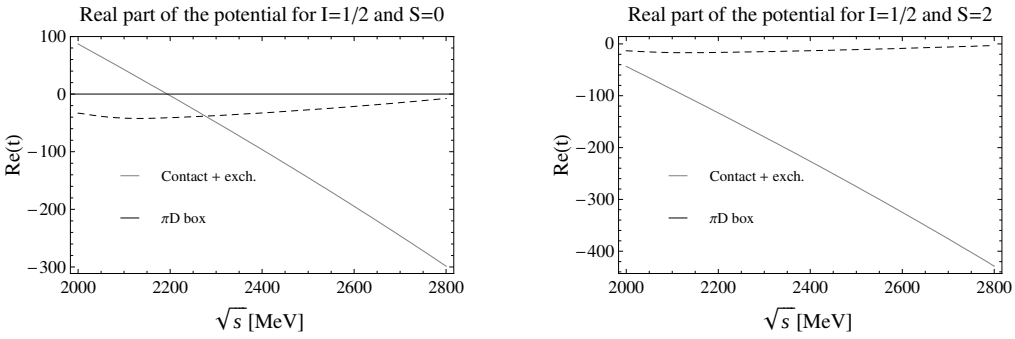

Figure 6.4: Real part of the potential for $I = 1/2$; $J = 0$; and $I = 1/2$; $J = 2$;.

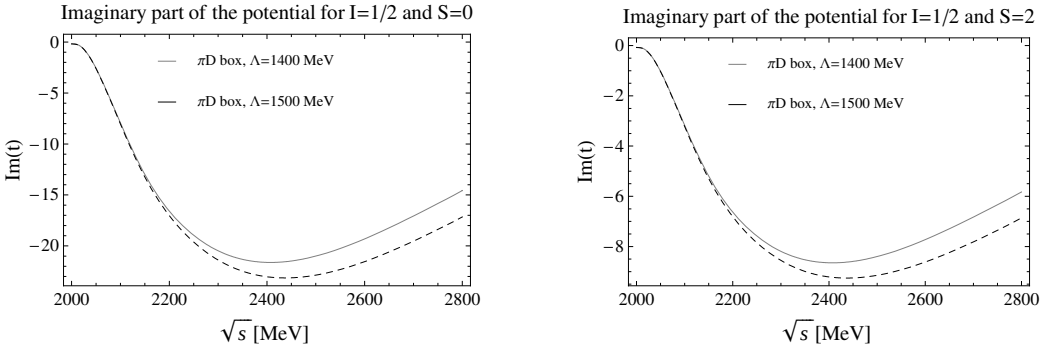

Figure 6.5: Imaginary part of the potential for $I = 1/2$; $J = 0$; and $I = 1/2$; $J = 2$;.

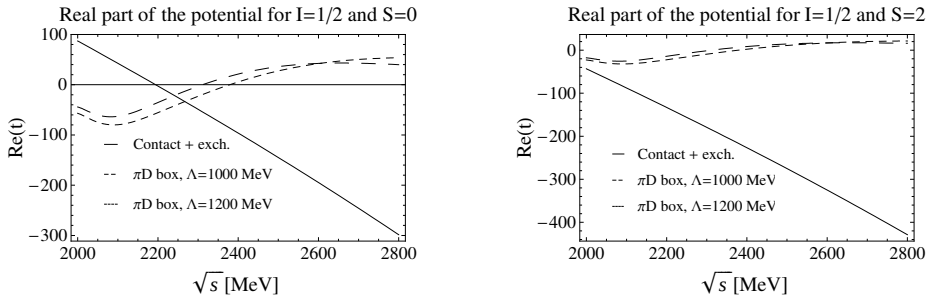

Figure 6.6: Real part of the potential for $I = 1/2$; $J = 0$; and $I = 1/2$; $J = 2$.

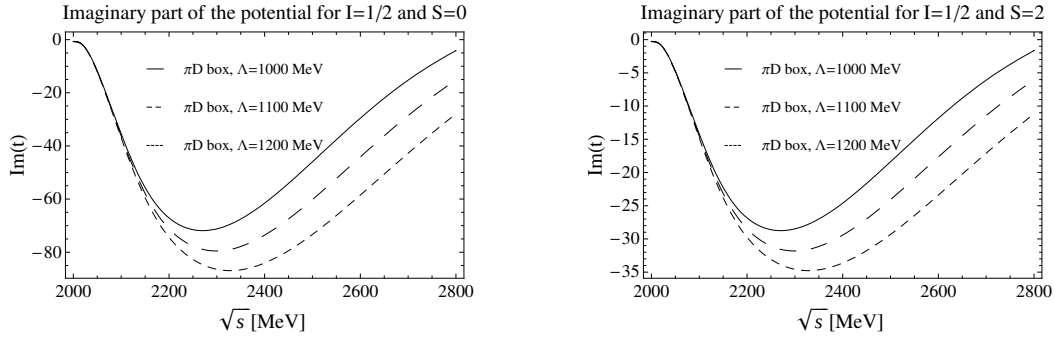

Figure 6.7: Imaginary part of the potential for $I = 1/2$; $J = 0$; and $I = 1/2$; $J = 2$.

	Theory			Experiment			
$I[J^{P(C)}]$	M[MeV]	Γ_A[MeV]	Γ_B[MeV]	Nombre	M[MeV]	Γ[MeV]	$I[J^{P(C)}]$
$(1/2, 0)$	2602	50	61	"$D_0^*(2600)$"		–	-
$(1/2, 1)$	2620	4	4	"$D^*(2640)$"	2637 ± 6	< 15	$1/2[?^?]$
$(1/2, 2)$	2465	20	40	"$D^*(2460)$"	2464.4 ± 1.9	37 ± 6	$1/2[2^+]$

Table 6.10: States obtained from the ρD^* interaction and its experimental counterpart if there is. Γ_A represents the width calculated using the form factor 1), Eq. (6.11), and Γ_B the form factor 2), Eq. (6.12).

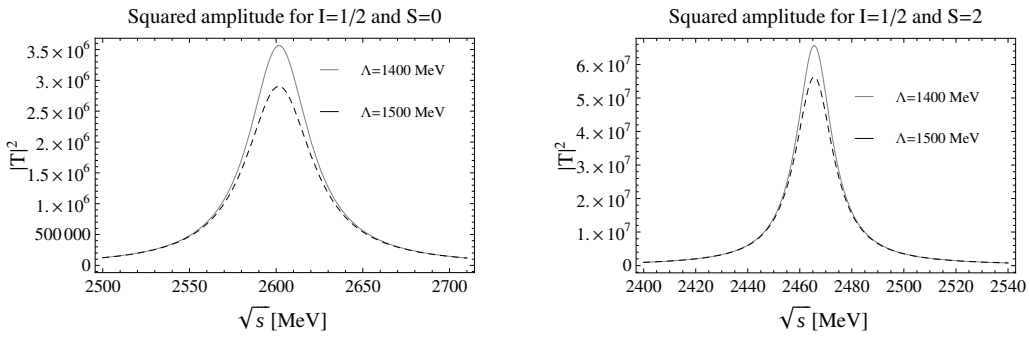

Figure 6.8: Squared amplitude for $J = 0$ and $J = 2$ including the convolution of the ρ-mass distribution and the πD-box diagram.

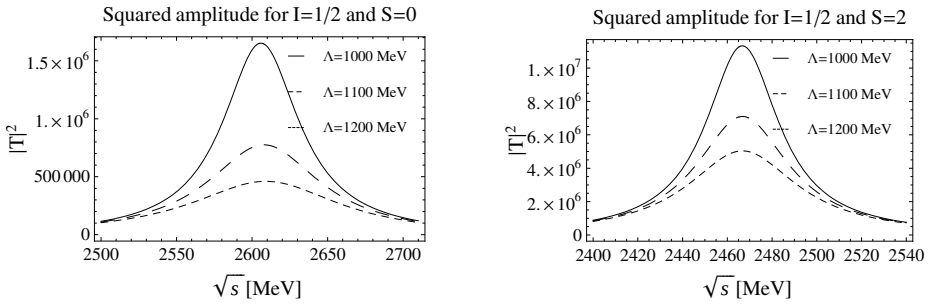

Figure 6.9: Squared amplitude for $J = 0$ and $J = 2$ including the convolution of the ρ-mass distribution and the πD-boxed diagram.

$D_2^*(2460)$, respectively, broader, a feature which was not expected at the beginning since this state is higher in mass than the $D_2(2460)$.

In summary, we have seen in this Chapter that the ρD^* interaction lead to three states for $J = 0, 1$ and 2 and we have made predictions for the quantum numbers of the $D^*(2640)$ state in the PDG, that should be $J^{PC} = 1^{++}$ according to our calculations. Whereas, a new state relatively broad with mass around ~ 2600 MeV for $J = 0$ has been predicted.

Chapter 7

The vector - vector interaction in the $C = 0, S = 0$ sector around 4000 MeV

We study the vector - vector system including all the possible channels with quantum numbers charm $= 0$, strangeness $= 0$ around the energy region of 4000 MeV. New states with hidden charm around 4000 MeV have been discovered by the B factories. They are intriguingly close to the $D^*\bar{D}^*$ and $D_s^*\bar{D}_s^*$ thresholds and do not have the properties of the charmonium states. We study the possible formation of $D^*\bar{D}^*$ and $D_s^*\bar{D}_s^*$ bound states in the framework of the Hidden Gauge formalism.

7.1 Introduction

The B factories at SLAC, KEK and CESR that originally were constructed to test matter-antimatter asymetries or CP violation, within or beyond the standard model, have discovered a number of charm and hidden charm mesons that do not seem to have the properties of

the charmonium states. Some of these states are collected in Table 7.1 taken from S. L. Olsen [124].

The first of these XYZ states is the X(3872), observed by the Belle collaboration as a narrow peak near 3872 MeV in the $\pi^+\pi^- J/\psi$ invariant mass distribution. The mass of the X(3872) is very close to the $D\bar{D}^*$ threshold which suggest it could be a bound state made of D and $\bar{D}^*$. Many theoretical studies testing this hypothesis have been made [1, 2, 4, 109, 128, 125, 126, 129, 127]. The decay $X(3872) \to \pi^+\pi^-\pi^0 J/\psi$ has been also observed and Belle quoted it to have the same ratio than to $\pi^+\pi^- J/\psi$, where the 3π or 2π come from ω or ρ, which in principle would imply a mixture of $I = 0$ and $I = 1$ [128]. However, an alternative explanation is given in [129]. Even though the X(3872) has mostly $I = 0$, and both components, $D^0\bar{D}^{*0}$ and $D^+\bar{D}^{*+}$ are needed in the same quantity to have isospin zero, it is the large ρ-width that makes the state to decay into $\pi^+\pi^- J/\psi$ for the lower components of the ρ-mass distribution. The states that we consider here are the X(3940), the Y(3940), the X(4160) and the Z(3930) and these are some of their common properties:

- They are close to the $D^*\bar{D}^*$ or $D^*\bar{D}_s$ thresholds
- They have C-parity$= +$
- They are relatively narrow
- The estimated partial decay widths to $\omega J/\psi$ or $\phi J/\psi$ usually are above 1 MeV, which is quite larger than the measured partial decay widths for any of the observed hadronic transitions between charmonium states
- They have been observed in B decays or in double charmonium production reaction $e^+e^- \to J/\psi + X$

Regarding the X(3940), we can say that whereas the $X(3940) \to D\bar{D}^*$ reaction has been observed, there is no signal for its decay into $D\bar{D}$ or $\omega J/\psi$. This lead to consider its assignment with a $J^{PC} = 0^{-+}$,

state	M (MeV)	Γ (MeV)	J^{PC}	Decay Modes	Production Modes
$Y_s(2175)$	2175 ± 8	58 ± 26	1^{--}	$\phi f_0(980)$	e^+e^- (ISR), J/ψ decay
$X(3872)$	3871.4 ± 0.6	< 2.3	1^{++}	$\pi^+\pi^- J/\psi$,$\gamma J/\psi$	$B \to KX(3872)$, $p\bar{p}$
$X(3875)$	3875.5 ± 1.5	$3.0^{+2.1}_{-1.7}$		$D^0\bar{D}^0\pi^0$	$B \to KX(3875)$
$Z(3940)$	3929 ± 5	29 ± 10	2^{++}	$D\bar{D}$	$\gamma\gamma$
$X(3940)$	3942 ± 9	37 ± 17	J^{P+}	$D\bar{D}^*$	$e^+e^- \to J/\psi X(3940)$
$Y(3940)$	3943 ± 17	87 ± 34	J^{P+}	$\omega J/\psi$	$B \to KY(3940)$
$Y(4008)$	4008^{+82}_{-49}	226^{+97}_{-80}	1^{--}	$\pi^+\pi^- J/\psi$	e^+e^-(ISR)
$X(4160)$	4156 ± 29	139^{+113}_{-65}	J^{P+}	$D^*\bar{D}^*$	$e^+e^- \to J/\psi X(4160)$
$Y(4260)$	4264 ± 12	83 ± 22	1^{--}	$\pi^+\pi^- J/\psi$	e^+e^-(ISR)
$Y(4350)$	4361 ± 13	74 ± 18	1^{--}	$\pi^+\pi^-\psi'$	e^+e^-(ISR)
$Z(4430)$	4433 ± 5	45^{+35}_{-18}	?	$\pi^\pm\psi'$	$B \to KZ^\pm(4430)$
$Y(4660)$	4664 ± 12	48 ± 15	1^{--}	$\pi^+\pi^-\psi'$	e^+e^-(ISR)
Y_b	$\sim 10,870$	?	1^{--}	$\pi^+\pi^-\Upsilon(nS)$	e^+e^-

Table 7.1: A summary of the properties of the candidate XYZ mesons discussed in the text. For simplicity, the quoted errors are quadratic sums of statistical and systematic uncertainties.

3^1S_1 charmonium state (η_c'' state), but then the mass sould be ~ 4050 MeV or even higher [130].

Concerning the Y(3940), although there are some small numerical discrepancies between the Belle's and Babar's central values for its mass and width, the measurements suggest a radially excited P-wave charmonium state, however, if it were the case, the $\chi_{c1}(2P) \to D\bar{D}^*$ decay mode, which has not been observed, would be the dominant decay mode. This ensures that despite of the close values of the mass and width to the X(3940), we are dealing with a different particle. For its assignment to a charmonium state with $J^{PC} = 0^{-+}(\eta_c)$ the mass is too low whereas for the $J^{PC} = 0^{++}(\chi'_{c0})$, the mass is too high [131]. In addition, one expects that the open charm decay modes are the dominant ones for $c\bar{c}$ states, and this state shows large estimated partial decay widths to $\omega J/\psi$ of 1 MeV or larger, which is very unusual for transitions between charmonium states.

The X(4160) has been observed as a mass peak in the $D^*\bar{D}^*$ system in the $e^+e^- \to J/\psi D^*\bar{D}^*$ reaction. The known charmonium states seen in $e^+e^- \to J/\psi D^*\bar{D}^*$ have $J = 0$, which suggests its identification with a $3'S_0(\eta_c'')$ or $4'S_0(\eta_c''')$ charmonium states, however, the mass predicted in the first case is smaller, ~ 4050 MeV, and higher 4400 MeV in the second case [130].

Finally, the Z(3930) has been observed in the $D\bar{D}$ spectrum from $\gamma\gamma$ collisions. The production mechanism ensures $J^{PC} = 0^{++}$, or 2^{++} but Belle favors the 2^{++} hypothesis from the study of angular distributions, making its assignment to the $2^3P_2(\chi'_{c2})$ charmonium state possible [124, 132].

The CDF collaboration has measured a peak very narrow near the $J/\psi\phi$ threshold, it has been called the Y(4140). Although the value of the mass is very close to the one of the X(4160), its small width lead to consider it as a different state.

There are some theoretical approaches. In [133], the authors solved the Schrödinger equation from a potential that includes vector, pion and σ exchange and they find molecualar solutions for the Y(3930) and Y(4140) with $J^P = 0^+, 2^+$, concluding that they

are molecular partners. In [134] the decay rates of the $Y(3940) \to J/\psi\omega$ and $Y(4140) \to J/\psi\phi$ are calculated under the assumption of hadronic molecuels with $J^{PC} = 0^{++}$ and they turn out to be consistent with the experimental data, which supports the molecular assumption. The coupling constants are calculated by means of the compositeness condition of Weinberg. In [135] it is argued that the peak at 4140 MeV named as the Y(4140) is just a $\phi J/\psi$ threshold effect.

In the following we calculate the vector - vector amplitudes in the hidden charm sector around 4000 MeV. See [136] for a detailed explanation.

7.2 Potential

We are interested in the sector charm= 0, strangeness= 0. Therefore the possible channels for isospin = 0 are

$$D^*\bar{D}^*(4017),\ D_s^*\bar{D}_s^*(4225),\ K^*\bar{K}^*(1783),\ \rho\rho(1551),\ \omega\omega(1565)$$

$$\phi\phi(2039),\ J/\psi J/\psi(6194),\ \omega J/\psi(3880),\ \phi J/\psi(4116),\ \omega\phi(1802)$$

where the magnitude between parenthesis is the sum of the masses of the two meson involved, and for isospin = 1 we have

$$D^*\bar{D}^*(4017),\ K^*\bar{K}^*(1783),\ \rho\rho(1551),\ \rho\omega(1558),\ \rho J\psi(3872),\ \rho\phi(1795).$$

The case of $I = 2$ that involves only the $\rho\rho$ channel was already considered in [86]. With the isospin doublets: $(-D^{*0},\ D^{*+})$, $(D^{*-},\ \bar{D}^{*0})$, $(-K^{*-},\ \bar{K}^{*0})$, $(K^{*0},\ K^{*+})$ and the triplet $(\rho^-,\ \rho^0,\ -\rho^+)$, we build the following isospin combinations for $D^*\bar{D}^*$:

$$\begin{aligned} |D^*\bar{D}^*, I = 0, I_3 = 0\rangle &= \frac{1}{\sqrt{2}}|D^{*+}D^{*-}\rangle + \frac{1}{\sqrt{2}}|D^{*0}\bar{D}^{*0}\rangle, \\ |D^*\bar{D}^*, I = 1, I_3 = 0\rangle &= \frac{1}{\sqrt{2}}|D^{*+}D^{*-}\rangle - \frac{1}{\sqrt{2}}|D^{*0}\bar{D}^{*0}\rangle. \quad (7.1) \end{aligned}$$

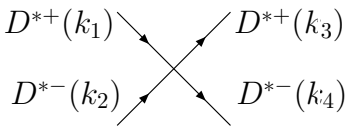

Figure 7.1: Contact term of the $D^{*+}D^{*-}$ interaction.

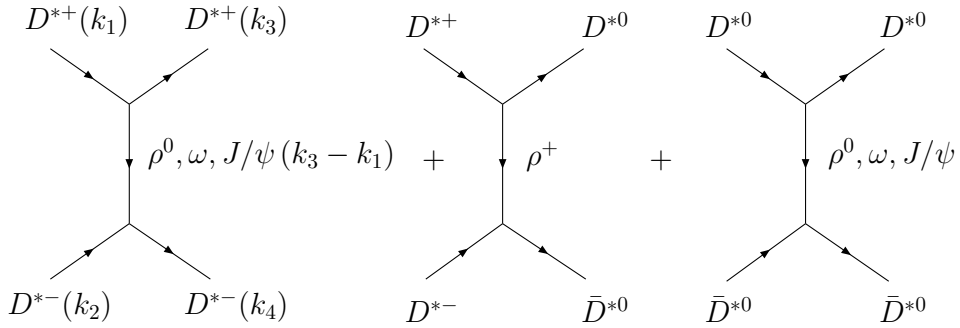

Figure 7.2: Vector exchange diagrams for $D^*\bar{D}^* \to D^*\bar{D}^*$.

and similarly for the $K^*\bar{K}^*$ and $\rho\rho$ channels. By means of the Lagrangians given for the four-vector-contact term, Eq. (3.4), and three-vector-contact term, Eq. (3.5), we build the amplitudes for diagrams like in Figs. 7.1 and 7.2, shown for the $D^{*+}D^{*-}$ interaction, in the approximation of neglecting the momenta of the external particles compared to the mass as done in the previous chapters. In Tables B.1 - B.6 of the Appendix B we give the amplitudes for the $D^*\bar{D}^* \to$ channel and $D_s^*\bar{D}_s^* \to$ channel reactions. We also need the amplitudes for the reactions involving only the nonet of vector mesons which are in the Tables V-X (contact term) and XVIII-XXI (exchange term) in [86]. Some of these amplitudes do not appear since they are zero. They are $J/\psi J/\psi$, $\omega J/\psi$, $\phi J/\psi \to K^*\bar{K}^*$, $\rho\rho$, $\omega\omega$, $\phi\phi$, $J/\psi J/\psi$, $\omega J/\psi$, $\phi J\psi$, $\omega\phi$ for $I = 0$ and $\rho J/\psi \to K^*\bar{K}^*$, $\rho\rho$, $\rho\omega$, $\rho J/\psi$, $\rho\phi$ for $I = 1$. Now we deal with pairs of two-heavy-vector mesons, heavy-

light or two-light-vector mesons and we use the following estrategy when setting the parameters, g^2 and α in Eqs. (3.4), (3.5) and (3.45). We take $\sqrt{g_i^2}$ for each external particle, being $g = M_\rho/(2f_\pi) = 4.17$ with $f_\pi = 93$ MeV for light mesons and $g_D = M_{D^*}/(2f_D) = 6.9$, $g_{D_s} = M_{D_s^*}/(2f_{D_s}) = 5.47$, $g_{\eta_c} = M_{J/\psi}/(2f_{\eta_c}) = 5.2$ with $f_D = 206/\sqrt{2} = 145.66$ MeV [78], $f_{D_s} = 273/\sqrt{2} = 193.04$ MeV [78] and $f_{\eta_c} = 420/\sqrt{2}$ MeV, taken from [137]. Thus, the exchange of one heavy vector meson is suppressed by the factor $\kappa = m_\rho^2/m_H^2 \sim 0.15$ for $m_l = m_\rho$ and $m_H = m_{D^*}$. We also saw that the strong attraction comes from the vector exchange diagrams, so the most important contribution will come from the light-vector exchange diagrams. From these tables we can observe that the interaction at the $D^*\bar{D}^*(D_s^*\bar{D}_s^*)$ thresholds becomes very attractive for $D^*\bar{D}^* \to D^*\bar{D}^*$, $D^*\bar{D}^*(D_s^*\bar{D}_s^*) \to D_s^*\bar{D}_s^*$, in isospin $= 0$; spin $= 0, 1, 2$. For isospin $= 1$, we see that the potential from the amplitudes $D^*\bar{D}^* \to D^*\bar{D}^*$ and $D^*\bar{D}^* \to \rho J/\psi$ is rather attractive for spin $= 2$. Since we are dealing with different kind of channels, large symmetry breaking effects are expected and we evaluate the uncertainties in Section 7.4.

Concerning the α parameter, the first thing to do is reproduce the results of Chapter 3. Thus, in Eq. (3.45) we fix $\mu = 1000$ MeV for all the channels, and set $\alpha_L = -1.65$ (following the procedure of [86]) for the amplitudes involving the nonet of vector mesons in order to reproduce the position of the $f_2(1275)$ as was done there. For the (heavy) vector-(heavy) vector channels we put $\alpha_H = -2.07$, in order to get the position of the pole found in $I = 0; J = 0$ around 3940 MeV. Finally, we put $\alpha_L = -1.65$ in the $\omega J/\psi$, $\phi J/\psi$ and $\rho J/\psi$ channels. In Section 7.4 we will also consider different options of setting the α parameter.

7.3 Results

We evaluate the transition matrix T between channels (Eq. (3.22)) and look for the poles in the second Riemann sheet of the complex

plane (see explanation around Eq. (3.49) to know how to go to the second Riemann sheet). If these poles are close to the real axis, they occur in $\sqrt{s}_p = (M \pm i\Gamma/2)$. The meaningful physical quantity is the value of the amplitude for real $\sqrt{s}$, therefore, only the poles that are not very far away from the real axis can be easily identified experimentally as a resonance. The amplitudes T (Eq. (3.22)) close to a pole look like

$$T_{ij} \approx \frac{g_i g_j}{s - s_p} \ , \tag{7.2}$$

The constants g_i ($i = channel$), which provide the coupling of the resonance to one particular channel are calculated by means of the residues of the amplitudes. The pole positions and coupling con-

$$\sqrt{s}_{pole} = 3943 + i7.4, \ I^G[J^{PC}] = 0^+[0^{++}]$$

$D^*\bar{D}^*$	$D_s^*\bar{D}_s^*$	$K^*\bar{K}^*$	$\rho\rho$	$\omega\omega$
$18810 - i682$	$8426 + i1933$	$10 - i11$	$-22 + i47$	$1348 + i234$

$\phi\phi$	$J/\psi J/\psi$	$\omega J/\psi$	$\phi J/\psi$	$\omega\phi$
$-1000 - i150$	$417 + i64$	$-1429 - i216$	$889 + i196$	$-215 - i107$

Table 7.2: Couplings g_i in units of MeV for $I = 0$, $J = 0$.

stants are given in Tables 7.2 -7.6. In the isospin = 0 sector we find four poles, three of them are around ~ 3940 MeV, one for each spin $J = 0, 1, 2$. We observe that these states couple most strongly to $D^*\bar{D}^*$. The widths are 14.8, 0 and 52 MeV respectively, therefore they are relatively narrow and the nonzero widths for the $J = 0$ and 2 states come from the decays into pairs of light-vector mesons or into $\omega(\phi)J/\psi$. For $I = 0$ and $J = 2$ another pole is found above the $D^*\bar{D}^*$ threshold with mass $M = 4169$ MeV and width $\Gamma = 132$ MeV.

$$\sqrt{s}_{pole} = 3945 + i0,\ I^G[J^{PC}] = 0^-[1^{+-}]$$

			Other channels: $\rho\rho$, $\omega\omega$,
$D^*\bar{D}^*$	$D_s^*\bar{D}_s^*$	$K^*\bar{K}^*$	$\phi\phi$, $J/\psi J/\psi$, $\omega J/\psi$, $\phi J/\psi$, $\omega\phi$
$18489 - i0.78$	$8763 + i2$	$11 - i38$	0

Table 7.3: Couplings g_i in units of MeV for $I = 0,\ J = 1$.

$$\sqrt{s}_{pole} = 3922 + i26,\ I^G[J^{PC}] = 0^+[2^{++}]$$

$D^*\bar{D}^*$	$D_s^*\bar{D}_s^*$	$K^*\bar{K}^*$	$\rho\rho$	$\omega\omega$
$21100 - i1802$	$1633 + i6797$	$42 + i14$	$-75 + i37$	$1558 + i1821$

$\phi\phi$	$J/\psi J/\psi$	$\omega J/\psi$	$\phi J/\psi$	$\omega\phi$
$-904 - i1783$	$1783 + i197$	$-2558 - i2289$	$918 + i2921$	$91 - i784$

Table 7.4: Couplings g_i in units of MeV for $I = 0,\ J = 2$.

$$\sqrt{s}_{pole} = 4169 + i66,\ I^G[J^{PC}] = 0^+[2^{++}]$$

$D^*\bar{D}^*$	$D_s^*\bar{D}_s^*$	$K^*\bar{K}^*$	$\rho\rho$	$\omega\omega$
$1225 - i490$	$18927 - i5524$	$-82 + i30$	$70 + i20$	$3 - i2441$

$\phi\phi$	$J/\psi J/\psi$	$\omega J/\psi$	$\phi J/\psi$	$\omega\phi$
$1257 + i2866$	$2681 + i940$	$-866 + i2752$	$-2617 - i5151$	$1012 + i1522$

Table 7.5: Couplings g_i in units of MeV for $I = 0$, $J = 2$ (second pole).

$$\sqrt{s}_{pole} = 3919 + i74,\ I^G[J^{PC}] = 1^-[2^{++}]$$

$D^*\bar{D}^*$	$K^*\bar{K}^*$	$\rho\rho$	$\rho\omega$	$\rho J/\psi$	$\rho\phi$
$20267 - i4975$	$148 - i33$	0	$-1150 - i3470$	$2105 + i5978$	$-1067 - i2514$

Table 7.6: Couplings g_i in units of MeV for $I = 1$, $J = 2$.

From the couplings, we can see that now this state couples stronger to $D_s^* \bar{D}_s^*$.

In the $I = 1$ sector we find only one pole for $J = 2$ below the $D^* \bar{D}^*$ threshold with mass $M = 3919$ MeV and width $\Gamma = 148$ MeV that couples mostly to $D^* \bar{D}^*$. In Table 7.1, the experimental states discovered around this mass are listed. The identification is subtle. We see that there are three experimental states around this mass. Nevertheless, one has to be careful in order not to do wrong identifications. The state that we have found has C-parity negative and all of the experimental states have C-parity positive. The Z(3930) has been seen in the spectrum of $D\bar{D}$ in $\gamma\gamma$ collisions which ensures $J = 0^{++}$ or 2^{++} for this states. The Belle Collaboration favors the 2^{++} hypothesis from the analysis of angular distributions. Thus, we identify our states with $I = 0$ and $J = 2$ at 3940 MeV with this state. In the case of the Y(3940) we find that the Belle's values for the mass and width are larger than the Babar's values (the Belle Collaboration reports $m = (3943 \pm 17)$ MeV and $\Gamma = (87 \pm 34)$ MeV and Babar $m = 3914.3^{+4.1}_{-3.8}$ and $\Gamma = 33$ MeV. Thus, we have some uncertainties in the width measurement for this state. Babar and Belle also report measurements for the products of branching fractions $B(B \to KY(3940))B(Y(3940) \to \omega J/\psi) = (7.1 \pm 3.4) \times 10^{-5}$ reported by Belle and $(4.9 \pm 1.1) \times 10^{-5}$ according to Babar. These measurement together with the assumption that $B(B \to KY) \leq 1 \times 10^{-3}$, the usual value for $B \to K$+charmonium decays, lead to $\Gamma(Y(3940) \to \omega J/\psi)$ larger than 1 MeV. We can also predict this decay width using the formula

$$\Gamma((3943, 0^+[0^{++}]) \to \omega J/\psi) = \frac{p\,|g_{Y\omega J/\psi}|^2}{8\pi\, M_Y^2} \tag{7.3}$$

and taking $g_{Y\omega J/\psi} = (-1429 - i216)$ MeV from Table 7.2. Thus, we find $\Gamma((3943, 0^+(0^{++})) \to \omega J/\psi) = 1.52$ MeV, which is compatible with the large decay width to $\omega J/\psi$ estimated for the Y(3940). We associated the $0^+(0^{++})$ state with the Y(3940). The second pole found in $I = 0; J = 2$ with mass $m = 4169$ MeV and $\Gamma = 132$ MeV is identified with the X(4160) by the proximity of the masses,

widths and quantum numbers. The states with $I = 0; J^{PC} = 1^{+-}$ and $I = 1; J^{PC} = 2^{++}$ are predictions of the model and cannot be associate with any of the states in Table 7.1 (the first one has C-parity negative and the width of the second state is too large). It is worth to mention that in [138], the authors predict also a $D^*\bar{D}^*$ meson - meson molecule with quantum numbers $I = 1; J^{PC} = 2^{++}$ by using a self-consistent quark-model based study of four-quark charmonium-like, but just above threshold with a mass of 4030 MeV, which could have some experimental counterpart, the X(4050), as called in the PDG [78].

The experimental state X(3940) in Table 7.1 does not decay into $\omega J/\psi$ and therefore cannot be associated with any of the $J = 0$ or $J = 2$ states for isospin = 0. Its nature must be different from the vector-vector structure. In Table 7.1 we see that the Z(3940) state decays into $D\bar{D}$. In Section 7.5 we will evaluate this decay by means the box-diagram containing four pseudoscalars.

7.4 Uncertainties

In order to get the pole positions of Tables 7.2 - 7.6. we have adjusted the α parameter to get the position of the $I = 0; J = 0$ state. In addition, we have chosen to put $\sqrt{g_i}$ for each external leg (however in this case we do not know what to put for the three vector vertex), since we deal with different kind of channels. Different options could have been chosen in order to adjust the α parameter or to set the "g" value in Eq. (2.3). In this section we use this freedom in the α and g^2 parameters to evaluate the uncertainties. We proceed in a very similar way as in the previous Chapter. We choose these three options to evaluate the uncertainties:

1) Use $g_L = M_\rho/(2\, f_\pi) \equiv g$ for all the cases. This is the option followed in [133].

2) Use a unique average $g' = (4g_D + 2g_{D_s} + g_{\eta_c} + 9g)/16$.

3) Use of $\sqrt{g_i}$, with $i = \pi, D, D_s, \eta_c$ for each external vector meson. This is the option used in the former sections.

First, we fix the α value, $\alpha = -2.07$, for (heavy) vector - (heavy) vector channels vary "g^2" from 1) to 3). The pole positions obtained can be seen in Table 7.7. We find variations in the pole positions of around 40 MeV with the exception of the predicted state with $I = 1$, where the uncertainties are larger. A realistic way when looking at the uncertainties is to set the α parameter to get the position of one of the states using the three options listed above, since this adjustment is always done in this kind of calculations. We show the results in Tables 7.8 - 7.11. We see that the uncertainites in the pole positions are smaller than before. While the mass for the $I = 0; J = 1$ state practically does not change, there is a band of energy of around 30 MeV for the two $I = 0; J = 2$ states and around 60 MeV for the predicted $I = 1; J = 2$ state. Concerning the couplings, we observe that the changes in the largest coupling are very small, of the order of 3% except for the $I = 0; J = 2$ sector, where we find 10% and 7% for the first and second state respectively. These results lead up to about 20% uncertainties in some observable (which require squared amplitudes). As we said, we could adjust α to get the position of the $I = 0; J = 2$ state instead of the $I = 0; J = 0$ state. The results after doing this exercise is shown in Tables 7.12 and 7.13. Here we use the option of $\sqrt{g_i}$ for each external leg and $\alpha_H = -2.048$. These results should be compared with option 3) in Tables 7.8 - 7.11. We observe differences below 3%.

With the results of this section we have an idea of the uncertainites in the pole positions and residues. We have seen that there is certain stability in the masses and especially the couplings, which are what one needs to calculate observables.

$\alpha_H = -2.07$	g^2	g'^2	$g_{V1}g_{V2}$
$I=0, J=0$	$3980 + i\,6$	$3967 + i\,12$	$3943 + i\,7.4$
$I=0, J=1$	$3981 + i\,0$	$3969 + i\,0$	$3945 + i\,0$
$I=0, J=2$	$3971 + i\,35$	$3930 + i\,38$	$3922 + i\,26$
$I=0, J=2$	$4198 + i\,86$	$4163 + i\,56$	$4169 + i\,66$
$I=1, J=2$	$3992 + i\,133$	$3926 + i\,89$	$3919 + i\,74$

Table 7.7: Pole positions in units of MeV for the different states with $\alpha_H = -2.07$ using g^2, g'^2 and $g_{V1}g_{V2}$.

7.5 The $D\bar{D}$ decay mode

In Table 7.1 we see that the Z(3930) decays to $D\bar{D}$. In this section we consider the $D\bar{D}$ decay mode by means of the diagrams of Fig. 7.3. The evaluation is very similar to the one done in Chapter 3. For the first two diagrams where a $\pi(K)$ is exchanged between the two $D^*(D_s^*)$ mesons we find

$$\begin{aligned} t_\pi^{(D\bar{D},I=0,J=0)} &= 45\,\tilde{V}^{(D\bar{D})} \\ t_\pi^{(D\bar{D},I=0,J=2)} &= 18\,\tilde{V}^{(D\bar{D})}\ , \end{aligned} \tag{7.4}$$

$$\begin{aligned} t_\pi^{(D\bar{D},I=1,J=0)} &= 5\,\tilde{V}^{(D\bar{D})} \\ t_\pi^{(D\bar{D},I=1,J=2)} &= 2\,\tilde{V}^{(D\bar{D})}\ , \end{aligned} \tag{7.5}$$

and

$$\begin{aligned} t_K^{(D\bar{D},I=0,J=0)} &= 40\,\tilde{V}_K^{(D\bar{D})} \\ t_K^{(D\bar{D},I=0,J=2)} &= 16\,\tilde{V}_K^{(D\bar{D})} \end{aligned} \tag{7.6}$$

Constant & α_H	$I = 0, J = 0$	$I = 0, J = 1$	$I = 0, J = 2$	$I = 0, J = 2$	$I = 1, J = 2$
1) g^2 & -2.195	$3943 + i\,6.5$	$3946 + i\,0$	$3936 + i\,37$	$4169 + i113$	$3965 + i\,164$
2) g'^2 & -2.145	$3943 + i\,12$	$3946 + i\,0$	$3907 + i\,45$	$4141 + i\,67$	$3904 + i\,104$
3) $g_{V1}g_{V2}$ & -2.07	$3943 + i7.4$	$3945 + i0$	$3922 + i26$	$4169 + i66$	$3919 + i\,74$

Table 7.8: Pole positions in units of MeV and subtraction constants obtained for the three different cases, g^2, g'^2 and $g_{V1}g_{V2}$, when one fixes the mass of the pole with $I = 0, J = 0$ quantum numbers.

Channel	$I=0, J=0$			$I=0, J=2$			$I=0, J=2$ (second pole)		
Cases:	1)	2)	3)	1)	2)	3)	1)	2)	3)
$D^*\bar{D}^*$	18230	18370	18822	19905	22283	21177	2470	1441	1319
$D_s^*\bar{D}^*{}_s$	9906	10487	8645	10832	9308	6990	21125	21048	19717
$K^*\bar{K}^*$	3	8	15	13	41	44	104	65	87
$\rho\rho$	52	46	52	49	76	84	95	48	73
$\omega\omega$	1377	1790	1368	3143	3218	2397	3199	2313	2441
$\phi\phi$	731	1173	1011	1892	2580	1999	3905	3133	3130
$J/\psi J/\psi$	401	475	422	2485	2250	1794	2629	2896	2841
$\omega J/\psi$	1608	1970	1445	4934	4719	3433	3864	2847	2885
$\phi J/\psi$	512	983	910	2327	3943	3062	7116	5929	5778
$\omega\phi$	51	180	240	237	1065	789	2201	1985	1828

Table 7.9: Modules of the couplings g_i in units of MeV for the pole in the $I=0, J=0$ and $I=0, J=2$ sectors in the different cases 1) using g^2 & $\alpha_H=-2.195$, 2) g'^2 & $\alpha_H=-2.145$ and 3) $g_{V1}g_{V2}$ & $\alpha_H=-2.07$.

Channel	$I = 0, J = 1$		
Cases:	1)	2)	3)
$D^*\bar{D}^*$	17914	17990	18489
$D_s^*\bar{D}^*{}_s$	9716	10210	8763
$K^*\bar{K}^*$	42	43	40

Table 7.10: Modules of the couplings g_i in units of MeV for the pole in the $I = 0, J = 1$ sector in the different cases 1) using g^2 & $\alpha_H = -2.195$, 2) g'^2 & $\alpha_H = -2.145$ and 3) $g_{V1}g_{V2}$ & $\alpha_H = -2.07$. The couplings of the resonance to the channels: $\rho\rho$, $\omega\omega$, $\phi\phi$, $J/\psi J/\psi$, $\omega J/\psi$, $\phi J/\psi$, $\omega\phi$, are equal to zero.

Channel	$I = 1, J = 2$		
Cases:	1)	2)	3)
$D^*\bar{D}^*$	20881	21625	20869
$K^*\bar{K}^*$	200	118	152
$\rho\rho$	0	0	0
$\rho\omega$	5093	4197	3656
$\rho J/\psi$	8874	7258	6338
$\rho\phi$	3784	3126	2731

Table 7.11: Modules of the couplings g_i in units of MeV for the pole in the $I = 1, J = 2$ sector for the different cases 1) using g^2 & $\alpha_H = -2.195$, 2) g'^2 & $\alpha_H = -2.145$ and 3) $g_{V1}g_{V2}$ & $\alpha_H = -2.07$.

	$I=0, J=0$	$I=0, J=1$	$I=0, J=2$	$I=0, J=2$
$\sqrt{s_p}$ (MeV)	$3950 + i\,7.5$	$3952 + i\,0$	$3929 + i\,25$	$4174 + i\,62$
channel		$\lvert g_i \rvert$ (MeV)		
$D^*\bar{D}^*$	18302	17961	20739	1302
$D_s^*\bar{D}_s^*$	8437	8556	6654	19359
$K^*\bar{K}^*$	16	55	44	86
$\rho\rho$	51	0	81	71
$\omega\omega$	1368	0	2328	2380
$\phi\phi$	1024	0	1963	3061
$J/\psi J/\psi$	425	0	1765	2818
$\omega J/\psi$	1446	0	3331	2816
$\phi J/\psi$	936	0	3028	5660
$\omega\phi$	252	0	794	1795

Table 7.12: Position of the poles and modules of the coupling in the $I = 0, J = 0, 1, 2$ sectors if the α_H is adjusted to get the mass of the Z(3930) in the $I = 0, J = 2$ sector. The value of α_H obtained is -2.048.

$\sqrt{s_p}$ (MeV)	$3926 + i\,70$
channel	$\lvert g_i\rvert$ (MeV)
$D^*\bar{D}^*$	20588
$K^*\bar{K}^*$	148
$\rho\rho$	0
$\rho\omega$	3579
$\rho J/\psi$	6210
$\rho\phi$	2674

Table 7.13: Position of the pole and modules of the coupling in the $I = 1, J = 2$ sector if the α_H is adjusted to get the mass of the Z(3930) in the $I = 0, J = 2$ sector. The value of α_H obtained is -2.048.

with

$$\begin{aligned}\tilde{V}^{(D\bar{D})} &= \frac{2\,g_H^4}{15\pi^2}\int_0^{q_{max}} dq\,\vec{q}^{\,6}\left(\omega_l^3+\omega_D^3+4\,\omega_l\omega_D^2+4\omega_l^2\omega_D-k_3^0\omega_D\right)\\ &\times\frac{1}{k_3^0-\omega_l-\omega_D+i\epsilon}\,\frac{1}{P^0-2\omega_D+i\epsilon}\,\frac{1}{P^0+2\omega_D}\\ &\times\frac{1}{k_1^0-\omega_l-\omega_D+i\epsilon}\left(\frac{1}{\omega_l}\right)^3\frac{1}{\omega_D}\left(\frac{1}{k_3^0+\omega_l+\omega_D}\right)^2 \qquad (7.7)\end{aligned}$$

where $\omega_l = \sqrt{\vec{q}^{\,2}+m_\pi^2}$, $\omega_D = \sqrt{\vec{q}^{\,2}+m_D^2}$, $P^0 = k_1^0 + k_2^0$, and t_π corresponds to the first diagram with $g_H = g_D$ and $l = \pi$ in Eq. (7.7) and t_K is the result of the second diagram in Fig. 7.3 and $g_H = g_{D_s}$ with $l = K$. For the third diagram of Fig. 7.3 we obtain

$$\begin{aligned}t_{K\pi}^{(D\bar{D},I=0,J=0)} &= \frac{15}{\sqrt{2}}\,\tilde{V}_{K\pi}^{(D\bar{D})}\\ t_{K\pi}^{(D\bar{D},I=0,J=2)} &= \frac{6}{\sqrt{2}}\,\tilde{V}_{K\pi}^{(D\bar{D})} \qquad (7.8)\end{aligned}$$

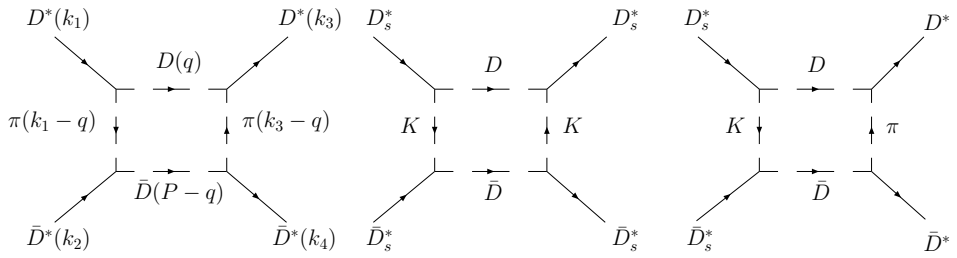

Figure 7.3: $D\bar{D}$-box diagrams for the $D^*\bar{D}^*$ and $D_s^*\bar{D}_s^*$ channels.

with

$$\begin{aligned}
\tilde{V}_{K\pi}^{(D\bar{D})} &= g_{D_s}^2 g_D^2 \frac{8}{15\pi^2}\int_0^{q_{max}} dq\,\vec{q}^{\,6}\,\frac{1}{\omega\,\omega_K\,\omega_D}\,\frac{1}{\omega+\omega_K} \\
&\times\frac{1}{k_1^0+\omega_K+\omega_D}\,\frac{1}{k_1-\omega_K-\omega_D+i\epsilon}\,\frac{1}{P^0-2\omega_D+i\epsilon} \\
&\times\frac{1}{P^0+2\omega_D}\,\frac{1}{k_3^0-\omega-\omega_D+i\epsilon}\,\frac{1}{k_3^0+\omega+\omega_D} \\
&\times(2\omega_D(\omega_D+\omega_K)^2+\omega^2(2\omega_D+\omega_K) \\
&+\omega(2\omega_D+\omega_K)^2-2k_3^{0\,2}\omega_D)\ . \qquad (7.9)
\end{aligned}$$

We regularize the above integrals with a cutoff of natural size, $q_{\max} = 1.2$ GeV, but we notice that the imaginary parts does not depend on it. As in Chapter 6 we use an exponential form factor for an offshell $\pi(K)$ in each vertex, which is

$$F(q) = e^{-\vec{q}^2/\Lambda^2} \qquad (7.10)$$

with $\Lambda = 1.2$ GeV. In Figs. 7.4 and 7.5 the real and imaginary parts of the potential are shown. We can see that the real parts can be neglected in comparison to the potential coming from the contact + exchange terms. We also see that the contribution of $D\bar{D}(\pi\pi)$ box is the largest one, being the $D\bar{D}(KK)$ contribution very small and the $D\bar{D}(K\pi)$ box negligible, which means that these two latter

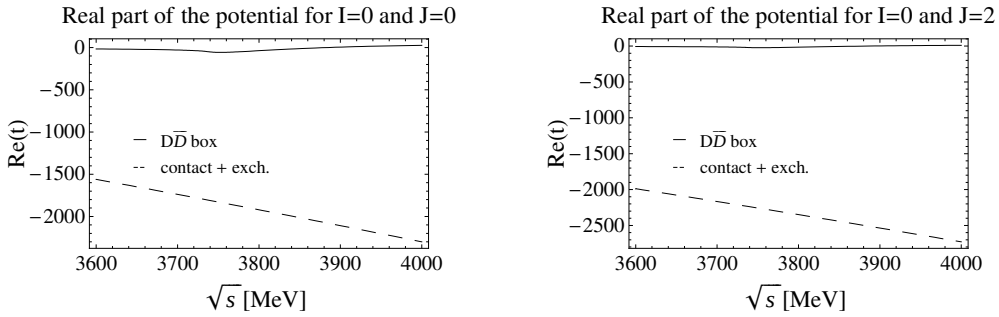

Figure 7.4: Real parts of the potential for the $D^*\bar{D}^*$ channel.

contributions practically do not affect to the second pole found in the $I = 0; J = 2$ sector, remember that also the width found there was quite large ~ 100 MeV in comparison with the others.

The results when these potentials are included are shown in Figs. 7.6, 7.7 and 7.8, and the masses and widths in the real axis obtained from these plots are given in Table 7.14 in comparison with the experiment. We also show the effect of the $D\bar{D}$ diagram in the $I = 0; J = 0$ state before and after including the $D\bar{D}$ box diagram, Fig. 7.9. We can see their small effect, which means that the sum of all the other light vector - light vector and light vector - J/ψ channels is much more important.

The results shown here are practically the same than those reported in Section 7.3. We summarize them in Table 7.14 with the assignment to the experimental states.

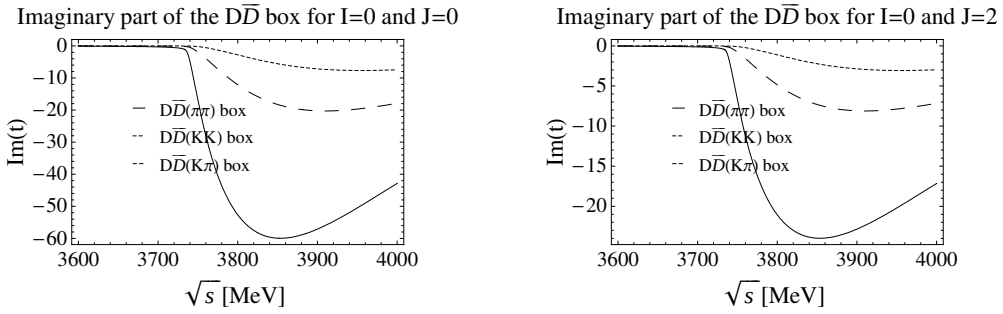

Figure 7.5: Imaginary parts of the $D\bar{D}$ box diagrams of Fig. 7.3.

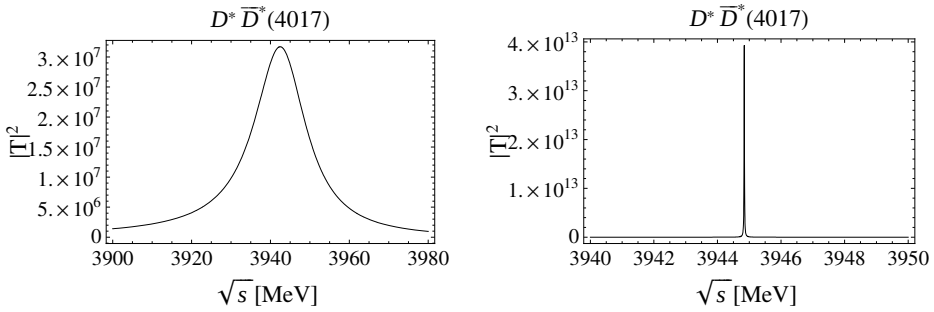

Figure 7.6: $|T|^2$ for $I = 0$ and $J = 0$ (left), $J = 1$ (right), in the main channel $D^*\bar{D}^*$.

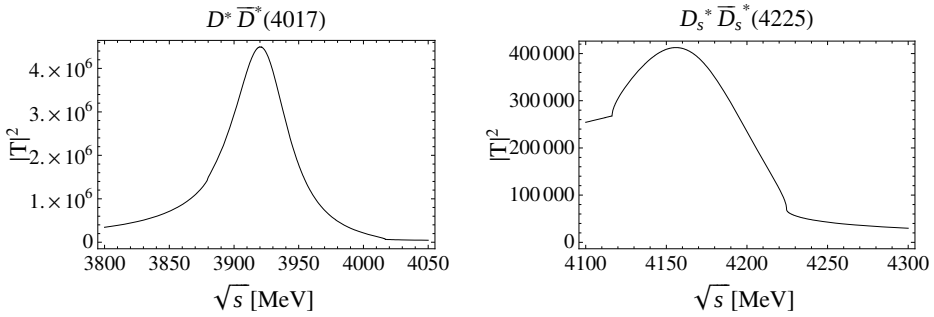

Figure 7.7: $|T|^2$ for $I = 0$ and $J = 2$ in the main channels $D^*\bar{D}^*$ (first pole, left) and $D_s^*\bar{D}_s^*$ (second pole, right).

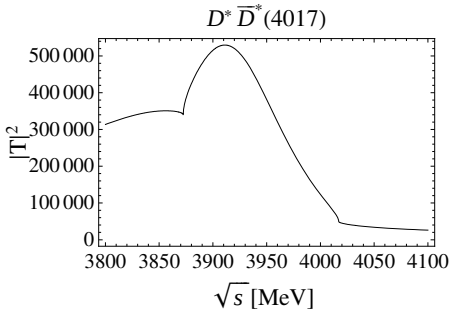

Figure 7.8: $|T|^2$ for $I = 1$ and $J = 2$ in the main channel $D^*\bar{D}^*$.

$I^G[J^{PC}]$	Theory		Experiment			
	Mass [MeV]	Width [MeV]	Name	Mass [MeV]	Width [MeV]	J^{PC}
$0^+[0^{++}]$	3943	17	$Y(3940)$	3943 ± 17	87 ± 34	J^{P+}
				$3914.3^{+4.1}_{-3.8}$	33^{+12}_{-8}	
$0^-[1^{+-}]$	3945	0	"$Y_p(3945)$"			
$0^+[2^{++}]$	3922	55	$Z(3930)$	3929 ± 5	29 ± 10	2^{++}
$0^+[2^{++}]$	4157	102	$X(4160)$	4156 ± 29	139^{+113}_{-65}	J^{P+}
$1^-[2^{++}]$	3912	120	"$Y_p(3912)$"			

Table 7.14: Comparison of the mass, width and quantum numbers with the experiment.

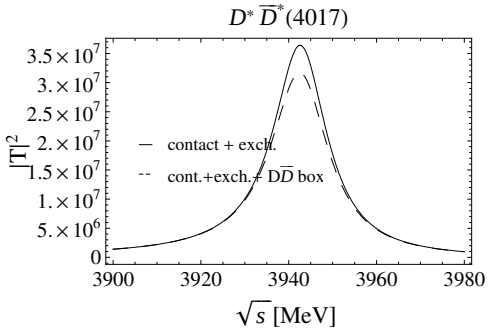

Figure 7.9: $|T|^2$ for $I = 0$ and $J = 0$ before and after the inclusion of the $D\bar{D}$ box diagrams.

Chapter 8

Radiative decays of the Y(3940), Z(3930) and X(4160)

The majority of the 'new' charmonium-like X, Y and Z mesons mainly discovered at the B-factories BELLE and BaBar cannot be easily accommodated in the $q\bar{q}$ model and are therefore interesting objects for meson structure besides the constituent quark model. The coupled channel approach combined with the Hidden Gauge Lagrangians [85, 116, 136] turned out to provide a useful tool to determine the mass and width of resonances. In the latter work of [136] some of the X, Y, Z resonances were generated dynamically from the vector - vector interaction and appear as poles in the corresponding scattering amplitude. A further interesting topic is the radiative decays of these states which are also a crucial test to hadron structure.

8.1 Introduction

In the hidden gauge formalism the electromagnetic interaction is included by using vector meson dominance (VMD) that is the photon couples to the resonance via the ρ, ω, ϕ or J/ψ vector mesons in the re-

spective coupled channels [81, 87, 141]. Radiative two-photon decays of heavy meson molecules were also studied in [96] and the radiative decays of the $f_0(1370)$ and $f_2(1270)$ into two photons have been also reported in Chapter 4, leading to numerical results in agreement with the experiment. In this Chapter we concentrate on the hidden-charm resonances around 4 GeV analyzed in Chapter 7 and study the two-photon and photon-vector meson decay properties. In Section 8.2 we evaluate the decay widths into $\gamma\gamma$ and $V\gamma$ of the Y(3940), Z(3930) and X(4160) mesons and the decay rates into $D^*\bar{D}\gamma$ or $D_s^*\bar{D}_s\gamma$ are evaluated in Section 8.3. The peculiar behaviour can shed light on the nature of the states. See [139] and [140] for a detailed review of these topics.

8.2 Evaluation of the one- and two- photon decay widths of the Y(3940), Z(3930) and X(4160)

The transition amplitude T between the initial and final coupled channels via resonance R from the Bethe Salpeter equation in Eq. (3.22) can be approximated close to a pole by

$$T_{ij}^{(J)} = g_i \mathcal{P}^{(J)}(i) \frac{1}{s - M_R^2 + i M_R \Gamma_R} g_j \mathcal{P}^{(J)}(j)\,, \tag{8.1}$$

where $\mathcal{P}^{(J)}$ are the spin projectors of the amplitudes for $J = 0, 1, 2$ given in Eq. (3.13). The indices l, m and s run over the spacial coordinates, i.e. $l, m, s = 1, 2, 3$. The product $\mathcal{P}^{(J)}(i)\mathcal{P}^{(J)}(j)$ in Eq. (8.1) stands for the product of two projectors of spin for channels i (particles (1,2)) and j (particles (3,4)), summing the indices l, m of the two projectors except for $\mathcal{P}^{(0)}\mathcal{P}^{(0)}$ where $\mathcal{P}^{(0)}$ is already a scalar. The coupling strength, g_i (g_j), to each particular channel is calculated by means of the residues of the amplitudes T_{ij} at the pole position, and gives an idea of the importance of the contribution of each channel

to the resonance. In the case of the Y(3940) and Z(3930), the $D^*\bar{D}^*$ coupling is dominant, which implies, e.g., that the Y(3940) is dominantly a $D^*\bar{D}^*$ bound state, in agreement with the $D^*\bar{D}^*$ molecular interpretations in [133, 134] while the X(4160) is mainly $D_s^*\bar{D}_s^*$. We study the radiative decays of dynamically generated resonances by coupling the photon via intermediate vector mesons as depicted in Fig. 8.1. The amplitude of the $V\gamma$ transition is given by the La-

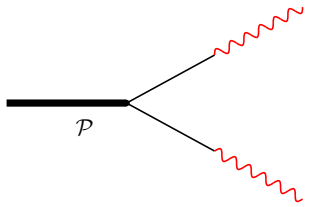

Figure 8.1: Photon coupling via VMD

grangian of Eq. (4.9) which leads to

$$t_{V\gamma} = \tilde{t}_{V\gamma}\epsilon_\mu(V)\epsilon^\mu(\gamma) \tag{8.2}$$

with

$$\tilde{t}_{V\gamma} = \mathcal{C}_{V\gamma}\frac{e}{g}M_V^2 \tag{8.3}$$

and $C_{V\gamma}$ given in Table 8.1. We fix g by $g = \frac{m_\rho}{2f_\pi}$ with $f_\pi = 93$ MeV. In

ρ^0	ω	ϕ	J/ψ
$\frac{1}{\sqrt{2}}$	$\frac{1}{3\sqrt{2}}$	$-\frac{1}{3}$	$\frac{2}{3}$

Table 8.1: Coefficient $\mathcal{C}_{V\gamma}$ in Eq. (8.3).

case of the charmonium, i.e. J/ψ, we consider $SU(4)$ breaking effects by using $g \equiv g_{\eta_c} = M_{J/\psi}/(2f_{\eta_c})$, where $f_{\eta_c} = 420/\sqrt{2}$ MeV, taken

from [137]. The vertex of Eqs. (8.2) and (8.3) effectively replace the vector polarization ($\epsilon_\nu(V)$) by the photon polarization ($\epsilon_\nu(\gamma)$). The amplitudes for the one- and two-photon decays are therefore given by

$$T^{(R)}(\gamma\gamma) \propto \sum_{V_1,V_2} g^{(R)}_{V_1V_2}\mathcal{P}^{(J)}_{\gamma\gamma}\Big(\frac{1}{-M^2_{V_1}}\Big)\tilde{t}_{V_1\gamma}\Big(\frac{1}{-M^2_{V_2}}\Big)\tilde{t}_{V_2\gamma}\times I \quad (8.4)$$

$$T^{(R)}(V_1\gamma) \propto \sum_{V_2} g^{(R)}_{V_1V_2}\mathcal{P}^{(J)}_{V_1\gamma}\Big(\frac{1}{-M^2_{V_2}}\Big)\tilde{t}_{V_2\gamma}\times I\,, \quad (8.5)$$

where $g_{V_1V_2}$ is the coupling of the resonance R to the V_1V_2 channel (see Tables 7.2 - 7.6). $\mathcal{P}^{(J)}_{\gamma\gamma}$, $\mathcal{P}^{(J)}_{V_1\gamma}$ stand for the projection operators of Eq. (3.13) with the polarizations of the two photons or one photon and one vector, and I represents the respective isospin Clebsch Gordan coefficients of the V_1V_2 component for a certain isospin state. Following our phase convention, $(-D^{*0}, D^{*+})$, $(D^{*-}, \bar{D}^{*0})$ and $(-\rho^+, \rho^0, \rho^-)$, the isospin states are given by

$$\begin{aligned}
\big|D^*\bar{D}^*, I=0, I_3=0\big\rangle &= \frac{1}{\sqrt{2}}\big(\big|D^{*+}D^{*-}\big\rangle + \big|D^{*0}\bar{D}^{*0}\big\rangle\big)\\
\big|D^*\bar{D}^*, I=1, I_3=0\big\rangle &= \frac{1}{\sqrt{2}}\big(\big|D^{*+}D^{*-}\big\rangle - \big|D^{*0}\bar{D}^{*0}\big\rangle\big)\\
\big|\rho\rho, I=0, I_3=0\big\rangle &= -\frac{1}{\sqrt{3}}\big(\big|\rho^+\rho^-\big\rangle + \big|\rho^-\rho^+\big\rangle + \big|\rho^0\rho^0\big\rangle\big)\\
\big|\rho\rho, I=1, I_3=0\big\rangle &= -\frac{1}{\sqrt{2}}\big(\big|\rho^+\rho^-\big\rangle - \big|\rho^-\rho^+\big\rangle\big)\,, \quad (8.6)
\end{aligned}$$

After summing over the intermediate vector polarizations in Eqs. (8.4) and (8.5), the amplitudes for the $R\to\gamma\gamma$ and $R\to V\gamma$ decays are given by

$$T^{(R)}_{\gamma\gamma} = (\frac{e}{g})^2 \sum_{V_1,V_2=\rho^0,\omega,\phi,J/\psi} g^{(R)}_{V_1V_2}\mathcal{P}^{(J)}_{\gamma\gamma}\,\mathcal{C}_{V_1\gamma}\mathcal{C}_{V_2\gamma}\times I\times F_{\gamma\gamma} \quad (8.7)$$

$$T^{(R)}_{V_1\gamma} = \frac{e}{g}\sum_{V_2=\rho^0,\omega,\phi,J/\psi} g^{(R)}_{V_1V_2}\mathcal{P}^{(J)}_{V_1\gamma}\,\mathcal{C}_{V_2\gamma}\times I\times F_{V\gamma}\,, \quad (8.8)$$

The use of the unitarity renormalization introduce an extra factor $\frac{1}{\sqrt{2}}$ in case of identical particles, we need to correct this factor when calculating observables. The unitarity normalization and the symmetry factors are combined in $F_{\gamma\gamma}$ and $F_{V\gamma}$ with

$$F_{\gamma\gamma} = \begin{cases} \sqrt{2} & \text{pair of identical particles, e.g} : \rho^0\rho^0 \\ 2 & \text{pair of differentparticles, e.g} : \rho^0\omega \end{cases} \quad (8.9)$$

$$F_{V\gamma} = \begin{cases} \sqrt{2} & \text{pair of identical particles, e.g} : \rho^0\rho^0 \\ 1 & \text{pair of different particles, e.g} : \rho^0\omega \end{cases} \quad (8.10)$$

The radiative decay width can be easily calculated from the transition amplitudes T by

$$\Gamma_{\gamma\gamma} = \frac{1}{2J+1}\frac{1}{16\pi M_R}\frac{1}{2} \times \sum_{spins} \left|T^{(R)}_{\gamma\gamma}\right|^2, \quad (8.11)$$

$$\Gamma_{V\gamma} = \frac{1}{2J+1}\frac{1}{8\pi M_R}\frac{|\vec{p}_\gamma|}{M_R} \times \sum_{spins} \left|T^{(R)}_{V\gamma}\right|^2, \quad (8.12)$$

where the summation over all spin states contributes the factors given in Table 8.2.

J	$\sum_{spins} \mathcal{P}^{(J)}_{\gamma\gamma}\mathcal{P}^{*(J)}_{\gamma\gamma}$	$\sum_{spins} \mathcal{P}^{(J)}_{V\gamma}\mathcal{P}^{*(J)}_{V\gamma}$
0	$\frac{2}{3}$	$\frac{2}{3}$
1	1	2
2	$\frac{7}{3}$	$\frac{10}{3}$

Table 8.2: Contribution of the summation over all spin states

In the former derivation we have assumed the momenta of the external particles small compared to the vector masses, which is correct for the vector-vector initial state. This is based on the approximations done in [136], which neglect the three momenta of the particles

with respect to the vector mass, $|\vec{p}|/M_{D^*} \simeq 0$. This is indeed the case for massive states but not if we deal with two photons in the final state since $|\vec{p}_\gamma| \simeq M_{D^*}$. Hence, improvements on the model are necessary. For this purpose we redo the calculations taking into account the finite momenta. This affects only the final electromagnetic vertex in the resonance decay. Thus we can evaluate $\sum |t_{VV\to\gamma\gamma}|^2$ and $\sum |t_{VV\to V'\gamma}|^2$ with finite momenta and multiply the widths obtained at $\vec{k} = 0$ by the ratio of these terms for a general $\vec{k}$ and $\vec{k} = 0$:

$$\Gamma(k) = \Gamma_0 \frac{\bar{\sum}_{\text{in}} \sum_{\text{fin}} |t|^2(k)}{\bar{\sum}_{\text{in}} \sum_{\text{fin}} |t|^2(k=0)} \tag{8.13}$$

with $t = t_{VV\to\gamma\gamma}$ or $t_{VV\to V'\gamma}$, $\Gamma_0 = \Gamma(k=0)$ (this corresponds to the width in the approximation of $|\vec{p}|/m_{D^*} \sim 0$) and $k = |\vec{k}|$, where t is the tree level amplitude containing the four-vector contact and meson exchange terms of Figs. (7.1) and (7.2) respectively. This is done only for the dominant terms involving $VV = D^*\bar{D}^*$, $D_s^*\bar{D}_s^*$. The detailed calculation is shown in the Appendix C.

8.2.1 Results

In order to compute the decay width of the Y(3940), Z(3930), X(4160) and the so far not observed $'Y_p(3912)'$ we take the couplings of the X, Y, Z states from Tables 7.2, 7.4, 7.5 and 7.6. For the other state with quantum numbers $I^G(J^{PC}) = 0^-(1^{+-})$ (see Table 7.3), all couplings to vector mesons with hidden flavor are zero due to C-parity violation. Therefore radiative decays via VMD are forbidden in this case.

The results for the radiative decay width are summarized in Table 8.3. The decay widths of the Y(3940) are in general smaller compared to the other resonances. A general feature observed is that in the results the $\rho\gamma$ and $\gamma\gamma$ decay modes are suppressed in comparison to the $\omega\gamma$ and $\phi\gamma$ decays except for the predicted $Y_p(3912)$ resonance, which shows a rather strong coupling to the $\rho\gamma$ decay channel. Experimental observations concerning the radiative decays are

pole [MeV]	$I^G\,J^{PC}$	meson	$\Gamma_{\rho\gamma}$	$\Gamma_{\omega\gamma}$	$\Gamma_{\phi\gamma}$	$\Gamma_{J/\psi\gamma}$	$\Gamma_{\gamma\gamma}$
$(3943, +i7.4)$	$0^+\,(0^{++})$	$Y(3940)$	0.036	2.37	32.71	0.94	0.031
$(3922, +i26)$	$0^+\,(2^{++})$	$Z(3930)$	0.016	6.06	38.26	11.16	0.059
$(4169, +i66)$	$0^+\,(2^{++})$	$X(4160)$	0.012	4.26	107.54	100.42	0.254
$(3919, +i74)$	$1^-\,(2^{++})$	$'Y_p(3912)'$	80.58	45.82	24.84	108.38	0.54

Table 8.3: Pole positions and radiative decay widths. The decay widths are given in units of KeV.

rare. However, the BELLE Collaboration searched for charmonium-like resonances in the $\gamma\gamma \to \omega J/\psi$ process [142] which resulted in an enhancement of the cross section around $M = 3915 \pm 3 \pm 2$ MeV. The peak was associated to a resonance denoted by X(3915). But it is thought that it could be the Y(3940) resonance, or even the Z(3930) which we have associated to our $J^P = 2^+$ resonance at 3922 MeV. In [142], the X(3915) has unknown spin and parity, but 0^+ or 2^+ are preferred. In the following we compare the ratios,

$$\Gamma_{\gamma\gamma}(X(3915))\mathcal{B}(X(3915) \to \omega J/\psi) = \begin{cases} (61 \pm 17 \pm 8)\text{eV} & J^P = 0^+ \\ (18 \pm 5 \pm 2)\text{eV} & J^P = 2^+ \end{cases}$$

quoted in [142], with the results of the present approach. Let us evaluate Eq. (8.14) for the two theoretical states 0^+ at 3943 MeV and 2^+ at 3922 MeV in Table 8.3. By using the formula for the decay width to $\omega J/\psi$:

$$\Gamma_{\omega J/\psi} = \frac{1}{8\pi}\frac{k g^2_{\omega J/\psi}}{M_R^2} \ , \tag{8.14}$$

with k the momentum of the final meson, and taking the couplings $g_{\omega J/\psi}$ from Tables 7.2 and 7.4, we obtain

$$\begin{aligned} \Gamma_{\omega J/\psi(0^+,3943)} &= 1.52\text{MeV} \\ \Gamma_{\omega J/\psi(2^+,3922)} &= 8.66\text{MeV} \ , \end{aligned} \tag{8.15}$$

together with the two photon decay widths of Table 8.3 we find

$$\begin{aligned} \Gamma_{\gamma\gamma}\mathcal{B}((0^+,3943) \to \omega J/\psi) &= 1.46\,\text{eV} \\ \Gamma_{\gamma\gamma}\mathcal{B}((2^+,3922) \to \omega J/\psi) &= 17.6\,\text{eV} \ , \end{aligned} \tag{8.16}$$

where in the evaluation of the branching ratios we have used the experimental central values of the widths of the Y(3940) and Z(3930), $\Gamma = 33^{+12}_{-8}$ MeV and 29 ± 10 MeV [124, 143] respectively. Comparing Eq. (8.16) with Eq. (8.14), the results of Eq. (8.16) are compatible

with the assumption that the X(3915) is the resonance (2^+, 3922), considered as the Z(3930) in Table 8.3.

On the other hand, if we assume that the X(3915) corresponds to our (0^+, 3943) resonance, the discrepancies are very large, more than a factor of forty. Our study, thus, favors the association of our (2^+, 3922) resonance to the X(3915) of [142].

8.2.2 Comparison with other works

In [134], the authors assume that the $Y(3940)$ and the $Y(4140)$ are hadronic molecules with quantum numbers $J^{PC} = 0^{++}$ or 2^{++} whose constituents are the charm vectors $D^*\bar{D}^*$ for the $Y(3940)$ and $D_s^{*+}\bar{D}_s^{*-}$ for the $Y(4140)$ and they calculate the decay rates of the observed modes $Y(3940) \to J/\psi\omega$ and $Y(4140) \to J/\psi$ for the case $J^{PC} = 0^{++}$. The coupling constants are determined by means of the compositeness condition [134] and the results for these decay modes support the molecular interpretation of the $Y(3930)$ and the $Y(4140)$. Note that with the results of [134] the opposite assignment would be favoured, as seen in Table 8.4 where we make a summary of our results and a comparison with those of [134].

The relatively small two-photon decay width $\Gamma(Y(3940) \to \gamma\gamma) =$ 0.031 KeV underestimates the corresponding result in the hadronic molecule interpretation (as a $D^*\bar{D}^*$ molecule) of $\Gamma(Y(3940) \to \gamma\gamma) =$ 0.33 KeV for $J^{PC} = 0^{++}$ in [134] by about one order of magnitude. However, the coupled channel analysis that we make, although it considers many channels, also finds the $D^*\bar{D}^*$ component as dominant. Due to the inclusion of the three-momenta of the photons, the decay widths undergo changes and the correction factors can be seen in Table C.1 in the Appendix C. The largest correction appears for the Y(3940) state, where the abnormally small former $\Gamma_{\gamma\gamma}$ width becomes a factor of 2.4 larger. We should note that appart from the differences in the input in the two approaches mentioned above, the prescription of the coupling of photons to vector mesons is different. We follow the rules of the local hidden gauge approach, where the γ couples to

	Ref. [134]			Present work		
state	$D^*\bar{D}^*$		$D_s^*\bar{D}_s^*$	$D^*\bar{D}^*$		$D_s^*\bar{D}_s^*$
J^{PC}	0^{++}	2^{++}	2^{++}	0^{++}	2^{++}	2^{++}
$\Gamma_{\gamma\gamma}$ [KeV]	0.33	0.27	0.50	0.031	0.059	0.25
$\Gamma_{\omega J/\psi}$ [MeV]	5.47	7.48		-1.52	8.66	12.02
$\Gamma_{\gamma\gamma}\mathcal{B}(X \to \omega J/\psi)$ [eV]	54.7	69.6		1.46	17.6	
$\Gamma_{\gamma\gamma}^{\exp}\mathcal{B}(X \to \omega J/\psi)$ [eV]	61	18		61	18	

Table 8.4: Comparison with the work of [134] and the experiment. To evaluate the branching ratios we have used the experimental central values of the widths of the Y(3940) and Z(3930), $\Gamma = 33^{+12}_{-8}$ MeV and 29 ± 10 MeV [124, 143] respectively.

the light vector mesons and these couple to the other vector mesons with the three vector couplings. In [134] a minimal substitution in the free Lagrangian of the vector mesons is done. As investigated in detail in [81], the two prescriptions can lead to sizeable differences in the radiative decay widths, and we must turn to this feature as the main responsible factor for the differences found with respect to [134].

It is unfortunate that not a unique prescription can be given for the coupling of the photons to vector mesons. In [144] the minimal coupling prescription was used to couple photons to vector mesons in the radiative decay of axial vector mesons to a pseudoscalar meson and a photon. Yet, since the axial vector mesons could be obtained as dynamically generated resonances using the hidden local gauge approach, it was found most appropiate to use the prescription provided by the same local hidden gauge approach to couple photons to vectors. This was done in [81], but the agreement with experiment became worse than using the minimal coupling. This was later on interpreted in [145] as an indication that the $a_1(1260)$ resonance might have not only vector-pseudoscalar components but also a sizeable fraction of a genuine $q\bar{q}$ component. Those are issues that are presently at stake and that might deserve further consideration. Yet, the former example leaves room for some interpretation of the disagreement of our results with those of [134] and eventually with data.

The inclusion of the photon three-momenta also leads to changes of the γV decay widths and the correction factors can be seen in Table C.1. Once again the largest change is for the $V\gamma$ decay of the Y(3940) where the rate is increased by a factor 2.4.

For the two-photon width of the X(4160) we obtain $\Gamma_{\gamma\gamma} = 0.254$ keV. In the present coupled channel approach the X(4160) is found to be dominantly a $D_s^*\bar{D}_s^*$ state. This is the same underlying structure as the $D_s^*\bar{D}_s^*$ bound state studied in [134]. In reference [134] the $D_s^*\bar{D}_s^*$ molecular state was associated with the narrow Y(4140) discovered by the CDF [146] because it was possible to explain the sizable observed $J/\psi\phi$ decay width of this state. Our association to

the broader X(4160) is suggested by the large total theoretical width which was not evaluated in [134]. It is fair to compare the results in both approaches with the caveat of the different input used, as discussed above. In this case the value obtained for the radiative width into two photons evaluated in [134] is $\Gamma_{\gamma\gamma} = 0.5$ KeV.

8.3 Decay of the Y(3940), Z(3930) and X(4160) into $D^*_{(s)}\bar{D}^*_{(s)}\gamma$

As one can see from Tables 7.2, 7.4 and 7.5, the states obtained correspond to basically bound $D^*\bar{D}^*$ or $D^*_s\bar{D}^*_s$ states, hence the decay into these pairs of mesons is forbidden, whereas the light vector - light vector channels provide the width of the states. However, if one looks at the decay channel of the $\bar{D}^*$ into $\bar{D}\gamma$, the process $X \to D^*\bar{D}\gamma$ is allowed, since the mass of the resonance X, for all the cases listed in Table 7.14, exceeds the sum of masses of the final state. In Fig. 8.2 the corresponding Feynman diagram to the $X \to D^{*+}D^-\gamma$ process is shown. The D^{*-} propagates virtually between the production point of $X \to D^{*+}D^{*-}$ and the decay point of $D^{*-} \to D^-\gamma$. This propagator is the relevant characteristic of the $X \to D^{*+}D^-\gamma$ decay. Thus, this diagram is peculiar to the assumed nature of the resonance X as a molecule of $D^*\bar{D}^*$ and should be largely dominant over other possible processes [97]. All one needs to evaluate these Feynmann diagrams is the coupling of the resonance to $D^{*+}D^{*-}$, together with the corresponding spin projection operator, and the vertex accounting for the decay of D^{*-} into $D^-\gamma$.

Take for example the case of the Y(3940), with $J = 0$, the first vertex in the diagram of Fig. 8.2 is $\frac{1}{\sqrt{3}}\epsilon_i^{(1)}\epsilon_i^{(2)}\, g_{D^*\bar{D}^*}$ I, where I is the isospin factor needed to change from the isospin basis, where the couplings are evaluated in [136], to the charge basis. In the case of $D^{*+}D^{*-}$, we have $\mathrm{I} = \frac{1}{\sqrt{2}}$. In what follows, we will call $\tilde{g}$ the coupling of the resonance to the VV state in isospin basis.

On the other hand the anomalous vertex for the $\bar{D}^*$ decay into

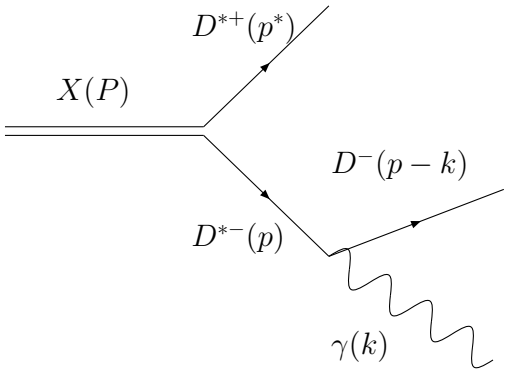

Figure 8.2: Decay of the X resonance to $D^{*+}D^-\gamma$.

$\bar{D}\gamma$ is given by

$$-it_{\bar{D}^*\to\bar{D}\gamma} = -ig_{PV\gamma}\,\epsilon_{\mu\nu\alpha\beta}\,p^\mu\,\epsilon^\nu(\bar{D}^*)\,k^\alpha\,\epsilon^\beta(\gamma), \tag{8.17}$$

where p, k are the momenta of the D^{*-} and γ respectively. This amplitude gives rise to a width

$$\Gamma_{\bar{D}^*\to\bar{D}\gamma} = \frac{1}{48\pi}g^2_{PV\gamma}\frac{k}{M^2_{\bar{D}^*}}(M^2_{\bar{D}^*} - m^2_{\bar{D}})^2. \tag{8.18}$$

Unfortunately, only the value for the radiative decay of the $D^{*-} \to D^-\gamma$ and of its positive state partner are known. In this case we will be able to provide an absolute value for the radiative decay width of the XYZ resonances. In the other cases we will give the ratio of the radiative decay of the resonance to that of the $\bar{D}^*$. The value of $g_{PV\gamma}$ for the $D^{*-} \to D^-\gamma$ decay is given by

$$g_{PV\gamma} = 1.53 \times 10^{-4} MeV^{-1}, \tag{8.19}$$

which can be easily deduced using Eq. (8.18) from the experimental value of the width $\Gamma = 1.54$ KeV.

Thus, the couplings of [136] for $D^*\bar{D}^*$ must be multiplied by $1/\sqrt{2}$ to get the appropriate coupling for the charged or neutral states (a

sign is irrelevant for the width), and do not require an extra factor for the case of $D_s^*\bar{D}_s^*$.

With the previous information we can already write the amplitude for the decay of the Y(3940) into $D^{*+}D^-\gamma$, which is given by

$$\begin{aligned} -it &= -i\frac{1}{\sqrt{2}}\,\tilde{g}\,\frac{1}{\sqrt{3}}\epsilon_i^{(1)}\epsilon_i^{(2)}\,\frac{i}{p^2-M_{D^*}^2+iM_{D^*}\Gamma_{D^*}} \\ &\quad\times(-i)\,g_{PV\gamma}\,\epsilon_{\mu\nu\alpha\beta}\,p^\mu\epsilon^{\nu(2)}\,k^\alpha\,\epsilon^\beta(\gamma), \end{aligned} \tag{8.20}$$

where the indices (1), (2) indicate the D^{*+} and the D^{*-} respectively. The sum over the intermediate D^{*-} polarizations can be readily done as

$$\sum_\lambda \epsilon_i^{(2)}\epsilon^{\nu(2)} = -g_i^\nu = -\delta_{i\nu}, \tag{8.21}$$

where we have neglected the three momenta of the intermediate D^{*-} which is in average very small compared with the D^{*-} mass, particularly at large invariant masses of the $D^-\gamma$ system which concentrates most of the strength, as we shall see. The sum of $|t|^2$ over the final polarizations of the vector and the photon is readily done and, neglecting again terms of order $\vec{p}^{\,2}/M_{D^*}^2$, we get the result

$$\begin{aligned} \sum|t|^2 &= \frac{1}{3}\frac{1}{2}\tilde{g}^2 g_{PV\gamma}^2\left|\frac{1}{p^2-M_{D^*}^2+iM_{D^*}\Gamma_{D^*}}\right|^2 2(p\cdot k)^2 \\ &= \frac{1}{6}\frac{1}{2}\tilde{g}^2 g_{PV\gamma}^2\left|\frac{p^2-m_D^2}{p^2-M_{D^*}^2+iM_{D^*}\Gamma_{D^*}}\right|^2. \end{aligned} \tag{8.22}$$

The differential mass distribution with respect to the invariant mass of the $D^-\gamma$ system, M_{inv}, with $M_{inv}^2 = p^2$, is finally given by

$$\frac{d\Gamma_R}{dM_{inv}} = \frac{1}{4M_R^2}\frac{1}{(2\pi)^3}\,p^*\tilde{p}_D\sum|t|^2, \tag{8.23}$$

where p^* is the momentum of the D^{*+} in the rest frame of the resonance X and $\tilde{p}_D$ is the momentum of the D^- in the rest frame of the

final $D^-\gamma$ system given by

$$\begin{aligned} p^* &= \frac{\lambda^{1/2}(M_R^2, M_{D^*}^2, M_{inv}^2)}{2M_R}, \\ \tilde{p}_D &= \frac{M_{inv}^2 - m_D^2}{2M_{inv}}. \end{aligned} \tag{8.24}$$

In the case of the tensor and spin one states we must do extra work since the projector operators are different. In this case we must keep the indices i, j in t and multiply with t^* with the same indices i, j and then perform the sum over the indices i, j. This sums over all possible final polarizations but also the initial X polarizations, so in order to take the sum and average over final and initial polarizations, respectively, one must divide the results of the $\sum_{i,j} tt^*$ by $(2J+1)$, where J is the spin of the resonance X. The explicit evaluation for the case of the tensor states, $J = 2$, of $D^*\bar{D}^*$ proceeds as follows: The t matrix is now written as

$$\begin{aligned} t &= \frac{1}{\sqrt{2}}\,\tilde{g}\,g_{PV\gamma}\left\{\frac{1}{2}\left(\epsilon_i^{(1)}\epsilon_j^{(2)} + \epsilon_j^{(1)}\epsilon_i^{(2)}\right) - \frac{1}{3}\epsilon_l^{(1)}\epsilon_l^{(2)}\delta_{ij}\right\} \\ &\quad \times \frac{1}{p^2 - M_{D^*}^2 + iM_{D^*}\Gamma_{D^*}}\,\epsilon_{\mu\nu\alpha\beta}\,p^\mu\epsilon^{\nu(2)}k^\alpha\epsilon^\beta(\gamma). \end{aligned} \tag{8.25}$$

As mentioned above, we must multiply $t_{i,j}$ by $t_{i,j}^*$, recalling that the indices i, j are spatial indices and divide by $(2J+1)$ (5 in this case) in order to obtain the modulus squared of the transition matrix, summed and averaged over the final and initial polarizations. Neglecting again terms that go like $\vec{p}^{\,2}/m_D^{*2}$ we obtain the same expression as in Eq. (8.22). It is also easy to see that this is again the case for the $J = 1$ states. The normalization of the spin projection operators in Eq. (3.13) makes this magnitude to be the same in all cases.

8.3.1 Convolution of the $d\Gamma/dM_{inv}$ due to the width of the XYZ states

Some of the dynamically generated XYZ states have a non negiglible width and, as a consequence, a mass distribution. That means there is a probability of these states to have a mass over the nominal mass and if one consider this fact, the $PV\gamma$ decay width should increase. In order to consider this, we convolute the $d\Gamma/dM_{inv}$ function over the mass distribution of the resonance R. We take $\Gamma/2$ to both sides of the peak of the resonance distribution which account for a large fraction of the strength and produces distinct shapes in the $\gamma\bar{D}$ mass distribution. We find:

$$\frac{d\Gamma^{\rm conv(\Gamma/2)}}{dM_{inv}} = \frac{1}{N}\int_{(M_R-\Gamma/2)^2}^{(M_R+\Gamma/2)^2} d\tilde{M}^2\,(-\frac{1}{\pi})\,Im\frac{1}{\tilde{M}^2-M_R^2+i\Gamma M_R} \times d\Gamma/dM_{inv}(\tilde{M}) \tag{8.26}$$

with

$$N=\int_{(M_R-\Gamma/2)^2}^{(M_R+\Gamma/2)^2} d\tilde{M}^2\,(-\frac{1}{\pi})\,Im\frac{1}{\tilde{M}^2-M_R^2+i\Gamma M_R}\ ,$$

The expression for $d\Gamma/dM_{inv}(\tilde{M})$ is given by Eq. (8.23) changing M_R to $\tilde{M}$. As we will see in the next section, the use of Eq. (8.26) leads to an increase of $\Gamma(R\to PV\gamma)$ with respect to the result with the nominal mass M_R. We shall also show results with a convolution from $M_R-\Gamma$ to $M_R+\Gamma$.

8.3.2 Results

We show here the results for different cases:

The Y(3940): Decay mode $D^{*+}D^-\gamma$

The results are the same reversing the signs of the charges.

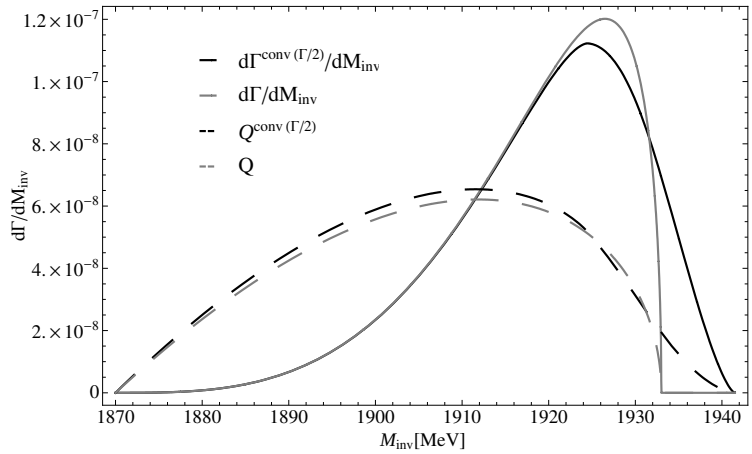

Figure 8.3: The $Y(3940) \to D^{*+}D^{-}\gamma$: Comparison of $d\Gamma/dM_{inv}$ and $d\Gamma^{\rm conv(\Gamma/2)}/dM_{inv}$, Q and $Q^{\rm conv(\Gamma/2)}$ as a function of the $D^{-}\gamma$ invariant mass.

In Fig. 8.3 we show the distribution of Eq. (8.23), together with Eq. (8.22), between the limits of M_{inv}: m_D and $M_R - m_{D^*}$. Also, in order to see the effects produced when one considers the width of the state, we plot in the same figure $d\Gamma^{\rm conv}/dM_{inv}$, taken from Eq. (8.26). We can see a very distinct picture, with most of the strength accumulated at the maximum values of M_{inv}. The propagator of the intermediate D^{*-} and the factor $(p.k)^2$ are responsible for that shape. In fact we show superposed in the same figure the result obtained (normalized to the same area) substituting the propagator by a constant and removing the factor $(p.k)^2$ (or equivalently the factor $(p^2 - m_D^2)^2$). We call Q the resulting distribution (or $Q^{\rm conv}$ when one convolute this function taking into account the width of the R state). We can see that the pictures of $d\Gamma/dM_{inv}$ and Q (or equivalently $d\Gamma^{\rm conv}/dM_{inv}$ and $Q^{\rm conv}$) are radically different and the reason is mostly due to the presence of the D^{*-} propagator which carries the memory that the resonance Y(3940) is assumed to be a $D^*\bar{D}^*$ molecule. The effects of considering the convolution are also

visible in this picture. Now, $d\Gamma^{\rm conv}/dM_{inv}$ spreads beyond $M_R - m_{D^*}$, and there is some probability for the state to decay into $PV\gamma$ up to $M_{inv} = M_R + \Gamma/2 - m_{D^*}$, where Γ is the width of the state. Also in this case, the difference between $d\Gamma^{\rm conv}/dM_{inv}$ and $Q^{\rm conv}$ is clearly visible.

For the case of decay into $D^{*0}\bar{D}^0\gamma$ the matrix element is formally the same except that now we do not know the experimental radiative decay width of the $\bar{D}^{*0}$. In this case we divide the mass distribution of the $D^{*0}\bar{D}^0\gamma$ decay by the width of the $\bar{D}^{*0} \to \bar{D}^0\gamma$ and plot the magnitude

$$\begin{aligned}\frac{1}{\Gamma_{D^*\to D\gamma}}\frac{d\Gamma_R}{dM_{inv}} &= \frac{1}{2}\frac{1}{6}\,\tilde{g}^2 g^2_{PV\gamma}\left|\frac{p^2 - m_D^2}{p^2 - M^2_{D^*} + iM_{D^*}\Gamma_{D^*}}\right|^2 \\ &\times\frac{48\pi\, M^2_{D^*}}{k(M^2_{D^*} - m_D^2)^2}\,\frac{1}{4M_R^2}\,\frac{1}{(2\pi)^3}\,p^*\tilde{p}_D, \quad (8.27)\end{aligned}$$

with

$$k = \frac{M^2_{D^*} - m_D^2}{2M_{D^*}}.$$

In Fig. 8.4 we show the results of the $d\Gamma_R/dM_{inv}\Gamma_{D^*D\gamma}$ distribution and also we compare with $d\Gamma^{\rm conv}_R/dM_{inv}\Gamma_{D^*D\gamma}$. We can see that the enlarged range of the mass distribution between the limits $M_{inv} = M_R - m_{D^*}$ and $M_R + \Gamma/2 - m_{D^*}$ is responsible for an increase in $\Gamma(Y(3940) \to D^{*0}\bar{D}^0\gamma)$.

The $Y_p(3945)$

This state has zero width, and here we show the difference between $d\Gamma_R/dM_{inv}$ and Q in the case of $Y_p(3945) \to D^{*+}D^-\gamma$ in Fig. 8.5 to see the effect of the inclusion of the $\bar{D}^*$ propagator in Eq. (8.22). As one can see, the shapes can be clearly distinguished. Also, in Fig. 8.6 we show the curves for $d\Gamma_R/dM_{inv}\Gamma_{D^*D\gamma}$ for the case of the neutral charm mesons in the final state.

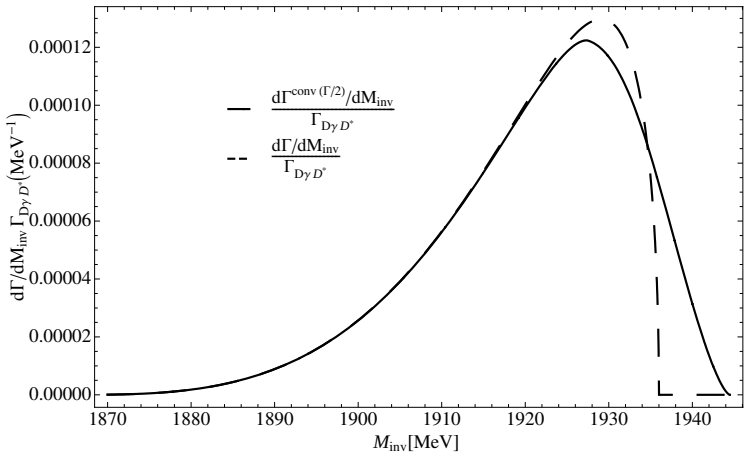

Figure 8.4: The $Y(3940) \to D^{*0}\bar{D}^0\gamma$: Comparison of $d\Gamma/dM_{inv}\Gamma_{D^*D\gamma}$ and $d\Gamma^{\mathrm{conv}(\Gamma/2)}/dM_{inv}\Gamma_{D^*D\gamma}$.

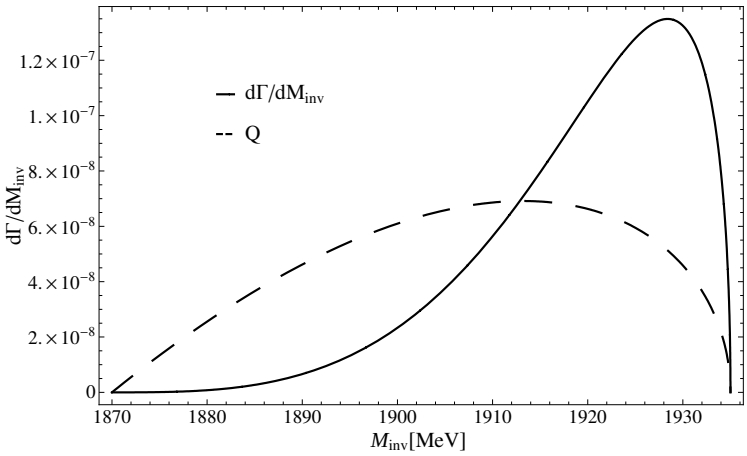

Figure 8.5: The $Y_p(3945) \to D^{*+}D^-\gamma$: $d\Gamma/dM_{inv}$ and Q as a function of M_{inv}.

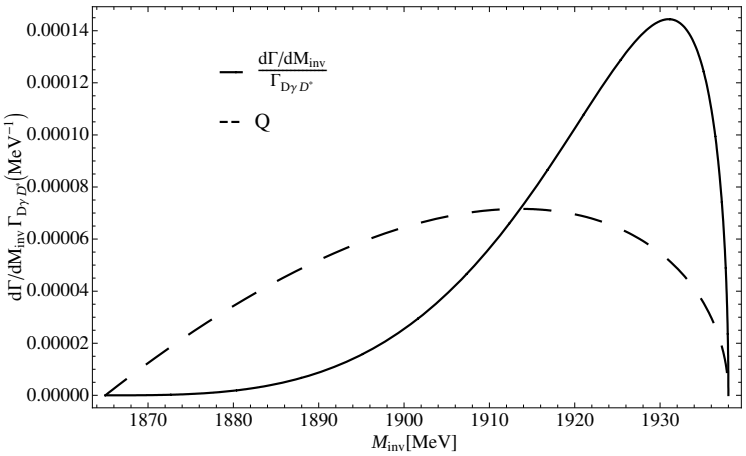

Figure 8.6: The $Y_p(3945) \to D^{*0}\bar{D}^0\gamma$: $d\Gamma/dM_{inv}\Gamma_{D^*D\gamma}$ and Q as a function of M_{inv}.

The Z(3930)

This state has a larger width compared with the Y(3940) and $Y_p(3945)$ states of 55 MeV, and for this reason the picture here is very different than in those cases when one takes into account this width. Thus, one can see a big difference between $d\Gamma_R/dM_{inv}$ and $d\Gamma_R^{\rm conv}/dM_{inv}$, Q and $Q^{\rm conv}$, as shown in Fig. 8.7. The relatively large width of the resonance taken (55 MeV) is responsible for the different shapes compared to Fig. 8.7 a). Similar results are obtained for $d\Gamma/dM_{inv}\Gamma_{D^*D\gamma}$ for decay into $D^{*0}\bar{D}^0\gamma$.

The $Y_p(3912)$

This case is very similar to that of the Z(3930). The shapes of $d\Gamma_R/dM_{inv}$ and Q are very different (also for $d\Gamma_R^{\rm conv}/dM_{inv}$ and $Q^{\rm conv}$) as one can see in Fig. 8.8. Now the width is considerably larger compared to that in the previous cases, since $\Gamma = 120$ MeV. Similar results are obtained for the case of $Y_p(3912) \to D^{*0}\bar{D}^0\gamma$.

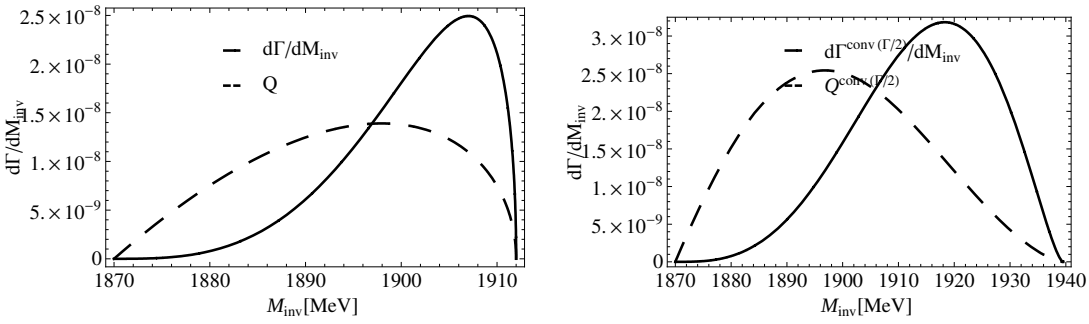

Figure 8.7: The $Z(3930) \to D^{*+}D^{-}\gamma$: a) $d\Gamma/dM_{inv}$ and Q as a function of M_{inv}. b) $d\Gamma^{\rm conv}/dM_{inv}$ and $Q^{\rm conv}$.

The X(4160)

In this case the isospin factor is I = 1 rather than $1/\sqrt{2}$. The formula is the same as before removing a factor 1/2 in Eq. (8.22). Once again we do not have the experimental decay rate for the radiative decay of D_s^{*-} and we plot the results for Eq. (8.27) in Fig. 8.9. In this case the decay into $D^{*+}D^{-}\gamma$ is also possible. However, the coupling to $D^*\bar{D}^*$ of this resonance (also assumed to be a $D_s^{*+}\bar{D}_s^{*-}$ molecule in [97] and [134]) is found small in [136], of the order of 17 times smaller, hence the rate for this channel should be drastically smaller. In order to test the $D^{*+}D^{*-}$ component of this molecule, the allowed strong decay into $D^*\bar{D}^*$ is preferable. This latter measurement is a more efficient tool to get the strength of this coupling and compare with the theoretical predictions.

In Tables 8.5 and 8.6 we show integrated values for $\Gamma(R \to PV\gamma)$ and also rates of $\Gamma(R \to PV\gamma)$ with respect to $\Gamma(D^*_{(s)} \to D_{(s)}\gamma)$.

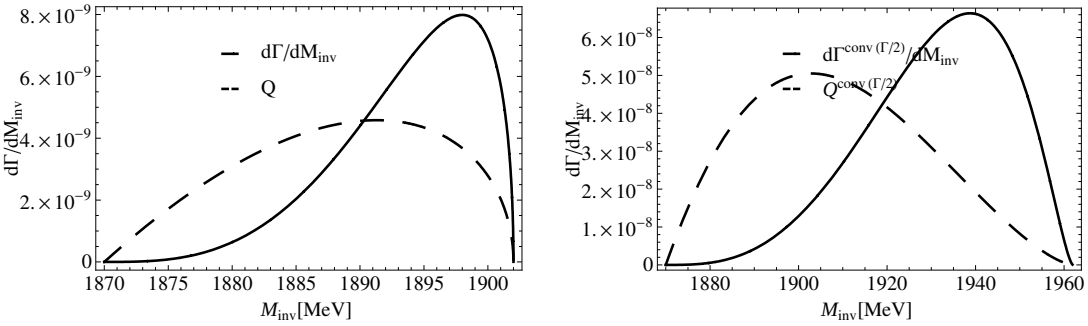

Figure 8.8: The $Y_p(3912) \to D^{*+}D^-\gamma$: a) $d\Gamma/dM_{inv}$ and Q as a function of M_{inv}. b) $d\Gamma^{\rm conv}/dM_{inv}$ and $Q^{\rm conv}$.

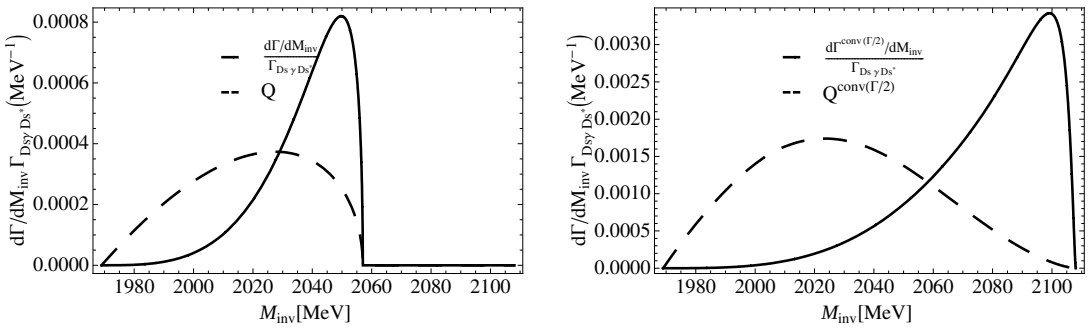

Figure 8.9: The $X(4160) \to D_s^{*+}D_s^-\gamma$: a) $d\Gamma_R/dM_{inv}\Gamma_{D_s^*D_s\gamma}$ and Q as a function of M_{inv}. b) $d\Gamma_R^{\rm conv(\Gamma/2)}/dM_{inv}\Gamma_{D_s^*D_s\gamma}$ and $Q^{\rm conv}$.

State	Decay	Γ [keV]	$\Gamma/\Gamma_{D^{*-}_{(s)}\to D^{-}_{(s)}\gamma}$	$\Gamma^{\mathrm{conv}(\Gamma/2)}$ [keV]	$\Gamma^{\mathrm{conv}(\Gamma/2)}/\Gamma_{D^{*-}_{(s)}\to D^{-}_{(s)}\gamma}$
Y(3940)	$D^{*+}D^{-}\gamma$	2.7×10^{-3}	1.8×10^{-3}	2.9×10^{-3}	1.9×10^{-3}
$Y_p(3945)$	$D^{*+}D^{-}\gamma$	3.1×10^{-3}	2.0×10^{-3}	–	–
Z(3930)	$D^{*+}D^{-}\gamma$	4.1×10^{-4}	2.6×10^{-4}	1.0×10^{-3}	6.7×10^{-4}
$Y_p(3912)$	$D^{*+}D^{-}\gamma$	1.0×10^{-4}	6.7×10^{-5}	2.7×10^{-3}	1.8×10^{-3}
X(4160)	$D_s^{*+}D_s^{-}\gamma$	< 39.9	2.3×10^{-2}	$< 2.4\times10^{2}$	0.14

Table 8.5: Decay of the XYZ resonances into $D^{*+}D^{-}\gamma$ and $D_s^{*+}D_s^{-}\gamma$.

State	Decay	Γ [keV]	$\Gamma/\Gamma_{\bar{D}^{*0}\to\bar{D}^0\gamma}$	$\Gamma^{\mathrm{conv}(\Gamma/2)}$ [keV]	$\Gamma^{\mathrm{conv}(\Gamma/2)}/\Gamma_{\bar{D}^{*0}\to\bar{D}^0\gamma}$
Y(3940)	$D^{*0}\bar{D}^0\gamma$	< 2.6	3.2×10^{-3}	< 2.7	3.4×10^{-3}
$Y_p(3945)$	$D^{*0}\bar{D}^0\gamma$	< 2.9	3.6×10^{-3}	$-$	$-$
Z(3930)	$D^{*0}\bar{D}^0\gamma$	< 0.48	6.0×10^{-4}	< 1.0	1.3×10^{-3}
$Y_p(3912)$	$D^{*0}\bar{D}^0\gamma$	< 0.15	1.9×10^{-4}	< 2.4	3.0×10^{-3}

Table 8.6: Decay of the XYZ resonances into $D^{*0}\bar{D}^0\gamma$.

State	Decay	$\Gamma^{\mathrm{conv}(\Gamma/2)}$ [keV]	$\Gamma^{\mathrm{conv}(\Gamma/2)}/\Gamma_{D^{*-}_{(s)}\to D^{-}_{(s)}\gamma}$
Y(3940)	$D^{*+}D^{-}\gamma$	3.3×10^{-3}	2.1×10^{-3}
Z(3930)	$D^{*+}D^{-}\gamma$	3.3×10^{-3}	2.2×10^{-3}

Table 8.7: Decay width of the XYZ resonances into $D^{*+}D^{-}\gamma$ and $D_s^{*+}D_s^{-}\gamma$ corresponding to a limits in the integral of Eq. (8.26) of $M_R-\Gamma$ and $M_R+\Gamma$.

State	Decay	$\Gamma^{\mathrm{conv}(\Gamma/2)}$ [keV]	$\Gamma^{\mathrm{conv}(\Gamma/2)}/\Gamma_{\bar{D}^{*0}\to\bar{D}^{0}\gamma}$
Y(3940)	$D^{*0}\bar{D}^{0}\gamma$	< 3.0	3.8×10^{-3}
Z(3930)	$D^{*0}\bar{D}^{0}\gamma$	< 3.0	3.7×10^{-3}

Table 8.8: Decay width of the XYZ resonances into $D^{*0}\bar{D}^{0}\gamma$ corresponding to a limits in the integral of Eq. (8.26) of $M_R-\Gamma$ and $M_R+\Gamma$.

In the case of the decays of the resonance into $D^{*0}\bar{D}^0\gamma$, $D_s^{*+}D_s^-\gamma$, $D^{*0}\bar{D}^0\pi^0$ and $D_s^{*+}D_s^-\pi^0$, we compute $g_{PV\gamma}$ in Eq. (8.18) taking $\Gamma(D^{*0}) < 2.1$ MeV and $\Gamma(D_s^{*+}) < 1.9$ MeV. We show in Table 8.5, the integrated values for $\Gamma(R \to D^{*+}D^-\gamma)$ which are very small, of the order of $10^{-1} - 1$ eV if one does not consider the convolution of the $d\Gamma/dM_{inv}$ distribution. However, when one considers the width of the XYZ resonances given in Table 7.14, these values become bigger (about one order of magnitude in some cases).

In the case of the X(4160) we can only put a boundary for the $\Gamma(X \to D_s^{*+}D_s^-\gamma)$, which is 39.9 KeV, but we give rates of $\Gamma(X \to D_s^{*+}D_s^-\gamma)$ with respect to $\Gamma(D_s^{*-} \to D_s^-\gamma)$ in Table 8.5. For this observable we get a value of 2.3×10^{-2} and 0.14 before and after convolution respectively. When the final state contains neutral charm mesons, we give both amplitudes and rates which can be seen in Table 8.6. In Table 8.6, we see that $\Gamma/\Gamma_{\bar{D}^{*0}\to\bar{D}^0\gamma}$ is of the order of $10^{-4}-10^{-3}$ for all the states before convoluting $d\Gamma_R/dM_{inv}$ and becomes larger when one convolutes this function.

We have also evaluated the widths making a convolution for the mass distribution of the resonances from $M_R - \Gamma$ to $M_R + \Gamma$. The results are shown in Tables 8.7 and 8.8. We show the results only for the first two states of Table 7.14 (the second one has zero width and the convolution has no effects). The reason for that is that the last two states are very wide, with a width larger than 100 MeV. When performing the convolution within a mass range of $M_R - \Gamma$ to $M_R + \Gamma$ then one opens the phase space for decay into real $D^*\bar{D}^*$ or $D_s^*\bar{D}_s^*$. In this case the mass of $D\gamma$ collects in a very narrow peak around the $D^*(D_s^*)$ mass and the shape of the distributions that we have discussed here is lost. One is no longer studying the radiative decay but rather the strong decay of the resonance (followed by the radiative decay of the D^*).

Some of the radiative widths look very small, but others are more within the range of partial decay widths known for some resonances. The results obtained here should be very useful to assess the feasibility of possible experiments in future.

Chapter 9

The $D^*_{s2}(2573)$ and flavour exotic mesons

After the succes of the application of the hidden gauge theory together with the unitary technics, being able to explain many properties of states of unknown nature in the PDG, we complete the study of the vector - vector interaction through its application in all the other sectors. This includes the charm $= 0$; strangeness $= 1$ (hidden charm), charm $= 1$; strangeness $= -1, 1, 2$ and charm $= 2$; strangeness $= 0, 1, 2$ sectors, some of them which are flavour exotic sectors.

9.1 Introduction

The $c\bar{s}$ spectrum presents some difficulties to be explained by the quark models. The heavy quark symmetry is introduced to study the heavy - light quark system. The lowest states are the D_s and D^*_s. With a unity of angular momentum of difference between the heavy and light quarks, the heavy quark symmetry that treats the full spin of the light degrees of freedom independently from the spin of the

heavy quark, predicts two doublets, one for $j_l = 3/2$ and $J^P = 1^+, 2^+$. While the predicted ones of the j_l doublet are relatively narrow, the ones with $j_l = 1/2$ would be very broad. The first state observed after the D_s and D_s^* was the $D_{s1}^*(2536)$, it was regarded as a member of the $j_l = 3/2$ doublet within this picture. Then, in 1994, the CLEO Collaboration observed the $D_{s2}^*(2573)$ and the experimentalist identified it as the $j_l = 3/2$ doublet partner of the $D_{s1}^*(2536)$. There was no evidence of the $j_l = 1/2$ doublet. The theoretical calculations predicted them to have masses of $2.48 - 2.49$ GeV and $2.53 - 2.57$ GeV [99, 147, 148] for the 0^+ and 1^+ states respectively and width between $300 - 700$ MeV. Then, the CLEO Collaboration observed the $D_{s0}^*(2317)$ and the $D_{s1}(2460)$ and Babar confirmed it. The observation of these states are obviously difficult to explain in terms of quark model potentials, when the masses of the observed states are around 100 MeV below their predictions, and, in addition, the experimental states are very narrow, the width of the $D_{s0}(2317)$ is < 3.5 MeV and for the $D_{s1}(2460)$ it is < 3.8 MeV. This has given place to other models and alternative explanations. The $D_{s0}(2317)$ and $D_{s1}(2460)$ are close to the DK and D^*K threshold and many theoretician support that the strong s-wave coupling to the $DK(D^*K)$ decay channel shift their respective masses [149, 150, 151, 152, 153, 154]. In particular, in [108], two models are constructed, one is a chiral Lagrangian for the pseudoscalar-pseudoscalar interaction, while the other is a phenomenological model that starts from a SU(4) symmetric Lagrangian which is broken into pieces that separate the heavy-meson currents from the light ones, with the diagrams where a heavy vector meson is exchanged suppressed by a breaking symmetry parameter. The chiral symmetry can be restored by setting the SU(4) symmetry breaking parameters to zero and using a unique f_π parameter [110]. Both models, the chiral Lagrangian and the phenomenological one, lead to the same result which is the $D_{s0}(2317)$ is found to be essentially a $DK(D_s\eta)$ bound state. In other models the $D_{s0}(2317)$ is obtained from an effective Lagrangian approach as a pure DK bound state in [111, 112, 113]. The study of [108] is ex-

tended to the pseudoscalar-vector interaction, and in a very similar procedure the $D_{s1}(2460)$ and the $D_{s1}(2536)$ are explained in terms of $KD^*(\eta D_s^*)$ and $DK^*(D_s(\omega(\phi))$ molecules respectively. Similar results were achieve for the $D_{s1}(2460)$ using different approaches in [114, 115, 117], where the interaction is provided by a chiral Lagrangian based on heavy quark symmetry and the authors neglect the exchange of heavy vector mesons.

9.2 Results

The amplitudes corresponding to the four contact term and vector exchange term are calculated. See the detailed evaluation in [155]. They are shown in the appendix D. We find that the potential is attractive in the sectors: $C = 1, S = -1, I = 0$; $C = 1, S = 1, I = 0, 1$; $C = 2, S = 0, I = 0$; and $C = 2, S = 1, I = 1/2$, and repulsive for $C = 0, S = 1, I = 1/2$ (hidden charm); $C = 1, S = -1, I = 1$; $C = 1, S = 2, I = 1/2$, $C = 2, S = 0, I = 1$ and $C = 2, S = 2, I = 0$. When we evaluate the T-matrix by means of the formula of Eq. (3.22) we use the following parameters: $g = M_\rho/2\, f_\pi$, we fix $\mu = 1500$ MeV for all the sectors and set the subtraction constant $\alpha = -1.6$ (value very close the one used in [109], -1.55, and [116], -1.74) in the sectors $C = 1; S = -1, 1, 2$. Note that μ and α are not independent which justifies the determination of μ and then adjusting α to the data. In the other sectors, $C = 0; S = 1$ (hidden charm) and $C = 2; S = 0, 1, 2$, we put $\alpha = -1.4$. The reason is that we use a different set of the parameters μ and α_H in comparison to the earlier study of the dynamically generated $D_{(s)}^* \bar{D}^*$ resonances in Chapter 7 with $\mu = 1000$ MeV and α_H =-2.07. In the present approach we set $\mu = 1500$ MeV as in [108, 109, 116] and have to adapt α_H accordingly in order to be able to reproduce the XYZ states in Chapter 7. First, we calculate the pole positions and coupling constants Eq. (3.50), then we replace the expression for G of Eq. (3.45) by the convoluted $\tilde{G}$ of Eq. (3.24) and additionally include the box diagrams in Fig.

9.1. We only use Eq. (3.24) for the cases where a ρ or $K^*(\bar{K}^*)$ meson are involved in a particular channel i. For the ρ meson, $\Gamma_1 = 146.2$ MeV, and $m_1 = m_2 = m_\pi$ while for the K^* meson we have $\Gamma_1 = 50.55$ MeV and $m_1 = m_K$, $m_2 = m_\pi$. We include these diagrams in the sectors where the interaction is strong enough to obtain bound states or resonances. Looking at the Tables in the Appendix D, these sectors (and the channels involved) are:

- $C = 1; S = -1; I = 0; J = 0, 1$ and 2:

$$D^*\bar{K}^*$$

- $C = 1; S = 1; I = 0; J = 0, 1$ and 2:

$$D^*K^*,\ D_s^*\phi,\ D_s^*\omega$$

- $C = 1; S = 1; I = 1; J = 0, 1$ and 2:

$$D^*K^*,\ D_s^*\rho$$

- $C = 2; S = 0; I = 0; J = 1$:

$$D^*D^*$$

- $C = 2; S = 1; I = 1/2; J = 1$:

$$D_s^*D^*$$

However, the box diagrams only have a contribution for the quantum numbers $J^P = 0^+$ and 2^+. As explained in the former Chapters, the reason is the following: the vector - vector system has positive parity in s wave, which forces the pseudoscalar - pseudoscalar intermediate state to be in $L = 0, 2$. Since the two pseudoscalar mesons do not have a spin, the only possibilities are $J^P = 0^+$ and 2^+. Hence we do not consider it for the last two sectors where $J = 1$. For the other

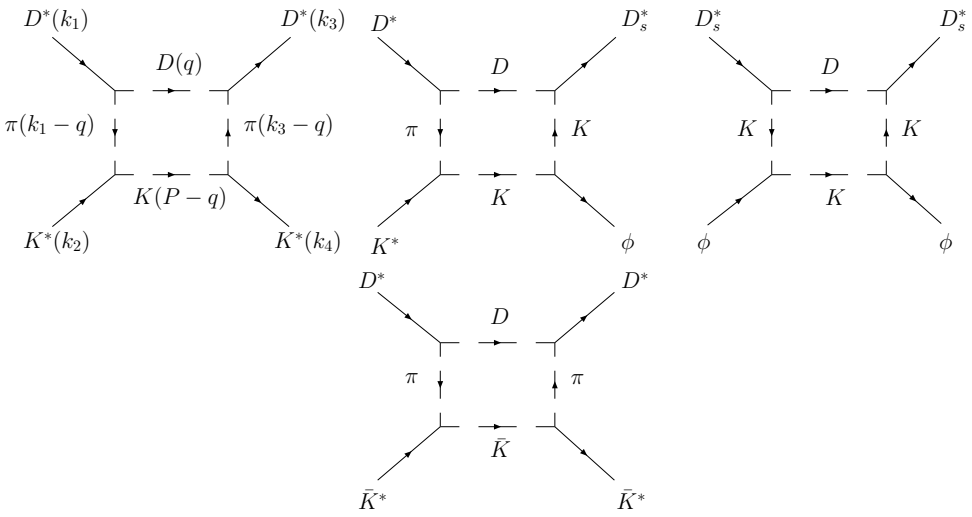

Figure 9.1: Box diagrams included in the calculus.

quantum numbers we consider the box diagrams in Fig. 9.1. We do not include any box diagram for the channel $D_s^*\rho$ since ρ goes to $\pi\pi$ and the vertex $D_s^*\pi D_s$ is equal to zero. Of course there exist other box diagrams involving the exchange in the t-channel of two pseudoscalars diferent from $\pi\pi$, πK or KK (the latter illustrated in Fig. 9.1) but they are suppressed and can therefore be neglected. Crossed box diagrams (with four pseudoscalar mesons in the intermediate state) and box diagrams involving anomalous couplings were also calculated in Chapter 3, but they were found to be much smaller, especially in the case of the anomalous coupling, than the contributions from the box diagram of Fig. 9.1. The final formula for each of the diagrams in Fig. 9.1 is given in the Appendix E. One can see in these formulas that the cuts plotted in the diagram in Fig. 9.1 are clearly visible in the denominators.

Following the ideas of [116] we include two different form factors in the integral of the box-diagram potential (formulas of the Appendix E). These are:

- Model A: We multiply the vertices in the diagram of Fig. 9.1 by:

$$F_1(q^2) = \frac{\Lambda_b^2 - m_1^2}{\Lambda_b^2 - (k_1^0 - q^0)^2 + |\vec{q}|^2}, \tag{9.1}$$

$$F_3(q^2) = \frac{\Lambda_b^2 - m_3^2}{\Lambda_b^2 - (k_3^0 - q^0)^2 + |\vec{q}|^2}, \tag{9.2}$$

  with $q^0 = \frac{s+m_2^2-m_4^2}{2\sqrt{s}}$, $\vec{q}$ being the running variable, and $\Lambda_b = 1.4, 1.5$ GeV [85, 86]. Therefore, we add $F_1(q^2)^2 F_3(q^2)^2$ to the integrand in Eqs. (E.1), (E.4) and (E.8) and we put $g = M_\rho/2\,f_\pi$.

- Model B: Here we use a exponential parametrization for a off-shell $\pi(K)$ evaluated using QCD sum rules [123],

$$F(q^2) = e^{((q^0)^2 - |\vec{q}|^2)/\Lambda^2}\ , \tag{9.3}$$

  with $\Lambda = 1, 1.2$ GeV and $q^0 = \frac{s+m_2^2-m_4^2}{2\sqrt{s}}$. So we add $F(q^2)^4$ to the integrand in Eqs. (E.1), (E.4) and (E.8). In this case we also change the factor g^4 in these equations by the corresponding product of g's, $g = M_\rho/2\,f_\pi$, with $f_\pi = 93$ MeV, $g_{D_s} = M_{D_s^*}/2\,f_{D_s} = 5.47$ with $f_{D_s} = 273/\sqrt{2}$ MeV [78] and $g_D = g^{\rm exp}_{D^*D\pi} = 8.95$ (experimental value) [120, 121, 122].

In Figs. 9.2 and 9.3 we compare the real parts of the box diagrams with the contact terms plus vector-exchange terms for the $D^*K^* \to D^*K^*$ and $D^*K^* \to D_s^*\phi$ amplitudes (the interaction is very attractive for these amplitudes, see Table D.4). As one can see in these figures, the box diagram has a small real part compared to the strong potential provided by the four-vector contact terms plus vector-exchange diagrams, particularly in the region of energies corresponding to the states that we find. Therefore, one can neglect the real part of the box diagrams as it was done in [85, 136, 116]. In Fig. 9.4 we depict the imaginary part of the box diagrams in Fig. 9.1 for the two models. Here we set $\Lambda = 1400$ MeV for the Model

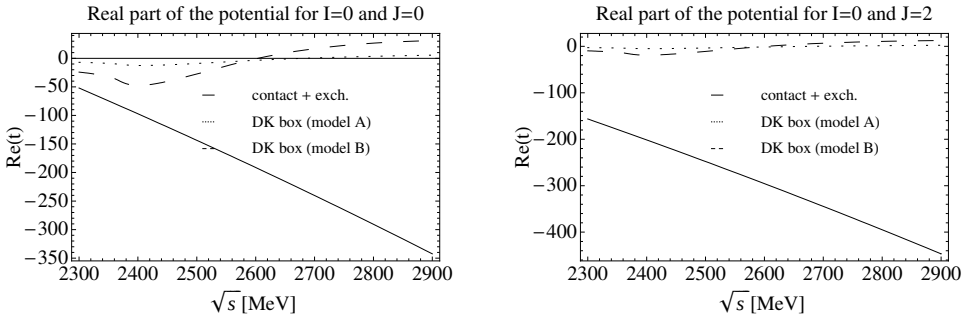

Figure 9.2: Comparison of the real part of the box diagram with the contact term plus vector-exchange term for the $D^*K^* \to D^*K^*$ amplitude and $I = 0$, $J = 0$ and $J = 2$ respectively.

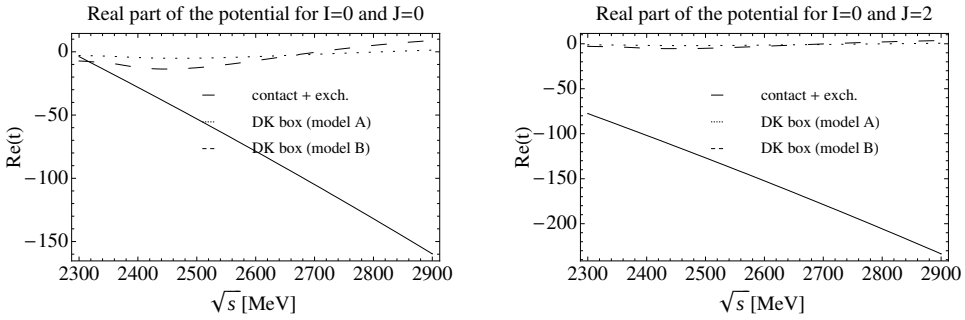

Figure 9.3: Comparison of the real part of the box diagram with the contact term plus vector-exchange term for the $D^*K^* \to D_s^*\phi$ amplitude and $I = 0$, $J = 0$ and $J = 2$ respectively.

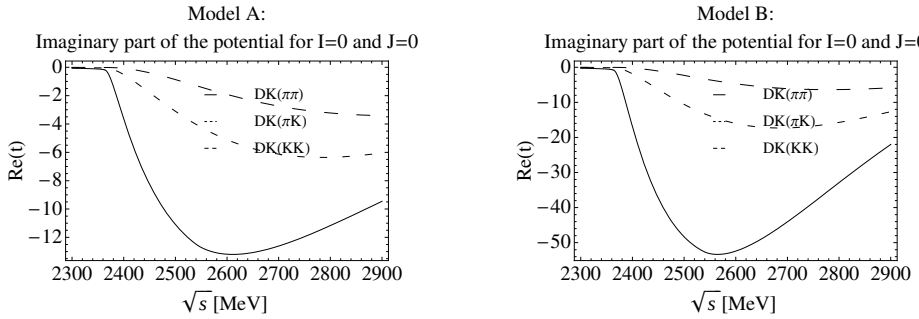

Figure 9.4: Imaginary part of the box diagrams in Fig. 9.1 for $I = 0$ and $J = 0$.

A, while we put $\Lambda = 1200$ MeV when using Model B. As this figure shows, the Model B with the form factor of Eq. (9.3) provides a larger imaginary part compared to Model A which results in a larger width of the resonance. These modifications do not practically change the positions of the poles and the couplings are barely affected. However, the convolution of the mass distribution and the consideration of the pseudoscalar decay channels in terms of box diagrams leads to a larger width of the respective resonances. The reevaluation of the Bethe-Salpeter equation, Eq. (3.22), leads to the squared transition amplitudes pictured in the Figs. 9.5 - 9.9. The corresponding masses and widths are given in Tables 9.2 - 9.6.

9.2.1 $C = 0; S = 1; I = 1/2$ (hidden charm)

The amplitudes from the four-vector contact terms plus vector-exchange diagrams can be found in Table D.1 in the Appendix D. We can see

from the tables that the potential is small and repulsive except for the $D_s^*\bar{D}^* \to J/\psi K^*$ and $D_s^*\bar{D}^* \to D_s^*\bar{D}^*$ amplitudes for $J = 1$ and 2 respectively. However, the attraction is too small to bind the system and therefore we do not get poles or possible states from the T-matrix.

9.2.2 $C = 0; S = 1; I = 1/2$ (hidden charm)

The amplitudes from the four-vector contact terms plus vector-exchange diagrams can be found in Table D.1 in the Appendix D. We can see from the tables that the potential is small and repulsive except for the $D_s^*\bar{D}^* \to J/\psi K^*$ and $D_s^*\bar{D}^* \to D_s^*\bar{D}^*$ amplitudes for $J = 1$ and 2 respectively. However, the attraction is too small to bind the system and therefore we do not get poles or possible states from the T-matrix.

9.2.3 $C = 1; S = -1; I = 0$

In contrast to the above sector the potential in the case of $C = 1$ and $S = -1$ is very attractive as indicated in Table D.2. For $I = 0$ and $J = 0, 1$ the potential is around $-10\, g^2$ whereas it is about $-16\, g^2$ for $J = 2$. In this sector the strong interaction from the potential leads to bound states. We obtain one resonance for each spin, $J = 0, 1$ and 2, where the corresponding pole positions and couplings are given in Table 9.1. The convolution of the G function due to the $\bar{K}^*$ width leads to a minor shift in the pole positions (only 3 MeV for $J = 2$) and around 3 MeV in the widths for the three states. This is a minor effect compared to the contribution of the box diagrams. Therefore we neglect the K^* width in the final $|T|^2$ analysis. $|T|^2$ is depicted in Figs. 9.5 and 9.6 for $J = 0$ and 2 and for the two models A and B after the inclusion of the corresponding box diagrams of Fig. 9.1. Here, the two models lead to similar results except for the model B with $\Lambda = 1200$ MeV. In Table 9.2 we show the values of the masses and final widths of the states. Since these states have exotic flavor

quantum numbers there is no possible $q\bar{q}$ counterpart.

$I[J^P]$	$\sqrt{s}_{\rm pole}$ (MeV)	$g_{D^*\bar{K}^*}$
$0[0^+]$	2848	12227
$0[1^+]$	2839	13184
$0[2^+]$	2733	17379

Table 9.1: $C = 1; S = -1; I = 0$. Quantum numbers, pole positions and couplings g_i in units of MeV. Here, $\alpha = -1.6$.

9.2.4 $C = 1; S = -1; I = 1$

In this sector, which also has exotic quantum numbers, we can see from Table D.3 that the interaction is very repulsive in contrast to the previous case of $I = 0$. Therefore, no bound states or resonances are found in this sector.

9.2.5 $C = 1; S = 1; I = 0$

The strong interaction coming from the contact terms plus vector-exchange diagrams leads to a potential of the order of $-18\,g^2$ to $-26\,g^2$, see Table D.4 in the Appendix D, which is enough to bind the D^* and K^* mesons. In this sector we obtain three poles with masses $M = 2683$, 2707 and 2572 MeV for $J = 0$, 1 and 2, respectively. The potentials in Tab. D.4 provide the kernel V of Eq. (3.22) which results in the pole positions and couplings summarized in Table 9.3. The state with $J = 2$ is more bound than the other poles for $J = 0$ and 1 which can be identified with the $D_2^*(2573)$ resonance in the PDG. Here, the D^*K^* channel is dominant for the three different spins. Nevertheless the other channels, $D_s^*\omega$ and $D_s^*\phi$ are not negligible.

$I[J^P]$	$\sqrt{s}_{\rm pole}$ (MeV)	Model	Γ (MeV)
$0[0^+]$	2848	A, $\Lambda = 1400$ MeV	23
		A, $\Lambda = 1500$ MeV	30
		B, $\Lambda = 1000$ MeV	25
		B, $\Lambda = 1200$ MeV	59
$0[1^+]$	2839	Convolution	3
$0[2^+]$	2733	A, $\Lambda = 1400$ MeV	11
		A, $\Lambda = 1500$ MeV	14
		B, $\Lambda = 1000$ MeV	22
		B, $\Lambda = 1200$ MeV	36

Table 9.2: $C = 1; S = -1; I = 0$. Mass and width for the states with $J = 0$ and 2.

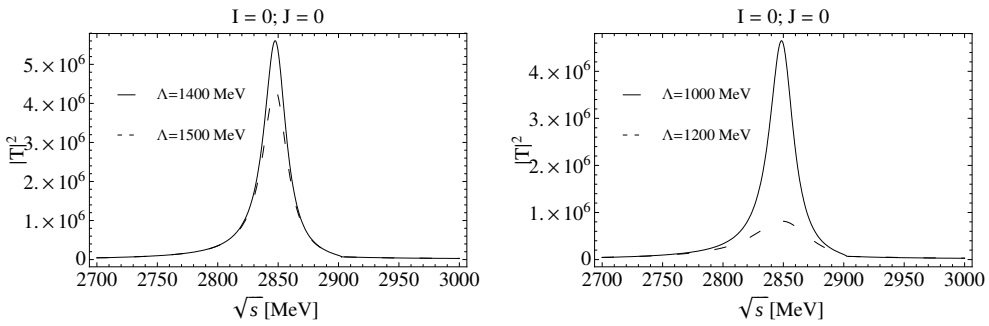

Figure 9.5: Squared amplitude in the $D^*\bar{K}^*$ channel for $I = 0$ and $J = 0$. Left: Model A, right: Model B.

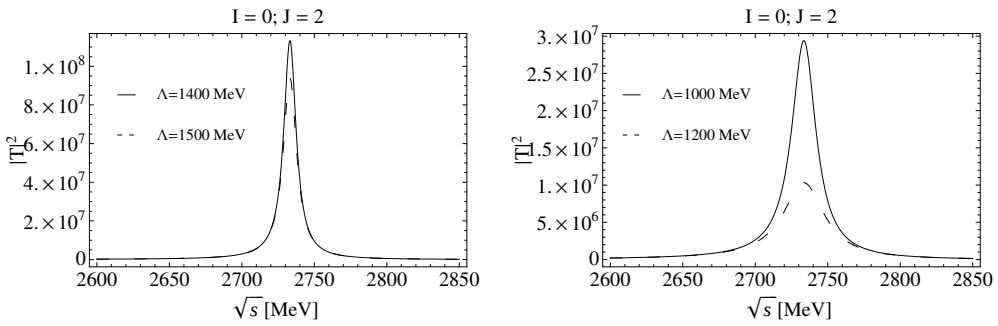

Figure 9.6: Squared amplitude in the $D^*\bar{K}^*$ channel for $I = 0$ and $J = 2$. Left: Model A, right: Model B.

When considering the K^* width, which is equivalent to replacing G by the convoluted $\tilde{G}$, neither the mass changes significantly (in fact only 2 MeV) nor the width is affected by this modification. Therefore, the effect of the convolution is so small that it does not need to be considered. Only the consideration of the box diagrams has some influence on the width. In Figs. 9.7 and 9.8 $|T|^2$ is plotted after the inclusion of the box diagrams of Fig. 9.1 for the two models A and B. We observe that these diagrams provide some width for the states with $J = 0$ and 2 (possible quantum numbers of the box diagrams), although the width provided by the model B is much bigger than that from model A. The values of the masses and widths are given in Table 9.4. Model B with $\Lambda = 1000$, 1200 MeV provides a width for the state appearing around 2572 MeV of $18 - 23$ MeV.

We associate this state with the $D_{s2}^*(2573)$ of the PDG [78] since the quantum numbers, position and width agree with those of the PDG. We should note that this is the case where we found the largest attraction, of the order of $-26\, g^2$, which is even bigger than what was found for $I = 0, J = 2$ in the $\rho\rho$ interaction ($\simeq -20\, g^2$) which lead to the production of the $f_2(1270)$ [85, 86].

$I[J^P]$	$\sqrt{s}_{\rm pole}$ (MeV)	$g_{D^*K^*}$	$g_{D_s^*\omega}$	$g_{D_s^*\phi}$
$0[0^+]$	2683	15635	-4035	6074
$0[1^+]$	2707	14902	-5047	4788
$0[2^+]$	2572	18252	-7597	7257

Table 9.3: $C = 1; S = 1; I = 0$. Quantum numbers, pole positions and couplings g_i in units of MeV for $I = 0$. Here $\alpha = -1.6$.

$I[J^P]$	$\sqrt{s}_{\rm pole}$ (MeV)	Model	$\Gamma_{\rm theo}$ (MeV)	$\Gamma_{\rm exp}$ (MeV)
$0[0^+]$	2683	A, $\Lambda = 1400$ MeV	20	-
		A, $\Lambda = 1500$ MeV	25	
		B, $\Lambda = 1000$ MeV	44	
		B, $\Lambda = 1200$ MeV	71	
$0[1^+]$	2707	Convolution	4×10^{-3}	-
$0[2^+]$	2572	A, $\Lambda = 1400$ MeV	7	20 ± 5 [78]
		A, $\Lambda = 1500$ MeV	8	
		B, $\Lambda = 1000$ MeV	18	
		B, $\Lambda = 1200$ MeV	23	

Table 9.4: $C = 1; S = 1; I = 0$. Mass and width for the states with $J = 0$ and 2.

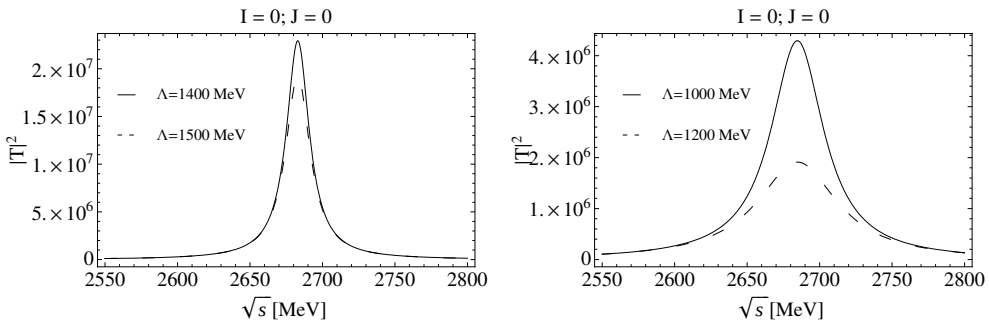

Figure 9.7: Squared amplitude in the D^*K^* channel for $I = 0$ and $J = 0$. Left: Model A, right: Model B.

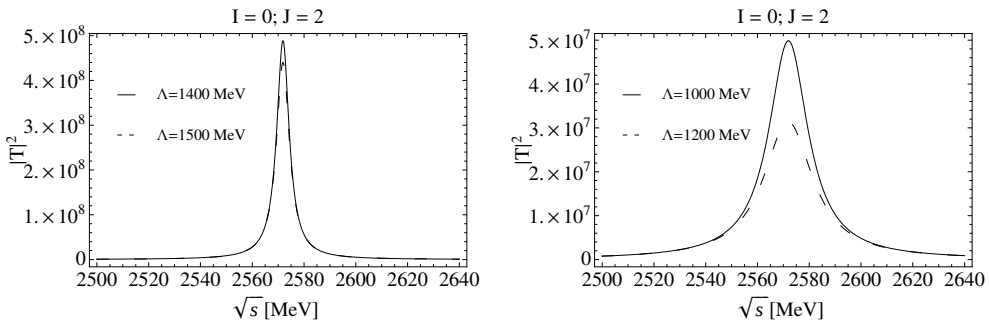

Figure 9.8: Squared amplitude in the D^*K^* channel for $I = 0$ and $J = 2$. Left: Model A, right: Model B.

9.2.6 $C = 1; S = 1; I = 1$

In this sector the potential is attractive for the $D^*K^* \to D_s^*\rho$ reaction. For $J = 0$ and 1 this potential is around $-7\,g^2$ whereas it is by a factor of two bigger $-13\,g^2$ for $J = 2$ (see Table D.5). In fact, we only obtain a pole for $J = 2$. For $J = 0$ and 1 we only observe a cusp in the $D_s^*\rho$ threshold. In Table 9.5 we show the pole position and couplings to the different channels. Both channels, D^*K^* and $D_s^*\rho$, are equally important as one can deduce from the corresponding couplings. The broad width of the ρ meson has to be taken into account by means of Eq. (3.24) which results in a width of 8 MeV. In this case the box diagrams in Fig. 9.1 for the D^*K^* channel only make a small contribution to the width of the resonance (see Fig. 9.9). In contrast to the previous situations the width of the resonance is mainly generated by the convolution of the ρ mass while the box diagrams play a minor role. In Table 9.6 we give the exact values of the width in the two models which give very similar results. No experimental counterpart is found for this state in the PDG.

$I^G[J^{PC}]$	$\sqrt{s}_{\rm pole}$ (MeV)	$g_{D^*K^*}$	$g_{D_s^*\rho}$
$1[2^+]$	2786	11041	11092

Table 9.5: $C = 1; S = 1; I = 1$. Quantum numbers, pole positions and couplings g_i in units of MeV. Here $\alpha = -1.6$.

9.2.7 $C = 1; S = 2; I = 1/2$

This sector is exotic since a double-strange state is not reached in $q\bar{q}$. As we can see from Table D.6 in the Appendix D, the potential is repulsive for all possible spins. Therefore we do not get any bound state or resonance in this sector.

$I[J^P]$	$\sqrt{s}_{\rm pole}$ (MeV)	Model	Γ (MeV)
$1[2^+]$	2786	A, $\Lambda = 1400$ MeV	8
		A, $\Lambda = 1500$ MeV	9
		B, $\Lambda = 1000$ MeV	9
		B, $\Lambda = 1200$ MeV	11

Table 9.6: $C = 1; S = 1; I = 1$. Mass and width for the state with $J = 1$ and 2.

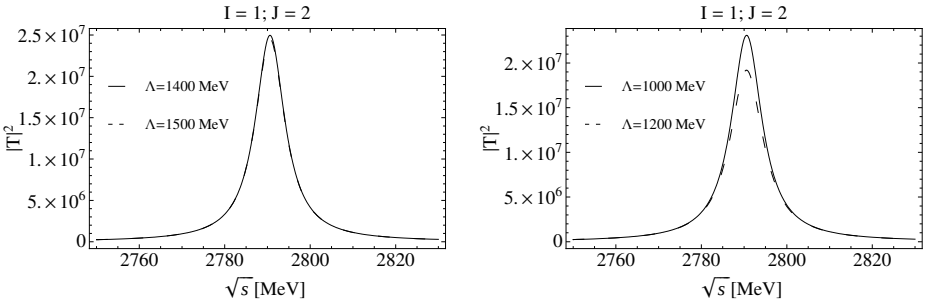

Figure 9.9: Squared amplitude in the D^*K^* channel for $I = 1$ and $J = 2$. Left: Model A, right: Model B.

9.2.8 $C = 2; S = 0; I = 0$

In this case we study double charmed states by coupled D^*D^* channels. The amplitudes are given in Table D.7, where the potential is zero for $J = 0$ and 2. This can be explained by the fact that the D^*D^* state is antisymmetric for $I = 0$. Therefore, the only possibility to obtain a fully symmetric wave function is provided by $J = 1$ which is equivalent to the rule $L + \tilde{S} + I =$ odd, since $L = 0$ for $s-$wave ($\tilde{S}$, spin $\equiv J$ for $L = 0$). For $J = 1$ the interaction is strongly attractive and we obtain a pole in the scattering matrix. The pole position and coupling to the D^*D^* channel is given in Table 9.7. The width of the D^* meson is very small (~ 100 keV or less in the case of the neutral charmed meson), hence, we do not perform the convolution of the G function. Since we deal with a $J = 1$ state we do not get contribution from the box diagram. Therefore we obtain a state with zero width or a very narrow width when considering the convolution. This sector with $C = 2$ is exotic and so far there are no experimental observations.

$I[J^P]$	$\sqrt{s}_{\rm pole}$ (MeV)	$g_{D^*D^*}$
$0[1^+]$	3969	16825

Table 9.7: $C = 2; S = 0; I = 0$. Quantum numbers, pole positions and couplings g_i in units of MeV. Here $\alpha = -1.4$.

9.2.9 $C = 2; S = 0; I = 1$

Here we deal with the reversed situation as in the previous $I = 0$ sector. The isospin combination for $I = 1$ of the D^*D^* channel is symmetric and therefore $J = 1$ is forbidden ($L+S+I =$ even). However, the potential is very repulsive for $J = 0$ and $J = 2$ (see Table D.8) and consequently we do not obtain any pole in the scattering matrix.

9.2.10 $C = 2; S = 1; I = 1/2$

This sector is also exotic. The amplitudes from the four-vector contact terms plus vector-exchange diagrams lead to a repulsive potential for $J = 0$ and 2 and is attractive for $J = 1$ as indicated in Table D.9. We get a pole almost at the $D_s^* D^*$ threshold (4121 MeV), and the pole position and the coupling are given in Table 9.8. This state comes with zero width since the box diagrams are not possible for $J = 1$ and any possible convolution of the G function would lead to a very small width. This state is also a prediction of the model and needs to be confirmed by experiment.

$I[J^P]$	$\sqrt{s}_{\rm pole}$ (MeV)	$g_{D_s^* D^*}$
$1/2[1^+]$	4101	13429

Table 9.8: $C = 2; S = 1; I = 1/2$. Quantum numbers, pole positions and couplings g_i in units of MeV . Here, $\alpha = -1.4$.

9.2.11 $C = 2; S = 2; I = 0$

The $D_s^* D_s^*$ channel allows us to study double-charm double-strange objects. Since we deal with two identical particles with isospin zero, the isospin $D_s^* D_s^*$-state is symmetric and hence we get interaction for $J = 0$ and 2 while the potential zero for $J = 1$ (see Table D.10). Since the potential is strongly repulsive we do not obtain any state in this sector.

In Table 9.9 we give a summary of the states obtained together with the only experimental counterpart observed so far.

C, S	$I[J^P]$	$\sqrt{s}$	$\Gamma_{\rm A}(\Lambda = 1400)$	$\Gamma_{\rm B}(\Lambda = 1000)$	State	$\sqrt{s}_{\rm exp}$	$\Gamma_{\rm exp}$
$1, -1$	$0[0^+]$	2848	23	25			
	$0[1^+]$	2839	3	3			
	$0[2^+]$	2733	11	22			
$1, 1$	$0[0^+]$	2683	20	44			
	$0[1^+]$	2707	4×10^{-3}	4×10^{-3}			
	$0[2^+]$	2572	7	18	$D_{s2}(2573)$	2572.6 ± 0.9	20 ± 5
	$1[2^+]$	2786	8	9			
$2, 0,$	$0[1^+]$	3969	0	0			
$2, 1$	$1/2[1^+]$	4101	0	0			

Table 9.9: Summary of the nine states obtained. The width is given for the model A, Γ_A, and B, Γ_B. All the quantities here are in MeV.

9.3 Conclusions

In the present work we can assign one resonance to an experimental counterpart, the $D_2^*(2573)$, giving a novel interpretation for this resonance as a vector - vector molecular state. Thus, the assumption of the D^*K^* structure of the $D_2^*(2573)$ is consistent with the DK nature assumed for the $D^*(2317)$, the D^*K molecular structure of the $D^*(2460)$ or the X(3872) ($D\bar{D}^*$). The other two states around 2700 MeV are predictions of the model without experimental evidence for these masses and quantum numbers up to now. For $I = 1$ we find only one state, of non exotic nature, a 2^+ state around 2786 MeV. In the flavor-exotic sectors, we obtain interesting predictions for new states. For $C = 1; S = -1; I = 0$ we obtain three new exotic states with $I[J^P] = 0[0^+]$, $0[1^+]$ and $0[2^+]$ respectively that can be interpreted as $D^*\bar{K}^*$ bound states. In the case of the double-charm sectors $C = 2; S = 0; I = 0$ and $C = 2; S = 1; I = 1/2$ the potential leads to a bound system for $J = 1$ only. Therefore, we deal with two very narrow states with masses close to the thresholds D^*D^* and $D_s^*D^*$ respectively. It is interesting to notice that in [156], the authors perform a systematic analysis of doubly charmed exotic states as meson - meson molecules and they conclude the existence of a stable isoscalar doubly charmed meson with quantum numbers $I[J^P] = 0[1^+]$ (here the authors consider a set of two coupled channels, DD^* and D^*D^*). To sum up, all states are relatively narrow and in the flavor exotic sectors, there is no experimental counterpart for all exotic structures which can be considered as D^*K^*, $D^*\bar{K}^*$, D^*D^* and $D_s^*D^*$ molecular states, rendering the experimental search for these new states out of the $q\bar{q}$ spectrum very challenging.

Chapter 10

Mesons with charm in the nuclear medium

We study the properties of charm and hidden charm mesons in the nuclear medium. The $D_{s0}(2317)$ is believed to be a DK bound state or dynamically generated resonance strongly coupled to DK. The X(3700) is a theoretical state predicted just below the $D\bar{D}$ threshold and it is like a $D\bar{D}$ bound state [108].

Although these two states are very narrow in the free space we will see that they experience a large change in the width inside a nuclear medium. The study of the properties of mesons in the medium brings valuable information on the nature of the particles and the reactions that occur when D mesons interact with nuclei.

10.1 Introduction

One of the features of the study of the properties in the medium is that new decay mechanisms take place. Since there is more available energy, new chains of reactions that did not occur in the free space will show up in the medium. We quote here two interesting examples:

the $\Lambda(1520)$ baryon and the ω meson. The $\Lambda(1520)$ is a dynamically generated resonance that couples strongly to $\pi\Sigma(1385)$, this channel is above the mass of the $\Lambda(1520)$ and hence the $\Lambda(1520)$ cannot decay into this channel. However, in the presence of the nucleus, the pion can give rise to a particle - hole excitation, there is an increase of 140 MeV of phase space for this reaction and the decay takes place. Finally, this leads to a large width of the $\Lambda(1520)$ in the medium.

One finds an analogy in the ω decay in the medium. In free space the ω meson decays into 3π. This decay could go through $\rho\pi$ but there is no enough phase space. Again, in the medium the ρ meson is modified in the nucleus through its decay into 2π and the π can become a ph excitation. At the end, one finds spectacular changes in the width of the ω-meson of $100 - 150$ MeV [157, 158, 159, 160].

The study of the properties of scalar mesons in the nuclear medium has been studied for a long time. The most studied has been the $\sigma(600)$. In [161] the σ and π mesons at high density were studied within the Nambu-Jona-Lasinio model and a subtantial drop of the m_σ was found. In contrast, the m_π increase with the density. In [162] Hatsuda et al. find that due to the partial restoration of the chiral symmetry, m_σ would approach m_π and similar conclusions are reached by the use of non-linear chiral Lagrangians [163, 164] where the modifications of the σ come from the strong p-wave coupling of the pions to ph and Δ-hole excitations. Experimentally, strong medium effects of the σ have been observed at low invariant masses in the A(π, 2π) and A(γ, 2π) reactions [165, 166, 167, 168]. See, however, a different interpretation of the A(γ, 2π) results in [169].

For a detailed revision of this Chapter see [110].

10.2 Brief discussion on the dynamical generation of the $D_{s0}(2317)$ and X(3700)

Here we summarize briefly the work done in [108] and the main conclusions achieved of relevance to us here. The authors start from two

different models for the interaction between pseudoscalar mesons of the 15-plet. Whereas one is a chiral Lagrangian in SU(4) that follows the general rules of SU(n) breaking [170], the other model is a phenomenological model that extrapolates directly the SU(3) chiral Lagrangian for the interaction between mesons to SU(4). Although at the begining the structure is SU(4) flavour symmetric, afterwards, the symmetry is strongly broken, 1) due to the consideration of real masses which is needed in order to respect thrsholds and fullfill unitarity, and 2) the heavy vector exchange diagrams are suppressed by the exchange of a heavy mass. Both models, the chiral Lagrangian and the phenomenological one, arrive to the same conclusions, with qualitative agreement, in the results, and the discussion serves to show uncertainties.

Once one derives the kernel (potential) from the lowest order Lagrangian it is included as input in the Bethe-Salpeter equation, Eq. (3.22). However the use of the cutoff, Eq. (3.23), is more convenient in the nuclear medium. The reason is that the dimensional regularization method relies upon Lorentz covariance, and this is lost in nuclei where one has a privileged reference frame, which is the one where the nucleus is at rest. As a consequence, the use of the dimensional regularization method introduces pathologies in the selfenergy that are avoided with the cutoff. For these reasons, the cutoff method is used in the channels where we renormalize the particles, DK and $D\bar{D}$ (those to which the resonance couples more strongly), and the cutoff is chosen to obtain the same value of the G function at threshold than in the free space, and is much bigger than the on-shell three - momenta of the particles in the loops. In the rest of the channels we use dimensional regularization.

The prescription for the $\eta - \eta'$ mixing used in [171] is followed. The couplings are shown in Tables 10.1 and 10.2

We can extract the following conclusions:

1) The hidden charm state X(3700) couples mostly to $D\bar{D}$ and $D_s\bar{D}_s$. From the square of the couplings which would enter into the selfenergy of the resonance we obtain a factor of two more

Channel	Re(g_X) [MeV]	Im(g_X) [MeV]	$\lvert g_X\rvert$ [MeV]
$\pi^+\pi^-$	9	83	84
K^+K^-	5	22	22
D^+D^-	5962	1695	6198
$\pi^0\pi^0$	6	83	84
$K^0\overline{K^0}$	5	22	22
$\eta\eta$	1023	242	1051
$\eta\eta'$	1680	368	1720
$\eta'\eta'$	922	−417	1012
$D^0\overline{D^0}$	5962	1695	6198
$D_s^+D_s^-$	5901	−869	5965
$\eta_c\eta$	518	659	838
$\eta_c\eta'$	405	9	405

Table 10.1: $X(3700)$: Couplings of the pole at (3722-i18) MeV to the channels (C=0, S=0,I=0).

Channel	Re($g_{D_{s0}}$) [MeV]	Im($g_{D_{s0}}$) [MeV]	$\lvert g_{D_{s0}}\rvert$ [MeV]
K^+D^0	5102	0	5102
K^0D^+	5102	0	5102
ηD_s^+	-2952	0	2952
$\eta' D_s^+$	4110	0	4110
$\eta_C D_s^+$	2057	0	2057

Table 10.2: $D_{s0}(2317)$: Couplings of the pole at 2317 MeV to the channels (C=1, S=1,I=0).

weight for the $D\bar{D}$ than $D_s\bar{D}_s$. In addition, the $D\bar{D}$ channel is 38 MeV above the X(3700) pole whereas the $D_s\bar{D}_s$ threshold is 238 MeV far away from the mass of the X(3700). This lead to a minor contribution of the $D_s\bar{D}_s$ channel of 10% of the $D\bar{D}$. When calculating corrections in the medium, we shall consider the normalization of D but not D_s.

2) The $D_{s0}(2317)$ is mostly a DK bound state. Although the contributions of other channels, as ηD_s and $\eta' D_s$, is not negligible, we can consider only the effects in the medium of the DK channel from similar considerations to those made in the previous paragraph. Since the KN interaction is weak and has no singularities, the DK channel can be renormalized in a very good approximation incorporating only the D-selfenergy. Therefore, we will only calculate the selfenergy of the D-meson.

Due to the differences between the masses of the 16-plet when we go from SU(3) to SU(4) we are introducing more uncertainties. This was the reason on why two models where used in [108] although it was found that the states that we study here where rather independent of the model. However, in this study the evaluation of the uncertainties

Channel	$\|g_i\|$ Model A [MeV]	$\|g_i\|$ Model B [MeV]
DK	7215	7503
$D_s\eta$	2952	3005
$D_s\eta\prime$	4110	4146
$D_s\eta_c$	2058	1246

Table 10.3: Couplings of the $D_{s0}(2317)$ to its building blocks. Model A refers to the model using both, f_π and f_D in the couplings, while in Model B only f_π is used, respecting constrains from chiral symmetry. The channels are in isospin basis. The position of the pole is fixed in both models to 2317 MeV, taking $\alpha_H = -1.48$ in the model A, and $\alpha_H = -1.16$ in the model B (α_H means the substraction constant used in [108] for the channels involving at least one heavy pseudoscalar meson).

plays a more important role and we do it carefully. In particular we vary the f_π and f_D parameters in the range $f_\pi \in [85, 115]$ MeV and $f_D \in [146, 218]$ MeV. The results with their uncertainties will be shown in the Section 10.5. Furthermore, for the case of the scattering of light mesons with heavy ones, chiral symmetry is recovered in the phenomenological model when f_π is used for all the cases. We do a fine tuning of the subtraction constant in order to get the position of the $D_{s0}(2317)$ at the right place and look at the couplings. The results using f_π and f_D (model A) and only f_π (model B) in the phenomenological model can be seen in Table 10.3. We can observe differences in the couplings of 4% in the main building block, the DK channel. This is an indication that the errors induced by the explicit chiral symmetry breaking are small and gives support to the model used in [108]. In the present paper we use the values of the couplings obtained with model B (only f_π).

10.3 The self-energy of the D-meson

10.3.1 s-wave self-energy

The D meson s-wave selfenergy is obtained from a selfconsistent coupled channel calculation where the coupled-channel structure includes the channels $\pi\Lambda_c$, $\pi\Sigma_c$, DN, $\eta\Lambda_c$, $K\Xi_c$, $\eta\Sigma_c$, $K\Xi_c'$, $D_s\Lambda$, $D_s\Sigma$, $\eta'\Lambda_c$ and $\eta'\Sigma_c$. The potentical comes from a broken SU(4) s-wave Weinberg-Tomozawa interaction supplemented by an attractive isoscalar-scalar term. However, the last term, the Σ_{DN} term, is a subject of controversy. Even though its inclusion is supported by QCD sum rules and mean - field approaches, the selfconsistent coupled channel calculation of [172] and [173] shows that considering it or not is not relevant, leading to results qualitatively identical. The differences found when using the two different options where smaller than the uncertainties from other sources (for example SU(4) breaking) and for this reason we ignore this term in the calculations of the D s-wave selfenergy. The Bethe-Salpeter equation is solved using the cutoff method and the cutoff is fixed when reproducing the $\Lambda_c(2593)$. When this is done, a new resonance appears around 2800 MeV, the $\Sigma_c(2800)$. The in-medium effects are included in the meson-baryon loop function and they are: 1) Pauli blocking effects on the nucleons (the scattered nucleons cannot go to states already occupied in the fermi sea), 2) Mean - field binding of baryons via a $\sigma-\omega$ model and 3) renormalization of π and D through the inclusion of the selfenergy in the intermediate propagator. Moreover, the s-wave D selfenergy is obtained iteratively in a selfconsistent procedure when one integrates the in medium s-wave DN amplitude over the nucleon Fermi sea $n(p)$:

$$\Pi_D^{(s)}(q^0,\vec{q},\rho) = \int \frac{d^3p}{(2\pi)^3} n(p)[\tilde{T}_{DN}^{(I=0)}(P^0,\vec{P},\rho) + 3\tilde{T}_{DN}^{(I=1)}(P^0,\vec{P},\rho)] \ , \tag{10.1}$$

10.3.2 *p*-wave selfenergy

We start by recalling the $SU(3)$ chiral Lagrangian [174, 175] for the coupling of pseudoscalar mesons of the octet of the π to the baryon octet of the proton p

$$\mathcal{L}_1^{(B)} = \frac{1}{2} D < \bar{B}\gamma^\mu\gamma_5\{u_\mu, B\} > + \frac{1}{2} F < \bar{B}\gamma^\mu\gamma_5[u_\mu, B] > , \quad (10.2)$$

where

$$u^2 = U = e^{i\frac{\sqrt{2}\phi}{f}} , \quad (10.3)$$

with ϕ the usual $SU(3)$ matrix of the meson fields, $f = 1.15 f_\pi$ with $f_\pi = 93$ MeV and

$$u_\mu = i u^\dagger \partial_\mu U u^\dagger = -\frac{\sqrt{2}}{f}\partial_\mu\phi + O(\phi^3) . \quad (10.4)$$

The B and $\bar{B}$ terms stand for the $SU(3)$ matrices of the baryon fields and $<>$ for the trace in $SU(3)$. Hence, at the one meson field level we have

$$\mathcal{L}_1^{(B)} = -\frac{1}{\sqrt{2}f} D < \bar{B}\gamma^\mu\gamma_5\{\partial_\mu\phi, B\} > -\frac{1}{\sqrt{2}f} F < \bar{B}\gamma^\mu\gamma_5[\partial_\mu\phi, B] > \quad (10.5)$$

The $\bar{u}(\vec{p}\,')\gamma^\mu\gamma_5 u(\vec{p})$ vertex, assuming $\vec{p} \simeq 0$ since it will be the momentum of a nucleon in the Fermi sea, can be expressed up to $O(1/M^2)$ in terms of the $\vec{\sigma}$ operator such that the T matrix corresponding to the diagram of Fig. 10.1 is given by

$$-it = \frac{1}{\sqrt{2}f}\vec{\sigma}\cdot\vec{q}(1 - \frac{q^0}{2M'})[(D+F) < \bar{B}\phi B > + (D-F) < \bar{B}B\phi >] \quad (10.6)$$

with M' the mass of the outgoing baryon in Fig. 10.1. We take $D = 0.80$ and $F = 0.46$ from [176, 177, 178]. In order to evaluate

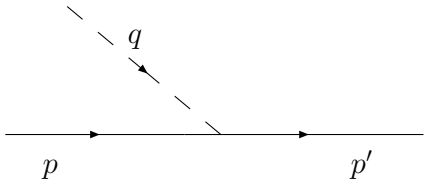

Figure 10.1: Meson-baryon scattering with an outgoing baryon. The labels p, p' and q refer to the momenta of the initial baryon, final baryon and meson respectively.

the coupling of the D meson to the nucleon and Λ_c, Σ_c we use $SU(4)$ symmetry. We couple the 20-plet of the baryons, to which the nucleon belongs, to the $\bar{20}$ representation of the antibaryons in order to give the 15-plet of the mesons of the π and the D [78]. By using the $SU(4)$ Clebsch-Gordan coefficients of [179], we have two independent irreducible matrix elements which can be related to the D and F coefficients. The result is that the couplings $D^0p \to \Lambda_c^+$, $D^0p \to \Sigma_c^+$, $D^+p \to \Sigma_c^{++}$, $D^0n \to \Sigma_c^0$, $D^+n \to \Lambda_c^+$, $D^+n \to \Sigma_c^+$ are identical to those of $K^-p \to \Lambda$, $K^-p \to \Sigma^0$, $\bar{K}^0p \to \Sigma^+$, $K^-n \to \Sigma^-$, $\bar{K}^0n \to \Lambda$, $\bar{K}^0n \to \Sigma^0$ given in [180] by

$$-iV_{DNY} = \vec{\sigma}\cdot\vec{q}\left(1-\frac{q^0}{2M'}\right)\left[\alpha\frac{D+F}{2f}+\beta\frac{D-F}{2f}\right] \ , \qquad (10.7)$$

with the coefficients α, β of the Table 10.4. We also take into account

	$D^0p\to\Lambda_c^+$	$D^0p\to\Sigma_c^+$	$D^0n\to\Sigma_c^0$	$D^+n\to\Lambda_c^+$	$D^+n\to\Sigma_c^+$	$D^+p\to\Sigma_c^{++}$
α	$-\frac{2}{\sqrt{3}}$	0	0	$-\frac{2}{\sqrt{3}}$	0	0
β	$\frac{1}{\sqrt{3}}$	1	$\sqrt{2}$	$\frac{1}{\sqrt{3}}$	-1	$\sqrt{2}$

Table 10.4: Coefficients for the DNY couplings

the coupling of the D meson with $\Sigma_c^*(2520)$ and N, in analogy to

the p-wave interaction of pions and kaons with nucleons. For pions and kaons it was shown that the $N^{-1}\Delta$ and $N^{-1}\Sigma^*(1385)$ excitations, respectively, are relevant for the calculation of the p-wave self-energy. Once again, we obtain the same result as in [180] for the $N^{-1}\Sigma^*(1385)$

$$-iV_{DNY^*} = a\vec{S}^\dagger \cdot \vec{q}\left(\frac{2\sqrt{6}}{5}\frac{D+F}{2f}\right) , \tag{10.8}$$

with $\vec{S}^\dagger$ being the spin $1/2 \to 3/2$ transition operator and a the coefficients given in Table 10.5.

	$D^0p \to \Sigma_c^{*+}$	$D^0n \to \Sigma_c^{*0}$	$D^+p \to \Sigma_c^{*++}$	$D^+n \to \Sigma_c^{*+}$
a	$-\frac{1}{\sqrt{2}}$	-1	-1	$\frac{1}{\sqrt{2}}$

Table 10.5: Coefficient for the $DN\Sigma_c^*(2520)$ couplings

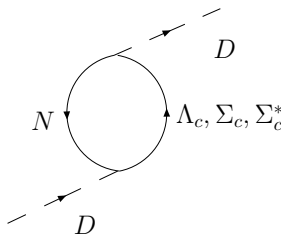

Figure 10.2: p-wave selfenergy diagram of the D meson.

With all those couplings, we can readily evaluate the p-wave D selfenergy given by the diagram of the Fig. 10.2, in complete analogy to [180]. The p-wave contribution coming from the $N^{-1}\Lambda_c$ and $N^{-1}\Sigma_c$ excitations reads

$$\begin{aligned}\Pi^{(p)}_{D^0}(q^0,\vec{q},\rho) &= \{\frac{1}{2}B^2_{D^0p\Lambda_c^+}\vec{q}^{\,2}U_{\Lambda_c^+}(q^0,\vec{q},\rho) + \frac{1}{2}B^2_{D^0p\Sigma_c^+}\vec{q}^{\,2}U_{\Sigma_c^+}(q^0,\vec{q},\rho) \\ &\quad + \frac{1}{2}B^2_{D^0n\Sigma_c^0}\vec{q}^{\,2}U_{\Sigma_c^0}(q^0,\vec{q},\rho)\}F_L^2(q^2) ,\end{aligned} \tag{10.9}$$

where

$$B_{DNY} = \left(1 - \frac{q^0}{2M_Y}\right)\left[\alpha\frac{D+F}{2f} + \beta\frac{D-F}{2f}\right] \ , \tag{10.10}$$

and U is the Lindhard function for the $N^{-1}Y$ excitation given by

$$\begin{aligned} \mathrm{Re}\, U_Y(q^0,\vec{q},\rho) &= \frac{3}{2}\rho\frac{M_Y}{qp_F}\left\{z + \frac{1}{2}(1-z^2)\ln\frac{\mid z+1\mid}{\mid z-1\mid}\right\} \\ \mathrm{Im}\, U_Y(q^0,\vec{q},\rho) &= -\pi\frac{3}{4}\rho\frac{M_Y}{qp_F}\left\{(1-z^2)\theta(1-\mid z\mid)\right\} \\ z &= \left(q^0 - \frac{q^2}{2M_Y} - (M_Y - M)\right)\frac{M_Y}{qp_F} \ , \end{aligned} \tag{10.11}$$

with $\rho = \rho_n + \rho_p$, the nuclear density, $p_F = (3\pi^2\rho/2)^{1/3}$ the Fermi momentum, M_Y the hyperon mass and M the nucleon mass. The same result holds for the p-wave D^+ selfenergy ignoring small mass differences between particles of the same isospin multiplet.

The p-wave selfenergy due to the excitation of the decuplet is also readily evaluated and we find

$$\begin{aligned} \Pi^{(p)*}_{D^0}(q^0,\vec{q},\rho) &= \{\frac{1}{3}C^2_{D^0p\Sigma_c^{+*}}\vec{q}^{\,2}U_{\Sigma_c^{+*}}(q^0,\vec{q},\rho) \\ &\quad + \frac{1}{3}C^2_{D^0n\Sigma_c^{0*}}\vec{q}^{\,2}U_{\Sigma_c^{0*}}(q^0,\vec{q},\rho)\}F_L^2(q^2) \ , \end{aligned} \tag{10.12}$$

where

$$C_{DNY} = af^*_Y\frac{2\sqrt{6}}{5}\frac{D+F}{2f} \ , \tag{10.13}$$

with a given in Table 10.5 and f^*_Y being a recoil factor [180], which we approximate by $f^*_Y \simeq (1 - M_D/M_Y)$.

In Eqs. (10.9) and (10.12), we include a form factor of monopole type at the D meson-baryon vertices by analogy to the one accompanying the Yukawa πNN vertex [180, 181, 182, 183].

$$F_L(q^2) = \frac{\Lambda^2}{\Lambda^2 + \vec{q}^{\,2}} \quad \text{with } \Lambda = 1.05 \text{ GeV}. \tag{10.14}$$

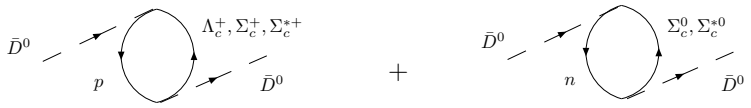

Figure 10.3: p-wave selfenergy diagrams of the $\bar{D}$ meson.

This form factor is suited for light hadrons, i.e., pion excitation of ph. However, it is unlikely that the range of Λ is the same when dealing with D mesons. There are indications that the form factor to account for off shell D mesons requires a value of Λ substantially larger [123]. We shall come back to this point at the end of the Section 10.5, reevaluating results with the heavy meson form factor and analyzing the uncertainties.

With regard to the p-wave D^+ selfenergy, it turns out to be the same as for D^0 in symmetric nuclear matter $\rho_n = \rho_p$.

For the $\bar{D}$ meson, we note that the p-wave $\bar{D}$ selfenergy would correspond to the diagrams in Fig. 10.3, which involve the difference between the sum of $\bar{D}$ and Y masses, and the nucleon mass. The contribution of those diagrams is negligible due to the large mass of the $\bar{D}$ and Σ_c, Λ_c. The same holds for the p-wave $\bar{D}$ selfenergy coming from the $N^{-1}\Sigma_c^*(2520)$ excitation.

10.4 Two meson loop function in the medium

The medium modification are introduced in the two meson loop function. For a $D\bar{D}$ intermediate state, it can be written as

$$\widetilde{G}(P^0, \vec{P}, \rho) = i \int \frac{d^4q}{(2\pi)^4} D_D(q, \rho) D_{\bar{D}}(P - q, \rho) \ . \tag{10.15}$$

The modifications of the $D(\bar{D})$ propagator in the medium go through the selfenergy of the meson:

$$D_D(q^0, \vec{q}, \rho) = \frac{1}{(q^0)^2 - \vec{q}^{\,2} - m_D^2 - \Pi_D(q^0, \vec{q}, \rho)} \ . \tag{10.16}$$

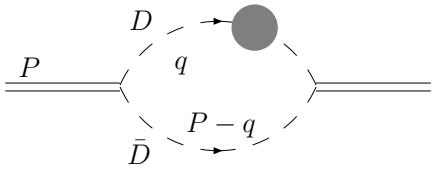

Figure 10.4: The $D\bar{D}$ loop function of the scalar meson. The shaded circle indicates the D selfenergy insertion.

An alternative way to write down propagators is to use the Lehmann representation

$$D_D(q^0, \vec{q}, \rho) = \int_0^\infty d\omega \left\{ \frac{S_D(\omega, \vec{q}, \rho)}{q^0 - \omega + i\eta} - \frac{S_{\bar{D}}(\omega, \vec{q}, \rho)}{q^0 + \omega - i\eta} \right\} , \qquad (10.17)$$

where the S_D and $S_{\bar{D}}$ stands for the spectral functions of D and $\bar{D}$ mesons respectively

$$S_{D(\bar{D})}(q^0, \vec{q}, \rho) = -\frac{1}{\pi} \frac{\mathrm{Im}\Pi_{D(\bar{D})}(q^0, \vec{q}, \rho)}{\left| (q^0)^2 - \vec{q}^{\,2} - m_D^2 - \Pi_{D(\bar{D})}(q^0, \vec{q}, \rho) \right|^2} . \qquad (10.18)$$

When evaluating the $D\bar{D}$ function loop in the medium we shall dress the D propagator and leave the $\bar{D}$ propagator free. The reason is that there is no absorption of $\bar{D}$ by nucleons, i.e. $\bar{D}N$ does not decay to baryonic resonances with c-quarks instead of $\bar{c}$ (and therefore $\mathrm{Im}\Pi_{\bar{D}} = 0$). Thus, the $\bar{D}$ selfenergy becomes very small compared to its mass and we neglect it leaving the propagator for $\bar{D}$ free. This is analogous to the K and $\bar{K}$ mesons, whereas the $\bar{K}$ can be absorved in the medium through reactions $\bar{K}N \to \pi\Lambda$, $\pi\Sigma$, the K^+ cannot. Thus, we evaluate the loop function of the diagram in Fig. 10.4, where the blob symbolizes the D selfenergy insertion. The $S_{\bar{D}}$ part in the propagator leads to a contribution of order $1/(P^0 + 2\omega_D)$ upon q^0 integration, which is very small and can be neglected. Therefore,

the $D\bar{D}$ loop function gets symplified, and we find

$$\begin{aligned}\widetilde{G}(P^0,\vec{P},\rho) &= i\int\frac{d^4q}{(2\pi)^4}\int_0^\infty d\omega\frac{S_D(\omega,\vec{q},\rho)}{q^0-\omega+i\eta}\,\frac{1}{(P^0-q^0)^2-\vec{q}^{\,2}-m_{\bar{D}}^2+i\eta}\\ &= \int\frac{d^3q}{(2\pi)^3}\int_0^\infty d\omega\frac{S_D(\omega,\vec{q},\rho)}{P^0-\omega-\omega_{\bar{D}}(\vec{q})+i\eta}\,\frac{1}{2\omega_{\bar{D}}(\vec{q})}\ , \quad (10.19)\end{aligned}$$

where $\omega_{\bar{D}}(\vec{q})=(\vec{q}^{\,2}+m_{\bar{D}}^2)^{1/2}$. The integral of Eq. (10.19) is evaluated with a three momentum cutoff of $q_{\rm max}=0.85, 0.9$ GeV for the X(3700) and $D_{s0}(2317)$ respectively, equivalent to the use of dimensional regularization of [108]. The discussion remains the same for the $D_{s0}(2317)$ but changing $\bar{D}$ by K.

The full selfenergy of the D-meson comes from the coherent sum of the s-wave and p-wave selfenergies.

10.5 Results

The s-wave and p-wave selfenergies of the D-meson are shown in Figs. 10.5 and 10.6. In Fig. 10.5 the structures around 1.7 GeV and 2 GeV correspond to the excitation of the $h\Lambda_c(2593)$ and $h\Sigma_c(2800)$, where $\Lambda_c(2593)$ and $\Sigma_c(2800)$ are the $1/2^-$ dynamically generated resonances of the theory. In Fig. 10.6, the structures seen in the p-wave selfenergy with peaks for the imaginary part and oscillations in the real one around 1.4 to 1.8 GeV correspond to the excitations of the $h\Lambda_c$, $h\Sigma_c$ and $h\Sigma_c^*$.

As we can observe in the Figs. 10.5 and 10.6, the p-wave selfenergy is more than one order of magnitude smaller than the s-wave selfenergy. This is in contrast to the π and K mesons. In the case of pions, the p-wave component was clearly dominant whereas for kaons it was larger, however, the relative importance compared to the s-wave was smaller. The reason is that the s-wave selfenergy goes roughly as the meson mass while the p-wave scales differently, more like the baryon mass. In Figs. 10.7 and 10.8 we show the real and imaginary parts of the two meson function loop in the medium for the X(3700) and

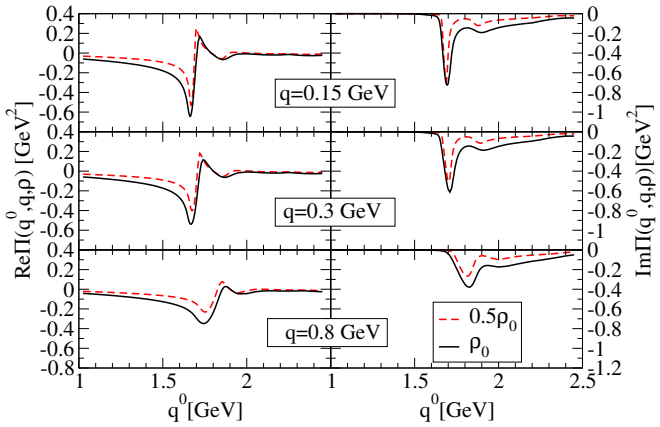

Figure 10.5: Real (left column) and Imaginary (right column) part of the s-wave D selfenergy for D three-momenta $q = 0.15, 0.3$ and 0.8 GeV as a function of the D energy q^0 at densities $\rho = 0.5\rho_0$ and $\rho = \rho_0$, with $\rho_0 = 0.17\text{fm}^{-3}$ the normal nuclear matter density.

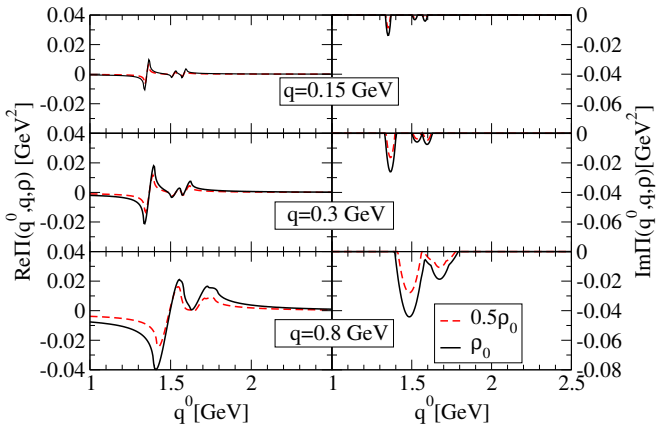

Figure 10.6: Real (left column) and Imaginary (right column) part of the p-wave D selfenergy for D three-momenta $q = 0.15, 0.3$ and 0.8 GeV as a function of the D energy q^0 at densities $\rho = 0.5\rho_0$ and $\rho = \rho_0$, with $\rho_0 = 0.17\text{fm}^{-3}$ the normal nuclear matter density.

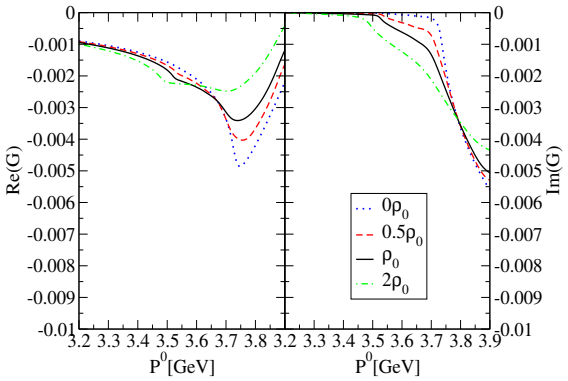

Figure 10.7: Loop function in the medium: $\mathrm{Re}\,\widetilde{G}(P^0,\vec{P},\rho)$ (left) and $\mathrm{Im}\,\widetilde{G}(P^0,\vec{P},\rho)$ (right) for $D\bar{D}$, the channel with the largest coupling to the X(3700) meson. $\widetilde{G}(P^0,\vec{P},\rho)$ is given from Eq. (10.15).

$D_{s0}(2317)$ respectively. We see that the real and imaginary parts of G gets modified considerably with density. Due to the opening of new channels, the imaginary part collects strength below the $D\bar{D}$ and DK thresholds. Thus, in the case of the DK loop, the D is renormalized and accounts for $DN \to \pi\Lambda_c$, $\pi\sigma_c$ or $DN \to \Lambda_c$, Σ_c, and the DK loop accounts for intermediate channels $h\pi\Lambda_c K$, $h\pi\Sigma_c K$ or $h\Lambda_c K$, $h\Sigma_c K$ (and similarly for the $D\bar{D}$ loop but with $\bar{D}$ instead of K). In Figs. 10.9 and 10.10 we show $|T|^2$ for the main channels, D^0K^+ and $D^0\bar{D}^0$ of the $D_{s0}(2317)$ and X(3700) resonances for different densities. We observe practically no change in the pole position and large changes in the widths of 100 MeV and 250 MeV at $\rho = \rho_0$ for the $D_{s0}(2317)$ and X(3700) respectively, which are spectacular. Note that these resonances have practically no width in the free space ($\Gamma_{\rho=0} = 0$ for the $D_{s0}(2317)$ and $\Gamma_{\rho=0} = 60$ MeV for the X(3700)). The source of these widths in the medium are the opening of new channels, $DN \to \Lambda_c$, Σ_c (p-wave selfenergy) and $DN \to \pi\Lambda_c$, $\pi\Sigma_c$ (s-wave selfenergy) and also the evaluation of the D selfenergy selfconsistently generates two-nucleon-induced D absorption channels like $DNN \to N\Lambda_c$, $\pi N\Lambda_c$, $\pi N\Sigma_c$, etc. These reactions make the D to get absorved inside the

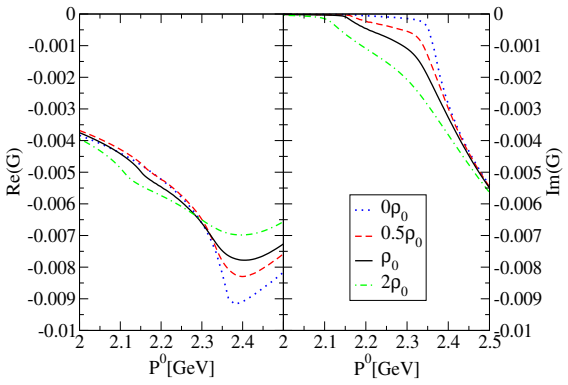

Figure 10.8: Loop function in the medium: $\mathrm{Re}\,\widetilde{G}(P^0,\vec{P},\rho)$ (left) and $\mathrm{Im}\,\widetilde{G}(P^0,\vec{P},\rho)$ (right) for DK, the channel with the largest coupling to the $D_{s0}(2317)$ meson. $\widetilde{G}(P^0,\vec{P},\rho)$ is given from Eq. (10.15).

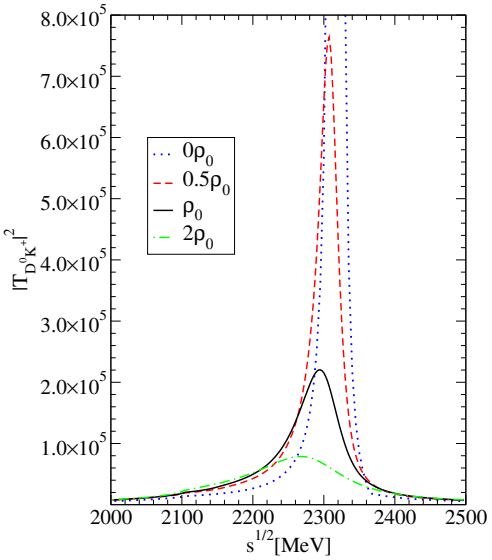

Figure 10.9: $D_{s0}(2317)$ resonance: $|T|^2$ for the $D^0K^+ \to D^0K^+$ amplitude for different densities.

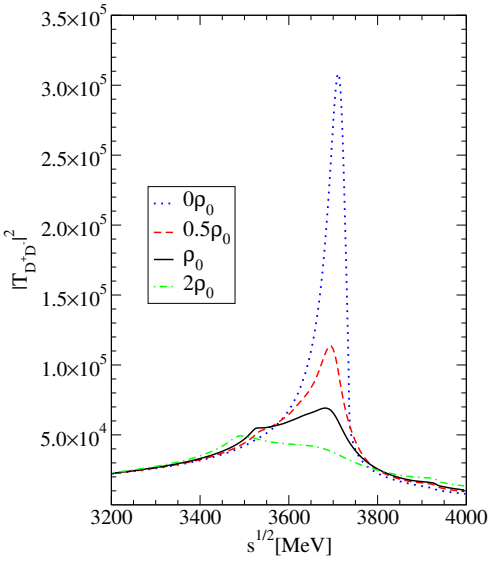

Figure 10.10: $X(3700)$ resonance: $|T|^2$ for the $D^0\bar{D}^0 \to D^0\bar{D}^0$ amplitude for different densities.

nuclear medium through DN or DNN elastic reactions. These mechanisms are implicit in the absorption of the resonances. For example, the new decay channel of the X(3700), X(3700)$N \to \bar{D}\pi\Lambda_c$, $\bar{D}\pi\Sigma_c$ has 400 MeV phase space available. This makes that the width of the X(3700) increases sizeable. This trend of the changes of $|T|^2$ with ρ is observed in resonance properties with temperature and/or density [52, 184, 185]. In addition, the study of such decay channels in the medium offers information on the couplings of the $D_{s0}(2317)$ to its main building block, DK, according with the assumption of dynamically generated resonance. For instance, the cut in the diagram of Fig. 10.11 shows the decay $D_{s0}(2317)N \to K\pi\Lambda_c$, $K\pi\Sigma_c$, whose observation would provide information on the $D_{s0}(2317) \to DK$ coupling and $DN \to \pi\Lambda_c(\Sigma_c)$ cross-section. This study is useful to investigate the nature of the resonances. In [186] the authors suggests a $q\bar{q}$ structure for the $D_{s0}(2317)$ and in [187, 188] a mixture of DK with $q\bar{q}$ is suggested. If the $D_{s0}(2317)$ was a $q\bar{q}$ state or have different na-

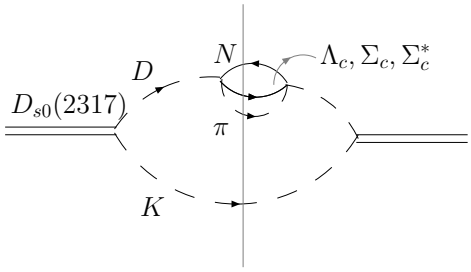

Figure 10.11: Decay channel of the $D_{s0}(2317)$ in the nucleus into $K\pi\Lambda_c$ or $K\pi\Sigma_c$.

ture from mostly DK, such large coupling would not appear and the width in the medium would be much smaller than the one predicted here. We also compute the uncertainties. We take a Monte Carlo sampling of the parameters $f_\pi \in [85, 115]$ and $f_D \in [146, 218]$ MeV and evaluate the mass and width at different densities from the $|T|^2$ plots. While the mass shift is of the same order of magnitude than the uncertainties and for this reason we do not extract any conclusion on the mass shift, the changes in the width are much larger than the uncertainties, what points a large increase of the width with density.

In addition, we analyze the uncertainties linked to the use of different form factors re-evaluating the result with a form factor for an off-shell D-meson [123]:

$$F_H(q^2) = \frac{\Lambda_D^2 - m_D^2}{\Lambda_D^2 - q^2} \quad \text{with } \Lambda_D = 3.5\,\text{GeV}. \tag{10.20}$$

and q^0 onshell:

$$q^0 = M_{D_{s0}} - \omega_K(q_{on}) \;, q_{on} = \frac{\lambda^{1/2}((M_{D_{s0}} + m_N)^2, M^2, m_K^2)}{2\,(M_{D_{s0}} + m_N)} \tag{10.21}$$

As we can see in Fig. 10.12 for the $D_{s0}(2317)$ there are small dif-

ρ	$\bar{M}$[MeV]	$\bar{\Gamma}$[MeV]
0.0	2316 ± 5	0
0.5	2306 ± 17	58 ± 10
1.0	2295 ± 23	115 ± 25
1.5	2283 ± 25	150 ± 25
2.0	2274 ± 31	190 ± 30

Table 10.6: Mass and width for the $D_{s0}(2317)$ at different densities with error bands due to the uncertainties of our model.

ρ	$\bar{M}$[MeV]	$\bar{\Gamma}$[MeV]
0.0	3710 ± 18	60 ± 10
0.5	3691 ± 10	135 ± 20
1.0	3638 ± 15	255 ± 25
1.5	3599 ± 15	320 ± 25
2.0	3565 ± 29	340 ± 25

Table 10.7: Mass and width for the $X(3700)$ at different densities with error bands due to the uncertainties of our model.

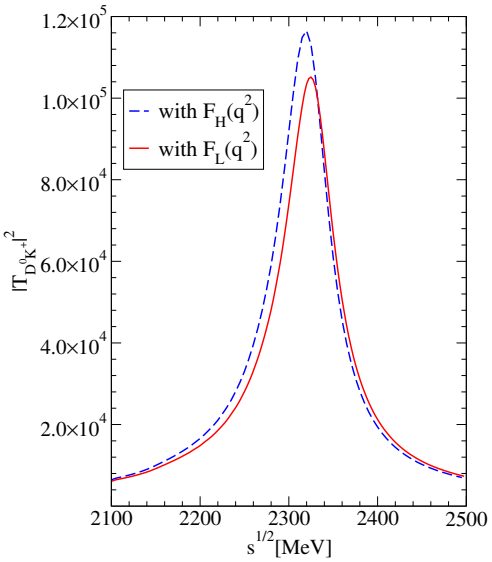

Figure 10.12: Comparison of $|T|^2$ in the case of the $D_{s0}(2317)$ resonance for the two different form factors at $\rho = \rho_0$: type 1 (dashed line) with $F_H(q^2)$ of Eq. (10.20) and type 2 (solid line) with $F_L(q^2)$ of Eq. (10.14).

ferences in the position of the peak and no differences in the width. In view of possible future experiments we recall the method that has proved to be the most efficient one: One should look at the production rate as function of the mass number normalized to a particular nucleus. This magnitude, the transparency ratio, measures the survival probability and is very sensitive to the absorption rate of the resonance inside the nucleus, i.e. the in-medium resonance width. See [158, 189] for ϕ and ω production. The results in this section are of relevance to studies planned for the FAIR facility.

Chapter 11

$\bar{K}^*$ mesons in dense matter

The interaction of vector mesons with nuclear matter is tied to fundamental aspects of QCD. Although there is much work done on the properties of the ρ, ω and ϕ mesons, the bibliography on the properties of strange vector mesons in nuclear matter is little or almost absent. Experimentally, the situation is rather similar. The local hidden gauge formalism allows to us study the interaction of vector mesons with nucleons. Thus, in this chapter we study the properties of strange-vector mesons with nuclear matter. The selfenergy will have two components, the in-medium $\bar{K}^*$ interaction with nucleons that accounts for Pauli-blocking and is incorporated in a selfconsistent way. In addition, the $\bar{K}\pi$ decay channel is taken into account in matter. Both components of the selfenergy, $\bar{K}^*N$ interaction and $\bar{K}\pi$ decay in matter are included in the spectral function. One way to look at the properties of mesons in nuclear matter is the transparency ratio, which is a function of the survival probability. Because of that, the transparency ratio [191] for the reaction $\gamma A \to K^+ K^{*-} A'$ is also evaluated.

11.1 Introduction

The former results on the issue are based on the Nambu Jona Lasinio model. This model predicts no shift of the masses of vector mesons in contrast with the production mass of the sigma meson in nuclear matter. Although, using qualitative arguments, G. E. Brown and M. Rho gave an attractive shift of the vector masses [192], more detailed calculations show no shift of the mass of the ρ meson in matter [193, 194, 195, 196, 197] and very small shift for the ϕ meson [198]. Experimentally, the NA60 and CLASS Collaborations have found a null mass shift of the ρ meson in the dilepton spectra. Also, some widening of the resonance is deduced from the experiments. On the opposite side, the KEK team had earlier announced an attractive mass shift of the ρ [199, 200]. The reason for different conclusions might depend on the way the background is subtracted [201].

The case of the ω seems to be more complicated. There is much work done claiming very different mass shifts from attractive to repulsive [157, 202, 203, 204, 205, 206]. Although the CBELSA, TAPS Collaboration claims a large shift mass of the ω from the photon - induced ω production in nuclei, with the ω detected through the $\pi^0\gamma$ decay channel [207]. In [157] the authors show that this shift is a consequence of the particular background subtraction. Recent analysis on the background of that reaction have concluded that the ω shift mass can not be determined from this reaction [208]. The width however, is increased largely as seen from the work of [157] and [158].

Nevertheless, the fact that the $\bar{K}^*$ cannot be detected throughout dileptons might be the reason for non experimental evidence on the $\bar{K}^*$ properties in the medium. On the theoretical side, the interaction of $\bar{K}^*$ with nucleons has been tackled in [209], assuming that the interaction between light quarks is spin and SU(3) flavour independent, and in [210, 211], where the interaction of the vector mesons with baryons from the octect and decuplet is obtained starting from the local hidden lagrangians. It will be shown that the $\bar{K}^*N$ interaction is very similar to the $\bar{K}N$ interaction while to evaluate the $\bar{K}^*$

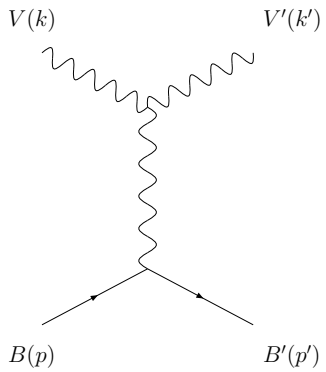

Figure 11.1: Feynmann diagram for the vector-baryon interaction.

selfenergy one has to consider the $\bar{K}\pi$ decay mode in nuclear matter. In addition, an experimental study on this issue is motivated through the evaluation of the transparency ratio of the $\gamma A \to K^+ \bar{K}^{*-} A'$ reaction. For a full revision on this issue see also [190].

11.2 The $\bar{K}^*$ interaction in the free space

Assuming vector meson dominance, the vector-baryon interaction is obtained through the Feynmann diagrams plotted in Fig. 11.1. The upper vertex is given by the local hidden lagrangians for the interaction between vector mesons, Eq. (3.5). Whereas the coupling of vectors with baryons is given by the lowest order quiral Lagrangian,

$$\mathcal{L}_{BBV} = g \left(\langle \bar{B} \gamma_\mu [V^\mu, B] \rangle + \langle \bar{B} \gamma_\mu B \rangle \langle V^\mu \rangle \right), \tag{11.1}$$

where B is now the SU(3) matrix of the baryon octet

$$B = \begin{pmatrix} \frac{1}{\sqrt{2}}\Sigma^0 + \frac{1}{\sqrt{6}}\Lambda & \Sigma^+ & p \\ \Sigma^- & -\frac{1}{\sqrt{2}}\Sigma^0 + \frac{1}{\sqrt{6}}\Lambda & n \\ \Xi^- & \Xi^0 & -\frac{2}{\sqrt{6}}\Lambda \end{pmatrix} . \tag{11.2}$$

We focus on the strangeness $S = -1$ vector meson - baryon sector with $I = 0$ and $I = 1$. For $S = -1$ and $I = 0$, we find five vector meson - baryon channels: $\bar{K}^*N$, $\omega\Lambda$, $\rho\Sigma$, $\phi\Lambda$ and $K^*\Xi$, whereas in the $S = -1$, $I = 1$ sector we have the following six channels: $\bar{K}^*N$, $\rho\Lambda$, $\rho\Sigma$, $\omega\Sigma$, $K^*\Xi$ and $\phi\Sigma$.

In the low energy approximation, the transition potential is given by

$$V_{ij} = -C_{ij}\,\frac{1}{4f^2}\,\left(k^0 + k'^0\right)\;\vec{\epsilon}\vec{\epsilon}', \tag{11.3}$$

where k^0 and k'^0 are the energies of the incoming and outgoing vector mesons. These amplitudes have the same structure than the pseudoscalar-baryon amplitudes except for the $\vec{\epsilon}\cdot\vec{\epsilon}'$ factor. The meson-baryon scattering amplitude is obtained from the coupled channel on-shell Bethe-Salpeter equation, but now G is the loop function of a vector meson of mass m and a baryon of mass M with total four-momentum P ($s = P^2$):

$$G(s, m^2, M^2) = \mathrm{i}2M \int \frac{d^4q}{(2\pi)^4}\,\frac{1}{(P-q)^2 - M^2 + \mathrm{i}\epsilon}\,\frac{1}{q^2 - m^2 + \mathrm{i}\epsilon}\;. \tag{11.4}$$

Eq. (11.4) is modified as in Eq. (3.24) to take into account the decay width of the ρ and $\bar{K}^*$ mesons by the convolution of the mass distributions of these mesons. The function loop G is regularized taking a natural value of -2 for the subtraction constant with $\mu = 630$ [43, 211]. When we sum over the polarization of internal vector mesons, the factor $\vec{\epsilon}\cdot\vec{\epsilon}'$ leads to a correction in the G function of $\vec{q}^{\,2}/3M_V^2$ that is neglected in the approximation of low momenta compared to the mass of the vector meson. This leads to a factorization of $\vec{\epsilon}\cdot\vec{\epsilon}'$ in the T-matrix. The method provides pairs of resonances degenerated in mass for $J^P = 1/2^-$, $3/2^-$. Close to the energy region of the $\bar{K}^*N$ threshold, there is one $\Lambda(1783)$ with $I = 0$ and one $\Sigma(1830)$ for $I = 1$. In the PDG we find a $\Lambda(1800)$ with $J^P = 1/2^-$, however, there is no spin partner observed, unless it was the $\Lambda(1690)$, which would imply a large breaking of the spin degeneracy inherent to the hidden gauge

model. For $I = 1$, the $\Sigma(1830)$ found is associated with the $\Sigma(1750)$ in the PDG [211]. However, we notice that the widths of the theoretical states are smaller than the experimental ones. This is due to the fact that the pseudoscalar-baryon decay mode is not included and the source of width of the states comes from the convolution of the loop function with the mass distributions of the ρ and $\vec{K}^*$ mesons. Surely, the inclusion of the pseudoscalar -baryon decay mechanism will make the widths larger and thus, closer to the experimental ones [212].

We point that this pattern of degenerate resonances with $J^P = 1/2^-$, $3/2^-$ is present in many experimental data in the PDG like: the $N^*(1650)(1/2^-)$ and $N^*(1700)(3/2^-)$; the $N^*(2080)(3/2^-)$ and $N^*(2090)(1/2^-)$; $\Sigma(1940)(3/2^-)$ and $\Sigma(2000)(1/2^-)$; $\Delta(1900)(1/2^-)$, $\Delta(1940)(3/2^-)$ and $\Delta(1930)(5/2^-)$.

11.3 The $\bar{K}$ self-energy in nuclear matter

We calculate separately the two contributions to the $\bar{K}^*$ selfenergy: The $\bar{K}\pi$ decay mode modified in the medium and the interaction of $\bar{K}^*$ with nucleons take place in the medium, which accounts for the quasielastic process $\vec{K}^*N \to \vec{K}^*N$ and the absorption channels $\vec{K}^*N \to \rho Y$, ωY, ϕY with $Y = \Lambda$, Σ. The last contribution is calculated selfconsistently and taking into account also the previously calculated part of the $\vec{K}^*$ selfenergy coming from the $\vec{K}\pi$ decay mode in the intermediate channels.

11.3.1 $\bar{K}^*$ selfenergy from the decay into $\bar{K}\pi$

In Fig. 11.2 we show the loops diagrams for the $\bar{K}\pi$ decay mode in the free space and renormalized in the nuclear medium. The VPP vertex can be calculated through the Lagrangian $\mathcal{L}_{VPP} = -ig\langle V^\mu[\phi, \partial_\mu\phi]\rangle$.

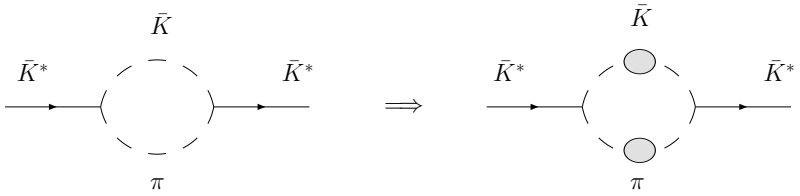

Figure 11.2: The $\bar{K}$ propagator renormalized to allow its decay into $\bar{K}\pi$, in the free space (left), and in the medium (right), including the self-energies of the $\bar{K}$ and π mesons.

In the free space, for the first diagram in Fig. (11.2) we have

$$\Pi^0_{\bar{K}^*}(q^0,\vec{q}) = 2g^2\vec{\epsilon}\cdot\vec{\epsilon}\,' \int \frac{d^4k}{(2\pi)^4}\frac{\vec{k}^{\,2}}{k^2-m_\pi^2}\frac{1}{(q-k)^2-m^2_{\bar{K}}+i\epsilon}\ , \quad (11.5)$$

The approximation of low momenta leads to the subtitution of the $\epsilon_\mu k^\mu \epsilon'_\nu k^\nu$ factor by $\epsilon_i k_i \epsilon'_j k_j$ that can be replaced in the integral by $\vec{\epsilon}\cdot\vec{\epsilon}\frac{1}{3}\vec{k}^{\,2}\delta_{ij}$. The imaginary part of the free $\bar{K}^*$ selfenergy at rest is

$$\mathrm{Im}\Pi^0_{\bar{K}^*}(q^0=m_{\bar{K}^*},\vec{q}=0) = \frac{g^2}{4\pi}\vec{\epsilon}\cdot\vec{\epsilon}\,' \mid \vec{k}\mid^3 \frac{1}{m_{\bar{K}^*}}\ , \quad (11.6)$$

which determines the value of the K^{*-} width

$$\Gamma_{K^{*-}} = -\mathrm{Im}\Gamma^0_{K^{*-}}/m_{K^{*-}} = 4\,2\,\mathrm{MeV} \quad (11.7)$$

Certainly, this is close to the experimental value $\Gamma^{\mathrm{exp}}_{K^{*-}} = 50.8 \pm 0.9\,\mathrm{MeV}$. In order to calculate the selfenergy of the $\bar{K}^*$ meson due to its decay into $\bar{K}\pi$, we need to include the selfenergies of the $\bar{K}$ and π in the loop of Fig. (11.2).

The selfenergy in symmetric nuclear matter incorporates s and p waves. For the s wave part, the interaction of the $\bar{K}$ meson with nucleons accounts for the following channels $\bar{K}N$, $\pi\Sigma$, $\eta\Lambda$, $K\Xi$ and $\bar{K}N$ for $I=0$ and $\pi\Lambda$, $\pi\Sigma$, $\eta\Sigma$ and $K\Xi$ for $I=1$. The amplitudes are

built from the Weinberg-Tomozawa term of the lowest order chiral Lagrangian and projected into s-wave. The evaluation of the amplitudes through the Bethe-Salpeter equation ensures unitarity. In the medium, the meson-baryon loop function is modified to incorporate Pauli-blocking corrections, mean-field bindings on the nucleons and hyperons via a $\sigma - \omega$ model and it is regularized with a cutoff momentum of $q_{\rm max} = 630$ MeV. Finally, selfconsistency is required for the computation of the amplitudes.

On the other hand, the p-wave contribution of the $\bar{K}$ selfenergy is evaluated accounting ΛN^{-1}, ΣN^{-1} and $\Sigma^* N^{-1}$ excitations.

In conclusion, the K^- feels a moderate attraction, the potential is $U_{K^-} = {\rm Re}\Pi_{K^-}/2m_{K^-} \sim -66$ MeV that agrees with other calculations that implement selfconsistency too [213, 214, 215, 222] (while in other models the attraction is rather larger).

In the medium the pion selfenergy is dominated by a p-wave component that takes into account ph, ΔN^{-1} and $2p2h$ excitations. The s-wave part, $\Pi_\pi^{(s)}(\rho)$ is small and momentum independent. The interaction is modified incorporating spin - isospin NN and $N\Delta$ short range correlations that are included in a phenomenological way with a single Landau-Migdal parameter g' [216].

Therefore, one has to replace the propagator of the $\bar{K}$ and π in Eq. (11.5) to include their respective selfenergies. This is done through the Lehman representation of the propagators:

$$\begin{aligned} -i\Pi_{\bar{K}^*}^{\rho,({\rm a})}(q^0,\vec{q}) &= 2g^2 \vec{\epsilon}\cdot\vec{\epsilon}\,' \int \frac{d^4k}{(2\pi)^4}\vec{k}^{\,2} \int_0^\infty \frac{d\omega}{\pi}(-2\omega)\frac{{\rm Im}D_\pi(\omega,\vec{k}\,)}{(k^0)^2-\omega^2+i\epsilon} \\ &\times \int_0^\infty \frac{d\omega'}{\pi}\left\{\frac{{\rm Im}D_K(\omega',\vec{q}-\vec{k}\,)}{q^0-k^0+\omega'-i\eta} - \frac{{\rm Im}D_{\bar{K}}(\omega',\vec{q}-\vec{k}\,)}{q^0-k^0-\omega'+i\eta}\right\} \end{aligned} \tag{11.8}$$

Since we are using the physical mass of the $\vec{K}^*$, the real part of the in-medium $\bar{K}^*$ selfenergy must vanish at $\rho = 0$. This can be done by subtracting the real part of the free $\bar{K}^*$ selfenergy, $\Pi^0_{\bar{K}^*}$ from $\Pi^{\rho(a)}_{\bar{K}^*}$. The part of negative energy of the $\bar{K}$ propagator, the last term in Eq.

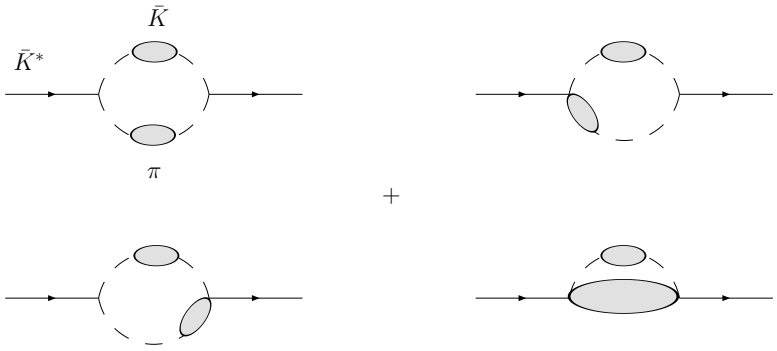

Figure 11.3: Self-energy diagrams at first order in the nuclear density contributing to the decay of the $\bar{K}^*$ meson in the medium.

(11.8), is small and does not contribute to the imaginary part of the $\bar{K}^*$ selfenergy. In a good approximation, this term cancels with the corresponding term of the free $\bar{K}$ selfenergy. After integrating over the k^0 variable, we get

$$\begin{aligned}\Pi^{\rho,(\mathrm{a})}_{\bar{K}^*}(q^0,\vec{q}) &= 2g^2\vec{\epsilon}\cdot\vec{\epsilon}\,'\left\{\int\frac{d^3k}{(2\pi)^3}\frac{\vec{k}^{\,2}}{\pi^2}\int_0^\infty d\omega\,\mathrm{Im}D_\pi(\omega,\vec{k}\,)\int_0^\infty d\omega'\right.\\ &\times\frac{\mathrm{Im}D_{\bar{K}}(\omega',\vec{q}-\vec{k}\,)}{q^0-\omega-\omega'+i\eta}-\mathrm{Re}\int\frac{d^3k}{(2\pi)^3}\frac{\vec{k}^{\,2}}{2\omega_\pi(k)}\frac{1}{2\omega_{\bar{K}}(q-k)}\\ &\left.\times\frac{1}{q^0-\omega_\pi(k)-\omega_{\bar{K}}(q-k)+i\epsilon}\right\}\,.\end{aligned}\tag{11.9}$$

Finally, the gauge invariance of the model is fullfilled by implementing the vertex corrections [217, 218], that are included only for the pions since the effect of dressing the pion is considerably larger than that of including the $\bar{K}$ selfenergy. The consideration of the vertex corrections for the pion implies the calculation of all the diagrams in Fig. 11.3. To do it, simply one replaces the p-wave pion

selfenergy with:

$$\Pi_\pi^{(p)} \Longrightarrow \frac{\Pi_\pi^{(p)}}{\vec{k}^{\,2}} \left(\vec{k}^{\,2} + \left[D_\pi^0(k) \right]^{-1} + \frac{3}{4} \frac{\left[D_\pi^0(k) \right]^{-2}}{\vec{k}^{\,2}} \right) \ , \qquad (11.10)$$

with $[D_\pi^0(k)]^{-1} = (k^0)^2 - \vec{k}^{\,2} - m_\pi^2$ [219].

11.3.2 The $\bar{K}^*$ selfenergy from the s-wave $\bar{K}^*N$ interaction

The $\bar{K}^*N$ interaction in the free space includes all the possible meson - baryon channels ($\bar{K}^*N$, $\omega\Lambda$, $\rho\Sigma$, $\phi\Lambda$, $K^*\Xi$ for $I = 0$ and $\bar{K}^*N$, $\rho\Lambda$, $\rho\Sigma$, $\omega\Sigma$, $K^*\Xi$ and $\phi\Sigma$ for $I = 1$) as explained in Section 11.2. In the medium the meson-baryon function loop is modified to consider Pauli-blocking which prevents the nucleons from being scattered into occupied states. We will modify only the $\bar{K}^*N$ channel and leave the loops free for the other meson-baryon channels since they couple more moderately to the $\bar{K}^*N$ channel. In nuclear matter, the meson-baryon loop function reads

$$\begin{aligned} G^\rho(P) &= G^0(\sqrt{s}) + \lim_{\Lambda\to\infty} \delta G_\Lambda^\rho(P), & (11.11) \\ \delta G_\Lambda^\rho(P) &\equiv G_\Lambda^\rho(P) - G_\Lambda^0(\sqrt{s}) \\ &= \ \mathrm{i}2M \int_\Lambda \frac{d^4q}{(2\pi)^4} \left(D_{\mathcal{B}}^\rho(P-q)\ D_{\mathcal{M}}^\rho(q) - D_{\mathcal{B}}^0(P-q)\ D_{\mathcal{M}}^0(q) \right), & (11.12) \end{aligned}$$

Formally, we proceed as in [220]. The meson-baryon loop in the free space, G^0, is calculated by means of dimensional regularization and the correction in the medium, $\delta G^\rho = \lim_{\Lambda\to\infty} \delta G_\Lambda^\rho(p)$ is calculated through a cutoff which will be numerically very big and thus this quantity will be UV finite and independent of the suptraction point used to regularize G^0.

The corresponding in-medium single-particle propagators are given by

$$\begin{aligned} D_N^\rho(p) &= \frac{1}{2E_N(\vec{p})}\left\{\sum_r u_r(\vec{p})\bar{u}_r(\vec{p})\left(\frac{1-n(\vec{p})}{p^0-E_N(\vec{p})+i\varepsilon}\right.\right. \\ &\left.\left.+\frac{n(\vec{p})}{p^0-E_N(\vec{p})-i\varepsilon}\right)\right\}+\frac{\sum_r v_r(-\vec{p})\bar{v}_r(-\vec{p})}{p^0+E_N(\vec{p})-i\varepsilon} \\ &= D_N^0(p)+2\pi i n(\vec{p})\frac{\delta\left(p^0-E_N(\vec{p})\right)}{2E_N(\vec{p})}\sum_r u_r(\vec{p})\bar{u}_r(\vec{p})\ , \end{aligned} \tag{11.13}$$

$$\begin{aligned} D_{\bar{K}^*}^\rho(q) &= \left((q^0)^2-\omega(\vec{q})^2-\Pi_{\bar{K}^*}(q)\right)^{-1} \\ &= \int_0^\infty d\omega\left(\frac{S_{\bar{K}^*}(\omega,\vec{q})}{q^0-\omega+i\varepsilon}-\frac{S_{K^*}(\omega,\vec{q})}{q^0+\omega-i\varepsilon}\right), \end{aligned} \tag{11.14}$$

where $n(\vec{p})$ in the Fermi gas nucleum momentum distribution, given by the step function $n(\vec{p})=\Theta(p_F-|\vec{p}|)$ with $p_F=(3\pi^2\rho/2)^{1/3}$. After integrating the integral over q^0, the $\bar{K}^*N$ loop function reads

$$\begin{aligned} G^\rho{}_{\bar{K}^*N}(P) &= G^0_{\bar{K}^*N}(\sqrt{s})+ \\ &+\int\frac{d^3q}{(2\pi)^3}\frac{M_N}{E_N(\vec{p})}\left[\frac{-n(\vec{p})}{(P^0-E_N(\vec{p}))^2-\omega(\vec{q})^2+i\varepsilon}\right. \\ &+(1-n(\vec{p}))\left(\frac{-1/(2\omega(\vec{q}))}{P^0-E_N(\vec{p})-\omega(\vec{q})+i\varepsilon}\right. \\ &\left.\left.+\int_0^\infty d\omega\,\frac{S_{\bar{K}^*}(\omega,\vec{q})}{P^0-E_N(\vec{p})-\omega+i\varepsilon}\right)\right]\Bigg|_{\vec{p}=\vec{P}-\vec{q}} \end{aligned} \tag{11.15}$$

The first term of the integral, which is proportional to $n(\vec{p})$, is the Pauli correction and accounts for the case where the Pauli blocking on the nucleon is considered and the meson in-medium selfenergy is neglected. The second term, which is proportional to $(1-n(\vec{p}))$, is exactly zero if the meson spectral function $S_{\bar{K}^*}$ is the free one, $S^0_{\bar{K}^*}(\omega,\vec{q})=\delta[\omega-\omega(\vec{q})]/2\omega$. Hence, this term gives the contribution of the in-medium meson modification to the loop function. Then, the

Bethe-Salpeter equation is solved in nuclear matter for the in-medium amplitudes in the isospin basis and the in-medium $\bar{K}^*$ selfenergy is obtained integrating $T^{\rho}_{\bar{K}^*N}$ over the nucleon Fermi sea.

$$\Pi^{\rho,(\mathrm{b})}_{\bar{K}^*}(q^0,\vec{q}) = \int \frac{d^3p}{(2\pi)^3}\, n(\vec{p}) \left[T^{\rho\,(I=0)}_{\bar{K}^*N}(P^0,\vec{P}) + 3T^{\rho\,(I=1)}_{\bar{K}^*N}(P^0,\vec{P}) \right] , \tag{11.16}$$

where $P^0 = q^0 + E_N(\vec{p})$ and $\vec{P} = \vec{q} + \vec{p}$ are the total energy and momentum of the $\bar{K}^*N$ pair in the nuclear matter rest frame, and the values $(q^0,\vec{q})$ stand for the energy and momentum of the $\bar{K}^*$ meson also in this frame. The $\bar{K}^*$ selfenergy will be the sum of the two parts (a) and (b), $\Pi^{\rho}_{\bar{K}^*} = \Pi^{\rho(a)}_{\bar{K}^*} + \Pi^{\rho(b)}_{\bar{K}^*}$, where the $\Pi^{\rho(b)}_{\bar{K}^*}$ selfenergy is determined selfconsistently.

11.4 Results

The $\bar{K}^*$ selfenergy coming from its decay into $\bar{K}\pi$ at $\vec{q}=0$ is shown in Fig. 11.4. The dotted line means the $\bar{K}^*$ selfenergy in the free space, then, adding the π selfenergy (dot-dashed line) and including both, the π and $\bar{K}$ selfenergies (dashed line) at normal nuclear matter density. We observe that the $\bar{K}$ width becomes about three times larger at $\rho = \rho_0$ than in vacuum, and the inclusion of the $\bar{K}$ selfenergy modifies only a bit the $\bar{K}^*$ selfenergy. The reason lies in the fact that the $\bar{K}^* \to K\pi$ decay process leaves the pion right in the energy region of ΔN^{-1} excitations having a quite large pionic strength. The vertex corrections moderate the effect of dressing the pion, leading to a final $\bar{K}^*$ width of $\Pi_{\bar{K}^*}(\rho = \rho_0) = 105$ MeV, which is like twice the value of the width in vacuum. The $\bar{K}^*N$ in-medium amplitude is displayed in Fig. 11.5, the dashed line shows the $\bar{K}^*N \to \bar{K}^*N$ amplitude in the free space and the solid line accounts for the in-medium $\bar{K}^*N \to \bar{K}^*N$ amplitude as solution of the Bethe Salpeter equation including Pauli blocking effects on the nucleons and the $\bar{K}^*$ selfenergy in a selfconsistent manner. We can see

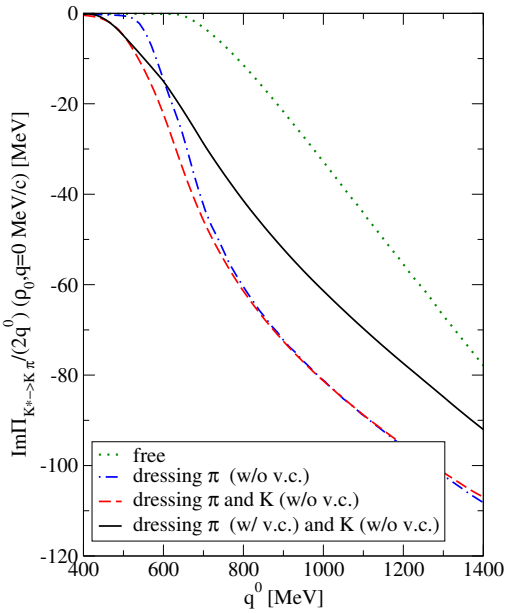

Figure 11.4: Imaginary part of the $\bar{K}^*$ self-energy at zero momentum, coming from the $\bar{K}\pi$ decay mode in dense matter at normal saturation density ρ_0. Different approaches are studied: (i) calculation in free space, (ii) including the π self-energy, (iii) including the π and $\bar{K}$ self-energies, and (iv) including the π dressing with vertex corrections and the $\bar{K}$ self-energy.

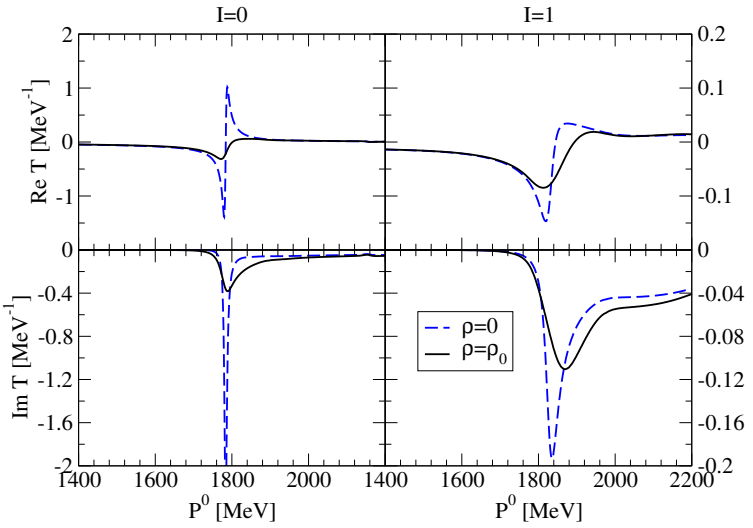

Figure 11.5: Real and imaginary parts of the $\bar{K}^*N \to \bar{K}^*N$ amplitude as function of the center-of-mass energy P_0 for a fixed total momentum $|\vec{P}| = 0$. Two new states are generated dynamically: $(I = 0)$ $\Lambda(1783)$ and $(I = 1)$ $\Sigma(1830)$.

that two resonances couple strongly to $\bar{K}^*N$, the $I = 0$ $\Lambda(1783)$ and the $I = 1$ $\Sigma(1830)$ which are clearly visible. However, we remark that their respective widths are smaller than the experimental ones, and the inclusion of pseudoscalar-baryon decays would make the widths closer to the experimental ones. The in-medium amplitudes are affected for two phenomena, on the one hand, we have Pauli blocking on the nucleons that cuts the phase space in the unitarized amplitude and pushes the resonances to higher energies. On the other hand, the attractive $\bar{K}^*$ selfenergy included in the $\bar{K}^*N$ intermediate states moves the resonance back to lower energies. As a result, the resonances stay close to their positions in the free space. This behaviour was already seen in the case of the $\Lambda(1405)$ for the pseudoscalar - baryon sector [213, 221, 222, 223, 224]. Note that, now the width of the resonances in matter are larger due to the opening of new decay channels. Besides that, new $\bar{K}^*$ absorption mechanisms appear, such as $\bar{K}^*N \to \pi\bar{K}N$ or $\bar{K}^*NN \to \bar{K}NN$ owing to the incorporation of the $\bar{K}^* \to \bar{K}\pi$ decay mechanism in the intermediate $\bar{K}^*N$ state. In Fig. 11.6, the $\bar{K}^*$ selfenergy and its different contributions, $(\bar{K}^* \to \bar{K}\pi)$ and $\bar{K}^*N$ in a selfconsistent calculation, are shown as a function of q^0 at $\vec{q} = 0$ are shown. We can see that the effect of the $\bar{K}^*N$ effective interaction dominates around $800 - 900$ MeV, where the $\Lambda(1783)N^{-1}$ and $\Sigma(1830)N^{-1}$ excitations are visible in the $\bar{K}^*$ selfenergy. Nevertheless, outside this region, at lower energies, where the $\bar{K}^*N \to VB$ channels are closed or as the energy increases, the $\bar{K}\pi$ decay mechanism becomes more important. At the end, both effects lead to a moderate attraction of the $\bar{K}^*$ in the medium, and the width of the $\bar{K}^*$ becomes as larger as 260 MeV at normal nuclear density, which means five times the width in the vacuum. The dependence of the full $\bar{K}^*$ selfenergy with density and momenta is shown in Fig. 11.7. As the momenta increases, the resonant-hole states shift to higher energies and this also happen with the density. On the whole, the imaginary part decreases systematically with the available phase space. The effects of the medium in the $\bar{K}^*$ meson are better visualized in the $\bar{K}^*$ meson spectral function, that is dis-

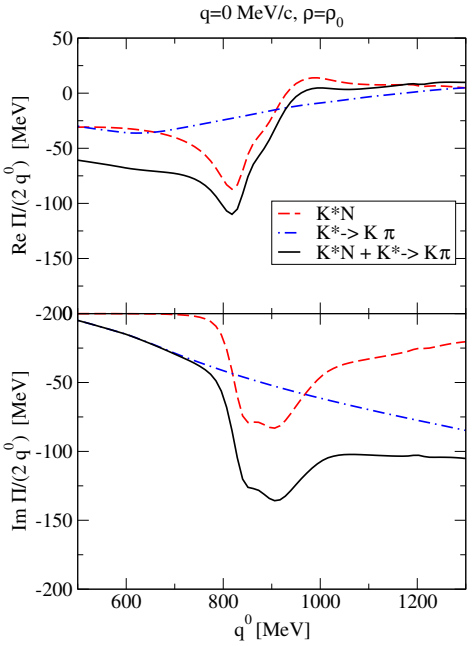

Figure 11.6: Real and imaginary parts of the $\bar{K}^*$ self-energy as functions of the meson energy q^0 for zero momentum and normal saturation density ρ_0 showing the different contributions: (i) self-consistent calculation of the $\bar{K}^*N$ interaction (dashed lines), (ii) self-energy coming from $\bar{K}^* \to \bar{K}\pi$ decay (dot-dashed lines), and (iii) combined self-energy from both previous sources (solid lines).

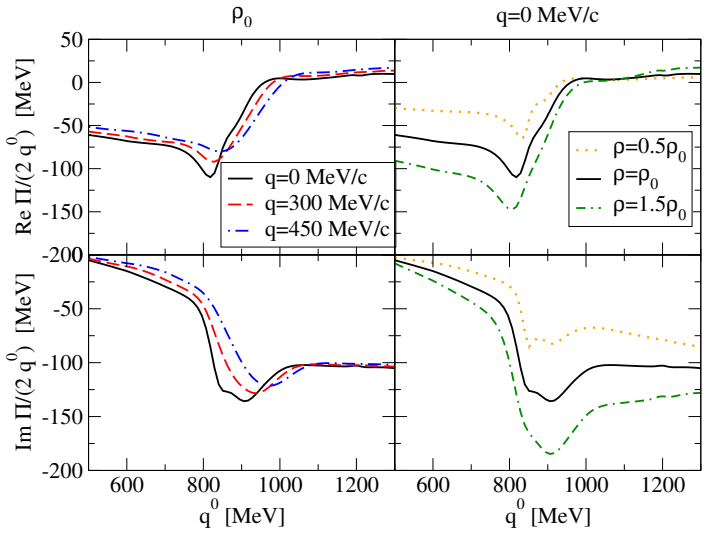

Figure 11.7: The $\bar{K}^*$ self-energy as a function of the meson energy q^0 for different momenta and densities.

played in Fig. 11.8 as a function of the meson energy q^0, for zero momentum and four densities from $\rho = 0$ to $\rho = 1.5\rho_0$. We observe a quite pronounced peak at the quasiparticle energy

that moves to lower energies with density. We can see the $\Lambda(1783)N^{-1}$ and $\Sigma(1830)N^{-1}$ excitations in the right hand side of the quasiparticle peak. Note that, although an attractive interaction of about $\mathrm{Re}\Pi/2m_{\bar{K}^*}(m_{\bar{K}^*}, \vec{q} = 0) = -50$ at $\rho = \rho_0$ is deduced from our calculation, see Fig. 11.6, the inclusion of the pseudoscalar-baryon decay mode in the $\bar{K}^*N$ interaction would lead to other subthreshold excitations, such as $\bar{K}NN^{-1}$, πYN^{-1}, YN^{-1} that have not been accounted for in the present calculations. The peak will be wider and the selfconsistent evaluation might even push the peak back to higher energies. To summarize, the main conclusion that can be clearly extracted from our work is the spectacular increase of the $\bar{K}^*$ width in matter. This effect could be observed experimentally through the

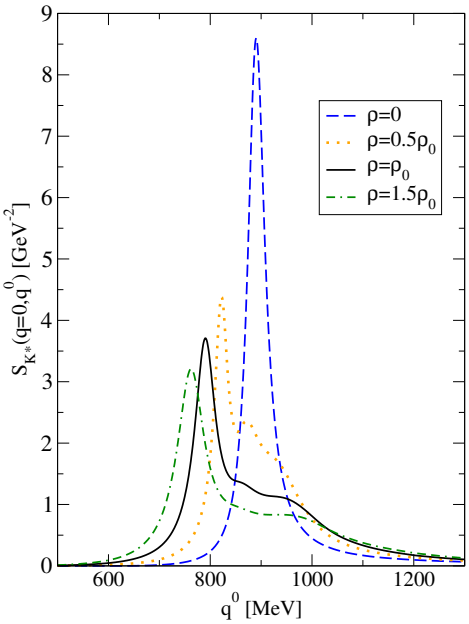

Figure 11.8: The $\bar{K}^*$ spectral function as function of the meson energy q^0 for different densities and zero momentum.

transparency ratio as we discuss in the next section.

11.5 Nuclear transparency in the $\gamma\ A \to K^+\ K^{*-}\ A'$ reaction

In this section we make a qualitative evaluation of the nuclear transparency ratio by comparing the cross sections of the photoproduction reaction $\gamma A \to K^+ K^{*-} A'$ in different nuclei, and tracing them to the in medium width of the K^{*-}. The idea is that the survival probability is an exponential function of the integral of the in-medium width, and hence very sensitive to this magnitude [191].

We write the nuclear transparency ratio as

$$\tilde{T}_A = \frac{\sigma_{\gamma A \to K^+\ K^{*-}\ A'}}{A\,\sigma_{\gamma N \to K^+\ K^{*-}\ N}}\ , \tag{11.17}$$

i.e. the ratio of the nuclear K^{*-}-photoproduction cross section divided by A times the same quantity on a free nucleon. The value of $\tilde{T}_A$ describes the loss of flux of K^{*-} mesons in the nucleus and is related to the absorptive part of the K^{*-}-nucleus optical potential and thus to the K^{*-} width in the nuclear medium. This method has been already proven to be very efficient in the study of the in-medium properties of the vector mesons [157, 226, 227], hyperons [228] and antiprotons [191]. In Ref. [158, 229] the transparency ratio has been already used to determine the width of the ω-meson in finite nuclei using a BUU transport approach.

We have done calculations for a vast sample of nuclear targets: ${}^{12}_{6}\mathrm{C}$, ${}^{14}_{7}\mathrm{N}$, ${}^{23}_{11}\mathrm{Na}$, ${}^{27}_{13}\mathrm{Al}$, ${}^{28}_{14}\mathrm{Si}$, ${}^{35}_{17}\mathrm{Cl}$, ${}^{32}_{16}\mathrm{S}$, ${}^{40}_{18}\mathrm{Ar}$, ${}^{50}_{24}\mathrm{Cr}$, ${}^{56}_{26}\mathrm{Fe}$, ${}^{65}_{29}\mathrm{Cu}$, ${}^{89}_{39}\mathrm{Y}$, ${}^{110}_{48}\mathrm{Cd}$, ${}^{152}_{62}\mathrm{Sm}$, ${}^{207}_{82}\mathrm{Pb}$, ${}^{238}_{92}\mathrm{U}$.

In the following, we evaluate the ratio between the nuclear cross sections in heavy nuclei and a light one, for instance ${}^{12}\mathrm{C}$, since in this way, many other nuclear effects not related to the absorption of the

K^{*-} cancel in the ratio [226]. We call this ratio T_A,

$$T_A = \frac{\tilde{T}_A}{\tilde{T}_{^{12}C}} \ , \tag{11.18}$$

and, by construction, it is normalized to unity for ^{12}C.

We obtain the nuclear transparency ratio taking an eikonal (or Glauber) approximation in the evaluation of the distortion factor associated to K^{*-} absorption. In this framework, the propagation of the K^{*-} meson in its way out of the nucleus is implemented by means of the exponential factor for the survival probability accounting for the loss of flux per unit length. This simple but rather reliable method allows us to get an accurate result for the integrated cross sections.

We proceed as follows: let $\Pi_{K^{*-}}$ be the K^{*-} self-energy in the nuclear medium as a function of the nuclear density, $\rho(r)$. We then have

$$\frac{\Gamma_{K^{*-}}}{2} = -\frac{\mathrm{Im}\Pi_{K^{*-}}}{2E_{K^{*-}}}; \qquad \Gamma_{K^{*-}} \equiv \frac{dP}{dt} \ , \tag{11.19}$$

where P is the probability of K^{*-} interaction in the nucleus, including K^{*-} quasi-elastic collisions and absorption channels. There is some problem when dealing with the free part of the K^{*-} self-energy. Indeed, if the K^{*-} decays inside the nucleus into $\bar{K}\pi$, the $\bar{K}$ or the π will also be absorbed with great probability or undergo a quasi-elastic collision, such that the $\bar{K}\pi$ invariant mass will no longer be the one of the K^{*-}. Thus, it is adequate to remove these events. Yet, if the decay occurs at the surface neither the $\bar{K}$ nor the π will be absorbed and an experimentalist will reconstruct the K^{*-} invariant mass from these two particles, in which case they should not be removed from the flux. The part of $\mathrm{Im}\Pi_{K^{*-}}$ due to quasi-elastic collisions $K^{*-}N \to K^{*-}N$ should not be taken into account in the distortion either, since the K^{*-} does not disappear from the flux in these processes. Yet, this part is small at low energies and we disregard this detail in the present qualitative estimate. In view of all this, we have taken the following approximate choice for $\mathrm{Im}\Pi_{K^{*-}}$ in

our estimate of T_A

$$\mathrm{Im}\,\Pi_{\bar{K}^*} = \begin{cases} (-2.5\times 10^5 + 0.4\times 10^5)\rho(r)/\rho_0 - 0.4\times 10^5 & r < 0.8\,R \\ (-2.5\times 10^5 + 0.4\times 10^5)\rho(r)/\rho_0 & r \geq 0.8\,R \end{cases} \tag{11.20}$$

where the units of $\mathrm{Im}\,\Pi_{\bar{K}^*}$ are MeV^2 being R the nuclear radius. The choice of Eq. (11.20) is justified by the fact that $\mathrm{Im}\Pi_{\bar{K}^*} = -2.5\times 10^5$ MeV^2 at $q^0 = m_{\bar{K}^*}$ and $\vec{q} = 0$ MeV/c at $\rho = \rho_0$ (see Fig. 11.7). This value also contains the contribution from the free decay, $\mathrm{Im}\Pi^0_{\bar{K}^*} \simeq -0.4\times 10^5$ MeV^2, which does not depend on ρ. It therefore needs to be subtracted from the term that implements the linear ρ dependence, and added as a constant value if $r < 0.8\,R$. Moreover, when the $\bar{K}^* \to \bar{K}\pi$ decay takes place in the surface of the nucleus, $r \geq 0.8\,R$, we remove $\mathrm{Im}\Pi^0_{\bar{K}^*}$ since experimentally the $\bar{K}\pi$ system will be reconstructed as a $\bar{K}^*$.

The probability of loss of flux per unit length is given by:

$$\frac{dP}{dl} = \frac{dP}{v\,dt} = \frac{dP}{\frac{|\vec{p}_{K^{*-}}|}{E_{K^{*-}}}dt} = -\frac{\mathrm{Im}\Pi_{K^{*-}}}{|\vec{p}_{K^{*-}}|}\ , \tag{11.21}$$

and the corresponding survival probability is determined from

$$\exp\left\{\int_0^\infty dl \frac{\mathrm{Im}\Pi_{K^{*-}}(\rho(\vec{r}\,'))}{|\vec{p}_{K^{*-}}|}\right\}, \tag{11.22}$$

where $\vec{r}\,' = \vec{r} + l\,\dfrac{\vec{p}_{K^{*-}}}{|\vec{p}_{K^{*-}}|}$ with $\vec{r}$ being the K^{*-} production point inside the nucleus.

With all these ingredients and taking into account the standard expression for K^{*-} production in the nucleus prior to the consideration of the eikonal distortion, the cross section for the $\gamma\, A \to$

K^+ K^{*-} A' reaction is obtained from

$$\begin{aligned}\sigma_{\gamma A\to K^+K^{*-}A'} &= \frac{M^2}{4(s-M^2)}\frac{1}{(2\pi)^4}\int d^3r\rho(r)\int_{m_{K^{*-}}}^{E_2^{\max}} p_2 dE_2\int_{m_{K^+}}^{E_3^{\max}} dE_3 \\ &\times\int_{-1}^{1} d\cos\theta_2\int_0^{2\pi} d\phi_2\frac{1}{|\vec{p}_\gamma-\vec{p}_2|}\theta(E_\gamma+M-E_2-E_3) \\ &\times\theta(1-A^2)|T|^2\exp\left\{\int_0^{2.5R} dl\,\mathrm{Im}\Pi(\rho(\vec{r}\,'))/p_2\right\}\ ,\end{aligned} \tag{11.23}$$

with

$$\begin{aligned}A &\equiv \cos\theta_3 \\ &= \frac{1}{2|\vec{p}_\gamma-\vec{p}_2|p_3}\{M^2+|\vec{p}_\gamma-\vec{p}_2|^2+\vec{p}_3^{\,2}-(E_\gamma+M-E_2-E_3)^2\}\end{aligned} \tag{11.24}$$

and

$$\begin{aligned}E_2^{\max} &= \frac{s+m_{K^{*-}}^2-(M+m_{K^+})^2}{2\sqrt{s}} \\ E_3^{\max} &= \frac{s+m_{K^+}^2-(M+m_{K^{*-}})^2}{2\sqrt{s}}\ ,\end{aligned} \tag{11.25}$$

where $(E_2,\vec{p}_2)$ and $(E_3,\vec{p}_3)$ are the four-momenta of the K^{*-} and K^+, respectively, in the frame of the nucleon at rest, and E_γ is the energy of the photon in this frame. Here, M is the mass of the nucleon while $m_{K^{*-}}$ and m_{K^+} are the masses of the K^{*-} and K^+ mesons, respectively. The value of $E_2^{\max}$ has been calculated when the particles 1 plus 3 go together (or 1 plus 2 in the case of $E_3^{\max}$). Since we are interested in ratios of cross sections we have taken $|T|^2=1$.

The results can be seen in Fig. 11.9, where the transparency ratio has been plotted for two different energies in the center of mass reference system $\sqrt{s}=3$ GeV and 3.5 GeV, which are equivalent to energies of the photon in the lab frame of 4.3 MeV and 6 MeV,

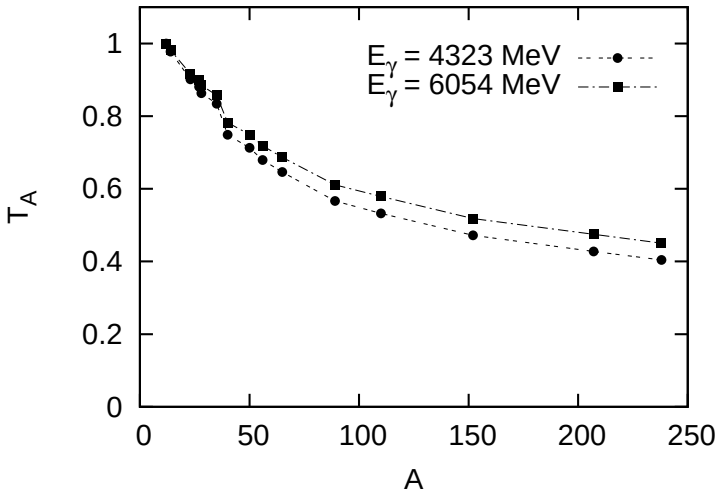

Figure 11.9: Transparency ratio

respectively. We observe a very strong attenuation of the $\bar{K}^*$ production process due to the decay or absorption channels $\bar{K}^* \to \bar{K}\pi$ and $\bar{K}^* N \to VY$ with increasing nuclear-mass number A. This is due to the larger path that the $\bar{K}^*$ has to follow before it leaves the nucleus, having then more chances to decay or get absorbed.

Chapter 12

$N^*_{c\bar{c}}$ and $\Lambda^*_{c\bar{c}}$ resonances around 4 GeV

We investigate the production of new hidden charmed baryons generated from the scattering of charmed pseudoscalar (vector) meson with a charmed baryon from the 20-plet representation. New vertices are built to include the charmed baryons, for which we use the SU(4) Clebsch Gordan Coefficients. In contrast with other similar studies regarding dynamically generated baryon resonances, the new N^* and Λ^* predicted states around 4.2 GeV (as brothers or systers of the $N^*(1535)$ and $\Lambda(1405)$) cannot be definetely $3q$ baryons. For this reason, the experimental observation of these hidden charm baryons is extremely relevant.

12.1 Introduction

All of the well known baryons can be described in terms of 3-quark configurations [78], though there are some theoretical approaches that predict some of them to be meson-baryon dynamically generated resonances or to have large couplings to $qqqq\bar{q}$ components. The way to

distinguish qqq configurations from pseudoscalar-baryon bound states or resonances is a hard task since several models that are around the same energy region, leave always some free parameters that are adjustable to the data. In this sense, the search of theoretical predictions as well as experimental observation of states that definetely cannot be accomodated as $3q$ is a challenging topic. The study of the pseudoscalar-baryon interaction using chiral lagrangians combined with unitary technics has produced interesting findings such as the prediction of the two $\Lambda(1405)$ or the generation of the $N^*(1535)$ resonance, being the $K\Sigma$ and $K\Lambda$ channels the main components of the last state [64, 230]. Indeed, many studies support the hidden strangeness nature of this state [231, 232]. In this way, the interaction of the octect of pseudoscalar mesons with the octect of stable baryons has led to $J^P = 1/2^-$ resonances which fit quite well the spectrum of the known low lying resonances with these quantum numbers [43, 44, 45, 47, 233]. The combination of pseudoscalar mesons with the decuplet of baryons has also received attention and leads to several dynamically generated states [66, 67]. In [210, 211], similar work is done but substituting the pseudoscalar mesons for vector ones.

The extension to the interaction of charmed pseudoscalar mesons with baryons has been treated in [172]. Through an extension of the known chiral lagrangians for the interaction of mesons with baryons to include charm mesons and breaking the symmetry afterwards, the $\Lambda_c(2593)$ is dynamically generated from this interaction being mostly DN, whereas one Σ_c^* around 3700 MeV is predicted there.

In this chapter, we explore the hidden charm sector of dynamically generated baryonic resonances from a pseudoscalar or vector meson with a baryon. We will introduce the new vertices for the interaction of charmed baryons with pseudoscalar mesons, and we will see that $N^*_{c\bar{c}}$ and $\Lambda^*_{c\bar{c}}$ states appear around 4000 MeV as brothers or systers of the well-known $N^*(1535)$ and $\Lambda^*(1405)$. The observation of these new states will be certainly important since these are states that cannot be $3q$. See [234] and [235] for a detailed revision.

12.2 Formalism

We study the vector-baryon and pseudoscalar-baryon interaction in the hidden-charm sector. This involves the study of the sectors of (isospin, strangeness): $(I, S) = (3/2, 0)$, $(1/2, 0)$, $(1/2, -2)$, $(1, -1)$, $(0, -1)$, $(0, -3)$.

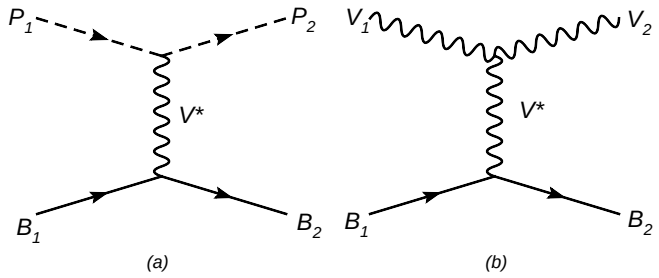

Figure 12.1: Feynman diagrams for the pseudoscalar-baryon (a) or vector- baryon (b) interaction via the exchange of a vector meson (P_1, P_2 are D^-, $\bar{D}^0$ or D_s^-, and V_1, V_2 are D^{*-}, $\bar{D}^{*0}$ or D_s^{*-}, and B_1, B_2 are Σ_c, Λ_c^+, Ξ_c, Ξ_c' or Ω_c, and V^* is ρ, K^*, ϕ or ω).

We follow the formalism described in [211] where the interaction between mesons and baryons comes through the exchange of vector mesons (vector meson dominance) as plotted in Fig. 12.1. The Lagrangian that provide BBV vertex is

$$\mathcal{L}_{BBV} = g(\langle \bar{B}\gamma_\mu [V^\mu, B]\rangle + \langle \bar{B}\gamma_\mu B\rangle\langle V^\mu\rangle) \tag{12.1}$$

respectively, where B and P are the standard matrices including the pseudoscalar and baryon nonets in SU(3). In order to go to SU(4), we can include the charmed mesons in an straightforward manner for the use of $\mathcal{L}_{3V}$ and $\mathcal{L}_{PPV}$, Eqs. (3.5) and (3.27). However, the extension of $\mathcal{L}_{BBV}$ in Eq. (12.1) to SU(4) is not direct but the coefficients that go with each product of particle fields are Clesch-Gordan coefficients of SU(3) and the extension to SU(4) can be done by means of the

SU(4) Clesch-Gordan tables [179]. Thus, we can evaluate the amplitude of the $3V$ or PPV interaction with the Lagrangians of $\mathcal{L}_{3V}$ and $\mathcal{L}_{PPV}$ or well by means of the SU(4) tables. We find for $P_1P_2 \to V$:

$$t_{P_1P_2V} = g_{15_F} C_{15_F}(15 \otimes 15)\,(q_1 + q_2)_\mu \epsilon^\mu \tag{12.2}$$

where $C_{15_F}(15 \otimes 15)$ is the $SU(4)$ Clebsch-Gordan coefficient for $15 \otimes 15 \to 15_F$ and g_{15_F} is the reduced matrix element that by comparison with the result of the Lagrangian is given by

$$g_{15_F} = -2\sqrt{2}g\ . \tag{12.3}$$

Note that the interaction occurs through only the 15_F representation, since we have an explicit conmutator in Eqs. $\mathcal{L}_{3V}$ and $\mathcal{L}_{PPV}$. The matrices P and V can be expressed in terms of the mathematical states of the 15-plet representation as

$$P = \begin{pmatrix} \frac{\pi^0}{\sqrt{2}} + \frac{\eta_8}{\sqrt{6}} + \frac{\tilde{\eta}_c}{\sqrt{12}} + \frac{\tilde{\eta}'_c}{\sqrt{4}} & \pi^+ & K^+ & \bar{D}^0 \\ \pi^- & -\frac{\pi^0}{\sqrt{2}} + \frac{\eta_8}{\sqrt{6}} + \frac{\tilde{\eta}_c}{\sqrt{12}} + \frac{\tilde{\eta}'_c}{\sqrt{4}} & K^0 & D^- \\ K^- & \bar{K}^0 & \frac{-2\eta_8}{\sqrt{6}} + \frac{\tilde{\eta}_c}{\sqrt{12}} + \frac{\tilde{\eta}'_c}{\sqrt{4}} & D_s^- \\ D^0 & D^+ & D_s^+ & -\frac{3\tilde{\eta}_c}{\sqrt{12}} + \frac{\tilde{\eta}'_c}{\sqrt{4}} \end{pmatrix}, \tag{12.4}$$

and

$$V_\mu = \begin{pmatrix} \frac{\rho^0}{\sqrt{2}} + \frac{\omega_8}{\sqrt{6}} + \frac{\tilde{\omega}_c}{\sqrt{12}} + \frac{\tilde{\omega}'_c}{\sqrt{4}} & \rho^+ & K^{*+} & \bar{D}^{*0} \\ \rho^- & -\frac{\rho^0}{\sqrt{2}} + \frac{\omega_8}{\sqrt{6}} + \frac{\tilde{\omega}_c}{\sqrt{12}} + \frac{\tilde{\omega}'_c}{\sqrt{4}} & K^{*0} & D^{*-} \\ K^{*-} & \bar{K}^{*0} & \frac{-2\omega_8}{\sqrt{6}} + \frac{\tilde{\omega}_c}{\sqrt{12}} + \frac{\tilde{\omega}'_c}{\sqrt{4}} & D_s^{*-} \\ D^{*0} & D^{*+} & D_s^{*+} & -\frac{3\tilde{\omega}_c}{\sqrt{12}} + \frac{\tilde{\omega}'_c}{\sqrt{4}} \end{pmatrix}_\mu . \tag{12.5}$$

which contains a singlet, $\tilde{\eta}_c$, or $\tilde{\omega}_c$ (for vectors), and the SU(4) singlet, $\tilde{\eta}'_c$ or $\tilde{\omega}'_c$. But, these fields can be related with the physical states. Taking π^0, η, η' and η_c as a basis for the neutral pseudoscalar mesons,

where η' is the singlet in $SU(3)$, $(u\bar{u}+d\bar{d}+s\bar{s})/\sqrt{3}$ and η stand for $c\bar{c}$, and recalling the standard quark composition of the SU(4) mesons

$$\begin{aligned}
\pi^0 &= \frac{1}{\sqrt{2}}(u\bar{u}-d\bar{d}) \\
\eta_8 &= \frac{1}{\sqrt{6}}(u\bar{u}+d\bar{d}-2s\bar{s}) \\
\tilde{\eta}_c &= \frac{1}{\sqrt{12}}(u\bar{u}+d\bar{d}+s\bar{s}-3c\bar{c}) \\
\tilde{\eta}'_c &= \frac{1}{\sqrt{4}}(u\bar{u}+d\bar{d}+s\bar{s}+c\bar{c}) \ , \qquad (12.6)
\end{aligned}$$

we have in the physical basis

$$\begin{aligned}
\eta_8 &= \eta \\
\eta' &= \frac{1}{2}\tilde{\eta}_c + \frac{\sqrt{3}}{2}\tilde{\eta}'_c \\
\eta_c &= \frac{1}{2}(-\sqrt{3}\tilde{\eta}_c + \tilde{\eta}'_c) \ , \qquad (12.7)
\end{aligned}$$

whereas for the vectors,

$$\begin{aligned}
\rho^0 &= \frac{1}{\sqrt{2}}(u\bar{u}-d\bar{d}) \\
\omega &= \frac{1}{\sqrt{2}}(u\bar{u}+d\bar{d}) \\
\phi &= s\bar{s} \\
J/\psi &= c\bar{c} \ , \qquad (12.8)
\end{aligned}$$

that are related to the mathematical states through

$$\begin{aligned}
\omega &= \frac{1}{6}(\sqrt{6}\tilde{\omega}_c + 2\sqrt{3}\omega_8 + 3\sqrt{2}\tilde{\omega}'_c) \\
\phi &= \frac{1}{6}(\sqrt{3}\tilde{\omega}_c - 2\sqrt{6}\omega_8 + 3\tilde{\omega}'_c) \\
J/\psi &= \frac{1}{2}(-\sqrt{3}\tilde{\omega}_c + \tilde{\omega}'_c) \ . \qquad (12.9)
\end{aligned}$$

The use of the SU(4) Clesch Gordan coefficients from [179] requires a phase convention. We have found a compatible and convenient phase convention of the isospin states implicit in the SU(4) tables and with the use of $\mathcal{L}_{VVV}$ and $\mathcal{L}_{PPV}$ in Eqs. (3.5) and (3.27) which is:

$$|K^0\rangle = -|1/2,-1/2\rangle \ ; \quad |\pi^+\rangle = -|1,1\rangle \ ; \qquad |\pi^0\rangle = -|1,0\rangle \ ;$$

$$|D_s^+\rangle = -|0,0\rangle \ ; \qquad |\bar{D}^0\rangle = -|1/2,1/2\rangle \ ; \quad |\tilde{\eta}_c\rangle = -|0,0\rangle \ ;$$

The necessity of the phases stems from demanding that the SU(4) singlet must be a symmetrical expression in the physical states (thus we evaluate $15 \otimes 15 \to 1$ and put appropiate phases to ensure that all terms come with the same sign). For the BBV vertex, we need now the $20' \otimes \bar{20}' \to 15_1, 15_2, 1$ Clebsch Gordan coefficient and the $B\bar{B} \to V$ amplitude can be written as a function of them as

$$\begin{aligned} t_{B_1\bar{B}_2V} \quad = \quad & \{g_{15_1}\, C_{15_1}(20' \otimes \bar{20}') + g_{15_2}\, C_{15_2}(20' \otimes \bar{20}') + g_1\, C_1(20' \otimes \bar{20}')\} \\ & \times \bar{u}_{r'}(p_2)\gamma \cdot \epsilon\, u_r(p_1) \ . \end{aligned} \tag{12.10}$$

The reduced matrix elements, g_{15_1}, g_{15_2} and g_1 are evaluated demandng the following constraints

1) The coupling $p\bar{p} \to J/\psi$ should be zero by OZI rules,

2) The coupling $p\bar{p} \to \phi$ should be zero by OZI rules,

3) The coupling $p\bar{p} \to \rho^0$ should be the one obtained in SU(3).

and finally, we obtain

$$g_{15_1} = -g; \quad g_{15_2} = 2\sqrt{3}\, g; \quad g_1 = 3\sqrt{5}\, g \ . \tag{12.11}$$

with $g = M_V/2f$ and $f = 93MeV$ the pion decay constant. And the phase convention motivated to agree formally with Eq. (12.1) is given by

$$|\bar{\Xi}^{--}_{cc}\rangle = -|1/2,-1/2\rangle \quad |\Omega^{+}_{cc}\rangle = -|0,0\rangle \quad |\Xi^{0}_{c}\rangle = -|1/2,-1/2\rangle$$

$$|\Xi^{\prime 0}_{c}\rangle = -|1/2,-1/2\rangle \quad |\bar{\Lambda}^{-}_{c}\rangle = -|0,0\rangle \quad |\Sigma^{+}_{c}\rangle = -|1,0\rangle$$

$$|\Sigma^{++}_{c}\rangle = -|1,1\rangle \quad |\bar{\Sigma}^{--}_{c}\rangle = -|1,-1\rangle \quad |n\rangle = -|1/2,-1/2\rangle$$

$$|\bar{\Xi}^{0}\rangle = -|1/2,-1/2\rangle \quad |\bar{\Sigma}^{+}\rangle = -|1,1\rangle \quad |\Sigma^{+}\rangle = -|1,1\rangle$$

$$|\Sigma^{0}\rangle = -|1,0\rangle \quad |\bar{\Sigma}^{0}\rangle = -|1,0\rangle \ ,$$

and once again the expression obtained for the $20' \otimes \bar{20}'$ in terms of $SU(4)$ isospin states is symmetric in the physical states with the convention given. As a result, the transition potential corresponding to the diagrams of Fig. 12.1 are given by

$$V_{ab(P_1B_1 \to P_2B_2)} = \frac{C_{ab}}{4f^2}(q_1^0 + q_2^0), \tag{12.12}$$

$$V_{ab(V_1B_1 \to V_2B_2)} = \frac{C_{ab}}{4f^2}(q_1^0 + q_2^0)\vec{\epsilon}_1 \cdot \vec{\epsilon}_2 \ , \tag{12.13}$$

where the indices a, b stand for the different channels $P_1B_1(V_1B_1)$ and $P_2B_2(V_2B_2)$. Where we have followed the approach of neglecting the three momenta of the particles compared to their masses as in [44]. The value of the C_{ab} coefficients for the different channels in each (isospin, strangeness) sector: $(3/2,0)$, $(1/2,0)$, $(1/2,-2)$, $(1,-1)$, $(0,-1)$, $(0,-3)$, are given in the Appendix F.

12.3 T matrix

We evaluate the unitary T matrix by solving the coupled channels Bethe-Salpeter equation in the on-shell factorization approach, Eq. (3.22), where now G is the pseudoscalar (vector) - baryon function

loop that in dimensional regularization is given by

$$\begin{aligned} G_{(P,B)} &= i2M_B \int \frac{d^4q}{(2\pi)^4} \frac{1}{(P-q)^2 - M_B^2 + i\varepsilon} \frac{1}{q^2 - M_P^2 + i\varepsilon}, \\ &= \frac{2M_B}{16\pi^2} \Big\{ a_\mu + \mathrm{Log}\frac{M_B^2}{\mu^2} + \frac{M_P^2 - M_B^2 + s}{2s} \mathrm{Log}\frac{M_P^2}{M_B^2} \\ &\quad + \frac{\bar{q}}{\sqrt{s}} \Big[\mathrm{Log}(s - (M_B^2 - M_P^2) + 2\bar{q}\sqrt{s}) \\ &\quad + \mathrm{Log}(s + (M_B^2 - M_P^2) + 2\bar{q}\sqrt{s}) \\ &\quad - \mathrm{Log}(-s - (M_B^2 - M_P^2) + 2\bar{q}\sqrt{s}) \\ &\quad - \mathrm{Log}(-s + (M_B^2 - M_P^2) + 2\bar{q}\sqrt{s}) \Big] \Big\} \ , \end{aligned} \tag{12.14}$$

where

$$\begin{aligned} s &= P^2, \\ \bar{q} &= \frac{\sqrt{(s - (M_B + M_P)^2)(s - (M_B - M_P)^2)}}{2\sqrt{s}} \ , \quad \mathrm{Im}(q) > 0 \ . \end{aligned} \tag{12.15}$$

It can also be solved by using a three-momentum cutoff

$$\begin{aligned} G_{(P,B)} &= i2M_B \int \frac{d^4q}{(2\pi)^4} \frac{1}{(P-q)^2 - M_B^2 + i\varepsilon} \frac{1}{q^2 - M_P^2 + i\varepsilon} \\ &= \int_0^\Lambda \frac{q^2 dq}{4\pi^2} \frac{2M_B(\omega_P + \omega_B)}{\omega_P\, \omega_B\, ((P^0)^2 - (\omega_P + \omega_B)^2 + i\epsilon)} \ , \end{aligned} \tag{12.16}$$

where

$$\begin{aligned} \omega_P &= \sqrt{\vec{q}^{\,2} + M_P^2} \ , \\ \omega_B &= \sqrt{\vec{p}^{\,2} + M_B^2} \ , \end{aligned} \tag{12.17}$$

and Λ is the cutoff parameter in the three-momentum of the loop integral. A difference with other works is that we do not have any

experimental evidence of a resonance close to the pseudoscalar (vector) - baryon thresholds that we deal with here, therefore, the most reliable procedure is calculate the uncertainties showing the results for different choices of the parameters. Thus, we take values close to [230], $a_\mu = -2$ and $\mu = 670$ MeV as a guideline and vary them. The ultimate choices around $a_\mu = -2.3$ are based on phenomenology, using values that prove suitable to reproduce other states in the charm sector that can be compared with experiment. The range of a values used (or cutoff parameter in Eq. (12.16)) is in line with the ones used in [108, 109, 116, 172]. Close to a pole, the amplitudes behave like

$$T_{ab} = \frac{g_a g_b}{\sqrt{s} - z_R} \tag{12.18}$$

The pole positions and coupling constants to the different channels are given in Tables 12.1, 12.2, 12.3 and 12.4. We find six poles, all of them are bound states. The uncertainties in the pole positions for PB and VB are of the order of 100 MeV, which is typical in hadron models. Although the pole positions of the first and third state are rather stable, the uncertainties for the second state turn out to be larger being quite unstable.

(I,S)	$\alpha = -2.2$	$\alpha = -2.3$	$\alpha = -2.4$
	($\Lambda = 0.7$ GeV)	($\Lambda = 0.8$ GeV)	($\Lambda = 0.9$ GeV)
	z_R	z_R	z_R
$(1/2, 0)$	4291(4273)	4269(4236)	4240(4187)
$(0, -1)$	4247(4120)	4213(4023)	4170(3903)
	4422(4394)	4403(4357)	4376(4308)

Table 12.1: Pole position from $PB \to PB$ using the two different G functions of Eqs. (12.14) and (12.16). The units are in MeV.

(I,S)	$\alpha=-2.2$ ($\Lambda=0.7$ GeV) z_R	$\alpha=-2.3$ ($\Lambda=0.8$ GeV) z_R	$\alpha=-2.4$ ($\Lambda=0.9$ GeV) z_R
$(1/2,0)$	4438(4410)	4418(4372)	4391(4320)
$(0,-1)$	4399(4256)	4370(4155)	4330(4030)
	4568(4532)	4550(4493)	4526(4441)

Table 12.2: Pole position from $VB \to VB$ using the two different G functions of Eqs. (12.14) and (12.16). The units are in MeV.

(I,S)	z_R (MeV)	g_a		
$(1/2,0)$		$\bar{D}\Sigma_c$	$\bar{D}\Lambda_c^+$	
	4269	2.85	0	
$(0,-1)$		$\bar{D}_s\Lambda_c^+$	$\bar{D}\Xi_c$	$\bar{D}\Xi_c'$
	4213	1.37	3.25	0
	4403	0	0	2.64

Table 12.3: Pole positions, z_R and coupling constants, g_a, for the states from $PB \to PB$.

(I,S)	z_R (MeV)	g_a		
$(1/2,0)$		$\bar{D}^*\Sigma_c$	$\bar{D}^*\Lambda_c^+$	
	4418	2.75	0	
$(0,-1)$		$\bar{D}_s^*\Lambda_c^+$	$\bar{D}^*\Xi_c$	$\bar{D}^*\Xi_c'$
	4370	1.23	3.14	0
	4550	0	0	2.53

Table 12.4: Pole position and coupling constants for the bound states from $VB \to VB$.

In Tables 12.3, 12.4 we can see that the state without strangeness couples to $\bar{D}\Sigma_c(\bar{D}\Sigma_c)$. This state is an N^*, whereas we get two Λ^* in the pseudoscalar - baryon system coupling to $\bar{D}_s\Lambda_c$, $\bar{D}\Xi_c$ and $\bar{D}\Xi_c'$ respectively (or well $\bar{D}_s^*\Lambda_c$, $\bar{D}^*\Xi_c$ and $\bar{D}^*\Xi_c'$ respectively). The instability of the second pole may be related with the additional channel $\bar{D}_s\Lambda_c$, $(\bar{D}_c^*\Lambda_c)$.

12.4 Decay mechanisms for the $N^*_{c\bar{c}}$ and $\Lambda^*_{c\bar{c}}$ states

We consider the decay of the pseudoscalar - baryon and vector-baryon states to light pseudoscalar - light baryon and light vector - light baryon pairs, as shown in Fig. 12.2. The possible decay channels which we take into account are πN, ηN, $\eta' N$ and $K\Sigma$ for the (isospin $= 1/2$, strangeness $= 0$) sector, (ρN, ωN and $K^*\Sigma$ for the vector-baryon system) and ($\bar{K}N$, $\pi\Sigma$, $\eta\Lambda$, $\eta'\Lambda$ and $K\Xi$) for the (isospin $= 0$, strangeness $= -1$) sector ($\bar{K}^*N$, $\rho\Sigma$, $\omega\Lambda$, $\phi\Lambda$ and $K^*\Xi$ for vector-baryon). This is not the only possibility. For the vector-baryon states, another way is to decay into pseudoscalar-baryon channels analogously to the two-pseudoscalar decay mode of the vector-

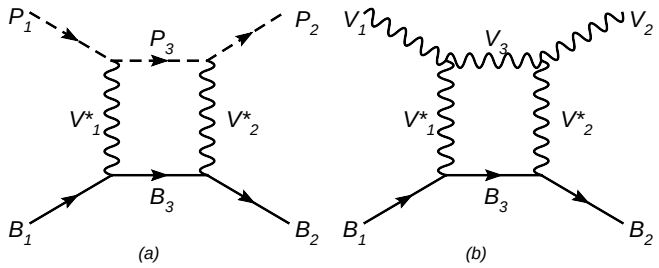

Figure 12.2: The Feynman diagrams of pseudoscalar-baryon (a) or vector-baryon (b) interaction via a box diagram. P_1, P_2, V_1, V_2, B_1, B_2 are the same particles than in Fig. 12.1. P_3, V_3 and B_3 are light particles belonging to the SU(3) octet of pseudoscalar mesons, vector mesons and stable baryons, respectively, and V_1^*, V_2^* are D^* or D_s^*.

vector states studied in the Chapter 3. Nevertheless, the box diagrams will contain the process $\bar{D}^* B \to \bar{D} B$ and it was found in Chapter 7 that the box diagram including $(\bar{D}^* \bar{D}^* \to \bar{D} D)$ is a very small contribution since the phase space available is small. Besides that, these VB box diagrams will contain either an anomalous vertex, VVP (vector exchange), or a BBP vertex (pseudoscalar exchange) that makes these terms to be smaller. Alternatively, one can have the pseudoscalar-baryon states decaying to vector-baryon channels but these diagrams will contain also VVP or BBP vertices leading to a minor contribution. We assume that P_3, V_3 and B_3 are on-shell and neglect the three - momentum of the initial and final particles. Then, using Eq. (12.1), the transition potential of these diagrams

can be written as:

$$V_{acb(P_1B_1\to P_3B_3\to P_2B_2)} = \frac{C_{ac}C_{cb}M^4_{V^*}}{16f^4}G_{(P_3,B_3)}\frac{(\sqrt{s}+M_{B_3})^2-M^2_{P_3}}{4\sqrt{s}\,M_{B_3}} \times\frac{-2E_{P_1}+\frac{(M_{B_3}-M_{B_1})(M^2_{P_1}+M^2_{V_1^*}-M^2_{P_3})}{M^2_{V_1^*}}}{M^2_{P_1}+M^2_{P_3}-2E_{P_3}E_{P_1}-M^2_{V_1^*}} \times\frac{-2E_{P_2}+\frac{(M_{B_3}-M_{B_2})(M^2_{P_2}+M^2_{V_2^*}-M^2_{P_3})}{M^2_{V_2^*}}}{M^2_{P_2}+M^2_{P_3}-2E_{P_3}E_{P_2}-M^2_{V_2^*}}, \tag{12.19}$$

and the same for vectors (see Fig. 12.2. (b)) changing E_{P_1}, E_{P_2}, E_{P_3} by E_{V_1}, E_{V_2}, E_{V_3} and M_{P_1}, M_{P_2}, M_{P_3} by M_{V_1}, M_{V_2}, M_{V_3}, respectively. Here c stands for a different group of $P_3(V_3)B_3$. Then, the kernel V in the Bethe Salpeter equation, Eq. (3.22), becomes now:

$$V_{ab(P_1B_1\to P_2B_2)} = \frac{C_{ab}}{4f^2}(E_{P_1}+E_{P_2})+\sum_c V_{acb}, \tag{12.20}$$

and similarly for the VB system. In Eq. (12.19) we have factorized the two $P_1B_1\to P_3B_3$ and $P_3B_3\to P_2B_2$ transition amplitudes outside the loop integral by taking their values when the system P_3B_3 is set on-shell. This is a good approximation, exact for the imaginary part of the diagram, which is the main contribution, since we are interested in the width of the resonances and it was found in the former Chapters that the box diagram has a small real part. The loop integral only affects then the P_3, B_3 propagators leading to the same G function defined in Eq. (12.14). Since the on-shell mass of the intermediate states is far away from the energies investigated, $\mathrm{Re}\,G(P_3,B_3)$ is small and we have checked that it is sufficiently smaller than the tree level contribution from the diagrams of Fig. (12.1), so that it can be ignored. For example, $V_{(\bar{D}\Sigma_c\to\pi N\to\bar{D}\Sigma_c)}=(0.38+2.9i)$ GeV^{-1} at the N^* pole position with $\sqrt{s}=4.265$ GeV.

Further on, we will include the $\eta_c N$, $\eta_c \Lambda$ channels for $PB \to PB$, and $J/\psi N$, $J/\psi \Lambda$ for $VB \to VB$ in the calculation. The partial decay widths measured directly from the $|T|^2$ plots including only the proper contribution are listed in Tables 12.5 and 12.6. We see that even though these are massive objects, all of them are above 4200 MeV, their widths are quite small. The reason stems from the difficulty of the $c\bar{c}$ components to decay into $u\bar{u}$, $d\bar{d}$ and $s\bar{s}$ ones, that needs in our model the exchange of a heavy vector meson.

In addition, we calculate the decay of the N^* and Λ^* states to $c\bar{c}$-meson light-baryon channels. To do so, we reevaluate the Bethe Salpeter equation but now we include the $\eta_c N$ and $J/\psi N$ channels in the V matrix Eq. (3.22) and search for the new poles and evaluate the new couplings constants. The results are given in Tables 12.5 and 12.6. As we can observe, these channels provide a width comparable to the sum of the other decay channels.

12.5 Production cross section in $p\bar{p}$ collisions

12.5.1 Estimate of the $p\bar{p} \to N^+_{c\bar{c}}(4265)\bar{p}$ cross section

We consider the $p\bar{p} \to N^{*+}_{c\bar{c}}(4265)\bar{p}$ cross section through the Feynmann diagrams depicted in Fig. 12.3 a) and b) respect to the $p\bar{p} \to p\bar{p}\eta_c$ collision (without the resonance), diagrams c) and d). Focusing on the first diagram a), for a $\bar{p}$ beam of 15 GeV (of the FAIR facility) one has $\sqrt{s} = 5470\ MeV$, which allows one to observe resonances in $\bar{p}X$ production up to a mass $M_X \simeq 4538\ MeV$, we shall make some rough estimate of the cross section for the $\bar{p}p \to \bar{p}N^{*+}_{c\bar{c}}$ production for the $C = 0, S = 0$ resonances that we have obtained from the pseudoscalar baryon interaction. Since one important decay channel of the $N^*_{c\bar{c}}$ is πN, we evaluate the cross section for the mechanism depicted in the Feynman diagram of Fig. 12.4.

(I,S)	M	Γ	Γ_i					
$(1/2,0)$			πN	ηN	$\eta' N$	$K\Sigma$		$\eta_c N$
	4261	56.9	3.8	8.1	3.9	17.0		23.4
$(0,-1)$			$\bar{K}N$	$\pi\Sigma$	$\eta\Lambda$	$\eta'\Lambda$	$K\Xi$	$\eta_c\Lambda$
	4209	32.4	15.8	2.9	3.2	1.7	2.4	5.8
	4394	43.3	0	10.6	7.1	3.3	5.8	16.3

Table 12.5: Mass (M), total width (Γ), and the partial decay width (Γ_i) for the states from $PB \to PB$, with units in MeV.

(I,S)	M	Γ	Γ_i					
$(1/2,0)$			ρN	ωN	$K^*\Sigma$			$J/\psi N$
	4412	47.3	3.2	10.4	13.7			19.2
$(0,-1)$			$\bar{K}^*N$	$\rho\Sigma$	$\omega\Lambda$	$\phi\Lambda$	$K^*\Xi$	$J/\psi\Lambda$
	4368	28.0	13.9	3.1	0.3	4.0	1.8	5.4
	4544	36.6	0	8.8	9.1	0	5.0	13.8

Table 12.6: Mass (M), total width (Γ), and the partial decay width (Γ_i) for the states from $VB \to VB$ with units in MeV.

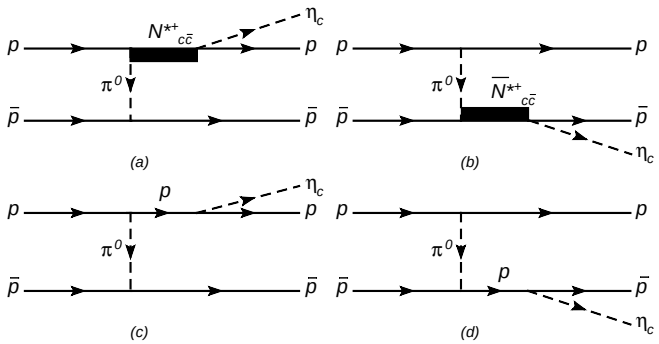

Figure 12.3: The different Feynman diagrams of the reaction $p\bar{p} \rightarrow p\bar{p}\eta_c$

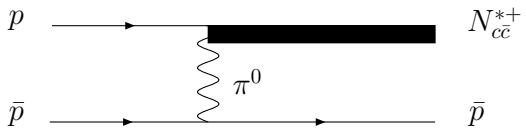

Figure 12.4: The $p\bar{p} \rightarrow N^{*+}_{c\bar{c}}\bar{p}$ mechanism.

The coupling of the $N^*_{c\bar{c}} \to \pi^0 p$ is obtained projecting over $\pi^0 p$ the isospin state $I = 1/2$, which provides the isospin coefficient $C_I = \sqrt{1/3}$. The coupling $N^*_{c\bar{c}} \to \pi N$ is calculated by the partial decay width of the $N^*_{c\bar{c}}$ into this channel, $\Gamma_{\pi N}$

$$g^2_{N^*_{c\bar{c}} \to \pi N} = \frac{2\pi M_{N^*_{c\bar{c}}} \Gamma_{\pi N}}{M_N p^{\rm on}_\pi} \tag{12.21}$$

with $p^{\rm on}_\pi = \lambda^{1/2}(M^2_{N^*_{c\bar{c}}}, m^2_\pi, M^2_N)/2M_{N^*_{c\bar{c}}}$, the value of the on-shell pion momentum from the $N^*_{c\bar{c}} \to \pi N$ decay. By taking the standard πNN vertex, $V_{\pi NN} = i g_\pi \gamma_5 \tau^\lambda$ ($g_\pi \simeq 13$), we obtain

$$\frac{d\sigma_{p\bar{p} \to N^{*+}_{c\bar{c}} \bar{p}}}{d\cos\theta} = \frac{g^2_\pi}{4} \frac{M^2_X}{s} \frac{\Gamma_{\pi N} C^2_I}{p^{\rm on}_\pi} \frac{2p.p' - 2M^2}{(2M^2 - \sqrt{s}E(p') + 2\vec{p}.\vec{p}')^2} \frac{p'}{p} \tag{12.22}$$

where p, p' are the initial, final momenta of the $\bar{p}$ in the center of mass frame (of the order of 2570, 620 MeV/c for $M_X \simeq 4300$ MeV). The biggest cross section corresponds to the forward $\bar{p}$ direction, which is the most indicated for the search. If we are interested in searching for these resonances, looking for $\bar{p}$ forward is the most recommendable measurement and one should look for a bump into the $d\sigma/d\cos\theta dM^2_I$ magnitude, where M_I is the invariant mass of the πN coming from the decay of the produced $N^{*+}_{c\bar{c}}$ state. Assuming a Lorentzian shape for this resonance, with total width $\Gamma_{N^{*+}_{c\bar{c}}}$, we would obtain at the peak of the πN distribution

$$\frac{d\sigma_{p\bar{p} \to N^{*+}_{c\bar{c}}(4265)\bar{p} \to \pi N \bar{p}}}{d\cos\theta dM^2_I} = \frac{1}{\pi} \frac{1}{M_{N^{*+}_{c\bar{c}}} \Gamma_{\rm tot}} \frac{d\sigma_{p\bar{p} \to N^{*+}_{c\bar{c}} \bar{p}}}{d\cos\theta} \frac{\Gamma_{\pi N}}{\Gamma_{\rm tot}} \tag{12.23}$$

which leads to the following cross section: $0.13\ \mu b/{\rm GeV}^2$ for $N^{*+}_{c\bar{c}}(4265)$.

We consider form factors for the π, p and $N^*_{c\bar{c}}$ exchange respectively:

$$F_{pp\pi} = \frac{\Lambda_\pi^2 - m_\pi^2}{\Lambda_\pi^2 - p_\pi^2}\ , \tag{12.24}$$

$$F_p = \frac{\Lambda_p^4}{\Lambda_p^4 + (p_p^2 - m_p^2)^2}, \tag{12.25}$$

$$F_{N^*_{c\bar{c}}} = \frac{\Lambda_N^4}{\Lambda_N^4 + (p^2_{N^*_{c\bar{c}}} - m^2_{N^*_{c\bar{c}}})^2}, \tag{12.26}$$

with $\Lambda_\pi = 1.3$ GeV and $\Lambda_p = \Lambda_N = 0.8 GeV$. Finally, we get a cross section of 0.71 $\mu b/GeV^2$ without the form factors of Eqs. (12.24), (12.25 and (12.26) and 0.072 $\mu b/GeV^2$ using these form factors (if one does not include the form factors of Eqs. (12.25) and (12.26) one gets 0.05 and 0.13 $\mu b/GeV^2$ with and without Eq. (12.24)).

In order to test the role played by the $N^*_{c\bar{c}}$ resonance in the process we should compare with the process $p\bar{p} \to pp\bar{p}\eta_c$ in Figs. 12.3 c),d). The evaluation of these diagrams is similar to the one performed for the diagram a) except for the $pp\eta_c$ vertex, which is given by:

$$\mathcal{L}_{\eta_c p\bar{p}} = g_{\eta_c p\bar{p}} \bar{u}_p \gamma^\mu \gamma^5 \partial_\mu \psi_{\eta_c} v_{\bar{p}}, \tag{12.27}$$

where the coupling constant, $g_{\eta_c p\bar{p}}$, can be calculated by the formula

$$g_{\eta_c p\bar{p}} = \sqrt{\frac{\pi \Gamma_{\eta_c} Br_{\eta_c p\bar{p}}}{|p_p^{on}| m_p^2}}. \tag{12.28}$$

with $p_p^{on} = \lambda^{1/2}(m^2_{\eta_c}, M_p^2, M_{\bar{p}}^2)/2m_{\eta_c}$, $\Gamma_{\eta_c} = 26.7$ MeV and $\mathrm{Br}_{\eta_c p\bar{p}} = 1.3 \times 10^{-3}$. The contributions of Fig. 12.3 c) and d) turn out to be very small, almost 10^{-4} μb, so it follows that the processes where the N^* appears are important in the $p\bar{p} \to pp\eta_c$ reaction with respect to the p exchange. This is shown in the Dalitz plot of Fig. 12.5 a), and the invariant mass spectra of $p\eta_c$, $\bar{p}\eta_c$ and $p\bar{p}$ are shown in b), c) and d), being the peaks of the $N^*(4265)$ very clear.

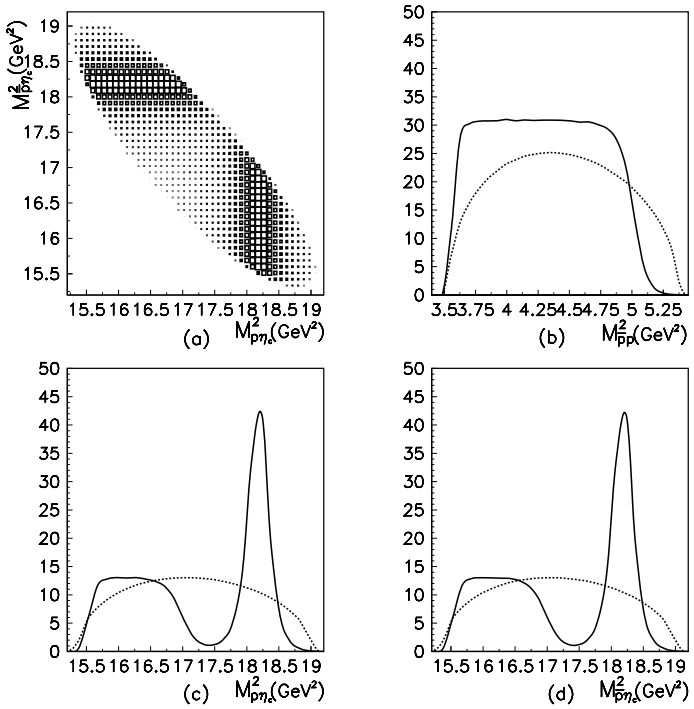

Figure 12.5: The Dalitz plot (a), the invariant mass spectrum of $p\bar{p}$(b), $p\eta_c$(c) and $\bar{p}\eta_c$(d) for the reaction $p\bar{p} \to p\bar{p}\eta_c$ at the beam momentum of $\bar{p}$ being 14.00GeV at lab system.

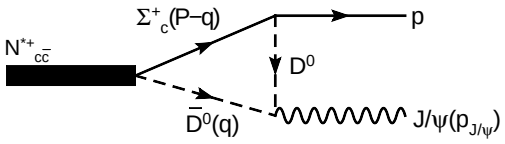

Figure 12.6: Feynman diagram for $N^{*+}_{c\bar{c}}(4265) \to J/\psi p$.

12.5.2 J/ψ production in $p\bar{p} \to \bar{p}pJ/\psi$

Here we calculate J/ψ production in $p\bar{p}$ through the pseudoscalar-baryon resonance, $N^*(4265)$ and the vector-baryon resonance $N^*(4418)$. Lets start with the first process which is the one of Fig. (12.3) a) but changing the η_c by the J/ψ. For this, one needs to know how the $N^*(4265)$ decays into $J/\psi p$, this is depicted in Fig. 12.6. The formula for the cross section for the whole process will be the same than the one of Eq. (12.23) but now we need to evaluate $\Gamma(R \to J/\psi p)$. In order to do it, the diagram of Fig. 12.6 requires the $DN\Sigma_c$ coupling, that was studied in Chapter 10 and has the form

$$-iV_{D^0 p\Sigma_c^+} = \vec{\sigma}\cdot\vec{q}\,'(1-\frac{q'^0}{2M'})\beta\frac{D-F}{2f} \tag{12.29}$$

being $\beta = 1$, and q'^0, $\vec{q}\,'$, the incoming energy, momentum of the D meson and M' the mass of the Σ_c. For D and F we take the standard values $D = 0.8$ and $F = 0.46$ [176, 177, 178]. The $J/\psi \to D\bar{D}$ coupling is obtained through the Lagrangian of Eq. (3.27), which leads to

$$-it_{J/\psi D\bar{D}} = i\,2g\,q_\mu\epsilon^\mu\ . \tag{12.30}$$

Following our phase convention,

$$|\bar{D}\Sigma_c; 1/2, 1/2\rangle = \sqrt{\frac{2}{3}}D^-\Sigma_c^{++} + \frac{1}{\sqrt{3}}\bar{D}^0\Sigma_c^+\ . \tag{12.31}$$

we find

$$-it_{D^0 p\Sigma_c^+} = \frac{0.26}{2f}\vec{\sigma}\cdot\vec{q}\,' \tag{12.32}$$

And the other possible vertex, $D^+p\Sigma_c^{++}$ is $\sqrt{2}$ times the $D^0p\Sigma_c^+$ vertex. Finally, we get

$$\begin{aligned} t_{J/\psi p\to R} &= 2\sqrt{3}\,g\int\frac{d^4q}{(2\pi)^4}\frac{0.26}{2f}g_{R\bar{D}\Sigma_c}\vec{\epsilon}\cdot\vec{q}\,\vec{\sigma}\cdot\vec{q}\,\frac{M_{\Sigma_c}}{E_{\Sigma_c}(q)}F(q) \\ &\times\frac{1}{q^2-m_D^2+i\epsilon}\frac{1}{(p_J-q)^2-m_D^2+i\epsilon} \\ &\times\frac{1}{P^0-q^0-E_{\Sigma_c}(q)+i\epsilon}\ , \end{aligned} \tag{12.33}$$

where we use a form factor $F(q) = \frac{\Lambda^2}{\Lambda^2+\vec{q}^2}$ with $\Lambda = 1.05$ GeV [110] in the integral of Eq. (12.33). Upon neglecting the small three momenta $\vec{p}_{J/\psi}$ compared to the J/ψ mass and performing the q^0 integral, Eq. (12.33) can be written as

$$\begin{aligned} -it_{J/\psi p\to R} &= -\frac{1}{\sqrt{3}}\frac{0.26}{f}\, g_{R\bar{D}\Sigma_c}\, g\, \vec{\sigma}\cdot\vec{\epsilon}\int \frac{d^3q}{(2\pi)^3}\vec{q}^{\,2}\,\frac{M_{\Sigma_c}}{E_{\Sigma_c}(q)} \\ &\times \frac{1}{2\omega_D(q)}\,\frac{1}{p_J^0+2\omega_D(q)}\,\frac{1}{p_J^0-2\omega_D(q)} \\ &\times \frac{1}{P^0-p_J^0-\omega_D(q)-E_{\Sigma_c}(q)}\,\frac{1}{P^0-\omega_D(q)-E_{\Sigma_c}(q)+i\epsilon} \\ &\times \{2(P^0-\omega_D(q)-E_{\Sigma_c}(q)-p_J^0-2\omega_D(q)\}\ , \end{aligned} \tag{12.34}$$

where $\omega_D(q) = \sqrt{q^2+m_D^2}$ and $E_{\Sigma_c}(q) = \sqrt{q^2+m_{\Sigma_c}^2}$. The width of $N^{*+}_{c\bar{c}} \to J/\psi p$ is now given by

$$\Gamma_{J/\psi p} = \frac{1}{2\pi}\frac{M_p}{M_R}p|\tilde{t}_{J/\psi p\to R}|^2 \tag{12.35}$$

where $\tilde{t}_{J/\psi p\to R}$ means $t_{J/\psi p\to R}$ omitting the $\vec{\sigma}\cdot\vec{\epsilon}$ operator. We take $P^0 = M_R = 4265$ MeV and $p = \lambda^{1/2}(M_R^2, M_{J/\psi}^2, M_p^2)/2M_R$, while M_p stands for the mass of the proton. By using the form factor of [110], we get

$$\Gamma_{R\to J/\psi p} = 0.01 \text{ MeV}\ , \tag{12.36}$$

with admitted uncertainties of the order of a factor two. Since $\Gamma_{\pi N}$ of the $N^{*+}_{c\bar{c}}(4265)$ was of the order of 2.4 MeV, now the cross section of Eq. (12.23) is about a factor 200 smaller than before. Yet, the fact that the background for $J/\psi p$ production is also smaller might compensate for it. From what we have said before, the cross section for $\eta_c p$ production is much bigger.

On the other hand, for the resonances made out by VB, the $J/\psi p$ production cross sections are larger. One can repeat the calculations

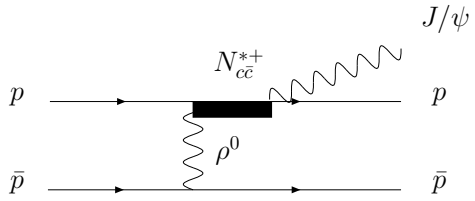

Figure 12.7: The $p\bar{p} \to J/\psi p\bar{p}$ mechanism throughout the resonance $N^{*+}_{c\bar{c}}$

in this case and one obtains cross sections of the order of that for $\eta_c p$ for the case of PB resonances. We sketch the derivation below.

We shall make the estimate based upon the mechanism of the Feynman diagram of Fig. 12.7, and we will consider the resonance $N^*_{c\bar{c}}(4418)$ coming from the interaction of vector mesons with baryons, one of which channels is $J/\Psi p$. By adding this new channel we redo the calculation and obtain $g_{XJ/\Psi N} = 0.85$, where the spin part can be ignored since the coupling is done in a way that allows us to evaluate decay widths in the same way as if the particles were spinless. Assuming the dominant decay channels of N^* as ρN and dominance of the γ^0 term in the $\rho^0 p\bar{p}$ vertex, which goes then as $g\gamma^0/\sqrt{2}$, we obtain now

$$\frac{d\sigma}{d\cos\theta} = \frac{g^2}{4}\frac{M_X^2}{s}\frac{\Gamma_{\rho N}}{p_\rho^{\rm on}}\frac{E(p')E(p) + \vec{p}.\vec{p}' + M^2}{(2M^2 - \sqrt{s}E(p') + 2\vec{p}.\vec{p}' - M_\rho^2)^2}\frac{p'}{p} \qquad (12.37)$$

with p', p the $\bar{p}$ outgoing, incoming momenta in the center of mass frame, and $p_\rho^{\rm on}$ the ρ momentum in the $N^*(4418)$ decay into ρN. By multiplying the cross section of Eq. (12.37) by the branching ratio of the resonance for the decay into $J/\psi p$ we can calculate the cross section of the reaction $p\bar{p} \to J/\psi p\bar{p}$ which is of the order of $2 \sim 37$ nb for a $\bar{p}$ beam of 15 GeV/c, depending on whether one includes or not the form factors. This cross section is larger than the one we would obtain from the standard mechanism of Fig. 12.8 which can be evaluated in analogy to the case of Fig. 12.3. Once again,

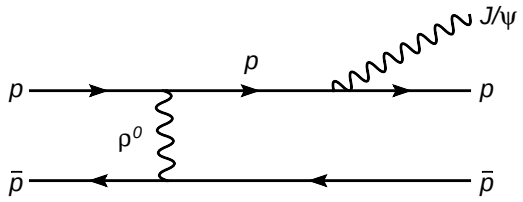

Figure 12.8: The standard $p\bar{p} \to J/\psi p\bar{p}$ mechanism.

using Eq. (12.23) and $\Gamma_{J/\psi p}$ of the resonance instead of $\Gamma_{\pi N}$ we can obtain the differential cross section of the peak of the resonance: $6 \sim 50nb/GeV^2$.

From the calculation above, we find that the cross section of this reaction is about two orders of magnitude smaller than that of the reaction $p\bar{p} \to p\bar{p}\eta_c$, but it could be also appropriate to find $N(4418)$ because the J/ψ has a large branching ratio to decay into lepton channels which are much easier to detect than hadron channels. Finally let us discuss the possibility of measurement of this reaction in the experiments. The PANDA (anti-Proton Annihilation at Darmstadt) Collaboration will study the $p\bar{p}$ reaction at FAIR, with the $\bar{p}$ beam energy in the range of 1.5 to 15 GeV/c and luminosity of about $10^{31}cm^2s^1$. The range of the beam energy is very suitable to find the $N(4265)$ and the $N(4418)$, with total cross sections estimated to be about 70 nb and 2 nb by the one-meson exchange propagators with off-shell form factors, which corresponds to an event production rate of 60000 and 1700 per day at PANDA/FAIR. There is a 4π solid angle detector with good particle identification for charged particles and photons at PANDA/FAIR. For the $p\bar{p} \to p\bar{p}\eta_c$ reaction, if p and $\bar{p}$ are identified, then the η_c can be easily reconstructed from the missing mass spectrum against p and $\bar{p}$. It is the same as the reaction $p\bar{p} \to p\bar{p}J/\psi$. So this reaction should be accessible at PANDA/FAIR.

Chapter 13

Conclusions

We have applied the Hidden Gauge Lagrangians to the study of the vector - vector interaction of a large variety of systems, from the $\rho\rho$ to $D^*\bar{D}^*$ or exotic systems like $D^*D_s^*$. The interaction comes from contact terms plus vector exchange terms in the t and u channels. We have seen that the s-channel represents a minor component of s-wave and that the strong interaction obtained is due to the exchange terms mostly. Amplitudes are unitarized by means of the Bethe Salpeter equation. We look for poles in the complex plane. While bound states appear in the real axis and below threshold, resonances are locate above threshold. The step to SU(4) is only given after the results obtained in SU(3) are shown to agree with the experiment. The extension must be done carefully and being aware of calculating uncertainties. The stability of the results when changing the free parameters gives us confidence on the results. Thus, we follow the work done in [108] and [109] for the study of the pseudoscalar-pseudoscalar and pseudoscalar-vector interaction in the charm sector. The strategy is construct an SU(4)-flavor symmetrical Lagrangian for the interaction of the 15-plet of vector mesons and then, the symmetry is broken down to SU(3) by suppressing exchanges of heavy vector mesons in the implicit Weinberg-Tomozawa term. This suppression

is justified by the vector exchange picture, where the interaction is driven by vector meson exchanges. From the Lagrangians, tree level amplitudes are evaluated projecting in s-wave and including all the possible amplitudes between channels in a matrix for a particular sector. This matrix in isospin basis is the kernel V of the Bethe Salpeter equation, which provides the unitarized T-matrix. A novelty in the study of the vector-vector interaction is the explicit calculation of several different decay modes to pseudoscalar mesons. First, by convoluting the two-meson loop function, thus, taking into account the width of the ρ or K^* mesons. This gives a mechanism for the vector-vector states obtained to decay into four pseudoscalars. Second, box-diagrams including four pseudoscalar mesons are constructed, the direct term (two-pseudoscalar in the main cut) provides the decay width of the states to two pseudoscalar mesons, and represents a much larger width in general than the convolution of the two-meson loop function. Additional terms are studied in Chapter 3, as box-diagrams with anomalous vertices $\rho\omega\pi$ and crossed-box diagrams including pseudoscalar mesons that provide decay widths to four pseudoscalars, the first kind do not have imaginary part and the second one represents about the 20% of the direct term which can be absorved by the freedom in the Λ parameter of the pseudoscalar-pseudoscalar-vector form factor.

In the following, we summary one by one the results obtained for each sector studied, including also the discussion on the results concerning the radiative decays studied for some of the resonances.

- **The $\rho-\rho$ interation.** Amongst all the spin and isospin allowed channels in s-wave, we found strong attraction, enough to bind the system, in $I = 0, S = 0$ and $I = 0, S = 2$. We also found that in the case of $I = 0, S = 2$ the interaction was more attractive, leading to a tensor state more bound than the scalar. The consideration of the ρ mass distribution gives a width to the two states, very small in the case of the tensor state because of its large binding. However, the biggest source of width comes from the decay into $\pi\pi$ that we have also studied within the same

formalism. We found the width much larger for the case of the scalar state. We also studied the effect of the crossed-$\pi\pi$-box diagrams and the contribution of $\omega\omega$-intermediate states with anomalous couplings, which were found to play a minor role. The states obtained could be associated with the $f_0(1370)$ and $f_2(1270)$, for which we found a qualitative agreement with experiment on the mass and width. The findings of the paper give support to the idea that these two resonances are dynamically generated from the $\rho\rho$ interaction, or in other words, that they qualify largely as $\rho\rho$ molecules. We extended the formalism to account for the radiative decay of the resonances into $\gamma\gamma$. The extension has been done following the standard method to deal with dynamically generated resonances, in which the photons are coupled to the components of the resonance, in this case $\rho\rho$. This is technically implemented by means of loop functions which involve the photon couplings to the components of the resonance. In the present case, the peculiarity of the hidden gauge approach, in which the photons couple directly to one ρ^0, allows a factorization of the strong part of the interaction and the final result is converted into a tree level contribution, hence rid of any ambiguity due to possible divergences of the loops. The results obtained for the radiative width of the $f_2(1270)$ are in perfect agreement with experimental data. So are those for the $f_0(1370)$ when they are compared with the experimental results of the Crystal Ball collaboration, or those of the more recent experiment by Belle within its large errors. Yet, the large systematic errors quoted in the work from Belle, that has much better statistics, should raise some caution on these experimental numbers. With the ultimate goal of learning about the nature of the two resonances discussed, and having in mind the picture as dynamically generated states emerging from the $\rho\rho$ interaction in the local hidden gauge approach, the test passed here in the radiative decay is a first step in the search of support for this idea, and further tests should

be most welcome. To further strengthen this idea it would be most useful to have good results for the radiative decay width of the $f_0(1370)$ state, as well as results from other theoretical models for both resonances which could tell us how stringent is the test of this radiative decay to discriminate among different models.

- **The $(\rho\omega)D^*$ interaction.** We found strong attraction, enough to bind the system, in $I = 1/2, S = 0$, $I = 1/2, S = 1$ and $I = 1/2, S = 2$. We also found that in the case of $I = 1/2, S = 2$ the interaction was more attractive than in the other two cases, leading to a tensor state more bound than the scalar and the axial vector. The consideration of the ρ mass distribution gives a width to the three states, rather small in all cases. Consideration of the πD decay channel, in an equivalent way to what was done in the case of the $\rho\rho$ interaction going to $\pi\pi$ in [85], makes the widths larger and realistic. Yet, the smaller phase space available here makes this contribution relatively smaller than in the case of the $\rho\rho$ interaction. We found that the tensor state obtained matches the properties of the tensor state $D_2^*(2460)$. We predict two more states with $S = 0$ and $S = 1$, which are less bound than the tensor state. We find in the PDG the state $D^*(2640)$ without experimental spin and parity assigned, but we conjecture that this state should be the $S = 1$ state found by us because we could find a natural explanation for the small experimental width of this state. The other state nearly degenerate in energy with this one, but with spin $S = 0$, would be stillto be found.

- **The XYZ particles.** We have made a full study of the vector - vector interaction in the $C = 0$ and $S = 0$ sector using the hidden gauge formalism. We have found a strong attraction in the $I = 0$, $J = 0, 1, 2$ and $I = 1$, $J = 2$ sectors, enough to bind the vector - vector system. By looking for poles in the second Riemann sheet, we have found five resonances, three

of which can be associated with the experimental data: The state $(3943, 0^+[0^{++}])$ to the $Y(3940)$, the $(3922, 0^+[2^{++}])$ to the $Z(3930)$ and the $(4157, 0^+[2^{++}])$ to the $X(4160)$. There is no experimental counterpart for our state $(3945, 0^-[1^{+-}])$, which is thus a prediction of our model. These three states with mass around 3940 MeV are basically composed by $D^*\bar{D}^*$, and decay into pairs of light vectors like $K^*\bar{K}^*$, or light vector - heavy vector as $\omega J/\psi$. Our model predicts another state around 4160 MeV, $(4157, 0^+[2^{++}])$, which we identify with the $X(4160)$ state in base to the proximity of mass and width and C-parity. This resonance has $J^{PC} = 2^{++}$ and is mostly $D_s^*\bar{D}_s^*$. In the $I = 1$ sector, the attraction is weak and we find only one resonance in the case of $J = 2$, $(3912, 1^-[2^{++}])$, the possible association of this state to the $X(3940)$ is unlikely since our state can decay to $D\bar{D}$, though with small intensity, but this decay is not seen for the $X(3940)$. The width that we obtain is also considerably larger than that of the $X(3940)$, $\Gamma = 120$ MeV.

According to their masses and widths three of them are good candidates for the $Y(3940)$, $Z(3930)$ and $X(4160)$ mesons discovered by BELLE and BaBar with the Z(3930) maybe corresponding to the recently observed X(3915). The calculation of their radiative decays into two photons or vector-photon is done. The information on the $\Gamma_{\gamma\gamma}$ decay rate of the X(3915) favors the association of this resonance to the (2^+, 3922) resonance that we obtain. Here, the quantum numbers 0^+ are clearly disfavored.

We find a very distinctive shape in the $\bar{D}\gamma$ and $\bar{D}_s\gamma$ invariant mass distributions of the $Y(3940)$, $Z(3930)$ and $X(4160)$, which is peculiar to the molecular nature of these states as basically bound states of two charmed vector mesons.

Unfortunately there is not much data on radiative decays of the X, Y and Z mesons. The large variety of results obtained by us concerning the different decays and different resonances

indicates that these measurements are very useful to shed light on the structure of these resonances.

- **Other sectors including exotic flavor.** We studied dynamically generated resonances from vector-vector interaction in the charm-strange and hidden-charm sectors and extended for the first time the formalism to flavor exotic sectors. Our analysis of the T matrix resulted in nine bound states. We can assign one resonance to an experimental counterpart, which is the $D_2^*(2573)$. For $C = 1, S = 1$ we obtain three states with masses $M = 2683$, 2707 and 2572 MeV for $I = 0$ and $J = 0, 1, 2$ respectively. The widths lie around 44, 0 and 18 MeV correspondingly (Model B with $\Lambda = 1000$ MeV). We associate the state for $J = 2$ with the $D_2^*(2573)$ giving a novel interpretation for this resonance as a vector-vector molecular state. The assumption of this structure is consistent with the DK nature assumed for the $D^*(2317)$, the D^*K molecular structure of the $D^*(2460)$ or the X(3872) ($D\bar{D}^*$). The other two states around 2700 MeV are predictions of the model without experimental evidence for these masses and quantum numbers up to now. For $I = 1$ we find only one state, of non exotic nature, a 2^+ state around 2786 MeV.

  In the flavor-exotic sectors which had not been studied before, we obtain interesting predictions for new states. In the sector $C = 1; S = -1; I = 0$ we obtain three new exotic states with masses $M = 2848$, 2839 and 2733 MeV and widths around $\Gamma = 25$, 3 and 22 MeV, for the quantum numbers $I[J^P] = 0[0^+]$, $0[1^+]$ and $0[2^+]$ respectively. In the case of the double-charm sectors $C = 2; S = 0; I = 0$ and $C = 2; S = 1; I = 1/2$ the potential leads to a bound system for $J = 1$ only. That is, we deal with two very narrow states with masses around $M =$ 3969 and 4101 MeV close to the thresholds of D^*D^* and $D_s^*D^*$ respectively. In summary, all states are relatively narrow. For the quantum numbers $J^P = 0^+, 2^+$ the widths are lower than

71 MeV (depending on the model) while all states with $J^P = 1^+$ come with practically no width since the box diagrams do not contribute. There is no experimental counterpart for all exotic structures which can be considered as D^*K^*, $D^*\bar{K}^*$, D^*D^* and $D_s^*D^*$ molecular states.

The results obtained here should stimulate the search for new states in the charm sector, in particular, more D states in the region of $2600\,MeV$. There could be also more resonances not yet seen in the region around 3940 MeV where we find a state with $I = 1$ and $J^{PC} = 2^{++}$ and another one with $I = 0$ and $J^{PC} = 1^{+-}$ without experimental counterparts. The findings of this work should motivate the experimentalist to look into this region in the channels that involve light vector - light vector or light vector - heavy vector like $K^*\bar{K}^*$ and $\rho J/\psi$. In addition, the existence of very interesting charmed resonances in the flavor exotic sectors is claimed.

Regarding the study of charmed and strange vector mesons in the medium, we have seen:

- **Charmed mesons in the nuclear medium.** We have evaluated the selfenergy of low lying scalar mesons with open and hidden charm in a nuclear medium, concretely of the $D_{s0}(2317)$ and the theoretical hidden charm state $X(3700)$. The many body calculation has been done following the lines of previous studies in the renormalization of the light scalar mesons in the nuclear medium. The medium effects for the $D_{s0}(2317)$ and $X(3700)$ resonances are spectacular. Those resonances, which have zero and small width in free space, respectively, develop widths of the order of 100 and 200 MeV at normal nuclear matter density, respectively. The study also allowed us to trace back the reactions in the medium which are responsible for the decay width of these mesons and which could be investigated in future reactions at hadron facilities.

  The experimental analysis of the charmed meson properties in the medium is a valuable test of the dynamics of the D me-

son interaction with nucleons and nuclei, and the nature of the charm and hidden charm scalar resonances, all of them topics which are subject of much debate at present. In particular, it should stimulate experimental work in this direction at FAIR [236], where the investigation of charm physics is one of the priorities. The option of looking at transparency ratios was also suggested as a mean to investigate the widths of these mesons in nuclei. It was also discussed that the experimental study of this width and the medium reactions contributing to it provide information on the basic features of the resonance and the selfenergy of the D meson in a nuclear medium.

- **Strange-vector mesons in the medium.** We have studied the properties of $\bar{K}^*$ mesons in symmetric nuclear matter within a self-consistent coupled-channel unitary approach using hidden-gauge local symmetry. The corresponding in-medium solution incorporates Pauli blocking effects and the $\bar{K}^*$ meson self-energy in a self-consistent manner.

  In particular, we have analyzed the behavior of dynamically-generated baryonic resonances in the nuclear medium and their influence in the self-energy and, hence, the spectral function of the $\bar{K}^*$ mesons. We have found a moderate attractive optical potential for the $\bar{K}^*$ of the order of -50 MeV at normal nuclear matter density. The corresponding quasiparticle peak in the spectral function might not be easily distinguished due to its merging with other excitations, apart from the fact that changes of mass are always very difficult to determine in experiments [208]. More remarkable are the changes in the width, which can be more easily addressed by means of transparency ratios in different reactions. At normal nuclear matter density the $\bar{K}^*$ width is found to be about 260 MeV, five times larger than its free width. This spectacular increase is much bigger than the width of the ρ meson in matter, evaluated theoretically in [193, 194, 195, 196] or measured recently [201, 225, 237, 238].

We have made an estimation of the transparency ratios in the $\gamma A \to K^+ \bar{K}^* A'$ reaction and found a substantial reduction from unity of that magnitude, which should be easy to observe experimentally. Other reactions like the $K^- A \to K^{*-} A'$ should also be good tools to investigate these important changes linked to the strong $\bar{K}^*$ interaction with the nuclear medium [239].

- $N^*_{c\bar{c}}$ **and** $\Lambda^*_{c\bar{c}}$ **resonances around** 4 **GeV.** A previous step done in this thesis in order to study the properties of the J/ψ meson in the nuclear medium is to study the interaction of charmed vector mesons with charmed baryons. Going further in this direction, in the last Chapter we have found two $N^*_{c\bar{c}}$ states and four $\Lambda^*_{c\bar{c}}$ states from PB and VB channels by using the local hidden gauge Lagrangian in combination with unitary techniques in coupled channels. All of these states have large $c\bar{c}$ components, so their masses are all larger than 4200 MeV. The width of these states decaying to light meson and baryon channels without $c\bar{c}$ components are all very small. On the other hand, the $c\bar{c}$ meson - light baryon channels are also considered to contribute to the width to these states. Then $\eta_c N$ and $\eta_c \Lambda$ are added to the PB channels, while $J/\psi N$ and $J/\psi \Lambda$ are added in the VB channels. The widths to these channels are not negligible, in spite of the small phase space for the decay, because the exchange D^* or D^*_s mesons are less off-shell than the corresponding one in the decay to light meson - light baryon channels. The total widths of these states are still very small. We made some estimates of cross sections for production of these resonances at the upcoming FAIR facility. The cross section of the reaction $p\bar{p} \to p\bar{p}\eta_c$ and $p\bar{p} \to p\bar{p}J/\psi$ are about $0.1\mu b$ and $0.2nb$, in which the main contribution comes from the predicted $N^*_{c\bar{c}}(4265)$ and $N^*_{c\bar{c}}(4415)$ states, respectively. With this theoretical results, one can estimate over 80000 and 1700 events per day at the PANDA/FAIR facility. Similar event rate is expected for the predicted $\Lambda^*_{c\bar{c}}(4210)$ state in the $p\bar{p} \to \Lambda\bar{\Lambda}\eta_c$

reaction. As a consequence, these three predicted new narrow N^* and Λ^* resonances could be observed by the PANDA/FAIR. The other three predicted $\Lambda^*_{c\bar{c}}$ resonances will remain for other future facilities to discover.

Although in the scheme of dynamical generated states these new $N^*_{c\bar{c}}$ and $\Lambda^*_{c\bar{c}}$ states are simply brothers or sisters of the well-known $N^*(1535)$ and $\Lambda^*(1405)$ in the hidden charm sector, their discovery will be extremely important. While for the $N^*(1535)$, $\Lambda^*(1405)$ and many other proposed dynamically generated states cannot be clearly distinguished them from those generated states in various quenched quark models with qqq for baryon states and $q\bar{q}$ for meson states due to many tunable model ingredients, these new narrow N^* and Λ^* resonances with mass above 4.2 GeV definitely cannot be accommodated by the conventional 3q quark models, although how to distinguish these meson-baryon dynamically generated states from possible five-quark states needs more detailed scrutiny. The existence of these new resonances with hidden charm may also have important implications to the long-standing puzzles relevant to charmonium production in various collisions involving nucleon in the initial state, such as the strikingly large spin-spin correlation observed in pp elastic scattering near charm production threshold [240] and difficulties in reproducing the cross sections and polarization observables of J/ψ production from high energy $\bar{p}p$, pp and γp reactions [153, 241]. These issues deserve further exploration.

Chapter 14

Resumen en español

14.1 Introducción

En la tesis, el campo vectorial juega un papel central. Así, comenzamos describiendo brevemente las distintas formas de trabajar con campos vectoriales. Existen diversas formas de introducir campos de mesones vectoriales en Lagrangianos efectivos dependiendo de [13, 14, 15]:

1) si se asigna un vector V_μ o un tensor antisimétrico $V_{\mu\nu} = V_{\nu\mu}$ [14, 16],

2) de cómo los campos se transforman bajo una realización de la simetría quiral, que puede ser lineal (directamente con los elementos g de la simetría, $V_\mu \to g V_\mu g^\dagger$) o no-lineal (por medio de una función $h(g)$). A su vez la transformación puede ser homogénea, $V_\mu \to h V_\mu h^\dagger$, o no homogénea, $V_\mu \to h V_\mu h^\dagger + \text{cte}\, h\partial_\mu h^\dagger$,

3) el origen de los mesones vectoriales, que pueden ser o no bosones gauge.

Los principales tipos de teorías en que los mesones vectoriales corresponden a bosones gauge son: las teorías de Yang Mills y las de hidden gauge [21]. En las teorías de Yang-Mills [13, 19, 20], los mesones vectoriales son los bosones gauge de la teoría de Yang-Mills, mientras que en las teorías de hidden gauge, la matriz $U(x)$ que contiene los bosones Goldstone se descompone en dos factores, $U(x) = \xi_L(x)\xi_R^\dagger(x)$ y esta factorización introduce una simetría artificial en la que aparecen los mesones vectoriales como bosones gauge de la simetría oculta en las derivadas covariantes. La clasificación de las distintas teorías que incorporan mesones vectoriales en los lagrangianos efectivos y sus características esenciales se resumen en la Tabla 14.1.

	Yang-Mills	hidden symmetry	WCCWZ	EGPdR
campo	vector			tensor
origen	bosón de gauge		dif. de bosón de gauge	
realización quiral	lineal	no lineal y homogénea		

Table 14.1: Características esenciales de los distintos modelos que incorporan campos de mesones vectoriales

Aunque las formas de los lagrangianos de las diversas teorías que incorporan mesones vectoriales y los tipos de acoplamientos son diferentes, todas ellas son en principio equivalentes y su variedad se debe simplemente a la libertad que uno tiene al escoger los campos de espín-1. La mayoría de ellas están motivadas en las ideas fenomenológicas de dominancia de mesones vectoriales y acoplamiento universal [17, 18], como en las teorías de Yang-Mills y de hidden gauge, donde los términos cinéticos y acoplamientos de los campos de espín 1 tienen la misma forma que en una teoría gauge, reflejando así el acoplamiento universal de estos mesones a las corrientes conservadas. Por medio de términos locales y asunciones básicas rela-

cionadas con dominancia de mesones vectoriales, se ha demostrado que los formalismos WCCWZ [15, 22, 23, 24] y EGPdR [14] son equivalentes hasta $O(p^4)$ [25], mientras que mediante un cambio de variables de los campos de espín 1, cualquier teoría de Yang Mills puede ser convertida en una WCCWZ equivalente. En las teorías de Yang-Mills masivas, los campos vectoriales y axiales se transforman bajo una realización lineal de la simetría quiral. El uso de una realización no lineal de la simetría quiral significa que cualquier mesón y su compañero quiral (p. ej. ρ y a_1) son tratados de la misma manera. Sin embargo, es posible escribir lagrangianos de Yang Mills con sólo el mesón ρ pero asegurándose la satisfacción de los teoremas de baja energía quirales por medio de términos adicionales. Ésto puede hacerse escribiendo una teoría hidden gauge que genere estos términos y reformulándola en un Lagrangiano de la forma de Yang Mills con un cambio de variables. En la formulación de hidden gauge, una simetría local es introducida en un modelo sigma no lineal por medio de una elección particular de los campos. El mesón se introduce como un bosón gauge de la simetría. La simetría local no implica nueva física asociada a ésta y puede ser eliminada fijando el gauge. En concreto, en el gauge unitario, la simetría se reduce a la realización no lineal de la simetría quiral bajo la cual los campos vectoriales se transforman inhomogéneamente, de forma opuesta al esquema WCCWZ. Sin embargo, cualquier lagrangiano de una teoría hidden gauge puede ser transformado mediante un cambio de variable en uno equivalente del esquema WCCWZ [31]. Realmente, la constante de acoplamiento gauge no es más que un parámetro de elección del campo vectorial. La elección convencional elimina las dependencias de momento de O(p^3) del acoplamiento $\rho\pi\pi$ dejando correcciones de orden p^5. Además, si el acoplamiento $\gamma\rho$ satisface una relación particular, entonces también se eliminan las correcciones de orden p^2 del mixing. Esta reducción de la dependencia de momento es responsable de que, en la formulación de hidden gauge, se satisfaga de modo natural (en ausencia de condiciones extra) la relación KSFR obervada empíricamente en la desintegración del mesón ρ [32, 33].

14.2 Formalismo

En el formalismo de hidden gauge, los campos de los mesones vectoriales son bosones gauge de una simetría local que se transforman inhomogéneamente. Una vez que se escoge el gauge unitario, estos campos se transforman exáctamente como en la realización no lineal de la simetría quiral [22]. En [25], se demuestra que este formalismo es equivalente al de [14], donde los vectores se transforman homogéneamente bajo una realización de la simetría quiral. El Lagrangiano que contiene campos de mesones, fotones y vectores al mismo tiempo, puede ser escrito como:

$$\mathcal{L} = \mathcal{L}^{(2)} + \mathcal{L}_{III} \tag{14.1}$$

donde

$$\mathcal{L}^{(2)} = \frac{1}{4} f^2 \langle D_\mu U D^\mu U^\dagger + \chi U^\dagger + \chi^\dagger U \rangle \tag{14.2}$$

$$\mathcal{L}_{III} = -\frac{1}{4}\langle V_{\mu\nu} V^{\mu\nu} \rangle + \frac{1}{2} M_V^2 \langle [V_\mu - \frac{i}{g}\Gamma_\mu]^2 \rangle, \tag{14.3}$$

siendo $\langle ... \rangle$ la traza sobre matrices de $SU(3)$. La derivada covariante se define como

$$D_\mu U = \partial_\mu U - ieQA_\mu U + ieUQA_\mu, \tag{14.4}$$

con $Q = diag(2, -1, -1)/3$, $e = -|e|$ la carga del electrón, y A_μ el campo del fotón. Por otro lado, la matriz quiral U está dada por

$$U = e^{i\sqrt{2}P/f} \tag{14.5}$$

siendo f la constante de desintegración del pión ($f = 93$ MeV). P y V_μ son matrices de $SU(3)$ que contienen los campos pseudoscalares y vectoriales, $V_{\mu\nu}$ viene dado por

$$V_{\mu\nu} = \partial_\mu V_\nu - \partial_\nu V_\mu - ig[V_\mu, V_\nu] \ , \tag{14.6}$$

siendo g,

$$g = \frac{M_V}{2f} \ , \tag{14.7}$$

Del Lagrangiano de la Ec. (14.3) podemos extraer los términos de contacto de tres y cuatro vectores, que son respectivamente,

$$\mathcal{L}_{III}^{(3V)} = ig\langle (\partial_\mu V_\nu - \partial_\nu V_\mu) V^\mu V^\nu \rangle \ , \tag{14.8}$$

y

$$\mathcal{L}_{III}^{(c)} = \frac{g^2}{2} \langle V_\mu V_\nu V^\mu V^\nu - V_\nu V_\mu V^\mu V^\nu \rangle \ . \tag{14.9}$$

Donde V_μ viene dado por

$$V_\mu = \begin{pmatrix} \frac{\rho^0}{\sqrt{2}} + \frac{\omega}{\sqrt{2}} & \rho^+ & K^{*+} \\ \rho^- & -\frac{\rho^0}{\sqrt{2}} + \frac{\omega}{\sqrt{2}} & K^{*0} \\ K^{*-} & \bar{K}^{*0} & \phi \end{pmatrix}_\mu \ . \tag{14.10}$$

En lo que sigue utilizaremos los Lagrangianos de Hidden Gauge explicados con anteriodad para calcular el potencial de interacción de dos mesones vectoriales. En primer lugar se calcula para el sistema de dos mesones ρ que es el caso más simple que puede haber [85]. El formalismo se extiende al caso general de cualquier par de mesones vectoriales de SU(3) en [86]. Más tarde, se incluyen en el modelo los mesones con encanto, tratando todos los sectores posibles, desde (encanto $= 1$; extrañeza $= 0$)[116], (encanto $= 0$; extrañeza $= 0$) (encanto oculto)[136] hasta los sectores exóticos como (encanto $= 1$; extrañeza $= -1$) o (encanto $= 2$; extrañeza $= 1$)[155]. Las amplitudes se unitarizarán por medio de la evaluación de la ecuación de Bethe Salpeter y finálmente se procederá a la búsqueda de polos de la amplitud de dispersión en el plano complejo de la energía y a la asociación de estos en los casos que sea posible con estados ya observados, mientras que otros estados darán lugar a predicciones de la teoría. También, los canales de desintegración a mesones pseudoscalares son incorporados pudiendo así explicar en muchos casos la mayor parte de la anchura observada.

14.2.1 Potencial de dispersión de dos vectores

El lagrangiano de la Ec. (14.9) da lugar al diagrama de la Fig. 14.1 a), y el término de contacto de tres vectores de la Ec. (14.8) proporciona los vértices del diagrama de intercambio de vectores de la Fig. 14.1 b) y c). Además, incluimos diagramas que involucran mesones pseudoscalares como los mostrados en la Fig. 14.1 d). Los diagramas de la Fig. 14.1 a)-d) son los mecanismos que contribuyen a construir el potencial de onda s de interacción de dos vectores y el kernel V de la ecuación de Bethe-Salpeter. Como veremos, los diagramas a) y b) son la parte fuerte del potencial y producen estados ligados por sí mismos. Mientras que los diagramas de la Fig. 14.1 d) dan esencialmente la parte imaginaria del potencial y así, dan cuenta de la anchura de desintegración de los estados. La amplitud del diagrama de la Fig. 14.1 c) es onda p y repulsivo para párticulas de la misma masa, mientras que resulta débilmente atractivo para partículas de masa diferente.

El vértice vector-pseudoscalar-pseudoscalar del diagrama con forma de caja de la Fig. 14.1 d) viene dado por el mismo formalismo del Lagrangiano de la Ec. (14.3), véase la Ec. (2.16). Para unitarizar las amplitudes de dispersión es necesario realizar una resumación de loops lo cuál viene implícito en la ecuación de Bethe Salpeter [55]. Para realizar esta resumación es necesario factorizar la estructura de espín en la serie de loops.

La estrucura de espín de la amplitud de dispersión de dos vectores es una combinación de todas las posibles contracciones de los vectores de polarización, que son, $\epsilon_1^\mu \epsilon_{2\mu} \epsilon_3^\nu \epsilon_{4\nu}$, $\epsilon_1^\mu \epsilon_2^\nu \epsilon_{\mu 3} \epsilon_{4\nu}$ y $\epsilon_1^\mu \epsilon_{2\nu} \epsilon_3^\nu \epsilon_{4\mu}$. Puesto que todos los estados posibles tienen espín definido, necesitamos proyectar las amplitudes en espín. Para hacer esto, uno construye unos tensores de espín que contienen estas combinaciones de vectores de polarización pero que poseen un espín definido. Los proyectores de espín se contruyen a partir de éstos y en la aproximación de despreciar el momento de las partículas externas respecto de la masa del mesón vectorial, $\vec{q}^2/M_V^2 \sim 0$, quedan estructuras muy

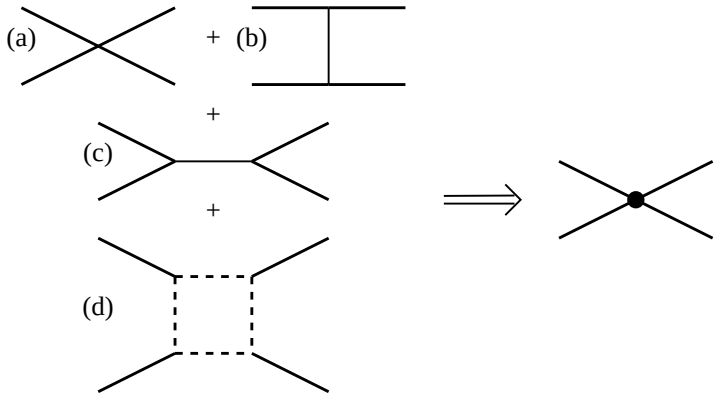

Figure 14.1: Mecanismos que contribuyen a la dispersión vector - vector a orden árbol, los cuales son incluidos en el potencial V en la ecuación de Bethe-Salpeter [55].

simplificadas. Los proyectores sobre espín$= 0, 1, 2$ son:

$$\begin{aligned}
\mathcal{P}^{(0)} &= \frac{1}{3}\epsilon_\mu\epsilon^\mu\epsilon_\nu\epsilon^\nu \\
\mathcal{P}^{(1)} &= \frac{1}{2}(\epsilon_\mu\epsilon_\nu\epsilon^\mu\epsilon^\nu - \epsilon_\mu\epsilon_\nu\epsilon^\nu\epsilon^\mu) \\
\mathcal{P}^{(2)} &= \{\frac{1}{2}(\epsilon_\mu\epsilon_\nu\epsilon^\mu\epsilon^\nu + \epsilon_\mu\epsilon_\nu\epsilon^\nu\epsilon^\mu) - \frac{1}{3}\epsilon_\alpha\epsilon^\alpha\epsilon_\beta\epsilon^\beta\} \ . \qquad (14.11)
\end{aligned}$$

Para la proyección de isospín, la normalización unitaria descrita en [51] es usada. El uso de esta normalización implica añadir un factor $\frac{1}{\sqrt{2}}$ extra para cada estado de isospín de partículas idénticas. De

modo que los estados de isospín$= 0, 1, 2$ para dos mesones ρ son:

$$\begin{aligned}
|\rho\rho, I=0\rangle &= -\frac{1}{\sqrt{6}}|\rho^+(k_1\epsilon_1)\rho^-(k_2\epsilon_2)+\rho^-(k_1\epsilon_1)\rho^+(k_2\epsilon_2) \\
&\quad +\rho^0(k_1\epsilon_1)\rho^0(k_2\epsilon_2)\rangle \qquad (14.12)\\
|\rho\rho, I=1, I_3=0\rangle &= -\frac{1}{2}|\rho^+(k_1\epsilon_1)\rho^-(k_2\epsilon_2)-\rho^-(k_1\epsilon_1)\rho^+(k_2\epsilon_2)\rangle \\
|\rho\rho, I=2, I_3=0\rangle &= -\frac{1}{\sqrt{2}}|\frac{1}{\sqrt{6}}(\rho^+(k_1\epsilon_1)\rho^-(k_2\epsilon_2)+\rho^-(k_1\epsilon_1)\rho^+(k_2\epsilon_2)) \\
&\quad -\sqrt{\frac{2}{3}}\rho^0(k_1\epsilon_1)\rho^0(k_2\epsilon_2)\rangle\ .
\end{aligned}$$

Mientras que las combinaciones para el sistema ρD^* con isoespín$=$ $1/2$ y $3/2$ son:

$$\begin{aligned}
|\rho D^*, I=1/2, I_3=1/2\rangle &= \sqrt{\frac{2}{3}}|\rho^+ D^{*0}\rangle - \frac{1}{\sqrt{3}}|\rho^0 D^{*+}\rangle, \\
|\rho D^*, I=1/2, I_3=3/2\rangle &= \frac{1}{\sqrt{3}}|\rho^+ D^{*0}\rangle + \sqrt{\frac{2}{3}}|\rho^0 D^{*+}\rangle\ .
\end{aligned} \qquad (14.13)$$

Donde hemos hecho uso de la convención de fases $|\rho^+\rangle = -|1,1\rangle$ y $|D^{*0}\rangle = -|1/2, 1/2\rangle$. Para el sistema $D^*\bar{D}^*$ tendremos:

$$\begin{aligned}
|D^*\bar{D}^*, I=0, I_3=0\rangle &= \frac{1}{\sqrt{2}}|D^{*+}D^{*-}\rangle + \frac{1}{\sqrt{2}}|D^{*0}\bar{D}^{*0}\rangle, \\
|D^*\bar{D}^*, I=1, I_3=0\rangle &= \frac{1}{\sqrt{2}}|D^{*+}D^{*-}\rangle - \frac{1}{\sqrt{2}}|D^{*0}\bar{D}^{*0}\rangle,
\end{aligned} \qquad (14.14)$$

Y del mismo modo para otros pares de mesones. Los resultados del cálculo de las amplitudes de la figura Fig. 14.1, término de contacto de cuatro vectores a) y de intercambio de un vector b), una vez que las estructuras se han proyectado en espín e isospín, se muestran en la Tabla 3.1 para la interacción entre dos ρ's (si se quiere ver el resto

de las amplitudes de dispersión entre dos vectores pertenecientes al nonete de SU(3), véanse las Tablas V-X y XVIII-XXI de [86]), Tablas 6.1, 6.2 y 6.3 del Capítulo 6 para el sistema ρD^* y Tablas B.1 - B.6 del Apéndice B para $D^*\bar{D}^*$, $D_s^*\bar{D}_s^*$ (sector $C=0; S=0$ alrededor de 4000 MeV). Las amplitudes del resto de sectores incluyendo aquellos que tienen sabor exótico se encuentran en las Tablas D.1 - D.10 del Apéndice D.

La estructura cinemática de las amplitudes correspondientes a los diagramas del intercambio de un vector tienen una estructura general, la cual es, para la reacción $(1+2 \to 3+4)$ y en el canal t

$$b_{ij}(k_1+k_3)\cdot(k_2+k_4)\epsilon_1\cdot\epsilon_3\epsilon_2\cdot\epsilon_4 \ , \tag{14.15}$$

y en el canal u

$$c_{ij}(k_1+k_4)\cdot(k_2+k_3)\epsilon_1\cdot\epsilon_4\epsilon_2\cdot\epsilon_3 \ , \tag{14.16}$$

siendo b_{ij} y c_{ij} constantes dependientes del canal inicial, "i" $=(1+2)$, y final, "j" $=(3+4)$. Es interesante observar que la estructura de espín de la Ec. (14.15) tiene iguales componentes para espín$=0,1$ y 2, mientras que la de la Ec. (14.16) tiene la misma proyección para espín$=0$ y 2 y de signo opuesto para espín$=1$. Tras proyectar las amplitudes en isospín, espín y onda s, ellas son insertadas en la ecuación de Bethe Salpeter como kernel V, la cual en el formalismo on-shell [43, 52, 77] puede ser expresada como

$$T=[\hat{1}-VG]^{-1}V \ . \tag{14.17}$$

El kernel V es una matriz cuyos elementos son las amplitudes $(V_1(k_1)V_2(k_2) \to V_3(k_3)V_4(k_4))$ evaluadas en la base de espín, de isospín y proyectadas en onda s. G es una matriz diagonal cuyos elementos son las funciones de loop de dos mesones G_i para cada canal V_1V_2:

$$G_i=i\int\frac{d^4q}{(2\pi)^4}\frac{1}{q^2-M_1^2+i\epsilon}\frac{1}{(P-q)^2-M_2^2+i\epsilon} \ , \tag{14.18}$$

la cual puede ser evaluada con regularización dimensional, Ec. (3.45), o cutoff, Ec. (3.23). En la Ec. (14.18), P es el cuadrimomento total

de los dos mesones. En el plano complejo de la energía, i.e. $\sqrt{s}$, los polos aparecen en la primera hoja de Riemann para valores de $\sqrt{s}$ por debajo del umbral y son interpretados como estados ligados. Las resonancias son identificadas con polos localizados por encima del umbral (del canal al que la partícula se desintegra) y deben buscarse en la segunda hoja de Riemann, en la cual, la función de loop cambia y se escribe como [55]:

$$G_i^{II}(\sqrt{s}) = G_i^I(\sqrt{s}) + i\frac{p}{4\pi\sqrt{s}} \qquad Im(p) > 0 \tag{14.19}$$

donde G_i^{II} se refiere a la función de loop en la segunda hoja de Riemann y G_i^I es la función de loop en la primera hoja de Riemann que viene dada por la Ec. (3.45), en el método de regularización dimensional, o (3.23), si un cutoff es usado para regularizar la integral, para cada canal i.

14.2.2 Convolución de la función de loop de dos mesones y cálculo del modo de desintegración a dos pseudoscalares

La inserción de las amplitudes del término de contacto de cuatro vectores + intercambio de un vector adecuadamente proyectadas como potencial V de la ecuación de Bethe Salpeter conduce a estados ligados (polos en el eje real y por debajo del umbral con anchura cero) de dos mesones vectoriales. Por el hecho de tratar con vectores, estos estados ligados tienen la posibilidad de desintegrarse en mesones pseudoscalares. Con objeto de incluir los canales de desintegración que contienen mesones pseudoscalares, se utilizan dos mecanismos diferentes, 1) Convolución de la función de loop de dos mesones vectoriales teniendo en cuenta la anchura de desintegración de los mesones ρ y K^* a $\pi\pi$ y $K\pi$ respectivamente, y 2) Cálculo de un diagrama con forma de caja que contiene cuatro pseudoscalares en su interior, de este modo las resonancias pueden desintegrarse a dos mesones pseu-

doscalares (cuatro si se cruzan las patas de este diagrama). Estos dos mecanismos se describen a continuación.

1) **Convolución de la función de loop de dos mesones**. El hecho de que el mesón ρ tiene una anchura grande, $\Gamma_\rho = 146.2$ MeV, implica que el mesón tiene una distribución de masas, y así, los estados generados dinámicamente a partir de la interacción de dos mesones ρ pueden desintegrarse en un estado intermedio de dos vectores para las componentes de menor masa de la distribución del ρ. Y de modo similar ocurriría para otros vectores con anchura apreciable distintos del ρ, como por ejemplo el mesón K^*. En el caso de la función de loop de dos mesones ρ, la convolución de la función G con la distribución de masas del mesón ρ, $\tilde{G}$, es

$$\begin{aligned}\tilde{G}(s) &= \frac{1}{N^2}\int_{(m_\rho-2\Gamma_\rho)^2}^{(m_\rho+2\Gamma_\rho)^2} d\tilde{m}_1^2(-\frac{1}{\pi})\mathcal{I}m\frac{1}{\tilde{m}_1^2 - m_\rho^2 + i\Gamma\tilde{m}_1} \\ &\times \int_{(m_\rho-2\Gamma_\rho)^2}^{(m_\rho+2\Gamma_\rho)^2} d\tilde{m}_2^2(-\frac{1}{\pi})\mathcal{I}m\frac{1}{\tilde{m}_2^2 - m_\rho^2 + i\Gamma\tilde{m}_2} \\ &\times G(s,\tilde{m}_1^2,\tilde{m}_2^2) \ ,\end{aligned} \tag{14.20}$$

con

$$N = \int_{(m_\rho-2\Gamma_\rho)^2}^{(m_\rho+2\Gamma_\rho)^2} d\tilde{m}_1^2(-\frac{1}{\pi})\mathcal{I}m\frac{1}{\tilde{m}_1^2 - m_\rho^2 + i\Gamma\tilde{m}_1} \ , \tag{14.21}$$

donde $\Gamma_\rho = 146.2\, MeV$ y para $\Gamma \equiv \Gamma(\tilde{m})$ tomamos la anchura del ρ para la desintegración en dos piones en onda p

$$\Gamma(\tilde{m}) = \Gamma_\rho(\frac{\tilde{m}^2 - 4m_\pi^2}{m_\rho^2 - 4m_\pi^2})^{3/2}\theta(\tilde{m} - 2m_\pi) \tag{14.22}$$

El uso de $\tilde{G}$ en la Ec. (14.17) proporciona alguna anchura a los estados. Para convolucionar la función de loop ρD^* véase la Ec. (6.4).

2) **Cálculo del diagrama con forma de caja**. La convolución de la función G proporciona anchura a los estados, sin embargo, como veremos, la anchura que proporciona no es mayor que unos pocos MeV en todos los casos considerados aquí, mientras que muchos estados observados a los que asociamos las resonancias generadas dinámicamente que obtenemos (por proximidad en números cuánticos y masas), tienen anchuras del orden de $100 - 200$ MeV. Por esta razón, otros mecanismos deben ser tenidos en cuenta si se quiere realizar un estudio completo de la interacción de dos vectores. Expondremos aquí el caso de la inclusión de un diagrama con forma de caja para la interacción de dos ρ's y el método usado puede extrapolar los resultados fácilmente a la interacción ρD^*, $D^*\bar{D}^*$, etc.

Para el caso de los estados $\rho\rho$ que nos interesa, los diagramas de la Fig. 14.2 proporcionan tales mecanismos, y de hecho el vértice $\rho\pi\pi$ es proporcionado por el Lagrangiano de hidden gauge de la Ec. (14.3),

$$\mathcal{L}_{VPP} = -ig\langle V^\mu [P, \partial_\mu P]\rangle \ . \tag{14.23}$$

Para el diagrama de la Fig. 14.3, en el que aparecen explícitamente los momentos, tenemos

$$\begin{aligned} -it^{(\pi\pi)} \ = \ & \int \frac{d^4q}{(2\pi)^4}(-i)(\sqrt{2}g)^4 (q-k_1+q)^\mu \, \epsilon_{1\mu} \\ & \times i(k_1 - q + P - q)_\nu \, \epsilon_2^\nu \, i(k_3 - q - q)_\alpha \, \epsilon_3^\alpha \\ & \times (-i)(q - k_3 - P + q)_\beta \, \epsilon_4^\beta \\ & \times \frac{i}{q^2 - m_\pi^2 + i\epsilon} \, \frac{i}{(k_1 - q)^2 - m_\pi^2 + i\epsilon} \\ & \times \frac{i}{(P-q)^2 - m_\pi^2 + i\epsilon} \, \frac{i}{(k_3 - q)^2 - m_\pi^2 + i\epsilon} \ . \end{aligned} \tag{14.24}$$

Bajo la aproximación de despreciar el momento respecto de la masa del mesón vectorial, todos los vectores de polarización

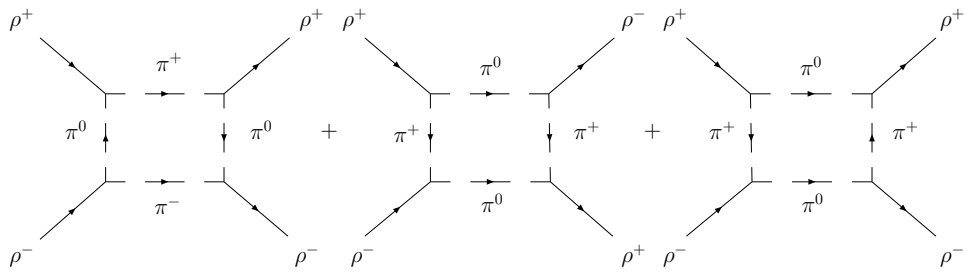

Figure 14.2: Diagramas considerados para tener en cuenta el mecanismo $\rho\rho \to \pi\pi$.

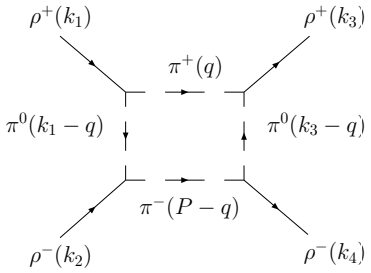

Figure 14.3: Detalle de uno de los diagramas de la Fig. 14.2.

vienen a ser espaciales y podemos reescribir la amplitud como

$$\begin{aligned} -it^{(\pi\pi)} &= (\sqrt{2}g)^4 \int \frac{d^4q}{(2\pi)^4} 16\, q_i q_j q_l q_m\, \epsilon_{1i}\epsilon_{2j}\epsilon_{3l}\epsilon_{4m} \\ &\times \frac{1}{q^2 - m_\pi^2 + i\epsilon}\, \frac{1}{(k_1 - q)^2 - m_\pi^2 + i\epsilon} \\ &\times \frac{1}{(P-q)^2 - m_\pi^2 + i\epsilon}\, \frac{1}{(k_3 - q)^2 - m_\pi^2 + i\epsilon}\ , \end{aligned} \tag{14.25}$$

esta integral es logarítmicamente divergente, y en la ausencia de datos para ajustar la constante de sustracción si se intentase evaluar por medio de regularización dimensional, lo que haremos es evaluarla por medio de un cutoff en el trimomento del orden de 1 GeV. Con este propósito, evaluamos la integral en q^0 analíticamente teniendo cuidado de dividir exactamente por el factor con polaridad indefinida ($\pm i\epsilon$ in the denominators). Realizando alguna manipulación algebráica obtenemos,

$$\begin{aligned} V^{(\pi\pi)} &= (\sqrt{2}g)^4\ (\epsilon_{1i}\epsilon_{2i}\epsilon_{3j}\epsilon_{4j} + \epsilon_{1i}\epsilon_{2j}\epsilon_{3i}\epsilon_{4j} + \epsilon_{1i}\epsilon_{2j}\epsilon_{3j}\epsilon_{4i}) \\ &\times \frac{8}{15\pi^2} \int_0^{q_{max}} dq\, \vec{q}^{\,6}\, \{10\omega^2 - (k_3^0)^2\} \frac{1}{\omega^3} \left(\frac{1}{k_1^0 + 2\omega}\right)^2 \\ &\times \frac{1}{P^0 + 2\omega} \left(\frac{1}{k_1^0 - 2\omega + i\epsilon}\right)^2 \frac{1}{P^0 - 2\omega + i\epsilon}\ , \end{aligned} \tag{14.26}$$

siendo $\omega = \sqrt{\vec{q}^{\,2} + m_\pi^2}$. Esta expresión muestra explícitamente las fuentes de parte imaginaria en los cortes $k_1^0 - 2\omega = 0$ y $P^0 - 2\omega = 0$, correspondiendo a $\rho \to \pi\pi$ y $\rho\rho \to \pi\pi$. El doble polo de la Ec. (14.26) puede ser eliminado fácilmente teniendo en cuenta la distribución de masas del mesón ρ. Una simple aproximación, lo suficientemente precisa para nuestros propósitos es sustituir el polo doble, $(k_1^0 - 2\omega + i\epsilon)^2$, por $(k_1^0 - 2\omega + \Gamma/4 + i\epsilon)(k_1^0 - 2\omega - \Gamma/4 + i\epsilon)$. En la práctica, los resultados

prácticamente no cambian si uno pone $\Gamma/2$ en lugar de $\Gamma/4$ o algún número razonable del orden de la anchura del ρ. El potencial de la Ec. (14.26) se proyecta en espín e isospín. Como sólo estamos interesados en isospín$=0$, donde la interacción es atractiva para espín$=0,2$, la amplitud del diagrama en caja de la Fig. 14.2 es

$$\begin{aligned} t^{(2\pi,I=0,S=0)} &= 20\,\tilde{V}^{(\pi\pi)} \\ t^{(2\pi,I=0,S=2)} &= 8\,\tilde{V}^{(\pi\pi)} \end{aligned} \tag{14.27}$$

donde $\tilde{V}^{(\pi\pi)}$ viene dado por la Ec. (14.26) tras eliminar los vectores de polarización. Los diagramas del tipo de la Fig. 14.2 no tienen espín$=1$. La razón es que los mesones ρ están en onda s y por tanto la paridad del sistema $\rho\rho$ es positiva, lo que fuerza a los dos piones a tener $L=0,2$, y así, ya que los piones no poseen espín, $J=L$ y únicamente los números cuánticos 0^+ y 2^+ son posibles.

Como puede verse en las Figs. 3.10, 6.4, 7.4, 9.2 y 9.3 el potencial que viene de la suma de los términos de contacto y de intercambio de un vector es mucho mayor que la parte real del diagrama en caja del tipo mostrado en la Fig. 14.2 y por tanto la parte real del diagrama puede ser despreciada. La parte imaginaria del diagrama en caja se muestra en las Figs. 3.10, 6.5, 7.5 y 9.4 para los distintos sectores. Esta parte imaginaria será la responsable de la anchura de desintegración de las resonancias encontradas a pares de pseudoscalares.

En el cálculo de la Ec. (14.26), el intercambio del pión entre los dos mesones ρ en el canal t está mayormente off-shell por lo que implementamos factores de forma empíricos para el vértice $\rho\pi\pi$ [79, 80] del tipo

$$F(q)=\frac{\Lambda^2-m_\pi^2}{\Lambda^2-(k-q)^2} \tag{14.28}$$

en cada vértice $\rho \to \pi\pi$, siendo

$$k^0 = \frac{\sqrt{s}}{2} \quad \vec{k} = 0 \quad q^0 = \frac{\sqrt{s}}{2} \ , \tag{14.29}$$

y $\vec{q}$ la variable de integración. La Ec. (14.28) se implementa para varios valores de $\Lambda \sim 1.3 - 1.4$ GeV [79, 80] y en la integral de la Ec. (14.26), se usa un valor del cutoff de $q_{\max} = 1.2$ GeV el cuál no afecta a la parte imaginaria de la integral, que representa el papel importante en el cálculo.

Existen también otras contribuciones a la anchura de los estados VV, como es por ejemplo el diagrama en caja cruzado de la Fig. 14.4, mostrado para el sistema $\rho\rho$ y que puede extrapolarse fácilmente a otros sectores. El resultado del cálculo de este diagrama es mostrado en la Fig. 3.10, éste tendría en cuenta la desintegración de la resonancia en cuatro mesones pseudoscalares. Hemos evaluado que la contribución de este diagrama representa un 20% del término directo con dos pseudoscalares en el estado intermedio. Para el caso $\rho\rho$, también es posible un diagrama con vértices anómalos tal como el de la Fig. 14.5, sin embargo, el potencial correspondiente a este diagrama no tiene parte imaginaria y la parte real negativa viene a ser contrarrestada con la parte real del potencial del diagrama en caja, véase la Fig. 3.10. En el caso del vértice $D^*D\pi$, además los cálculos son realizados con otro factor de forma basado en reglas de suma de QCD [123]. Para un π offshell, éste es:

$$F'(q^2) = g_{D^*D\pi} e^{q^2/\Lambda^2} \quad \text{with } \Lambda = 1.2\,\text{GeV} \ , \tag{14.30}$$

junto con el uso del valor experimental del acoplamiento $D^*D\pi$ medido por la Colaboración CLEO, $g^{\exp}_{D^*D\pi} = 8.95$. En la Ec. (14.30), debe cambiarse $q \to k_1 - q$, con $q_0 \sim 769.4$ MeV y $k_1 - q^0 \sim 6$ MeV lo cual conduce a $(k^0 - q^0)^2/\Lambda^2 \sim 10^{-5}$. Por lo tanto, la componente cero del cuadrimomento del pión puede ser despreciada. Así, reemplazamos g^4 en la Ec. (6.8) por

$$g^2_{\rho\pi\pi} \, (g^{exp}_{D^*D\pi})^2 \, (e^{-\vec{q}^{\,2}/\Lambda^2})^4 \ , \tag{14.31}$$

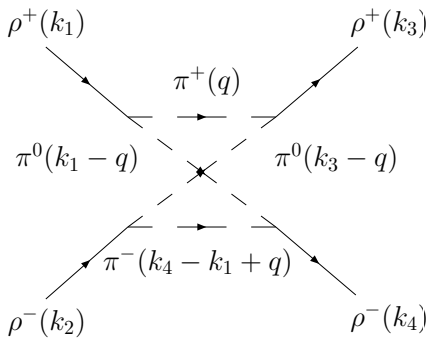

Figure 14.4: Diagrama de caja cruzado considerado para la desintegración en cuatro piones.

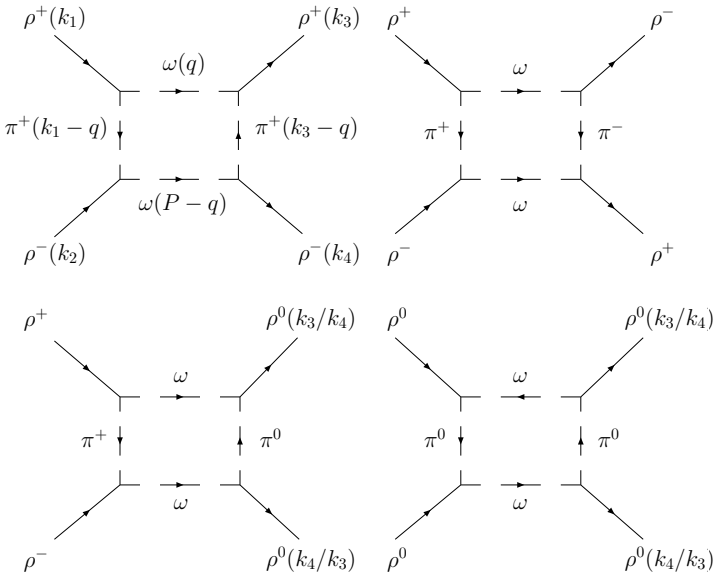

Figure 14.5: Diagrama de caja con vértices anómalos y con dos ω's en el estado intermedio.

con $g_{\rho\pi\pi} = m_\rho/2\, f_\pi = 4.2$ y $g^{exp}_{D^*D\pi} = 8.95$ MeV (el valor experimental), $\Lambda \sim 1 - 1.2$ GeV y $\vec{q}$ como variable de integración.

Las partes reales e imaginarias son mostradas en las Figs. 6.6 y 6.7 para el diagrama en caja ρD^*. Como puede verse, la parte real del diagrama en caja πD de nuevo es mucho más pequeña que el término de contacto + término de intercambio y puede ser despreciada.

14.3 Resultados

En esta sección discutimos los resultados obtenidos para cada sector cuando el potencial de interacción de dos vectores de la sección anterior es introducido en la Ec. (14.17).

1. **El sistema** $\rho\rho$. Como puede observarse de la Tabla 3.1 para el caso de la interacción de dos $\rho's$, el potencial es atractivo para los casos $(I,S) = (1,1); (0,0)$; y $(0,2)$, mientras que resulta ser repulsivo para $(I,S) = (2,0)$ y $(2,2)$. En los casos $(I,S) = (0,1); (1,0); (1,2)$; y $(2,1)$, que no se encuentran en la Tabla, el potencial es cero, lo cuál es consistente con la regla para partículas idénticas $L + S + I =$ par. Nótese que la atracción obtenida en el sector $(I,S) = (1,1)$ es mucho más pequeña que para $(I,S) = (0,0)$ y $(0,2)$. Este caso es especial puesto que corresponde a los números cuánticos de la resonancia $b_1(1235)$. Esta resonancia es dinámicamente generada de la interacción de vectores con pseudoscalares siendo el canal $K\bar{K}^*$ el dominante. El hecho de que la atracción entre dos $\rho's$ sea pequeña para estos números cuánticos indica que la influencia de este canal en la dinámica de la resonancia $b_1(1235)$ será pequeña, estando dominada por la interacción $K\bar{K}^*$. Aunque esta débil atracción puede conducir a una resonancia ancha a elevadas energías que es estudiada con detalle en [86]. Es interesante ver que en el modelo no se pueden generan estados con $I = 2$ ya que el potencial es repulsivo aquí. Por otro lado, encontramos una mayor atracción en el sector $(I,S) = (0,2)$ que en $(I,S) = (0,0)$, lo

que indica que un posible estado generado de la interacción $\rho\rho$ en ese sector estaría más ligado que para $(I, S) = (0, 0)$. Es curioso observar que la misma tendencia es seguida por las resonancias $f_0(1370)$ y $f_2(1270)$. Además, vale la pena mencionar que los diagramas de intercambio de un vector son mayormente responsables de la atracción final, pero es debido al término de contacto que estos estados finalmente no serán degenerados en masa [85].

El resultado final de la matriz $|T|^2$ en el eje real es mostrado en la Fig. 14.6. En la evaluación de la T matriz de la figura no incluimos los diagramas de las Figs. 14.4 y 14.5 ya que ellas representan contribuciones de menor importancia que pueden ser absorvidas por la variación del parámetro Λ de la Ec. (14.28). Las amplitudes son evaluadas para dos valores diferentes del cutoff en la Ec. (3.23), $q_{\max} = 875$ y 1000 MeV, el resultado puede verse en la Fig. 14.7. Obtenemos dos estados con masas alrededor de 1500 y 1270 MeV para $J = 0$ y $J = 2$ respectivamente. Como puede observarse, conforme Λ crece, Fig.14.6, la anchura de los estados se hace mayor, lo cual nos proporciona una idea de las incertidumbres.

2. **Extensión al nonete de vectores de SU(3)**. Este estudio es realizado en detalle por L. S. Geng [86] y reproducido usando los mismos parámetros en esta tesis. A continuación se resumen brevemente los principales resultados de este estudio. En el resto de los casos de interacción entre vectores pertenecientes al nonete de SU(3) distintos a $\rho\rho$, se encuentra un potencial lo suficientemente atractivo para dar lugar a la generación de polos, en los sectores (extrañeza= 0, isoespín= 0); (extrañeza= 0, isoespín= 1) y (extrañeza= 1, isoespín= 1/2). De los once polos encontrados, cinco de ellos pueden ser asociados con estados observados experimentalmente. Las posiciones de los polos, constantes de acoplamiento a los diferentes canales evaluadas de los residuos de las amplitudes (ver Ec. (3.50)) y la com-

paración entre teoría y experimento viene dada en las Tablas 3.4, 3.5, 3.6 y 3.7 respectivamente. Las cinco resonancias asociadas con estados observados son: La $f_0(1370)$ y $f_2(1270)$, se obtiene que se acoplan principalmente a $\rho\rho$ y las tasas de desintegración evaluadas son, $\sim 88\%$ a $\pi\pi$, $\sim 10\%$ para $K\bar{K}$ y $< 1\%$ para $\eta\eta$, en muy buen acuerdo con el experimento, que proporciona las medidas para las tasas de desintegración, 84.8% para $\pi\pi$, 4.6% para KK y $< 1\%$ para $\eta\eta$. La $f_0(1710)$ y la $f_2'(1525)$, que se acoplan principalmente a $K^*\bar{K}^*$ y las tasas de desintegración calculadas para la $f_0(1710)$ son $\sim 55\%$ para $K\bar{K}$, $\sim 27\%$ para $\eta\eta < 1\%$ para $\pi\pi$ y $\sim 18\%$ para la componente vector-vector. Aunque se encuentra buen acuerdo con el cociente $\Gamma(\eta\eta)/\Gamma(K\bar{K})$, la fracción obtenida para $\Gamma(\pi\pi)/\Gamma(K\bar{K})$ es más pequeña que el valor experimental. Sin embargo, entre los distintos experimentos, el experimento realizado por BES a partir de la reacción $J/\psi \to \omega K^+K^-$ da $\Gamma(\pi\pi)/\Gamma(K\bar{K}) < 11\%$ a un 95% de nivel de confianza, por lo que creemos que son necesarios más análisis experimentales para clarificar ésto. Respecto a la $f_2'(1525)$, de los cálculos se deduce que el $\sim 66\%$ de las veces la resonancia se desintegra en $K\bar{K}$, mientras que se obtienen $\sim 21\%$ para $\eta\eta$, $\sim 1\%$ para $\pi\pi$ y 13% para la componente vector-vector, lo cual está en muy buen acuerdo con el experimento (88.7% a $K\bar{K}$, 10.4% para $\eta\eta$ y 0.8% para $\pi\pi$). El último estado que puede ser claramente asociado a un estado experimental es la $K_2^*(1430)$. De los cálculos se obtiene que el modo de desintegración $K\pi$ ocurre un $(49.9 \pm 1.2)\%$ de las veces mientras que el canal $K^*\pi\pi$ representa el $(13.4 \pm 2.2)\%$. La masa y anchura encontradas en el eje real son 1431 y 56 MeV respectivamente, mientras que el PDG da los valores 1429 ± 1.4 y 104 ± 4 MeV. El acuerdo con el experimento es razonable [86].

3. **Interacción $\rho - \mathbf{D}^*$.** En este estudio se tratan los canales ρD^* y ωD^*. En este caso, ver Tablas 6.1, 6.2 y 6.3, vemos que las amplitudes correspondientes al intercambio de un mesón

D^* son proporcionales a $\kappa = m_\rho^2/m_{D^*}^2 \sim 0.15$. Hemos calculado que estos términos representan correcciones del orden del 10% de los términos de intercambio de un mesón ρ. De estas tablas podemos extraer las siguientes conclusiones: Hay atracción en el sector de $I = 1/2$ mientras que la interacción en el sector $I = 3/2$ es repulsiva. Debido a que este último sector es exótico, $I = 3/2$, esto es una característica bienvenida que parece ser universal en otros estudios [86, 118, 119]. Los potenciales $\rho D^* \to \omega D^*$ y $\omega D^* \to \omega D^*$ son repulsivos y pequeños. Finalmente, de las tablas vemos que es el término de intercambio del ρ el que domina la interacción.

Tomamos parámetros α y μ en la Ec. (3.45) similares a los trabajos de D. Gamermann [108] y [109]. Esto es, $\mu = 1500$ MeV y ajustamos α para obtener la masa de la $D_2^*(2460)$, esto da $\alpha = -1.74$. Se encuentran tres estados, uno para cada espín$= 0, 1, 2$ y similarmente al estudio de la interacción $\rho\rho$, obtenemos un estado más ligado con espín$= 2$ que para espín$= 0, 1$. En la Tabla 6.5 damos los valores de los acoplamientos g_i en unidades de GeV a los diferentes canales. Los resultados que se obtienen usando la formula del cutoff para G, Ec. (3.23), son muy similares, con diferencias de alrededor del 10% con el empleo de la fórmula de la Ec. (3.45) para un cutoff $q_{\rm max} = 1-1.2$ GeV. Los estados aparecen con masas 2602, 2620 y 2465 y anchuras $\sim 61, 4$ y 40 para espín$= 0, 1$ and 2 respectivamente y $\Lambda = 1$ GeV en la Ec. (14.30). Los valores de las masas y anchuras de los dos últimos estados son consistentes con los observados experimentalemnte para la $D^*(2640)$ (de espín desconocido) y la $D_2^*(2460)$, por lo que asociamos estos dos estados a los estados de espín$= 1$ y 2 encontrados en el modelo, respectivamente. Un punto remarcable es la predicción de los números cuánticos de la $D^*(2640)$ ya que el modelo proporciona una explicación de porqué este estado tendría una anchura mucho más pequeña que el estado de espín$= 2$, la $D_2^*(2460)$, a pesar de tener una masa mayor, debido a que el diagrama en

caja calculado que proporciona la anchura de desintegración a dos pseudoscalares sólo puede tener espín= 0 y 2 [116].

4. **Sector $\mathbf{C=0; S=0 \sim 4000}$ MeV(encanto oculto)**. En las Tablas B.1 - B.6 del Apéndice B pueden verse las amplitudes de las reacciones $D^*\bar{D}^* \rightarrow$ channel y $D_s^*\bar{D}_s^* \rightarrow$ channel. En este sector, las amplitudes evaluadas en [86] (véase Apéndice de este artículo) para SU(3) también son usadas en el cálculo. De estas tablas podemos observar que la interacción es muy atractiva para $D^*\bar{D}^* \rightarrow D^*\bar{D}^*$, $D^*\bar{D}^*(D_s^*\bar{D}_s^*) \rightarrow D_s^*\bar{D}_s^*$ y isoespín= 0; espín= $0, 1, 2$. Para isoespín= 1, vemos que el potencial de la interacción $D^*\bar{D}^* \rightarrow D^*\bar{D}^*$ y $D^*\bar{D}^* \rightarrow \rho J/\psi$ es bastante atractivo para espín= 2. Ya que estamos tratando con diferentes tipos de canales, se esperan grandes efectos de rotura de la simetría y por esta razón es importante evaluar las incertidumbres. Sin embargo, como veremos, los resultados parecen ser bastante estables. Para ajustar el parámetro α, lo primero que se hace es reproducir los resultados de SU(3), ya que estas amplitudes son necesarias en el cálculo, de modo que siguiendo [86], fijamos $\mu = 1000$ MeV para todos los canales y ponemos $\alpha_L = -1.65$ para los canales vector (ligero) - vector (ligero). En los otros canales de vector (pesado) - vector (pesado) ajustamos α_H para reproducir el polo encontrado con $I = 0; J = 0$ alrededor de 3940 MeV, esto da $\alpha_H = -2.07$. Finalmente, en el resto de canales vector (pesado) - vector (ligero) ponemos $\alpha_L = -1.65$ también. Las posiciones de los polos y constantes de acoplamiento obtenidas vienen dadas en las Tablas 7.2 -7.6. Para isoespín= 0 encontamos cuatro polos, tres de ellos alrededor de $\sim$ 3940 MeV, uno para cada espín $J = 0, 1, 2$, y que se acoplan fuertemente a $D^*\bar{D}^*$. Estos estados son relativamente estrechos y los que tienen $J = 0$ y 2 se desintegran en $\omega(\phi)J/\psi$ principalmente. Para $I = 0$ y $J = 2$ encontramos otro polo por encima del umbral $D^*\bar{D}^*$ con masa $M = 4169$ MeV y anchura $\Gamma = 132$ MeV. De los acoplamientos vemos

que este estado se acopla más a $D_s^*\bar{D}_s^*$. Para $I = 1$ encontramos un solo polo con $J = 2$ y debajo del umbral $D^*\bar{D}^*$, con masa $M = 3919$ MeV y anchura $\Gamma = 148$ MeV. Este estado se acopla también más fuertemente a $D^*\bar{D}^*$. La identificación con los estados de la Tabla 7.1 debe hacerse cuidadosamente. Aunque existen tres estados con masa alrededor de 3940 MeV, uno de nuestros estados, concretamente el de espín= 1, tiene C paridad negativa, mientras que todos los estados experimentales tienen C paridad positiva. La Colaboración Belle favorece la asociación de los números cuánticos $J^{PC} = 2^{++}$ para este estado, con lo que identificamos el estado encontrado para espín= 2 alrededor de 3940 MeV con la Z(3930). En el caso de la Y(3940), existen varias medidas para la masa y anchura realizadas por las distintas Colaboraciones Belle y Babar para este estado, que son, $m = (3943 \pm 17)$ MeV y $\Gamma = (87 \pm 34)$ MeV (Belle) y $m = 3914.3^{+4.1}_{-3.8}$ y $\Gamma = 33$ MeV (Babar). Babar y Belle también reportan medidas para el producto $B(B \to KY(3940))B(Y(3940) \to \omega J/\psi) = (7.1 \pm 3.4) \times 10^{-5}$ (Belle) y $(4.9 \pm 1.1) \times 10^{-5}$ (Babar). Esta medida junto con la hipótesis de que $B(B \to KY) \leq 1 \times 10^{-3}$, el valor usual para desintegraciones $B \to K$+charmonium, conduce a $\Gamma(Y(3940) \to \omega J/\psi)$ mayor que 1 MeV. Tomando el acoplamiento $g_{Y\omega J/\psi} = (-1429 - i216)$ MeV de la Tabla 7.2, nosotros obtenemos un valor para $\Gamma((3943, 0^+(0^{++})) \to \omega J/\psi) = 1.52$ MeV, el cual es compatible con la gran anchura de desintegración estimada para la Y(3940). Por lo que asociamos el estado con $0^+(0^{++})$ con la Y(3940).

El segundo polo encontrado con masa $m = 4169$ MeV y $\Gamma = 132$ MeV es identificado con la X(4160) por la proximidad de la masa, anchura y números cuánticos. Los estados con $I = 0; J^{PC} = 1^{+-}$ y $I = 1; J^{PC} = 2^{++}$ son predicciones del modelo y no pueden ser asociados con ningún estado de la Tabla 7.1 (el primero tiene C paridad negativa y la anchura del segundo es demasiado grande). Por otra parte, el estado experimental X(3940) en la Tabla 7.1 no se desintegra a $\omega J/\psi$ y por tanto

no puede ser asociado con ninguno de los estados con $J = 0$ o 2 para isoespín= 0. La naturaleza de este estado debe ser distinta a la de vector - vector.

Un estudio detallado de las incertidumbres es realizado. Para ello, se fija primero el valor de $\alpha = -2.07$ y se varía g^2 cogiendo valores intermedios que van desde $(M_\rho/(2\,f_\pi))^2$ hasta $(M_{D^*}/(2\,f_D))^2$. Las posiciones de los polos encontradas son dadas en la Tabla 7.7 y se observan variaciones de alrededor de 40 MeV a excepción del estado predicho con $I = 1$, donde las incertidumbres son un poco mayores. Un modo realista de calcular las incertidumbres es ajustar el parámetro α para obtener la posición de uno de los estados usando uno de los valores intermedios de g^2 escogidos anterirmente, ya que este ajuste del parámetro α siempre es realizado en este tipo de cálculos. Los resultados son mostrados en las Tablas 7.8 - 7.11. Vemos que las incertidumbres en las posiciones de los polos son un poco menores que en el caso anterior. La masa encontrada para el estado $I = 0; J = 1$ prácticamente no cambia, y las diferencias son de alrededor de unos 30 MeV para los dos estados con $I = 0; J = 2$ y de alrededor de unos 60 MeV para la predicción con $I = 1; J = 2$. Respecto a los acoplamientos, observamos que los cambios en la constante de acoplo mayor son muy pequeños, del orden del 3% excepto en el sector $I = 0; J = 2$, donde encontramos 10% y 7% para el primer y segundo estado respectivamente. En global, estos cálculos conducen a hasta un 20% de error en la evaluación de observables, los cuales requieren amplitudes al cuadrado.

En el cálculo, también podía haberse ajustado α para obtener la posición del estado con $I = 0; J = 2$ en lugar de la del estado con $I = 0; J = 0$. Ésto es realizado ahora y los resultados se muestran en las Tablas 7.8 - 7.11. Se observan diferencias por debajo del 3% [136].

5. **Otros sectores incluyendo sabor exótico**. En el Apéndice

D se muestran las amplitudes obtenidas para el resto de sectores posibles. El potencial resulta ser atractivo en los sectores $C = 1, S = -1, I = 0$; $C = 1, S = 1, I = 0, 1$; $C = 2, S = 0, I = 0$; y $C = 2, S = 1, I = 1/2$, y repulsivo para $C = 0, S = 1, I = 1/2$ (encanto oculto); $C = 1, S = -1, I = 1$; $C = 1, S = 2, I = 1/2$, $C = 2, S = 0, I = 1$ y $C = 2, S = 2, I = 0$. Los parámetros usados en la Ec. (14.17) son los siguientes: fijamos $\mu = 1500$ MeV para todos estos sectores (de acuerdo a los trabajos de D. Garmermann [108] y [109] que tratan estados D y D^*) y ajustamos $\alpha = -1.6$ (valor muy cercano al de [109], -1.55, y [116], -1.74) en los sectores $C = 1; S = -1, 1, 2$. Notese que μ y α no son independientes lo cual justifica fijar μ y entonces ajustar α a los datos. En el resto de sectores, $C = 0; S = 1$ (encanto oculto) y $C = 2; S = 0, 1, 2$, ponemos $\alpha = -1.4$. La razón de esta elección es que hemos usado un conjunto diferente de parámetros μ y α en comparación con el estudio realizado anteriormente de resonancias generadas dinámicamente a partir de $D^*_{(s)}\bar{D}^*$ (estados XYZ) con $\mu = 1000$ y eligiendo así α podemos reproducir de nuevo los estados XYZ. Sólo una resonancia puede ser asociada a un estado experimental, la $D^*_2(2573)$, lo que supone una nueva interpretación de esta resonancia de naturaleza vector - vector. La hipótesis de estructura D^*K^* para esta resonancia, es consistente con la naturaleza DK asumida para la $D^*(2317)$ y la estructura molecular D^*K asumida para la $D^*(2460)$ o $D\bar{D}^*$ para la X(3872). Los otros estados representan predicciones del modelo sin ninguna evidencia experimental. En los estados exóticos, obtenemos interesantes predicciones de estados con doble encanto, doble encanto y extrañeza o encanto y extrañeza (estados ligados de D^*D^* y $D^*D^*_s$ o $D^*\bar{K}^*$), particularmente estrechos [155]. Las masas y anchuras obtenidas pueden verse en la Tabla 14.2, donde además se recogen todos los otros estados obtenidos (se omiten los estados de [86]), tomados de las Tablas 3.3, 6.10, 7.14 y 9.9. En total hemos obtenido 19 estados, 8 de los cuales son asociados con estados

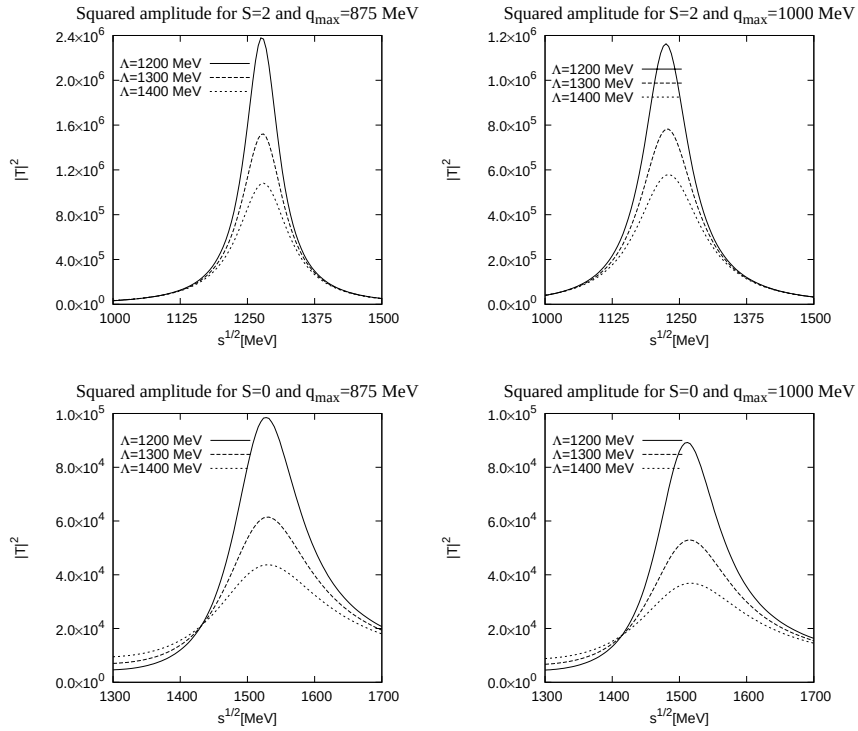

Figure 14.6: $|T|^2$ incluyendo el diagrama en forma de caja con $\pi\pi$ en el estado intermedio para distintos valores de $\Lambda = 1200, 1300, 1400\, MeV$ y $q_{max} = 875, 1000\, MeV$ para $S = 0$ y $S = 2$

observados. Resumimos así los resultados de la primera parte de la tesis respecto al estudio de la interacción vector - vector.

14.4 Interacción de mesones con el medio nuclear

En la tesis estudiamos las propiedades de los mesones escalares con encanto, concretamente la $D_{s0}(2317)$ y la X(3700), siendo la primera

	Teoría			Experimento			
Sector	$I[J^{P(C)}]$	M[MeV]	Γ[MeV]	Nombre	M[MeV]	Γ[MeV]	$I[J^{P(C)}]$
$\rho\rho$	$(0,0)$	1532	212	$f_0(1370)$	1200 to 1500	200 to 500	$0[0^{++}]$
$\rho\rho$	$(0,2)$	1275	100	$f_2(1270)$	1275.1 ± 1.2	$185.1^{+2.9}_{-2.4}$	$0[2^{++}]$
$(C=1;S=0)$	$(1/2,0)$	2602	61	"$D_0^*(2600)$"			
$(C=1;S=0)$	$(1/2,1)$	2620	4	$D^*(2640)$	2637 ± 6	< 15	$1/2[?^?]$
$(C=1;S=0)$	$(1/2,2)$	2465	40	$D^*(2460)$	2464.4 ± 1.9	37 ± 6	$1/2[2^+]$
$(C=0;S=0)$	$0^+[0^{++}]$	3943	17	$Y(3940)$	3943 ± 17	87 ± 34	$0[J^{P+}]$
					$3914.3^{+4.1}_{-3.8}$	33^{+12}_{-8}	
$(C=0;S=0)$	$0^-[1^{+-}]$	3945	0	"$Y_p(3945)$"			
$(C=0;S=0)$	$0^+[2^{++}]$	3922	55	$Z(3930)$	3929 ± 5	29 ± 10	$0[2^{++}]$
$(C=0;S=0)$	$0^+[2^{++}]$	4157	102	$X(4160)$	4156 ± 29	139^{+113}_{-65}	$0[J^{P+}]$
$(C=0;S=0)$	$1^-[2^{++}]$	3912	120	"$Y_p(3912)$"			
$(C=1;S=-1)$	$0[0^+]$	2848	25				
	$0[1^+]$	2839	3				
	$0[2^+]$	2733	22				
$(C=1;S=1)$	$0[0^+]$	2683	44				
	$0[1^+]$	2707	4×10^{-3}				
	$0[2^+]$	2572	18	$D_{s2}(2573)$	2572.6 ± 0.9	20 ± 5	$0[2^+]$
	$1[2^+]$	2786	9				
$(C=2;S=0)$	$0[1^+]$	3969	0				
$(C=2;S=1)$	$1/2[1^+]$	4101	0				

Table 14.2: Estados obtenidos de la interacción vector-vector junto con el estado experimental asignado si existe.

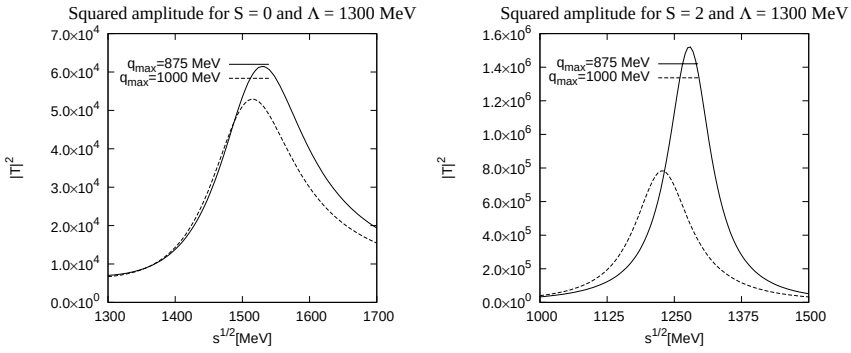

Figure 14.7: $|T|^2$ teniendo en cuenta el diagrama en forma de caja $\pi\pi$ con $\Lambda = 1300\, MeV$, $q_{max} = 875, 1000\, MeV$ para $S = 0$ y $S = 2$.

una resonancia generada dinámicamente que se acopla fuertemente a DK, y la segunda, el estado teórico dinámicamente generado de la interacción pseudoscalar - pseudoscalar con una masa justo por debajo del umbral $D\bar{D}$ en [108]. También estudiamos las propiedades de mesones extaños, i. e. el mesón $\bar{K}^*$, en el medio nuclear.

El estudio de los mesones escalares en el medio ha sido una constante a lo largo de los últimos años. El más estudiado de todos es la $\sigma(600)$. En el modelo de Nambu-Jona-Lasinio [161] se encuentra un sustancial descenso de la masa de la $\sigma(600)$ con el aumento de la densidad. En contraste, la masa del pión aumenta con la densidad. En [162] Hatsuda y al. concluyen que debido a la restauración parcial de la simetría quiral, m_σ se aproxima a m_π al aumentar la densidad y similares resultados son encontrados tanbién en [163, 164] con Lagrangianos quirales no lineales donde las modificaciones de la σ en el medio tienen su origen en el fuerte acoplamiento en onda p de los piones a partícula - agujero (ph) y Δ - agujero.

Por el contrario, respecto a los mesones vectoriales, aunque usando argumentos cualitativos, G. E. Brown y M. Rho predicen desplazamientos atractivos en las masas de los vectores, cálculos más

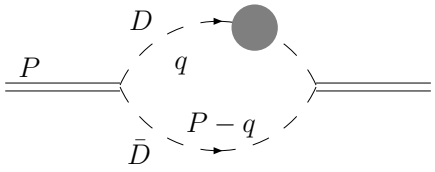

Figure 14.8: La función de loop $D\bar{D}$ del mesón escalar. El círculo sombreado indica la inserción de la autoenergía del mesón D.

detallados hallan un cambio nulo en las masas de los mesones de los mesones ρ y ϕ en el medio [193, 194, 195, 196, 197, 198]. Experimentalmente, las Colaboraciones NA60 y CLASS han observado un cambio nulo de la masa del mesón ρ del espectro de dileptones, de donde también se deduce un ensanchamiento de la anchura del mesón. Aunque la colaboración KEK anunció un cambio de masa atractivo basándose en experimentos preliminares, las medidas podrian estar fuertemente afectadas por el modo en que se realiza la sustracción del background [201].

Uno de los rasgos que caracterizan este tipo de estudios es que nuevos mecanismos de desintegración tienen lugar en el medio. Debido a que en el medio tenemos los nucleones, pueden ocurrir ahora nuevas cadenas de desintegraciones que no ocurrían en el vacío. Un ejemplo es la $\Lambda(1520)$, ésta es una resonancia dinámicamente generada que se acopla fuertemente a $\pi\Sigma(1385)$. Este canal, al estar por encima de la masa de $\Lambda(1520)$, está prohibido para la desintegración de la $\Lambda(1520)$ (excepto por efectos de la $\Sigma(1385)$). Sin embargo, en el medio, la excitación del pión en partícula - agujero proporciona una energía extra de 140 MeV más de espacio fásico y tiene lugar la desintegración.

14.4.1 La $D^*_{s0}(2317)$ y la X(3700) en el medio nuclear

Estos dos mesones fueron generados dinámicamente en el trabajo de D. Gamermann [108], donde se obtienen como estados ligados de DK y $D\bar{D}$ respectivamente y anchura prácticamente nula. En los cálculos relacionados con el medio nuclear, las modificaciones respecto al vacío se introducen en la función de loop G. En el caso de la X(3700), por ejemplo, esto se muestra en la Fig. 14.8 por medio de la inserción de un círculo sombreado que representa la autoenergía del mesón D que ha de ser calculada e introducida en la función de loop $D\bar{D}$. Similarmente también existiría un círculo sombreado en el propagador de la $\bar{D}$ en la Fig. 14.8. Sin embargo, la autoenergía del mesón $\bar{D}$ es muy pequeña debido a que no hay absorción de mesones $\bar{D}$ por nucleones, i. e., $\bar{D}N$ no se desintegra a resonancias bariónicas con un quark c con lo que $\mathrm{Im}\Pi_{\bar{D}} = 0$, de modo que es una buena aproximación dejar el propagador del mesón $\bar{D}$ libre. Esto es análogo a lo que ocurre con los mesones K y $\bar{K}$. Para un estado intermedio $D\bar{D}$ tenemos

$$\widetilde{G}(P^0, \vec{P}, \rho) = i \int \frac{d^4q}{(2\pi)^4} D_D(q, \rho) D_{\bar{D}}(P - q, \rho) \ , \tag{14.32}$$

donde las modificaciones del propagador $D(\bar{D})$ son incorporadas a través de la autoenergía:

$$D_D(q^0, \vec{q}, \rho) = \frac{1}{(q^0)^2 - \vec{q}^{\,2} - m_D^2 - \Pi_D(q^0, \vec{q}, \rho)} \ . \tag{14.33}$$

Siendo más conveniente usar la representación de Lehmann para escribir el propagador del mesón D en el medio,

$$D_D(q^0, \vec{q}, \rho) = \int_0^\infty d\omega \left\{ \frac{S_D(\omega, \vec{q}, \rho)}{q^0 - \omega + i\eta} - \frac{S_{\bar{D}}(\omega, \vec{q}, \rho)}{q^0 + \omega - i\eta} \right\} \ . \tag{14.34}$$

S_D y $S_{\bar{D}}$ representan las funciones espectrales de los mesones D y $\bar{D}$ respectivamente,

$$S_{D(\bar{D})}(q^0, \vec{q}, \rho) = -\frac{1}{\pi} \frac{\mathrm{Im}\Pi_{D(\bar{D})}(q^0, \vec{q}, \rho)}{\left| (q^0)^2 - \vec{q}^{\,2} - m_D^2 - \Pi_{D(\bar{D})}(q^0, \vec{q}, \rho) \right|^2} \ . \tag{14.35}$$

La autoenergía del mesón D posee dos partes, ondas s y p. La parte de onda s se obtiene realizando un cálculo autoconsistente que incluye los canales $\pi\Lambda_c$, $\pi\Sigma_c$, DN, $\eta\Lambda_c$, $K\Xi_c$, $\eta\Sigma_c$, $K\Xi'_c$, $D_s\Lambda$, $D_s\Sigma$, $\eta'\Lambda_c$ y $\eta'\Sigma_c$. El potencial viene de la interacción de Weinberg-Tomozawa en onda s con rotura de la simetría de SU(4) mas un término atractivo isoescalar - escalar, Σ_{DN}. La inclusión de este último término es objeto de debate ya que aunque es sustentada por las aproximaciones de campo medio y reglas de suma de QCD, los cálculos autoconsistentes de [172] y [173] encuentran que, en realidad, los resultados finales son independientes de este término y las pequeñas diferencias de incluirlo o no, son más pequeñas que las incertidumbres del cálculo debido a otras fuentes, por lo que finalmente se opta por no incluirlo en la autoenergía en onda s del mesón D. Cuando se resuelve la ecuación de Bethe - Salpeter, aparecen dos resonancias, la $\Lambda_c(2593)$ y una $\Sigma_c(2800)$. Los efectos del medio son incluidos en la función de loop mesón - barión, ellos son: 1) efectos del bloqueo de Pauli sobre los nucleones (los nucleones dispersados no pueden ir a estados ya ocupados en el mar de Fermi), 2) ligadura de campo medio de bariones vía el modelo $\sigma - \omega$, y 3) renormalización de los mesones π y D a través de la inclusión de sus respectivas autoenergías en los propagadores intermedios. Además, la autoenergía en onda s del mesón D es evaluada de forma autoconsistente al integrar la amplitud DN sobre el mar de Fermi $n(p)$:

$$\Pi_D^{(s)}(q^0, \vec{q}, \rho) = \int \frac{d^3p}{(2\pi)^3}\, n(p)\, [\tilde{T}_{DN}^{(I=0)}(P^0, \vec{P}, \rho) + 3\tilde{T}_{DN}^{(I=1)}(P^0, \vec{P}, \rho)] \ . \tag{14.36}$$

La parte de onda p se calcula de modo similar al de la partícula $\bar{K}$ y tiene en cuenta los procesos: $DN \to \Lambda_c$, Σ_c y Σ_c^*. Las correspondientes autoenergías para la excitación de la $\Lambda_c(\Sigma_c)$ o Σ_c^* vienen dadas por las Ecs. 10.9 y 10.12 respectivamente y los coeficientes α, β y a involucrados en el cálculo estan dados en las Tablas 10.4 y 10.5 y ellos son obtenidos por medio de los coeficientes de Clebsch Gordan de SU(4) [179]. Resultan ser idénticos a los de la $\bar{K}$ ya que viene a

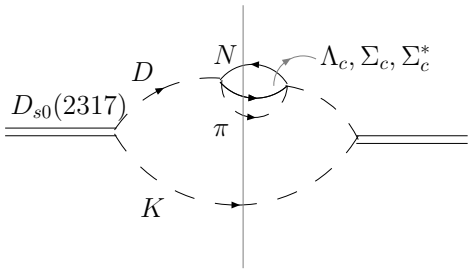

Figure 14.9: Canal de desintegración de la $D_{s0}(2317)$ en el núcleo dando lugar a las excitaciones $K\pi\Lambda_c$ o $K\pi\Sigma_c$.

ser la sustitución de un quark s por uno c.

Las autoenergías de onda s y p del mesón D se muestran en las Figs. 10.5 y 10.6. En la Fig. 10.5 aparecen unas estructuras alrededor de 1.7 GeV y 2 GeV que corresponden a la excitación de la $h\Lambda_c(2593)$ y $h\Sigma_c(2800)$. La autoenergía de onda p, ver Fig. 10.6, presenta picos en la parte imaginaria y oscilaciones en la parte real alrededor de $1.4 - 1.8$ GeV que corresponden a las excitaciones $h\Lambda_c$, $h\Sigma_c$ y $h\Sigma_c^*$. Como puede deducirse de estas figuras, la autoenergía de onda p viene a ser un orden de magnitud más pequeña que la de onda s, en contraste con los resultados obtenidos para los mesones π y K, donde la parte de onda p es dominante para el π y en el caso del mesón K, ambas componentes son importantes. La razón estriba en que la autoenergía de onda s aumenta con la masa del mesón mientras que la parte de onda p escala más con la masa del barión.

Mientras que la autoenergía en onda s del mesón D da cuenta de excitaciones tipo $DN \to \pi\Lambda_c$, $\pi\sigma_c$, la parte de onda p tiene en cuenta reacciones del tipo $DN \to \Lambda_c$, Σ_c, Σ_c^*. Así, por ejemplo, las modificaciones en el loop DK para el mesón $D_{s0}^*(2317)$ darían lugar a canales intermedios $h\pi\Lambda_c K$, $h\pi\Sigma_c K$ (onda s y véase la Fig. 14.9) o $h\Lambda_c K$, $h\Sigma_c K$ (onda p) y similarmente para $D\bar{D}$ en el caso de la X(3700).

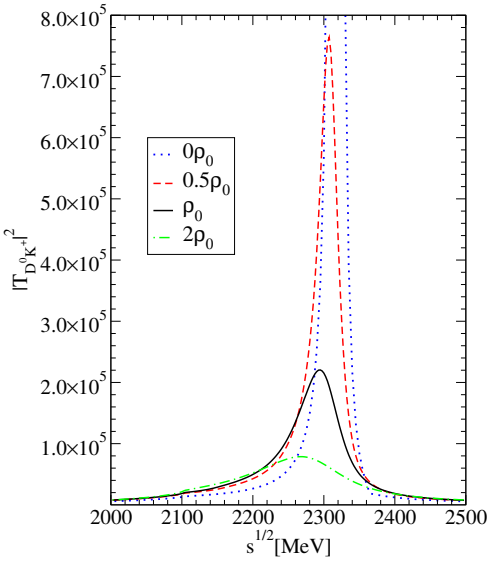

Figure 14.10: La resonancia $D_{s0}(2317)$: $|T|^2$ para la amplitud $D^0K^+ \to D^0K^+$ a distintas densidades.

En las Figs. 14.10 y 14.11 se muestra $|T|^2$ para las resonancias $D_{s0}(2317)$ and X(3700) en los canales principales D^0K^+ y $D^0\bar{D}^0$. Se observa un cambio prácticamente nulo en la posición de los polos, mientras que los cambios en la anchura son del orden de 100 y 250 MeV a $\rho = \rho_0$ para la $D_{s0}(2317)$ y X(3700) respectivamente. Ésto contrasta con la pequeña anchura de estas resonancias en el vacío, nula para la $D_{s0}(2317)$ y de 60 MeV para la X(3700). Como se ha explicado anteriormente, el origen de esta anchura viene de la apertura de nuevos canales de desintegración tales como $DN \to \Lambda_c$ o $\pi\Sigma_c$. También, la evaluación autoconsistente genera canales de absorción de dos nucleones como $DNN \to N\Lambda_c$, $\pi N\Lambda_c$, $\pi N\Sigma_c$, etc. Por ejemplo, el nuevo canal, X(3700)$N \to \bar{D}\pi\Lambda_c$ tiene ahora 400 MeV de espacio fásico disponible, lo que hace que la anchura de la X(3700) aumente considerablemente.

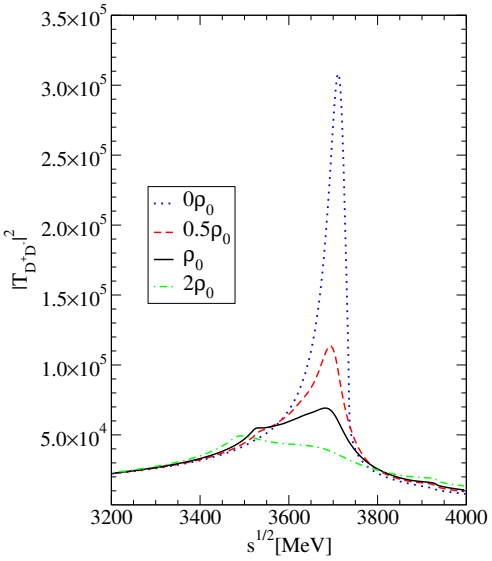

Figure 14.11: La resonancia $X(3700)$: $|T|^2$ para la amplitud $D^0\bar{D}^0 \to D^0\bar{D}^0$ a distintas densidades.

14.4.2 La $\bar{K}^*$ en el medio

El estudio de las modificaciones de la $\bar{K}^*$ en el medio puede hacerse gracias a que la interacción $\bar{K}^*N$ fue investigada en [44]. Así, la autoenergía de la $\bar{K}^*$ tiene dos componentes, por un lado, la interacción de la $\bar{K}^*$ con nucleones, que incluye el bloqueo de Pauli y es calculada de forma autoconsistente. Por otro lado, el canal de desintegración $\bar{K}\pi$ es vestido en materia nuclear. Ambas componentes de la autoenergía, interacción $\bar{K}^*N$ y desintegración $\bar{K}\pi$ en materia nuclear, son incluidas en la función espectral.

Para evaluar la parte de la autoenergía correspondiente a la desintegración $\bar{K}\pi$, se reemplazan los propagadores de la $\bar{K}$ y π para incluir sus respectivas autoenergías. Esto se hace a través de la rep-

resentación de Lehmann, y simplicando un poco se obtiene

$$\begin{aligned}\Pi^{\rho,(\mathrm{a})}_{\bar{K}^*}(q^0,\vec{q}) &= 2g^2\vec{\epsilon}\cdot\vec{\epsilon}'\left\{\int\frac{d^3k}{(2\pi)^3}\frac{\vec{k}^{\,2}}{\pi^2}\int_0^\infty d\omega\,\mathrm{Im}D_\pi(\omega,\vec{k}\,)\right.\\ &\times\int_0^\infty d\omega'\frac{\mathrm{Im}D_{\bar{K}}(\omega',\vec{q}-\vec{k}\,)}{q^0-\omega-\omega'+i\eta}\\ &-\mathrm{Re}\int\frac{d^3k}{(2\pi)^3}\frac{\vec{k}^{\,2}}{2\omega_\pi(k)}\frac{1}{2\omega_{\bar{K}}(q-k)}\\ &\left.\times\frac{1}{q^0-\omega_\pi(k)-\omega_{\bar{K}}(q-k)+i\epsilon}\right\}\ . \qquad (14.37)\end{aligned}$$

donde se ha sustraido la parte real de la autoenergía $\bar{K}^*$ en el vacío, $\Pi^0_{\bar{K}^*}$ de la $\Pi^{\rho(a)}_{\bar{K}^*}$ ya que se usa la masa física de la $\bar{K}^*$ en el vacío.

Por otra parte, la interacción $\bar{K}^*N$ incluye los posibles canales mesón - barión, $\bar{K}^*N$, $\omega\Lambda$, $\rho\Sigma$, $\phi\Lambda$, $K^*\Xi$ para $I=0$ y $\bar{K}^*N$, $\rho\Lambda$, $\rho\Sigma$, $\omega\Sigma$, $K^*\Xi$ y $\phi\Sigma$ en $I=1$. En el cálculo, se renormaliza el canal $\bar{K}^*N$, mientras que los otros canales de mesón - barión se dejan igual que en el vacío. En materia nuclear, la función de loop mesón - barión se escribe

$$\begin{aligned}G^\rho(P) &= G^0(\sqrt{s})+\lim_{\Lambda\to\infty}\delta G^\rho_\Lambda(P),\\ \delta G^\rho_\Lambda(P) &\equiv G^\rho_\Lambda(P)-G^0_\Lambda(\sqrt{s})\\ &= \mathrm{i}2M\int_\Lambda\frac{d^4q}{(2\pi)^4}\left(D^\rho_{\mathcal{B}}(P-q)\ D^\rho_{\mathcal{M}}(q)-D^0_{\mathcal{B}}(P-q)\ D^0_{\mathcal{M}}(q)\right),\end{aligned} \qquad (14.38)$$

La función de loop en el espacio libre, G^0, es calculada mediante regularización dimensional y las correcciones en el medio, $\delta G^\rho = \lim_{\Lambda\to\infty}\delta G^\rho_\Lambda(p)$, se calculan cogiendo un valor grande del cutoff en la integral, con lo que se consigue que ésta sea una cantidad finita e independiente del punto de sustracción usado para regularizar G^0 [220]. Los correspondientes propagadores en el medio vienen dados por la Ec. (11.14). Finalmente, la ecuación de Bethe Salpeter se

resuelve en materia nuclear y la autoenergía de la $\bar{K}^*$ se obtiene integrando $T^{\rho}_{\bar{K}^*N}$ sobre el mar de Fermi,

$$\Pi^{\rho,(\mathrm{b})}_{\bar{K}^*}(q^0,\vec{q}) \;=\; \int \frac{d^3p}{(2\pi)^3}\, n(\vec{p}) \,\Big[\, T^{\rho(I=0)}_{\bar{K}^*N}(P^0,\vec{P}) + 3T^{\rho(I=1)}_{\bar{K}^*N}(P^0,\vec{P})\Big] \;, \tag{14.39}$$

donde $P^0 = q^0 + E_N(\vec{p})$ y $\vec{P} = \vec{q} + \vec{p}$ representan la energía total y el momento del par $\bar{K}^*N$ en el sistema de referencia de materia nuclear en reposo, mientras que $(q^0,\vec{q})$ es la energía y el momento del mesón $\bar{K}^*$ también en este sistema de referencia. La autoenergía de la $\bar{K}^*$ será la suma de las dos partes (a) y (b), provenientes de renormalizar el canal de desintegración $\bar{K}\pi$ y de la interacción $\bar{K}^*N$ respectivamente, $\Pi^{\rho}_{\bar{K}^*} = \Pi^{\rho(a)}_{\bar{K}^*} + \Pi^{\rho(b)}_{\bar{K}^*}$, donde $\Pi^{\rho(b)}_{\bar{K}^*}$ es evaluada autoconsistentemente.

En la Fig. 14.12, la autoenergía de la $\bar{K}^*$ y sus diferentes contribuciones, $\bar{K}^* \to \bar{K}\pi$ e interacción $\bar{K}^*N$ calculada autoconsistentemente, son mostradas como función de q^0 a $\vec{q} = 0$. Como puede verse, el efecto de la interacción efectiva $\bar{K}^*N$ domina alrededor de $800 - 900$ MeV, siendo las excitaciones $\Lambda(1783)N^{-1}$ y $\Sigma(1830)N^{-1}$ visibles. Sin embargo, fuera de esta región, el mecanismo de desintegración $\bar{K}\pi$ domina, ya que a bajas energías, por ejemplo, los canales $\bar{K}^*N \to VB$ están cerrados. Al final, ambos efectos conducen a una moderada atracción de la $\bar{K}^*$ de unos -50 MeV y lo que es más importante, un espectacular aumento de la anchura de la $\bar{K}^*$ en el medio, de 260 MeV a ρ_0, lo que significa cinco veces mayor que en el vacio. Este efecto de la anchura pueden verse visualizado también en la función espectral mostrada en la Fig. 14.13 en función de la energía del mesón q^0, a momento cero y para cuatro densidades desde $\rho = 0$ a $\rho = 1.5\rho_0$.

También, el cociente de transparencia de la reacción $\gamma A \to K^+K^{*-}A'$ es evaluado. Los resultados pueden verse en la Fig. 11.9, donde éste se dibuja para distintas energías en el centro de masas, $\sqrt{s} = 3$ GeV y 3.5 GeV, equivalentes a 4.3 MeV y 6 MeV en el lab. Se observa una atenuación muy fuerte del proceso de producción de la $\bar{K}^*$ debido a

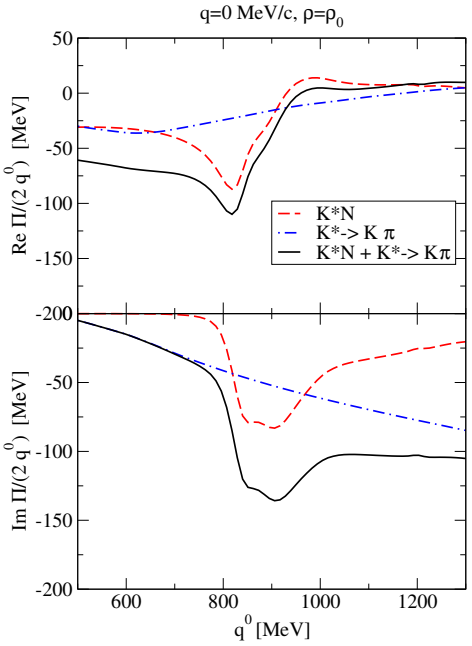

Figure 14.12: Partes real e imaginaria de la autoenergía de la $\bar{K}^*$ en función de la energía del mesón q^0 a momento cero y densidad nuclear normal ρ_0 mostrando las distintas contribuciones: (i) cálculo autoconsistente de la interacción $\bar{K}^*N$ (línea a trazos), (ii) autoenergía procedente de la desintegración $\bar{K}^* \to \bar{K}\pi$ (línea mixta), y (iii) autoenergía incluyendo ambos procesos (línea contínua).

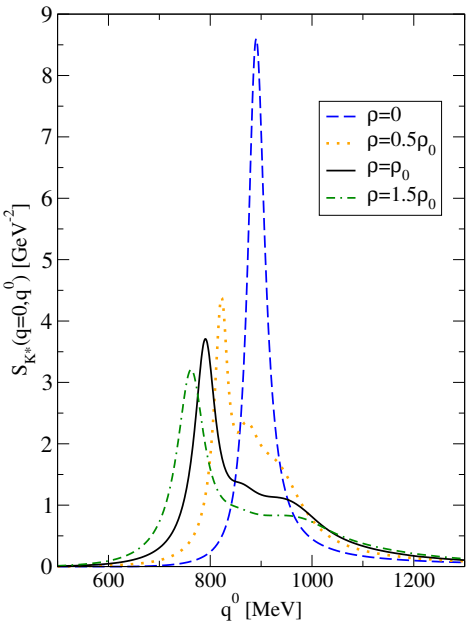

Figure 14.13: La función espectral del mesón $\bar{K}^*$ en función de la energía del mesón q^0 a distintas densidades y momento cero.

su desintegración o canales de absorción $\bar{K}^* \to \bar{K}\pi$ y $\bar{K}^* N \to VY$ conforme aumenta el número másico A. Esto es debido a la larga trayectoria que tiene que recorrer el mesón $\bar{K}^*$ antes de abandonar el núcleo, teniendo así más posibilidades de desintegrarse o ser absorbido.

14.5 Producción de resonancias N^* y Λ^* en la región de 4.3 GeV

En la tesis también se investiga la producción de nuevas resonancias bariónicas generadas a partir de la interacción de un meson y barión ambos a energías alrededor de 4.3 GeV en el sector de encanto oculto.

Para incluir los bariones con encanto, nuevos vértices similares a los proporcionados por el lagrangiano quiral basado en la interacción de Weinberg Tomozawa [211] son construidos a patir de los coeficientes de Clebsch Gordan de SU(4). La simetría es rota en los términos donde un vector pesado es intercambiado y todas las amplitudes correspondientes a SU(3) son reproducidas [211].

En ausencia de evidencia experimental de alguna resonancia bariónica a estas energías, se usan distintos valores de la constante de sustracción, a, que van desde -2.2 a -2.4 o del cutoff, $q_{\rm max}$, de 0.7 a 0.9 (ver Tablas 12.1 y 12.2), en la función de loop mesón - barión. Los canales de desintegración a $P_l B$ o $V_l B$ siendo P_l y V_l un pseudoscalar o vector ligero también son incluidos por medio de diagramas en caja similares a los del estudio de la interacción vector - vector. Se encuentran seis resonancias, tres de la interacción pseudoscalar - barión y otras tantas de la interacción vector - barión con espín 1/2 (y otras seis para espín 3/2 ya que el potencial es degenerado). Se producen una N^* y dos Λ^* que se acoplan fuertemente a $\bar{D}_s\Lambda_c$, $\bar{D}\Xi_c$ y $\bar{D}\Xi_c'$ respectivamente (o bien $\bar{D}_s^*\Lambda_c$, $\bar{D}^*\Xi_c$ y $\bar{D}^*\Xi_c'$ para vector - barión). Las masas y anchuras de desintegración vienen dadas en las Tablas 12.5 y 12.6. Mientras que los acoplamientos a los distintos canales vienen dados en las Tablas 12.3 y 12.4. Vemos que aunque estos son objetos masivos, todas las resonancias están por encima de 4200 MeV, sus anchuras son bastante pequeñas. Esto es debido a la dificultad que tienen las componentes $c\bar{c}$ de desintegrarse en $u\bar{u}$, $d\bar{d}$ y $s\bar{s}$, que necesitan el intercambio de un mesón pesado en el modelo.

A diferencia de otros estudios de resonancias dinámicamente generadas, donde los parámetros de ajuste tanto en estos como en los modelos de quark oscurecen naturaleza de los estados, la importancia de este trabajo radica en que los nuevos estados N^* y Λ^* predichos alrededor de 4.2 GeV (que vendrían a ser parientes de la $N^*(1535)$ y $\Lambda(1405)$), definitivamente no corresponden a bariones de $3q$, aunque un análisis más detallado seria necesario para distinguirlas de estados de cinco quarks. Por esta razón, la observación experimental de estos bariones con encanto oculto viene a ser relevante.

14.6 Conclusiones

El estudio de la interacción vector - vector se ha hecho por medio de los Lagrangianos de hidden gauge, que primero se aplican al sistema $\rho\rho$, para después, una vez que este estudio es extendido a SU(3), contrastando los resultados con las observaciones experimentales, incorporar los mesones D^* y D_s^*, investigando así otros sectores que van desde ρD^* hasta $D^*\bar{D}^*$ o sectores de sabor exótico como $D^*D_s^*$. El potencial es calculado a partir de un diagrama de contacto de cuatro vectores mas un diagrama de intercambio de un vector del tipo Weinberg-Tomozawa. Aunque el canal s representa una contribución menor, los canales t y u proporcionan un potencial fuertemente atractivo y responsable de la aparición de estados ligados. Los polos son buscados en el plano complejo de la energía e identificados con estados ligados o resonancias. Cuando los mesones con encanto son incluidos, se construye inicialmente un Lagrangiano simétrico de SU(4) y más tarde la simetría es rota al usar los valores físicos de las masas, los términos de intercambio de vectores pesados quedan suprimidos por el factor $\kappa = m_\rho^2/m_{D^*}^2$. Éste es el mismo procedimiento seguido en [108] y [109] donde se estudia la interacción entre dos pseudoscalares con encanto y pseudoscalar - vector (ambos mesones con encanto) respectivamente.

Del estudio de la interacción entre dos mesones ρ se obtienen dos polos en la matriz de dispersión que son identificados con las resonancias $f_0(1370)$ y $f_2(1270)$. La naturaleza de éstas es explicada así en términos de estados ligados de dos mesones ρ. Las masas obtenidas son 1532 y 1275 MeV, con anchuras 212 y 100 MeV respectivamente. De los cálculos se deduce que la desintegración en dos piones es el principal canal de desintegración mientras que el canal de cuatro piones representa un 20% de la anterior componente.

La interacción de vectores con algún quark c da lugar a resultados muy interesantes desde el punto de vista teórico y experimental. En el sector (charm $= 1$; extraeza $= 0$) se obtienen tres resonancias: $D_2^*(2460)$ y dos D^* con masa alrededor de 2600 MeV, una con espín=0

y otra con espín=2. Mientras que existe una evidencia experimental de la primera, sólo existe un estado en el PDG con masa 2600 MeV y anchura menor de 15 MeV. Aunque nada se sabe de sus números cuánticos, éste último dato es el que nos permite identificar nuestro estado con espín= 1 a aquél estado del PDG ya que según nuestros cálculos, el estado de espín= 1 es el único que no se puede desintegrar en dos pseudoscalares puesto que el diagrama de caja sólo está permitido para espín= 0 y 2 [116]. En el sector de encanto oculto, encontramos cinco estados ligados que se acoplan mayormente a $D^*\bar{D}^*$, o bien, $D_s^*\bar{D}_s^*$. Tres pueden ser identificados con los nuevos estados observados experimentalmente, la Y(3940), la Z(3930) y la X(4160), con números cuánticos $J^{PC} = 0^{++}$, 2^{++} y 2^{++} respectivamente. En el modelo, los canales de desintegración a dos mesones vectoriales ligeros y $\omega(\phi)$ J/ψ, serían los principales [136]. El resto de sectores también son estudiados, en total aparecen nueve resonancias más, sólo una de ellas ha sido observada experimentalmente, la $D_{s2}(2573)$, que es un estado ligado de D^*K^* en el modelo. La masa y anchura experimentales son reproducidas. Los otros ocho estados son estados ligados de D^*K^*, $D^*\bar{K}^*$, D^*D^* o $D^*D_s^*$. Los últimos tres estados de sabor exóticos obviamente no pueden ser $q\bar{q}$, y los últimos dos poseen anchura cero [155].

Del estudio de la interacción de un mesón vectorial con un barión en el sector de encanto oculto se obtienen dos N^* y cuatro Λ^* alrededor de 4300 MeV para espín= 1/2 (y otras tantas para espín 3/2 puesto que el potencial es simétrico), relativamente estrechas debido a que la componente $c\bar{c}$ dificulta su desintegración en canales de mesón (ligero) - barion (ligero). Éstas serían simplemente parientes de la $N^*(1535)$ y $\Lambda^*(1405)$ en el sector hidden charm y su descubrimiento sería muy importante en el sentido de que no pueden ser acomodadas en el espectro qqq [234].

Los estudios relativos al medio conducen a resultados de interés para los nuevos experimentos que se están planeando por ejemplo en FAIR. Por un lado, la $D_{s0}(2317)$ y la X(3700) [108] que tienen anchura prácticamente cero en el vacío, adquieren anchuras de 100 y 200 MeV

a densidad nuclear normal respectivamente [110]. El estudio permite trazar las reacciones que tendrían lugar en el medio y las reacciones en las facilidades experimentales. Por otro lado, el estudio de la $\bar{K}^*$ en el medio conduce a un resultado espectacular: su anchura aumenta cinco veces (260 MeV) la anchura en vacío a densidad nuclear normal. Mientras que el potencial óptico tiene un moderado valor de -50 MeV [190]. Este aumento es mayor que el encontrado para el ρ en otros estudios. Del cálculo del cociente de transparencia se deduce una reducción sustancial de la unidad (0.4 para núcleos con $A = 200$ para energías en el centro de masas entre 3 y 3.5 GeV). Este experimento puede llevarse a cabo en las instalaciones del Jefferson Lab en USA [239].

Appendix A

Factors $\mathrm{F_I}$, $\mathrm{F'_I}$ for the $R \to P\gamma$ amplitude

This appendix shows the factors $\mathrm{F_I}$, $\mathrm{F'_I}$ for each channel r in Eq. (5.37) and the partial decay widths of the diagrams in Figs. 5.2 and 5.3.

V_1	V_2	P_l	V_f	P_f	A	B	λ	g_I	F$_{\rm I}$	Γ_i(KeV)
K^{*0}	ρ^+	π^-	ω	K^+	-1	$\sqrt{2}$	$\frac{1}{3\sqrt{2}}$	$-\sqrt{\frac{2}{3}}$	$\frac{1}{3\sqrt{3}}$	6.05
K^{*+}	ρ^0	π^0	ω	K^+	$-\frac{1}{\sqrt{2}}$	$\sqrt{2}$	$\frac{1}{3\sqrt{2}}$	$-\frac{1}{\sqrt{3}}$	$\frac{1}{6\sqrt{3}}$	
ρ^0	K^{*+}	K^-	ρ^0	K^+	$\frac{1}{\sqrt{2}}$	$\frac{1}{\sqrt{2}}$	$\frac{1}{\sqrt{2}}$	$-\frac{1}{\sqrt{3}}$	$-\frac{1}{4\sqrt{3}}$	5.05
			ω			$\frac{1}{\sqrt{2}}$	$\frac{1}{3\sqrt{2}}$		$-\frac{1}{12\sqrt{3}}$	
			ϕ			1	$-\frac{1}{3}$		$\frac{1}{6\sqrt{3}}$	
ρ^+	K^{*0}	$\bar{K}^0$	ρ^0	K^+	1	$-\frac{1}{\sqrt{2}}$	$\frac{1}{\sqrt{2}}$	$-\sqrt{\frac{2}{3}}$	$\frac{1}{2\sqrt{3}}$	
			ω			$\frac{1}{\sqrt{2}}$	$\frac{1}{3\sqrt{2}}$		$-\frac{1}{6\sqrt{3}}$	
			ϕ			1	$-\frac{1}{3}$		$\frac{1}{3\sqrt{3}}$	
K^{*+}	ρ^0	η	ρ^0	K^+	$-\frac{2}{\sqrt{3}}$	$\frac{2}{\sqrt{3}}$	$\frac{1}{\sqrt{2}}$	$-\frac{1}{\sqrt{3}}$	$\frac{2}{3\sqrt{3}}$	6.78
		η'			$\frac{1}{\sqrt{6}}$	$\sqrt{\frac{2}{3}}$	$\frac{1}{\sqrt{2}}$	$-\frac{1}{\sqrt{3}}$	$-\frac{1}{6\sqrt{3}}$	0.24

Table A.1: K^{*+} decay diagrams involving the ρK^* channel and the PPV vertex.

V_1	V_2	P_l	V_f	P_f	A	B	λ	g_I	$\mathrm{F_I}$	Γ_i(KeV)
K^{*+}	ω	π^0	ρ^0	K^+	$-\frac{1}{\sqrt{2}}$	$\sqrt{2}$	$\frac{1}{\sqrt{2}}$	1	$-\frac{1}{2}$	0.77
ω	K^{*+}	K^-	ρ^0	K^+	$\frac{1}{\sqrt{2}}$	$\frac{1}{\sqrt{2}}$	$\frac{1}{\sqrt{2}}$	1	$\frac{1}{4}$	0.07
			ω			$\frac{1}{\sqrt{2}}$	$\frac{1}{3\sqrt{2}}$		$\frac{1}{12}$	
			ϕ			1	$-\frac{1}{3}$		$-\frac{1}{6}$	
K^{*+}	ω	η	ω	K^+	$-\frac{2}{\sqrt{3}}$	$\frac{2}{\sqrt{3}}$	$\frac{1}{3\sqrt{2}}$	1	$-\frac{2}{9}$	9.5×10^{-2}
			ϕ						0	
		η'	ω		$\frac{1}{\sqrt{6}}$	$\sqrt{\frac{2}{3}}$	$\frac{1}{3\sqrt{2}}$	1	$\frac{1}{18}$	3.2×10^{-3}
			ϕ						0	
ϕ	K^{*+}	K^-	ρ^0	K^+	-1	$\frac{1}{\sqrt{2}}$	$\frac{1}{\sqrt{2}}$	1	$-\frac{1}{2\sqrt{2}}$	8.4×10^{-2}
			ω			$\frac{1}{\sqrt{2}}$	$\frac{1}{3\sqrt{2}}$		$-\frac{1}{6\sqrt{2}}$	
			ϕ			1	$-\frac{1}{3}$		$\frac{1}{3\sqrt{2}}$	
K^{*+}	ϕ	η	ω	K^+					0	0.17
			ϕ		$-\frac{2}{\sqrt{3}}$	$-\frac{2}{\sqrt{3}}$	$-\frac{1}{3}$	1	$-\frac{2\sqrt{2}}{9}$	
		η'	ω						0	2.6×10^{-2}
			ϕ		$\frac{1}{\sqrt{6}}$	$2\sqrt{\frac{2}{3}}$	$-\frac{1}{3}$	1	$-\frac{\sqrt{2}}{9}$	

Table A.2: K^{*+} decay diagrams involving the ωK^* and ϕK^* channels and the PPV vertex.

V_1	V_2	P_l	V_f	P_f	A	B	λ	g_I	F$_{\rm I}$	Γ_i(KeV)
K^{*0}	ρ^0	π^0	ω	K^0	$\frac{1}{\sqrt{2}}$	$\sqrt{2}$	$\frac{1}{3\sqrt{2}}$	$\frac{1}{\sqrt{3}}$	$\frac{1}{6\sqrt{3}}$	6.05
K^{*+}	ρ^-	π^+	ω	K^0	-1	$\sqrt{2}$	$\frac{1}{3\sqrt{2}}$	$-\sqrt{\frac{2}{3}}$	$\frac{1}{3\sqrt{3}}$	
ρ^-	K^{*+}	K^-	ρ^0	K^0	1	$\frac{1}{\sqrt{2}}$	$\frac{1}{\sqrt{2}}$	$-\sqrt{\frac{2}{3}}$	$-\frac{1}{2\sqrt{3}}$	0
			ω			$\frac{1}{\sqrt{2}}$	$\frac{1}{3\sqrt{2}}$		$-\frac{1}{6\sqrt{3}}$	
			ϕ			1	$-\frac{1}{3}$		$\frac{1}{3\sqrt{3}}$	
ρ^0	K^{*0}	$\bar{K}^0$	ρ^0	K^0	$-\frac{1}{\sqrt{2}}$	$-\frac{1}{\sqrt{2}}$	$\frac{1}{\sqrt{2}}$	$\frac{1}{\sqrt{3}}$	$\frac{1}{4\sqrt{3}}$	
			ω			$\frac{1}{\sqrt{2}}$	$\frac{1}{3\sqrt{2}}$		$-\frac{1}{12\sqrt{3}}$	
			ϕ			1	$-\frac{1}{3}$		$\frac{1}{6\sqrt{3}}$	
K^{*0}	ρ^0	η	ρ^0	K^0	$-\frac{2}{\sqrt{3}}$	$\frac{2}{\sqrt{3}}$	$\frac{1}{\sqrt{2}}$	$\frac{1}{\sqrt{3}}$	$-\frac{2}{3\sqrt{3}}$	6.78
		η'			$\frac{1}{\sqrt{6}}$	$\sqrt{\frac{2}{3}}$	$\frac{1}{\sqrt{2}}$	$\frac{1}{\sqrt{3}}$	$\frac{1}{6\sqrt{3}}$	0.24

Table A.3: K^{*0} decay diagrams involving the ρK^* channel and the PPV vertex.

V_1	V_2	P_l	V_f	P_f	A	B	λ	g_I	F_I	Γ_i(KeV)
K^{*0}	ω	π^0	ρ^0	K^0	$\frac{1}{\sqrt{2}}$	$\sqrt{2}$	$\frac{1}{\sqrt{2}}$	1	$\frac{1}{2}$	0.77
ω	K^{*0}	$\bar{K}^0$	ρ^0	K^0	$\frac{1}{\sqrt{2}}$	$-\frac{1}{\sqrt{2}}$	$\frac{1}{\sqrt{2}}$	1	$-\frac{1}{4}$	0.28
			ω			$\frac{1}{\sqrt{2}}$	$\frac{1}{3\sqrt{2}}$		$\frac{1}{12}$	
			ϕ			1	$-\frac{1}{3}$		$-\frac{1}{6}$	
K^{*0}	ω	η	ω	K^0	$-\frac{2}{\sqrt{3}}$	$\frac{2}{\sqrt{3}}$	$\frac{1}{3\sqrt{2}}$	1	$-\frac{2}{9}$	9.5×10^{-2}
			ϕ						0	
		η'	ω		$\frac{1}{\sqrt{6}}$	$\sqrt{\frac{2}{3}}$	$\frac{1}{3\sqrt{2}}$	1	$\frac{1}{18}$	3.4×10^{-3}
			ϕ						0	
ϕ	K^{*0}	$\bar{K}^0$	ρ^0	K^0	-1	$-\frac{1}{\sqrt{2}}$	$\frac{1}{\sqrt{2}}$	1	$\frac{1}{2\sqrt{2}}$	0.34
			ω			$\frac{1}{\sqrt{2}}$	$\frac{1}{3\sqrt{2}}$		$-\frac{1}{6\sqrt{2}}$	
			ϕ			1	$-\frac{1}{3}$		$\frac{1}{3\sqrt{2}}$	
K^{*0}	ϕ	η	ω	K^0					0	0.17
			ϕ		$-\frac{2}{\sqrt{3}}$	$-\frac{2}{\sqrt{3}}$	$-\frac{1}{3}$	1	$-\frac{2\sqrt{2}}{9}$	
		η'	ω						0	2.6×10^{-2}
			ϕ		$\frac{1}{\sqrt{6}}$	$2\sqrt{\frac{2}{3}}$	$-\frac{1}{3}$	1	$-\frac{\sqrt{2}}{9}$	

Table A.4: K^{*0} decay diagrams involving the ωK^* and ϕK^* channels and the PPV vertex.

V_1	V_2	V_f	V_l	P_f	D	B	λ	g_I	F'_I	Γ_i(KeV)
K^{*0}	ρ^+	ρ^0	ρ^-	K^+	$\sqrt{2}$	1	$\frac{1}{\sqrt{2}}$	$-\sqrt{\frac{2}{3}}$	$\frac{1}{\sqrt{3}}$	12.8
ρ^0	K^{*+}	ρ^0	K^{*-}	K^+	$\frac{1}{\sqrt{2}}$	$\frac{1}{\sqrt{2}}$	$\frac{1}{\sqrt{2}}$	$-\frac{1}{\sqrt{3}}$	$\frac{1}{4\sqrt{3}}$	2.31
		ω			$\frac{1}{\sqrt{2}}$		$\frac{1}{3\sqrt{2}}$		$\frac{1}{12\sqrt{3}}$	
		ϕ			-1		$-\frac{1}{3}$		$\frac{1}{6\sqrt{3}}$	
ω	K^{*+}	ρ^0	K^{*-}	K^+	$\frac{1}{\sqrt{2}}$	$\frac{1}{\sqrt{2}}$	$\frac{1}{\sqrt{2}}$	1	$-\frac{1}{4}$	0.29
		ω			$\frac{1}{\sqrt{2}}$		$\frac{1}{3\sqrt{2}}$		$-\frac{1}{12}$	
		ϕ			-1		$-\frac{1}{3}$		$-\frac{1}{6}$	
ϕ	K^{*+}	ρ^0	K^{*-}	K^+	$\frac{1}{\sqrt{2}}$	1	$\frac{1}{\sqrt{2}}$	1	$-\frac{1}{2\sqrt{2}}$	0.56
		ω			$\frac{1}{\sqrt{2}}$		$\frac{1}{3\sqrt{2}}$		$-\frac{1}{6\sqrt{2}}$	
		ϕ			-1		$-\frac{1}{3}$		$-\frac{1}{3\sqrt{2}}$	

Table A.5: K^{*+} decay diagrams involving the $3V$ vertex. Terms which involve a $\gamma K^* K^*$ coupling with a neutral K^* are zero and are omitted from the table.

V_1	V_2	V_f	V_l	P_f	D	B	λ	g_I	F'_I	Γ_i(KeV)
K^{*+}	ρ^-	ρ^0	ρ^+	K^0	$-\sqrt{2}$	1	$\frac{1}{\sqrt{2}}$	$-\sqrt{\frac{2}{3}}$	$-\frac{1}{\sqrt{3}}$	12.8
ρ^-	K^{*+}	ρ^0	K^{*-}	K^0	$\frac{1}{\sqrt{2}}$	1	$\frac{1}{\sqrt{2}}$	$-\sqrt{\frac{2}{3}}$	$\frac{1}{2\sqrt{3}}$	9.27
		ω			$\frac{1}{\sqrt{2}}$		$\frac{1}{3\sqrt{2}}$		$\frac{1}{6\sqrt{3}}$	
		ϕ			-1		$-\frac{1}{3}$		$\frac{1}{3\sqrt{3}}$	

Table A.6: K^{*0} decay diagrams involving the $3V$ vertex. Terms which involve a $\gamma K^* K^*$ coupling with a neutral K^* are zero and are omitted from the table.

V_1	V_2	P_l	V_f	P_f	A	B	λ	g_I	$\mathrm{F_I}$	Γ_i(KeV)
$\bar{K}^{*0}$	K^{*+}	K^+	ρ^0	π^+	-1	$\frac{1}{\sqrt{2}}$	$\frac{1}{\sqrt{2}}$	1	$-\frac{1}{2\sqrt{2}}$	1.55
			ω			$\frac{1}{\sqrt{2}}$	$\frac{1}{3\sqrt{2}}$		$-\frac{1}{6\sqrt{2}}$	
			ϕ			1	$-\frac{1}{3}$		$\frac{1}{3\sqrt{2}}$	
K^{*+}	$\bar{K}^{*0}$	K^0	ρ^0	π^+	1	$-\frac{1}{\sqrt{2}}$	$\frac{1}{\sqrt{2}}$	1	$-\frac{1}{2\sqrt{2}}$	6.2
			ω			$\frac{1}{\sqrt{2}}$	$\frac{1}{3\sqrt{2}}$		$\frac{1}{6\sqrt{2}}$	
			ϕ			1	$-\frac{1}{3}$		$-\frac{1}{3\sqrt{2}}$	
ρ^+	ω	π^0	ρ^0	π^+	$-\sqrt{2}$	$\sqrt{2}$	$\frac{1}{\sqrt{2}}$	-1	1	18.8

Table A.7: a^+ decay diagrams involving the PPV vertex.

V_1	V_2	V_f	V_l	P_f	D	B	λ	g_I	$\mathrm{F'_I}$	Γ_i(KeV)
$\bar{K}^{*0}$	K^{*+}	ρ^0	K^{*+}	π^+	$\frac{1}{\sqrt{2}}$	1	$\frac{1}{\sqrt{2}}$	1	$-\frac{1}{2\sqrt{2}}$	8.9
		ω			$\frac{1}{\sqrt{2}}$		$\frac{1}{3\sqrt{2}}$		$-\frac{1}{6\sqrt{2}}$	
		ϕ			-1		$-\frac{1}{3}$		$-\frac{1}{3\sqrt{2}}$	
ω	ρ^+	ρ^0	ρ^+	π^+	$\sqrt{2}$	$\sqrt{2}$	$\frac{1}{\sqrt{2}}$	-1	1	8.6

Table A.8: a^+ decay diagrams involving the $3V$ vertex. Terms which involve a $\gamma K^* K^*$ coupling with a neutral K^* are zero and are omitted from the table.

Appendix B

$VV \to VV$ amplitudes in the sector $C = 0; S = 0$

This appendix shows the amplitudes ($VV \to VV$) needed in Chapter 7.

	Contact	V-exchange	$\sim$ Total$[I[J^P]]$
$D^*\bar{D}^* \to D^*\bar{D}^*$	$6\, g_D^2$	$\frac{g_D^2\,(2M_\omega^2 M_\rho^2+M_{J/\psi}^2(3M_\omega^2+M_\rho^2))(4M_{D^*}^2-3s)}{4\,M_{J/\psi}^2 M_\omega^2 M_\rho^2}$	$-49.1\, g_D^2$
$D^*\bar{D}^* \to D_s^*\bar{D}_s^*$	$2\sqrt{2}\, g_D g_{D_s}$	$\frac{g_D g_{D_s}(2M_{D^*}^2+2M_{D_s^*}^2-3s)}{\sqrt{2}\,M_{K^*}^2}$	$-25.1\, g_D g_{D_s}$
$D^*\bar{D}^* \to K^*\bar{K}^*$	$-2\, g g_D$	$-\frac{g g_D(2M_{D^*}^2+2M_{K^*}^2-3s)}{2M_{D_s^*}^2}$	$2.3\, g g_D$
$D^*\bar{D}^* \to \rho\rho$	$-2\sqrt{3}\, g g_D$	$-\frac{\sqrt{3} g g_D(2M_{D^*}^2+2M_\rho^2-3s)}{2\,M_{D_s^*}^2}$	$4.9\, g g_D$
$D^*\bar{D}^* \to \omega\omega$	$2\, g g_D$	$\frac{g g_D(2M_{D^*}^2+2M_\omega^2-3s)}{2\,M_{D^*}^2}$	$-2.8\, g g_D$
$D^*\bar{D}^* \to \phi\phi$	0	0	0
$D^*\bar{D}^* \to J/\psi J/\psi$	$4\, g_D g_{\eta_c}$	$\frac{g_D g_{\eta_c}(2M_{D^*}^2+2M_{J/\psi}^2-3s)}{M_{D^*}^2}$	$-1.2\, g_D g_{\eta_c}$
$D^*\bar{D}^* \to \omega J/\psi$	$-4\, g g_D$	$-\frac{g g_D(2M_{D^*}^2+M_{J/\psi}^2+M_\omega^2-3s)}{M_{D^*}^2}$	$3.5\, g g_D$
$D^*\bar{D}^* \to \phi J/\psi$	0	0	0
$D^*\bar{D}^* \to \omega\phi$	0	0	0
$D_s^*\bar{D}_s^* \to D_s^*\bar{D}_s^*$	$4\, g_{D_s}^2$	$\frac{g_{D_s}^2(M_{J/\psi}^2+M_\phi^2)(4M_{D_s^*}^2-3s)}{2\,M_{J/\psi}^2 M_\phi^2}$	$-12.3\, g_{D_s}^2$
$D_s^*\bar{D}_s^* \to K^*\bar{K}^*$	$-2\sqrt{2}\, g g_{D_s}$	$-\frac{g g_{D_s}(2M_{D_s^*}^2+2M_{K^*}^2-3s)}{\sqrt{2}M_{D^*}^2}$	$3.8\, g g_{D_s}$
$D_s^*\bar{D}_s^* \to \rho\rho$	0	0	0
$D_s^*\bar{D}_s^* \to \omega\omega$	0	0	0
$D_s^*\bar{D}_s^* \to \phi\phi$	$2\sqrt{2}\, g g_{D_s}$	$\frac{g g_{D_s}(2M_{D_s^*}^2+2M_\phi^2-3s)}{\sqrt{2}M_{D_s^*}^2}$	$-3\, g g_{D_s}$
$D_s^*\bar{D}_s^* \to J/\psi J/\psi$	$2\sqrt{2}\, g_{D_s} g_{\eta_c}$	$\frac{g_{D_s} g_{\eta_c}(2M_{D_s^*}^2+2M_{J/\psi}^2-3s)}{\sqrt{2}M_{D_s^*}^2}$	$-0.4\, g_{D_s} g_{\eta_c}$
$D_s^*\bar{D}_s^* \to \omega J/\psi$	0	0	0
$D_s^*\bar{D}_s^* \to \phi J/\psi$	$-4\, g g_{D_s}$	$-\frac{g g_{D_s}(2M_{D_s^*}^2+M_{J/\psi}^2+M_\phi^2-3s)}{M_{D_s^*}^2}$	$2.5\, g g_{D_s}$
$D_s^*\bar{D}_s^* \to \omega\phi$	0	0	0

Table B.1: Amplitude projected in isospin and spin for $I = 0$ and $J = 0$. The approximate Total is obtained at the threshold of $D^*\bar{D}^*$.

	Contact	V-exchange	$\sim$ Total$[I[J^P]]$
$D^*\bar{D}^* \to D^*\bar{D}^*$	$9\, g_D^2$	$\frac{g_D^2\,(2M_\omega^2 M_\rho^2+M_{J/\psi}^2(3M_\omega^2+M_\rho^2))(4M_{D^*}^2-3s)}{4\,M_{J/\psi}^2 M_\omega^2 M_\rho^2}$	$-46.1\, g_D^2$
$D^*\bar{D}^* \to D_s^*\bar{D}_s^*$	$3\sqrt{2}\, g_D g_{D_s}$	$\frac{g_D g_{D_s}(2M_{D^*}^2+2M_{D_s^*}^2-3s)}{\sqrt{2}\,M_{K^*}^2}$	$-23.7\, g_D g_{D_s}$
$D^*\bar{D}^* \to K^*\bar{K}^*$	$3\, g g_D$	$\frac{g g_D(2M_{D^*}^2+2M_{K^*}^2-3s)}{2M_{D_s^*}^2}$	$-1.3\, g g_D$
$D^*\bar{D}^* \to \rho\rho$	0	0	0
$D^*\bar{D}^* \to \omega\omega$	0	0	0
$D^*\bar{D}^* \to \phi\phi$	0	0	0
$D^*\bar{D}^* \to J/\psi J/\psi$	0	0	0
$D^*\bar{D}^* \to \omega J/\psi$	0	0	0
$D^*\bar{D}^* \to \phi J/\psi$	0	0	0
$D^*\bar{D}^* \to \omega\phi$	0	0	0
$D_s^*\bar{D}_s^* \to D_s^*\bar{D}_s^*$	$6\, g_{D_s}^2$	$\frac{g_{D_s}^2(M_{J/\psi}^2+M_\phi^2)(4M_{D_s^*}^2-3s)}{2\,M_{J/\psi}^2 M_\phi^2}$	$-10.3\, g_{D_s}^2$
$D_s^*\bar{D}_s^* \to K^*\bar{K}^*$	$-3\sqrt{2}\, g g_{D_s}$	$-\frac{g g_{D_s}(2M_{D_s^*}^2+2M_{K^*}^2-3s)}{\sqrt{2}M_{D^*}^2}$	$2.4\, g g_{D_s}$
$D_s^*\bar{D}_s^* \to \rho\rho$	0	0	0
$D_s^*\bar{D}_s^* \to \omega\omega$	0	0	0
$D_s^*\bar{D}_s^* \to \phi\phi$	0	0	0
$D_s^*\bar{D}_s^* \to J/\psi J/\psi$	0	0	0
$D_s^*\bar{D}_s^* \to \omega J/\psi$	0	0	0
$D_s^*\bar{D}_s^* \to \phi J/\psi$	0	0	0
$D_s^*\bar{D}_s^* \to \omega\phi$	0	0	0

Table B.2: Amplitude projected in isospin and spin for $I = 0$ and $J = 1$.The approximate Total is obtained at the threshold of $D^*\bar{D}^*$.

	Contact	V-exchange	$\sim Total[I[J^P]]$
$D^*\bar{D}^* \to D^*\bar{D}^*$	$-3\,g_D^2$	$\frac{g_D^2\,(2M_\omega^2 M_\rho^2+M_{J/\psi}^2(3M_\omega^2+M_\rho^2))(4M_{D^*}^2-3s)}{4\,M_{J/\psi}^2 M_\omega^2 M_\rho^2}$	$-58.1\,g_D^2$
$D^*\bar{D}^* \to D_s^*\bar{D}_s^*$	$-\sqrt{2}\,g_D g_{D_s}$	$\frac{g_D g_{D_s}(2M_{D^*}^2+2M_{D_s^*}^2-3s)}{\sqrt{2}\,M_{K^*}^2}$	$-29.4\,g_D g_{D_s}$
$D^*\bar{D}^* \to K^*\bar{K}^*$	$g g_D$	$-\frac{g g_D(2M_{D^*}^2+2M_{K^*}^2-3s)}{2M_{D_s^*}^2}$	$5.4\,g g_D$
$D^*\bar{D}^* \to \rho\rho$	$\sqrt{3}\,g g_D$	$-\frac{\sqrt{3} g g_D(2M_{D^*}^2+2M_\rho^2-3s)}{2\,M_{D_s^*}^2}$	$10.1\,g g_D$
$D^*\bar{D}^* \to \omega\omega$	$-g g_D$	$\frac{g g_D(2M_{D^*}^2+2M_\omega^2-3s)}{2\,M_{D^*}^2}$	$-5.8\,g g_D$
$D^*\bar{D}^* \to \phi\phi$	0	0	0
$D^*\bar{D}^* \to J/\psi J/\psi$	$-2\,g_D g_{\eta_c}$	$\frac{g_D g_{\eta_c}(2M_{D^*}^2+2M_{J/\psi}^2-3s)}{M_{D^*}^2}$	$-7.2\,g_D g_{\eta_c}$
$D^*\bar{D}^* \to \omega J/\psi$	$2\,g g_D$	$-\frac{g g_D(2M_{D^*}^2+M_{J/\psi}^2+M_\omega^2-3s)}{M_{D^*}^2}$	$9.5\,g g_D$
$D^*\bar{D}^* \to \phi J/\psi$	0	0	0
$D^*\bar{D}^* \to \omega\phi$	0	0	0
$D_s^*\bar{D}_s^* \to D_s^*\bar{D}_s^*$	$-2\,g_{D_s}^2$	$\frac{g_{D_s}^2(M_{J/\psi}^2+M_\phi^2)(4M_{D_s^*}^2-3s)}{2\,M_{J/\psi}^2 M_\phi^2}$	$-18.3\,g_{D_s}^2$
$D_s^*\bar{D}_s^* \to K^*\bar{K}^*$	$\sqrt{2}\,g g_{D_s}$	$-\frac{g g_{D_s}(2M_{D_s^*}^2+2M_{K^*}^2-3s)}{\sqrt{2}M_{D^*}^2}$	$8.\,g g_{D_s}$
$D_s^*\bar{D}_s^* \to \rho\rho$	0	0	0
$D_s^*\bar{D}_s^* \to \omega\omega$	0	0	0
$D_s^*\bar{D}_s^* \to \phi\phi$	$-\sqrt{2}\,g g_{D_s}$	$\frac{g g_{D_s}(2M_{D_s^*}^2+2M_\phi^2-3s)}{\sqrt{2}M_{D_s^*}^2}$	$-7.3\,g g_{D_s}$
$D_s^*\bar{D}_s^* \to J/\psi J/\psi$	$-\sqrt{2}\,g_{D_s} g_{\eta_c}$	$\frac{g_{D_s} g_{\eta_c}(2M_{D_s^*}^2+2M_{J/\psi}^2-3s)}{\sqrt{2}M_{D_s^*}^2}$	$-4.6\,g_{D_s} g_{\eta_c}$
$D_s^*\bar{D}_s^* \to \omega J/\psi$	0	0	0
$D_s^*\bar{D}_s^* \to \phi J/\psi$	$2\,g g_{D_s}$	$-\frac{g g_{D_s}(2M_{D_s^*}^2+M_{J/\psi}^2+M_\phi^2-3s)}{M_{D_s^*}^2}$	$8.5\,g g_{D_s}$
$D_s^*\bar{D}_s^* \to \omega\phi$	0	0	0

Table B.3: Amplitude projected in isospin and spin for $I = 0$ and $J = 2$. The approximate Total is obtained at the threshold of $D^*\bar{D}^*$.

	Contact	V-exchange $\sim Total[I[J^P]]$	
$D^*\bar{D}^* \to D^*\bar{D}^*$	$2\, g_D^2$	$\frac{g_D^2\,(2M_\omega^2 M_\rho^2 + M_{J/\psi}^2(-M_\omega^2+M_\rho^2))(4M_{D^*}^2-3s)}{4\,M_{J/\psi}^2 M_\omega^2 M_\rho^2}$	$0.6\, g_D^2$
$D^*\bar{D}^* \to K^*\bar{K}^*$	$2\, g g_D$	$\frac{g g_D(2M_{D^*}^2+2M_{K^*}^2-3s)}{2\,M_{D_s^*}^2}$	$1.2\, g g_D$
$D^*\bar{D}^* \to \rho\rho$	0	0	0
$D^*\bar{D}^* \to \rho\omega$	$-2\sqrt{2}\, g g_D$	$-\frac{g g_D(2M_{D^*}^2+M_\omega^2+M_\rho^2-3s)}{\sqrt{2}\,M_{D^*}^2}$	$4.\, g g_D$
$D^*\bar{D}^* \to \rho J/\psi$	$4\, g g_D$	$\frac{g g_D(2M_{D^*}^2+M_{J/\psi}^2+M_\rho^2-3s)}{M_{D^*}^2}$	$-3.5\, g g_D$
$D^*\bar{D}^* \to \rho\phi$	0	0	0

Table B.4: Amplitude projected in isospin and spin for $I = 1$ and $J = 0$. The approximate Total is obtained at the threshold of $D^*\bar{D}^*$.

	Contact	V-exchange $\sim Total[I[J^P]]$	
$D^*\bar{D}^* \to D^*\bar{D}^*$	$3\, g_D^2$	$\frac{g_D^2\,(2M_\omega^2 M_\rho^2 + M_{J/\psi}^2(-M_\omega^2+M_\rho^2))(4M_{D^*}^2-3s)}{4\,M_{J/\psi}^2 M_\omega^2 M_\rho^2}$	$1.6\, g_D^2$
$D^*\bar{D}^* \to K^*\bar{K}^*$	$-3 g g_D$	$-\frac{g g_D(2M_{D^*}^2+2M_{K^*}^2-3s)}{2\,M_{D_s^*}^2}$	$-2.5\, g g_D$
$D^*\bar{D}^* \to \rho\rho$	$-3\sqrt{2}\, g g_D$	$-\frac{g g_D(2M_{D^*}^2+2M_\rho^2-3s)}{\sqrt{2}\,M_{D^*}^2}$	$-1.3\, g g_D$
$D^*\bar{D}^* \to \rho\omega$	0	0	
$D^*\bar{D}^* \to \rho J/\psi$	0	0	0
$D^*\bar{D}^* \to \rho\phi$	0	0	0

Table B.5: Amplitude projected in isospin and spin for $I = 1$ and $J = 1$. The approximate Total is obtained at the threshold of $D^*\bar{D}^*$.

	Contact	V-exchange	$\sim Total[I[J^P]]$
$D^*\bar{D}^* \to D^*\bar{D}^*$	$-g_D^2$	$\frac{g_D^2\,(2M_\omega^2 M_\rho^2 + M_{J/\psi}^2(-M_\omega^2+M_\rho^2))(4M_{D^*}^2-3s)}{4\,M_{J/\psi}^2 M_\omega^2 M_\rho^2}$	$-2.4\,g_D^2$
$D^*\bar{D}^* \to K^*\bar{K}^*$	$-gg_D$	$\frac{gg_D(2M_{D^*}^2+2M_{K^*}^2-3s)}{2\,M_{D_s^*}^2}$	$2.7\,gg_D$
$D^*\bar{D}^* \to \rho\rho$	0	0	0
$D^*\bar{D}^* \to \rho\omega$	$\sqrt{2}\,gg_D$	$-\frac{gg_D(2M_{D^*}^2+M_\omega^2+M_\rho^2-3s)}{\sqrt{2}\,M_{D^*}^2}$	$8.3\,gg_D$
$D^*\bar{D}^* \to \rho J/\psi$	$-2\,gg_D$	$\frac{gg_D(2M_{D^*}^2+M_{J/\psi}^2+M_\rho^2-3s)}{M_{D^*}^2}$	$-9.5\,gg_D$
$D^*\bar{D}^* \to \rho\phi$	0	0	0

Table B.6: Amplitude projected in isospin and spin for $I = 1$ and $J = 2$. The approximate Total is obtained at the threshold of $D^*\bar{D}^*$.

Appendix C

Momentum corrective factors for the widths

In what follows we calculate the momentum corrective factors to multiply by the widths for zero momentum in Chapter 8. The gauge invariance of the amplitudes was proved in [87].

Thus, the amplitude of the vertex in Fig. C.1 is

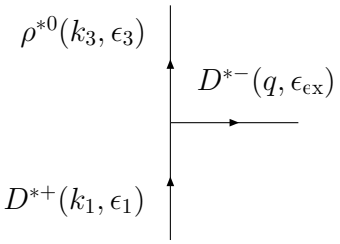

Figure C.1: Three vector contact diagram.

$$\begin{aligned} t_{III} &= \frac{g}{\sqrt{2}}\{(k_1-q)_\nu \epsilon_{\rm ex}^\mu \epsilon_{1\,\mu}\epsilon_3^\nu + (q+k_3)_\nu \epsilon_3^\mu \epsilon_{{\rm ex}\,\mu}\epsilon_1^\nu \\ &\quad -(k_1+k_3)_\nu \epsilon_{1\,\mu}\epsilon_3^\mu \epsilon_{\rm ex}^\nu\}\ . \end{aligned} \tag{C.1}$$

With this expression we find the amplitude for the vector exchange diagram given in Fig. C.2 including the momenta of the final particles (we neglect the momenta of the $D^*(D_s^*)$ particle compared with its mass, $|\vec{k}_{1,2}|/M_V \sim 0$, and therefore $\epsilon^0_{1,2} \sim 0$). In addition, when we couple one or two photon to the final state, the ρ mesons converts into photons, and in the above equations $\epsilon(\rho^0) \longrightarrow \epsilon(\gamma)$ and we can make use of the Coulomb gauge for photons ($\epsilon^0 = 0$ and $\epsilon_i k_i = 0$). In case the ρ meson with momenta k_4 couples to the photon, the amplitude of the diagram in Fig. C.2 taking into account the Coulomb gauge for the $\rho^0(k_4)$ is

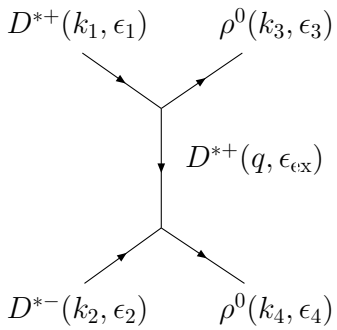

Figure C.2: Exchange vector diagram

$$
\begin{aligned}
t_{\rm ex} \;=\; & \frac{g^2}{2}\{-(k_1^0+k_3^0)(k_2^0+k_4^0)\epsilon_{1\,i}\epsilon_3^i\epsilon_2^j\epsilon_{4\,j} + 2k_{3\,i}\epsilon_1^i(k_2^0+k_4^0)\epsilon_3^0\epsilon_{2\,j}\epsilon_4^j \\
& -|\vec{k}_3|^2\epsilon_1^i\epsilon_{3\,i}\epsilon_2^k\epsilon_{4\,k} + 4k_1^0\epsilon_3^0 k_{4\,k}\epsilon_2^k\epsilon_{1\,l}\epsilon_{4\,l} + 4k_{3\,i}\epsilon_1^i k_{4\,k}\epsilon_2^k\epsilon_{3\,l}\epsilon_{4\,l} \\
& +\frac{1}{M_V^2}(-|\vec{k}_3|^4\epsilon_1^i\epsilon_{3\,i}\epsilon_2^k\epsilon_{4\,k})\} \times \frac{1}{\vec{k}_3^2+M_V^2}\;, \qquad \text{(C.2)}
\end{aligned}
$$

where $M_V = M_{D^*(D_s^*)}$. And we take the same expression but with $\epsilon_3^0 = 0$ in the case of two photons in the final state. The other possibility is to have a four vector contact diagram, as depicted in Fig. C.3. The amplitude in this case can be calculated by means of the Lagrangian of Eq. (3.4) and we get,

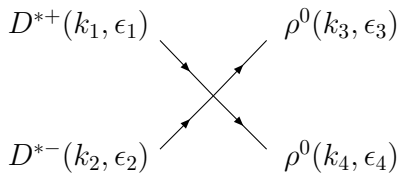

Figure C.3: Four vector contact diagram

$$t_c = \frac{g^2}{2}\{2\epsilon_1^i\epsilon_{2\,i}\epsilon_{3\,j}\epsilon_4^j - (\epsilon_1^i\epsilon_{3\,i}\epsilon_{2\,j}\epsilon_4^j + \epsilon_1^i\epsilon_{4\,i}\epsilon_{2\,j}\epsilon_3^j)\}\ . \tag{C.3}$$

In order to calculate the momentum corrective factors to the widths for zero momentum, we sum Eqs. (C.2) and (C.3) and calculate the squared total amplitude averaging over initial polarizations and summing over final polarizations of the photons ($\sum_\lambda \epsilon_i(\gamma)\epsilon_j(\gamma) = \delta_{ij} - \frac{k_{4\,i}k_{4\,j}}{|\vec{k_4}^2|}$ and $\sum_r \epsilon_\mu(\rho^0)\epsilon_\nu(\rho^0) = -g_{\mu\nu} + \frac{k_{3\,\mu}k_{3\,\nu}}{M_V^2}$) and we divide it by the same expression obtained for zero momentum. This is, we evaluate

$$\frac{\bar{\sum}_{\rm in}\sum_{\rm fin}|t|^2}{\bar{\sum}_{\rm in}\sum_{\rm fin}|t|^2(k=0)} \tag{C.4}$$

with $|t|^2 = t_c^2 + 2t_c \times t_{\rm ex} + t_{\rm ex}^2$ and $k = |\vec{k}_3| = |\vec{k}_4|$ in the center of mass reference system. In what follows we give the expressions of t_c^2, $t_c \times t_{\rm ex}$ and $t_{\rm ex}^2$ for $\gamma\gamma$ and $V\gamma$ in the final state, and spin $S = 0, 2$. For the sake of simplicity we take $k_1^0 \simeq k_3^0 = k^0$ in the expressions.

C.1 State with $S = 0$ going to $\gamma\gamma$

- $t_{\rm ex}^2$

$$\bar{\sum_{\text{in}}}\sum_{\text{fin}} t_{\text{ex}}^2 = g^4\{\frac{8}{3}k_0^4 + \frac{4}{3}(k_0k)^2 + \frac{16}{3}(k_0k)^2 + \frac{4}{3}\frac{k_0^2k^4}{M_V^2} + \frac{k^4}{6} + \frac{4}{3}k^4 + \frac{1}{3}\frac{k^6}{M_V^2} + \frac{8}{3}k^4 + \frac{4}{3}\frac{k^6}{M_V^2} + \frac{1}{6}\frac{k^8}{M_V^4}\} \times \frac{4}{(k^2+M_V^2)^2} \tag{C.5}$$

where the t and u channels have been taken into account by means of the factor 4 at the end of the above equation.

- $t_c \times t_{\text{ex}}$

$$\bar{\sum_{\text{in}}}\sum_{\text{fin}} t_c \times t_{\text{ex}} = \frac{g^4}{2}\{-\frac{32}{3}k_0^2 - \frac{40}{3}k^2 - \frac{8}{3}\frac{k^4}{M_V^2}\}\frac{1}{k^2+M_V^2} \tag{C.6}$$

- t_c^2

$$\bar{\sum_{\text{in}}}\sum_{\text{fin}} t_c^2 = \frac{8}{3}\,g^4 \tag{C.7}$$

- Momentum corrective factor (F):

$$\frac{\bar{\sum}_{\text{in}}\sum_{\text{fin}}|t|^2}{\bar{\sum}_{\text{in}}\sum_{\text{fin}}|t|^2(k=0)} = \frac{k^4+3k^2M_V^2+4k_0^2M_V^2-2M_V^4)^2}{4(k^2+M_V^2)^2(-2k_0^2+M_V^2)^2} \tag{C.8}$$

with $|t|^2 = t_c^2 + 2t_c \times t_{\text{ex}} + t_{\text{ex}}^2$.

C.2 State with $S = 2$ going to $\gamma\gamma$

- $t_{\rm ex}^2$

$$\begin{aligned}\bar{\sum_{\rm in}}\sum_{\rm fin} t_{\rm ex}^2 &= g^4\{\frac{28}{15}k_0^4+\frac{14}{15}(k_0k)^2-\frac{16}{15}(k_0k)^2+\frac{14}{15}\frac{k_0^2k^4}{M_V^2}\\ &\quad+\frac{7k^4}{60}-\frac{4}{15}k^4+\frac{7}{30}\frac{k^6}{M_V^2}+\frac{16}{15}k^4-\frac{4}{15}\frac{k^6}{M_V^2}+\frac{7}{60}\frac{k^8}{M_V^4}\}\\ &\quad\times\frac{4}{(k^2+M_V^2)^2}\end{aligned} \tag{C.9}$$

- $t_c \times t_{\rm ex}$

$$\bar{\sum_{\rm in}}\sum_{\rm fin} t_c\times t_{\rm ex} = g^4\{\frac{28}{15}k_0^2+\frac{4}{5}k_0^2-\frac{1}{15}k^2+\frac{4}{5}k_0^2+\frac{7}{15}\frac{k^4}{M_V^2}\}\frac{1}{k^2+M_V^2} \tag{C.10}$$

- t_c^2

$$\bar{\sum_{\rm in}}\sum_{\rm fin} t_c^2 = \frac{7}{15}\,g^4 \tag{C.11}$$

- Momentum corrective factor (F):

$$\begin{aligned}\frac{\bar{\sum}_{\rm in}\sum_{\rm fin}|t|^2}{\bar{\sum}_{\rm in}\sum_{\rm fin}|t|^2(k=0)} &= (7k^8+12k^6M_V^2+112k_0^4M_V^4+104k_0^2M_V^6\\ &\quad+7M_V^8+k^4(56k_0^2M_V^2+74M_V^4)\\ &\quad+\frac{12k^2(8k_0^2M_V^4+M_V^6))}{(7(k^2+M_V^2)^2(4k_0^2+M_V^2)^2)}\end{aligned} \tag{C.12}$$

C.3 State with $S = 0$ going to $V\gamma$

- $t_{\rm ex}^2$

$$\bar{\sum_{\rm in}}\sum_{\rm fin}|t_1|^2 = g^4\{\frac{8}{3}k_0^4+\frac{4}{3}(k_0k)^2+\frac{16}{3}(k_0k)^2+\frac{4}{3}\frac{k_0^2k^4}{M_V^2} +\frac{k^4}{6}+\frac{4}{3}k^4+\frac{1}{3}\frac{k^6}{M_V^2}+\frac{8}{3}k^4+\frac{4}{3}\frac{k^6}{M_V^2} +\frac{1}{6}\frac{k^8}{M_V^4}\}\times\frac{4}{(k^2+M_V^2)^2} \tag{C.13}$$

- $t_c \times t_{\rm ex}$

$$\bar{\sum_{\rm in}}\sum_{\rm fin}|t_2|^2 = g^4\frac{1}{2}\{-\frac{32}{3}k_0^2-\frac{40}{3}k^2-\frac{8}{3}\frac{k^4}{M_V^2}\}\frac{1}{k^2+M_V^2} \tag{C.14}$$

- t_c^2

$$\bar{\sum_{\rm in}}\sum_{\rm fin}t_c^2 = \frac{8}{3}\,g^4 \tag{C.15}$$

- Momentum corrective factor (F):

$$\frac{\bar{\sum}_{\rm in}\sum_{\rm fin}|t|^2}{\bar{\sum}_{\rm in}\sum_{\rm fin}|t|^2(k=0)} = \frac{k^4+3k^2M_V^2+4k_0^2M_V^2-2M_V^4)^2}{4(k^2+M_V^2)^2(-2k_0^2+M_V^2)^2)} \tag{C.16}$$

C.4 State with $S = 2$ going to $V\gamma$

- $t_{\rm ex}^2$

$$\begin{aligned}\bar{\sum_{\text{in}}}\sum_{\text{fin}}|t_1|^2 &= \{4k_0^4(\frac{2}{3}+\frac{1}{5}\frac{k^2}{m_{V_l}^2})+2k_0^2k^2(\frac{2}{3}+\frac{1}{5}\frac{k^2}{m_{V_l}^2})-\frac{16}{15}k_0^2k^2\\ &+2(\frac{2}{3}+\frac{1}{5}\frac{k^2}{m_{V_l}^2})\frac{k^4k_0^2}{M_V^2}-\frac{4}{15}k^4+\frac{k^6}{2M_V^2}(\frac{2}{3}+\frac{1}{5}\frac{k^2}{m_{V_l}^2})\\ &-\frac{4}{15}\frac{k^6}{M_V^2}+\frac{k^4}{6}+\frac{k^6}{20m_{V_l}^2}+\frac{16}{15}k^4+\frac{k^8}{4M_V^4}(\frac{2}{3}+\frac{1}{5}\frac{k^2}{m_{V_l}^2})\\ &-\frac{8}{5}\frac{k_0^4k^2}{m_{V_l}^2}-\frac{2}{5}\frac{k^4k_0^2}{m_{V_l}^2}-\frac{8}{5}k_0^2k^2+\frac{8}{5}\frac{k_0^4k^2}{m_{V_l}^2}-\frac{2}{5}\frac{k^6k_0^2}{m_{V_l}^2M_V^2}\\ &+\frac{4}{5}k^2k_0^2(-1+\frac{k_0^2}{m_{V_l}^2})-\frac{8}{5}\frac{k_0^4k^2}{m_{V_l}^2}-\frac{2}{5}\frac{k_0^2k^4}{m_{V_l}^2}\\ &-\frac{2}{5}\frac{k_0^2k^6}{m_{V_l}^2M_V^2}+\frac{4}{5}k_0^2k^2(-1+\frac{k_0^2}{m_{V_l}^2})\}4\frac{1}{(k^2+M_V^2)}\end{aligned} \tag{C.17}$$

- $t_c \times t_{\text{ex}}$

$$\begin{aligned}\bar{\sum_{\text{in}}}\sum_{\text{fin}}t_c\times t_{\text{ex}} &= \{2(\frac{2}{3}+\frac{1}{5}\frac{k^2}{M_{V_l}^2})4k_0^2-\frac{4}{5}\frac{k^2}{M_{V_l}^2}2k_0^2+2(\frac{2}{3}\\ &+\frac{1}{5}\frac{k^2}{M_{V_l}^2})k^2-\frac{8}{5}k_0^2\frac{k^2}{M_{V_l}^2}-\frac{16}{15}k^2\\ &+2(\frac{2}{3}+\frac{1}{5}\frac{k^2}{M_{V_l}^2})\frac{k^4}{M_V^2}\}\frac{1}{k^2+M_V^2}\end{aligned} \tag{C.18}$$

- t_c^2

$$\bar{\sum_{\text{in}}}\sum_{\text{fin}}t_c^2 = (\frac{2}{3}+\frac{1}{5}\frac{k^2}{M_{V_l}^2})\,g^4 \tag{C.19}$$

- Momentum corrective factor (F):

$$\begin{aligned}\frac{\bar{\sum}_{\rm in}\sum_{\rm fin}|t|^2}{\bar{\sum}_{\rm in}\sum_{\rm fin}|t|^2(k=0)} &= (3k^{10}+10M_V^4(4k_0^2+M_V^2)^2M_{V_l}^2 \\ &\quad +6k^6M_V^2(-4k_0^2+3M_V^2+4M_{V_l}^2) \\ &\quad +2k^8(6M_V^2+5M_{V_l}^2) \\ &\quad +3k^2M_V^4(-4k_0^2+M_V^2)(-4k_0^2+M_V^2+8M_{V_l}^2) \\ &\quad +k^4(12M_V^6+92M_V^4M_{V_l}^2 \\ &\quad +\frac{k_0^2(-48M_V^4+80M_V^2M_{V_l}^2)))}{2(k^2+M_V^2)^2(12k^2k_0^2M_V^2+5(4k_0^2+M_V^2)^2M_{V_l}^2)}\end{aligned} \tag{C.20}$$

pole [MeV]	$I^G\,J^{PC}$	meson	F($V=\rho,\omega,\phi;\gamma$)	F($J/\psi\gamma$)	F($\gamma\gamma$)
$(3943,+i7.4)$	$0^+\,(0^{++})$	$Y(3940)$	2.4	1.3	2.4
$(3922,+i26)$	$0^+\,(2^{++})$	$Z(3930)$	0.4	0.8	0.7
$(4169,+i66)$	$0^+\,(2^{++})$	$X(4160)$	0.4	0.8	0.7
$(3919,+i74)$	$1^-\,(2^{++})$	$'Y_p(3912)'$	0.4	0.8	0.7

Table C.1: Momentum corrective factors

Appendix D

$VV \to VV$ amplitudes in other sectors

The VV amplitudes for the sectors charm $= 0$; strangeness $= 1$ (hidden charm), charm $= 1$; strangeness $= -1, 1, 2$, charm $= 2$, strangeness $= 0, 1, 2$ involved in Chapter 9.

J	Amplitude	Contact		V-exchange	$\sim$ Total
0	$D_s^*\bar{D}^* \to D_s^*\bar{D}^*$	$2g^2$		$-\frac{g^2(p_1+p_3).(p_2+p_4)}{m^2_{J/\psi}}$	$0.23g^2$
0	$D_s^*\bar{D}^* \to J/\psi K^*$	$-4g^2$	$\frac{g^2(p_1+p_4).(p_2+p_3)}{m^2_{D^*}} + \frac{g^2(p_1+p_3).(p_2+p_4)}{m^2_{D_s^*}}$		$3.6g^2$
0	$J/\psi K^* \to J/\psi K^*$	0		0	0
1	$D_s^*\bar{D}^* \to D_s^*\bar{D}^*$	$3g^2$		$-\frac{g^2(p_1+p_3).(p_2+p_4)}{m^2_{J/\psi}}$	$1.2g^2$
1	$D_s^*\bar{D}^* \to J/\psi K^*$	0	$-\frac{g^2(p_1+p_4).(p_2+p_3)}{m^2_{D^*}} + \frac{g^2(p_1+p_3).(p_2+p_4)}{m^2_{D_s^*}}$		$-0.43g^2$
1	$J/\psi K^* \to J/\psi K^*$	0		0	0
2	$D_s^*\bar{D}^* \to D_s^*\bar{D}^*$	$-g^2$		$-\frac{g^2(p_1+p_3).(p_2+p_4)}{m^2_{J/\psi}}$	$-2.8g^2$
2	$D_s^*\bar{D}^* \to J/\psi K^*$	$2g^2$	$\frac{g^2(p_1+p_4).(p_2+p_3)}{m^2_{D^*}} + \frac{g^2(p_1+p_3).(p_2+p_4)}{m^2_{D_s^*}}$		$9.6g^2$
2	$J/\psi K^* \to J/\psi K^*$	0		0	0

Table D.1: Amplitudes for $C = 0$, $S = 1$ and $I = 1/2$.

J	Amplitude	Contact	V-exchange	$\sim$ Total
0	$D^*\bar{K}^* \to D^*\bar{K}^*$	$4g^2$	$-\frac{g^2(p_1+p_4).(p_2+p_3)}{m^2_{D_s^*}} + \frac{1}{2}g^2(\frac{1}{m^2_\omega} - \frac{3}{m^2_\rho})(p_1+p_3).(p_2+p_4)$	$-9.9g^2$
1	$D^*\bar{K}^* \to D^*\bar{K}^*$	0	$\frac{g^2(p_1+p_4).(p_2+p_3)}{m^2_{D_s^*}} + \frac{1}{2}g^2(\frac{1}{m^2_\omega} - \frac{3}{m^2_\rho})(p_1+p_3).(p_2+p_4)$	$-10.2g^2$
2	$D^*\bar{K}^* \to D^*\bar{K}^*$	$-2g^2$	$-\frac{g^2(p_1+p_4).(p_2+p_3)}{m^2_{D_s^*}} + \frac{1}{2}g^2(\frac{1}{m^2_\omega} - \frac{3}{m^2_\rho})(p_1+p_3).(p_2+p_4)$	$-15.9g^2$

Table D.2: Amplitudes for $C = 1$, $S = -1$ and $I = 0$.

J	Amplitude	Contact	V-exchange	$\sim$ Total
0	$D^*\bar{K}^* \to D^*\bar{K}^*$	$-4g^2$	$\frac{g^2(p_1+p_4).(p_2+p_3)}{m^2_{D_s^*}} + \frac{g^2}{2}(\frac{1}{m^2_\omega} + \frac{1}{m^2_\rho})(p_1+p_3).(p_2+p_4)$	$9.7g^2$
1	$D^*\bar{K}^* \to D^*\bar{K}^*$	0	$-\frac{g^2(p_1+p_4).(p_2+p_3)}{m^2_{D_s^*}} + \frac{g^2}{2}(\frac{1}{m^2_\omega} + \frac{1}{m^2_\rho})(p_1+p_3).(p_2+p_4)$	$9.9g^2$
2	$D^*\bar{K}^* \to D^*\bar{K}^*$	$2g^2$	$\frac{g^2(p_1+p_4).(p_2+p_3)}{m^2_{D_s^*}} + \frac{g^2}{2}(\frac{1}{m^2_\omega} + \frac{1}{m^2_\rho})(p_1+p_3).(p_2+p_4)$	$15.7g^2$

Table D.3: Amplitudes for $C = 1$, $S = -1$ and $I = 1$.

J	Amplitude	Contact	V-exchange	$\sim$ Total
0	$D^*K^* \to D^*K^*$	$4g^2$	$-\frac{g^2}{2}(\frac{3}{m_\rho^2}+\frac{1}{m_\omega^2})(p_1+p_3).(p_2+p_4)$	$-19.8g^2$
0	$D^*K^* \to D_s^*\omega$	$-4g^2$	$\frac{g^2(p_1+p_4).(p_2+p_3)}{m_{D_s^*}^2}+\frac{g^2(p_1+p_3).(p_2+p_4)}{m_{K^*}^2}$	$6.8g^2$
0	$D^*K^* \to D_s^*\phi$	$2\sqrt{2}g^2$	$-\frac{\sqrt{2}g^2(p_1+p_3).(p_2+p_4)}{m_{K^*}^2}$	$-9.2g^2$
0	$D_s^*\omega \to D_s^*\omega$	0	0	0
0	$D_s^*\omega \to D_s^*\phi$	0	0	0
0	$D_s^*\phi \to D_s^*\phi$	$-2g^2$	$\frac{g^2(p_1+p_4).(p_2+p_3)}{m_{D_s^*}^2}$	$0.20g^2$
1	$D^*K^* \to D^*K^*$	$6g^2$	$-\frac{g^2}{2}(\frac{3}{m_\rho^2}+\frac{1}{m_\omega^2})(p_1+p_3).(p_2+p_4)$	$-17.7g^2$
1	$D^*K^* \to D_s^*\omega$	0	$-\frac{g^2(p_1+p_4).(p_2+p_3)}{m_{D_s^*}^2}+\frac{g^2(p_1+p_3).(p_2+p_4)}{m_{K^*}^2}$	$6.6g^2$
1	$D^*K^* \to D_s^*\phi$	$3\sqrt{2}g^2$	$-\frac{\sqrt{2}g^2(p_1+p_3).(p_2+p_4)}{m_{K^*}^2}$	$-7.8g^2$
1	$D_s^*\omega \to D_s^*\omega$	0	0	0
1	$D_s^*\omega \to D_s^*\phi$	0	0	0
1	$D_s^*\phi \to D_s^*\phi$	$3g^2$	$-\frac{g^2(p_1+p_4).(p_2+p_3)}{m_{D_s^*}^2}$	$0.8g^2$
2	$D^*K^* \to D^*K^*$	$-2g^2$	$-\frac{g^2}{2}(\frac{3}{m_\rho^2}+\frac{1}{m_\omega^2})(p_1+p_3).(p_2+p_4)$	$-25.8g^2$
2	$D^*K^* \to D_s^*\omega$	$2g^2$	$\frac{g^2(p_1+p_4).(p_2+p_3)}{m_{D_s^*}^2}+\frac{g^2(p_1+p_3).(p_2+p_4)}{m_{K^*}^2}$	$12.8g^2$
2	$D^*K^* \to D_s^*\phi$	$-\sqrt{2}g^2$	$-\frac{\sqrt{2}g^2(p_1+p_3).(p_2+p_4)}{m_{K^*}^2}$	$-13.5g^2$
2	$D_s^*\omega \to D_s^*\omega$	0	0	0
2	$D_s^*\omega \to D_s^*\phi$	0	0	0
2	$D_s^*\phi \to D_s^*\phi$	g^2	$\frac{g^2(p_1+p_4).(p_2+p_3)}{m_{D_s^*}^2}$	$3.2g^2$

Table D.4: Amplitudes for $C = 1$, $S = 1$ and $I = 0$.

J	Amplitude	Contact	V-exchange	$\sim$ Total
0	$D^*K^* \to D^*K^*$	0	$\frac{g^2}{2}(\frac{1}{m_\rho^2} - \frac{1}{m_\omega^2})(p_1+p_3).(p_2+p_4)$	$0.11g^2$
0	$D^*K^* \to D_s^*\rho$	$4g^2$	$-\frac{g^2(p_1+p_4)(p_2+p_3)}{m_{D^*}^2} - \frac{g^2(p_1+p_3).(p_2+p_4)}{m_{K^*}^2}$	$-6.8g^2$
0	$D_s^*\rho \to D_s^*\rho$	0	0	0
1	$D^*K^* \to D^*K^*$	0	$\frac{g^2}{2}(\frac{1}{m_\rho^2} - \frac{1}{m_\omega^2})(p_1+p_3).(p_2+p_4)$	$0.11g^2$
1	$D^*K^* \to D_s^*\rho$	0	$\frac{g^2(p_1+p_4)(p_2+p_3)}{m_{D^*}^2} - \frac{g^2(p_1+p_3).(p_2+p_4)}{m_{K^*}^2}$	$-6.6g^2$
1	$D_s^*\rho \to D_s^*\rho$	0	0	0
2	$D^*K^* \to D^*K^*$	0	$\frac{g^2}{2}(\frac{1}{m_\rho^2} - \frac{1}{m_\omega^2})(p_1+p_3).(p_2+p_4)$	$0.11g^2$
2	$D^*K^* \to D_s^*\rho$	$-2g^2$	$-\frac{g^2(p_1+p_4)(p_2+p_3)}{m_{D^*}^2} - \frac{g^2(p_1+p_3).(p_2+p_4)}{m_{K^*}^2}$	$-12.8g^2$
2	$D_s^*\rho \to D_s^*\rho$	0	0	0

Table D.5: Amplitudes for $C = 1$, $S = 1$ and $I = 1$.

J	Amplitude	Contact	V-exchange	$\sim$ Total
0	$D_s^*K^* \to D_s^*K^*$	$-4g^2$	$\frac{g^2(p_1+p_4)(p_2+p_3)}{m_{D^*}^2} + \frac{g^2(p_1+p_3).(p_2+p_4)}{m_\phi^2}$	$5.5g^2$
1	$D_s^*K^* \to D_s^*K^*$	0	$-\frac{g^2(p_1+p_4)(p_2+p_3)}{m_{D^*}^2} + \frac{g^2(p_1+p_3).(p_2+p_4)}{m_\phi^2}$	$5.0g^2$
2	$D_s^*K^* \to D_s^*K^*$	$2g^2$	$\frac{g^2(p_1+p_4)(p_2+p_3)}{m_{D^*}^2} + \frac{g^2(p_1+p_3).(p_2+p_4)}{m_\phi^2}$	$11.5g^2$

Table D.6: Amplitudes for $C = 1$, $S = 2$ and $I = 1/2$.

J	Amplitude	Contact	V-exchange	$\sim$ Total
0	$D^*D^* \to D^*D^*$	0	0	0
1	$D^*D^* \to D^*D^*$	0	$\frac{1}{4}g^2(\frac{2}{m_{J/\psi}^2} + \frac{1}{m_\omega^2} - \frac{3}{m_\rho^2})\{(p_1+p_4).(p_2+p_3)$ $+(p_1+p_3).(p_2+p_4)\}$	$-25.4g^2$
2	$D^*D^* \to D^*D^*$	0	0	0

Table D.7: Amplitudes for $C = 2$, $S = 0$ and $I = 0$.

J	Amplitude	Contact	V-exchange	$\sim$ Total
0	$D^*D^* \to D^*D^*$	$-4g^2$	$\frac{1}{4}g^2(\frac{2}{m^2_{J/\psi}}+\frac{1}{m^2_\omega}+\frac{1}{m^2_\rho})\{(p_1+p_4).(p_2+p_3)$ $+(p_1+p_3).(p_2+p_4)\}$	$24.3g^2$
1	$D^*D^* \to D^*D^*$	0	0	0
2	$D^*D^* \to D^*D^*$	$2g^2$	$\frac{1}{4}g^2(\frac{2}{m^2_{J/\psi}}+\frac{1}{m^2_\omega}+\frac{1}{m^2_\rho})\{(p_1+p_4).(p_2+p_3)$ $+(p_1+p_3).(p_2+p_4)\}$	$30.3g^2$

Table D.8: Amplitudes for $C = 2$, $S = 0$ and $I = 1$.

J	Amplitude	Contact	V-exchange		$\sim$ Total
0	$D_s^*D^* \to D_s^*D^*$	$-4g^2$	$\frac{g^2(p_1+p_4).(p_2+p_3)}{m^2_{K^*}}$	$+\frac{g^2(p_1+p_3).(p_2+p_4)}{m_{J/\psi^2}}$	$19.0g^2$
1	$D_s^*D^* \to D_s^*D^*$	0	$-\frac{g^2(p_1+p_4).(p_2+p_3)}{m^2_{K^*}}$	$+\frac{g^2(p_1+p_3).(p_2+p_4)}{m_{J/\psi^2}}$	$-19.5g^2$
2	$D_s^*D^* \to D_s^*D^*$	$2g^2$	$\frac{g^2(p_1+p_4).(p_2+p_3)}{m^2_{K^*}}$	$+\frac{g^2(p_1+p_3).(p_2+p_4)}{m_{J/\psi^2}}$	$25.0g^2$

Table D.9: Amplitudes for $C = 2$, $S = 1$ and $I = 1/2$.

J	Amplitude	Contact	V-exchange	$\sim$ Total
0	$D_s^*D_s^* \to D_s^*D_s^*$	$-4g^2$	$\frac{g^2}{2}(\frac{1}{m^2_{J/\psi}}+\frac{1}{m^2_\phi})\{(p_1+p_4).(p_2+p_3)$ $+(p_1+p_3).(p_2+p_4)\}$	$15.0g^2$
1	$D_s^*D_s^* \to D_s^*D_s^*$	0	0	0
2	$D_s^*D_s^* \to D_s^*D_s^*$	$2g^2$	$\frac{g^2}{2}(\frac{1}{m^2_{J/\psi}}+\frac{1}{m^2_\phi})\{(p_1+p_4).(p_2+p_3)$ $+(p_1+p_3).(p_2+p_4)\}$	$21.0g^2$

Table D.10: Amplitudes for $C = 2$, $S = 2$ and $I = 0$.

Appendix E

Box diagrams for the D^*K^*, $D_s^*\phi$ and $D^*\bar{K}^*$ channels

E.1 $D^*K^* \to D^*K^*$

We show the potential for the $D^*K^* \to D^*K^*$ box diagram with $m_1 = \pi$, $m_2 = D$, $m_3 = \pi$ and $m_4 = K$.

$$\begin{aligned} V_{D^*K^*}(s) &= \frac{g^4}{15\pi^2}\int_0^{q_{max}} dq \frac{q^6}{\omega^3\omega_K\omega_D}\frac{1}{(-k_3^0+\omega+\omega_D-i\epsilon)^2} \\ &\times\frac{1}{(-k_4^0+\omega+\omega_K-i\epsilon)^2}\frac{1}{(k_3^0+\omega+\omega_D)^2}\frac{1}{(\sqrt{s}+\omega_D+\omega_K)} \\ &\times\frac{1}{(-\sqrt{s}+\omega_D+\omega_K-i\epsilon)}\frac{1}{(k_4^0+\omega+\omega_K)^2}\times P(s)\ , \end{aligned} \tag{E.1}$$

with

$$
\begin{aligned}
P(s) \;=\; & -2(2k_3^0\sqrt{s}(\omega+\omega_D)\omega_K(4\omega^4 - s(4\omega^2+3\omega\omega_D+\omega_D^2) \\
& +4\omega^2(\omega_D+\omega_K)^2 + 3\omega\omega_D(\omega_D+\omega_K)^2 + \omega_D^2(\omega_D+\omega_K)^2 \\
& +4\omega^3(\omega_D+2\omega_K)) \\
& +2(k_3^0)^3\sqrt{s}\omega_K(-4\omega^3 - \omega_D(-s+(\omega_D+\omega_K)^2)) \\
& +(k_3^0)^4(2\omega^3(\omega_D+\omega_K) + \omega_D\omega_K(-s+(\omega_D+\omega_K)^2)) \\
& -(k_3^0)^2(4\omega^5(\omega_D+\omega_K) + 8\omega^4(\omega_D+\omega_K)^2 \\
& +4\omega^3(\omega_D^3 - 3s\omega_K + 6\omega_D^2\omega_K + 6\omega_D\omega_K^2 + \omega_K^3) \\
& +14\omega^2\omega_D\omega_K(-s+(\omega_D+\omega_K)^2) + 4\omega\omega_D\omega_K(\omega_D+\omega_K) \\
& \times(-s+(\omega_D+\omega_K)^2) + \omega_D\omega_K(s^2+(\omega_D+\omega_K)^2(\omega_D^2+\omega_K^2) \\
& -2s(\omega_D^2+\omega_D\omega_K+\omega_K^2))) + (\omega+\omega_D)^2(2\omega^5(\omega_D+\omega_K) \\
& +4\omega^4(\omega_D^2+3\omega_D\omega_K+2\omega_K^2) + 2\omega^3(\omega_D^3 - 2s\omega_K + 7\omega_D^2\omega_K \\
& +12\omega_D\omega_K^2 + 6\omega_K^3) + \omega_D\omega_K(s-\omega_K^2)(s-(\omega_D+\omega_K)^2) \\
& +\omega^2\omega_K(5\omega_D+8\omega_K)(-s+(\omega_D+\omega_K)^2) \\
& +2\omega\omega_K(s^2+\omega_K(\omega_D+\omega_K)^2(2\omega_D+\omega_K) \\
& -s(\omega_D^2+4\omega_D\omega_K+2\omega_K^2)))) \;.
\end{aligned}
\tag{E.2}
$$

Where $\omega = \sqrt{q^2+m_\pi^2}$, $\omega_D = \sqrt{q^2+m_D^2}$, $\omega_K = \sqrt{q^2+m_K^2}$, $k_3^0 = \frac{s+m_{D^*}^2-m_{K^*}^2}{2\sqrt{s}}$ and $k_4^0 = \frac{s+m_{K^*}^2-m_{D^*}^2}{2\sqrt{s}}$. After projecting in spin and isospin, the potential is

$$
\begin{aligned}
V_{D^*K^*}^{I=0,J=0}(s) &= \frac{9}{4}\,5\,V_{D^*K^*}(s) \\
V_{D^*K^*}^{I=0,J=2}(s) &= \frac{9}{4}\,2\,V_{D^*K^*}(s) \\
V_{D^*K^*}^{I=1,J=0}(s) &= \frac{1}{4}\,5\,V_{D^*K^*}(s) \\
V_{D^*K^*}^{I=1,J=2}(s) &= \frac{1}{4}\,2\,V_{D^*K^*}(s)\;.
\end{aligned}
\tag{E.3}
$$

E.2 $D^*K^* \to D_s^*\phi$

We show the potential for the $D^*K^* \to D_s^*\phi$ box diagram with $m_1 = \pi$, $m_2 = D$, $m_3 = K$ and $m_4 = K$.

$$
\begin{aligned}
V_{D^*K^*\to D_s^*\phi}(s) \;=\; & \frac{4g^4}{15\pi^2}\int_0^{q_{max}} dq \frac{q^6}{\omega\omega_D\omega_K^2}\frac{1}{(-k_1^0+\omega+\omega_D-i\epsilon)} \\
& \times \frac{1}{(-k_1^0+k_3^0+\omega+\omega_K-i\epsilon)}\frac{1}{(-k_2^0+\omega+\omega_K-i\epsilon)} \\
& \times \frac{1}{(-k_3^0+\omega_D+\omega_K-i\epsilon)}\frac{1}{(-k_4^0+2\omega_K-i\epsilon)} \\
& \times \frac{1}{(-\sqrt{s}+\omega_D+\omega_K-i\epsilon)}\frac{1}{(k_1^0+\omega+\omega_D)} \\
& \times \frac{1}{(k_3^0+\omega_D+\omega_K)}\frac{1}{(k_2^0+\omega+\omega_K)}\frac{1}{(k_4^0+2\omega_k)} \\
& \times \frac{1}{(\sqrt{s}+\omega_D+\omega_k)}\frac{1}{(k_1^0-k_3^0+\omega+\omega_K-i\epsilon)} \times P(s)\ ,
\end{aligned}
\tag{E.4}
$$

with

$$
\begin{aligned}
P(s) \;=\;& -\omega_K(2(k_1^0)^3\omega(-(k_3^0)^2\sqrt{s}\omega_K + (k_3^0)^3(\omega_D+\omega_K)\\
&+\sqrt{s}(\omega_D+\omega_K)(s-\omega_D^2-3\omega_D\omega_K-4\omega_K^2)\\
&-k_3^0(\omega_D^3+s\omega_K+4\omega_D^2\omega_K+7\omega_D\omega_K^2+4\omega_K^3))\\
&-(k_1^0)^4\omega(-2k_3^0\sqrt{s}\omega_K+(k_3^0)^2(\omega_D+\omega_K)\\
&+(\omega_D+\omega_K)(s-2(\omega_D^2+3\omega_D\omega_K+2\omega_K^2)))\\
&+2k_1^0(k_3^0+\sqrt{s})\omega((k_3^0)^3\sqrt{s}\omega_K\\
&-(k_3^0)^2(\omega_D^3+2s\omega_K+2\omega_D^2\omega_K+2\omega_D\omega_K^2+\omega_K^3\\
&+\omega^2(\omega_D+\omega_K)+2\omega(\omega_D+\omega_K)^2)+k_3^0\sqrt{s}(\omega_D^3+s\omega_K\\
&+4\omega_D^2\omega_K+4\omega_D\omega_K^2-2\omega_K^3+\omega^2(\omega_D+2\omega_K)\\
&+2\omega(\omega_D^2+4\omega_D\omega_K+2\omega_K^2))+(\omega_D+\omega_K)(\omega_D^4\\
&+3\omega_D^3\omega_K+4\omega_D^2\omega_K^2+4\omega_D\omega_K^3+4\omega_K^4+\omega^2(\omega_D^2\\
&+3\omega_D\omega_K+4\omega_K^2)+2\omega(\omega_D^3+3\omega_D^2\omega_K+4\omega_D\omega_K^2+4\omega_K^3)\\
&-s(\omega^2+\omega_D^2+\omega_D\omega_K+\omega_K^2+2\omega(\omega_D+\omega_K))))\\
&-(k_1^0)^2\omega(2(k_3^0)^3\sqrt{s}\omega_K+(k_3^0)^4(\omega_D+\omega_K)\\
&-2(k_3^0)^2(\omega_D^3+\omega_D^2\omega_K+3\omega_D\omega_K^2+\omega^2(\omega_D+\omega_K)\\
&+3\omega_K(s+\omega_K^2)+\omega(\omega_D^2+3\omega_D\omega_K+2\omega_K^2))\\
&+2k_3^0\sqrt{s}\omega_K(s+2(\omega^2-\omega_D^2-4\omega_D\omega_K-3\omega_K^2\\
&+\omega(\omega_D+2\omega_K)))+(\omega_D+\omega_K)(s^2-2s(\omega^2+\omega_D^2+3\omega_K^2\\
&+\omega(\omega_D+2\omega_K))+2(\omega_D+\omega_K)(\omega_D^3+2\omega_D^2\omega_K\\
&+5\omega_D\omega_K^2+4\omega_K^3+2\omega^2(\omega_D+2\omega_K)\\
&+2\omega(\omega_D+2\omega_K)^2)))+(\omega+\omega_D)(2(k_3^0)^3\sqrt{s}\omega_K(s-\omega^2\\
&-(\omega_D+\omega_K)^2-\omega(\omega_D+2\omega_K))+(k_3^0)^4(\omega^2(\omega_D+\omega_K)\\
&+\omega(\omega_D^2+3\omega_D\omega_K+2\omega_K^2)+\omega_K(-s\\
&+(\omega_D+\omega_K)^2))+2k_3^0\sqrt{s}\omega_K(\omega^4+(\omega_D+\omega_K)^4\\
&+\omega^3(\omega_D+4\omega_K)+\omega^2(\omega_D^2+4\omega_D\omega_K+6\omega_K^2)+\omega(\omega_D^3\\
&+4\omega_D^2\omega_K+6\omega_D\omega_K^2+4\omega_K^3)-s(\omega^2+(\omega_D+\omega_K)^2\\
&+\omega(\omega_D+2\omega_K)))-(k_3^0)^2(\omega^4(\omega_D+\omega_K)\\
&+\omega^3(\omega_D^2+5\omega_D\omega_K+4\omega_K^2)\\
&+\omega^2(\omega_D^3-2s\omega_K+9\omega_D^2\omega_K+18\omega_D\omega_K^2+10\omega_K^3)
\end{aligned}
\tag{E.5}
$$

$$
\begin{aligned}
&+\omega(\omega_D^4 + 2s\omega_D\omega_K + 5\omega_D^3\omega_K \\
&-4s\omega_K^2 + 18\omega_D^2\omega_K^2 + 26\omega_D\omega_K^3 + 12\omega_K^4) \\
&+\omega_K(s^2 - 2s(\omega_D^2 + 2\omega_D\omega_K + 3\omega_K^2) \\
&+(\omega_D + \omega_K)^2(\omega_D^2 + 2\omega_D\omega_K + 5\omega_K^2))) \\
&+(\omega + \omega_K)(\omega_D + \omega_K)(s^2(\omega + \omega_D + \omega_K) \\
&+2(\omega + \omega_K)(\omega_D + \omega_K)(2\omega_K(\omega_D + \omega_K)^2 \\
&+\omega^2(\omega_D + 2\omega_K) + \omega(\omega_D + 2\omega_K)^2) \\
&-s(\omega^3 + \omega_D^3 + 3\omega_D^2\omega_K + 7\omega_D\omega_K^2 + 5\omega_K^3 \\
&+\omega^2(\omega_D + 3\omega_K) + \omega(\omega_D^2 + 7\omega_D\omega_K + 7\omega_K^2))))) \ . \qquad \text{(E.6)}
\end{aligned}
$$

Where $\omega = \sqrt{q^2 + m_\pi^2}$, $\omega_D = \sqrt{q^2 + m_D^2}$, $\omega_K = \sqrt{q^2 + m_K^2}$, $k_1^0 = \frac{s + m_{D^*}^2 - m_{K^*}^2}{2\sqrt{s}}$, $k_2^0 = \frac{s + m_{K^*}^2 - m_{D^*}^2}{2\sqrt{s}}$ and $k_3^0 = \frac{s + m_{D_s^*}^2 - m_\phi^2}{2\sqrt{s}}$. And its spin-isospin projection is

$$
\begin{aligned}
V^{I=0,J=0}_{D^*K^*\to D_s^*\phi}(s) &= \frac{3}{\sqrt{2}}\, 5\, V_{D^*K^*\to D_s^*\phi}(s) \\
V^{I=0,J=2}_{D^*K^*\to D_s^*\phi}(s) &= \frac{3}{\sqrt{2}}\, 2\, V_{D^*K^*\to D_s^*\phi}(s) \ . \qquad \text{(E.7)}
\end{aligned}
$$

E.3 $D_s^*\phi \to D_s^*\phi$

We show the potential for the $D_s^*\phi \to D_s^*\phi$ box diagram with $m_1 = K$, $m_2 = D$, $m_3 = K$ and $m_4 = K$.

$$
\begin{aligned}
V_{D_s^*\phi}(s) &= \frac{g^4}{15\pi^2}\int_0^{q_{max}} dq \frac{q^6}{\omega_D\omega_K^3}\frac{1}{(-k_3^0 + \omega_D + \omega_K - i\epsilon)^2} \\
&\times \frac{1}{(-k_4^0 + 2\omega_K - i\epsilon)^2}\frac{1}{(\sqrt{s} + \omega_D + \omega_K)}\frac{1}{(k_4^0 + 2\omega_K)^2} \\
&\times \frac{1}{(k_3^0 + \omega_D + \omega_K)^2}\frac{1}{(-\sqrt{s} + \omega_D + \omega_K - i\epsilon)} \times P(s) \ , \qquad \text{(E.8)}
\end{aligned}
$$

with

$$\begin{aligned}
P(s) &= 2((k_3^0)^4(s\omega_D-\omega_D^3-2\omega_D^2\omega_K-3\omega_D\omega_K^2-2\omega_K^3)\\
&+2(k_3^0)^3\sqrt{s}(-s\omega_D+\omega_D^3+2\omega_D^2\omega_K+\omega_D\omega_K^2+4\omega_K^3)\\
&-2k_3^0\sqrt{s}(\omega_D+\omega_K)(\omega_D^4+5\omega_D^3\omega_K+11\omega_D^2\omega_K^2\\
&+15\omega_D\omega_K^3+16\omega_K^4-s(\omega_D^2+3\omega_D\omega_K+4\omega_K^2))\\
&+(k_3^0)^2(s^2\omega_D+\omega_D^5+6\omega_D^4\omega_K+32\omega_D^3\omega_K^2+74\omega_D^2\omega_K^3\\
&+63\omega_D\omega_K^4+16\omega_K^5-2s(\omega_D^3+3\omega_D^2\omega_K+10\omega_D\omega_K^2+6\omega_K^3))\\
&-(\omega_D+\omega_K)^2(s^2(\omega_D+2\omega_K)+4\omega_K^2(3\omega_D^3+12\omega_D^2\omega_K\\
&+17\omega_D\omega_K^2+8\omega_K^3)-s(\omega_D^3+4\omega_D^2\omega_K+15\omega_D\omega_K^2+16\omega_K^3)))\ .
\end{aligned} \tag{E.9}$$

Where $\omega=\sqrt{q^2+m_\pi^2}$, $\omega_D=\sqrt{q^2+m_D^2}$, $\omega_K=\sqrt{q^2+m_K^2}$, $k_3^0=\frac{s+m_{D_s^*}^2-m_\phi^2}{2\sqrt{s}}$, $k_4^0=\frac{s+m_\phi^2-m_{D_s^*}^2}{2\sqrt{s}}$ and $\epsilon=1$ MeV. Finally, we project it in spin and isospin

$$\begin{aligned}
V_{D_s^*\phi}^{I=0,J=0}(s) &= 2\times 5\, V_{D_s^*\phi}(s)\\
V_{D_s^*\phi}^{I=0,J=2}(s) &= 2\times 2\, V_{D_s^*\phi}(s)\ .
\end{aligned} \tag{E.10}$$

E.4 $D^*\bar{K}^*\to D^*\bar{K}^*$

We show the potential for the $D^*\bar{K}^*\to D^*\bar{K}^*$ box diagram with $m_1=\pi$, $m_2=D$, $m_3=\pi$ and $m_4=\bar{K}$. The potential is the same than that given by Eq. (E.1) with:

$$\begin{aligned}
V_{D^*\bar{K}^*}^{I=0,J=0}(s) &= \frac{9}{4}\,5\, V_{D^*K^*}(s)\\
V_{D^*\bar{K}^*}^{I=0,J=2}(s) &= \frac{9}{4}\,2\, V_{D^*K^*}(s)\\
V_{D^*\bar{K}^*}^{I=1,J=0}(s) &= \frac{1}{4}\,5\, V_{D^*K^*}(s)\\
V_{D^*\bar{K}^*}^{I=1,J=2}(s) &= \frac{1}{4}\,2\, V_{D^*K^*}(s)\ .
\end{aligned} \tag{E.11}$$

Appendix $\mathcal{F}$

The value of C_{ab} for the PB and VB amplitudes

This Appendix gives the coefficients C in Eqs. (12.12), (12.13), (12.19), (12.19) and (12.20) for the various IS sectors studied.

	$\bar{D}\Sigma_c$	πN	$K\Sigma$
$\bar{D}\Sigma_c$	2	-1	1

Table F.1: Coefficients C_{ab} in the Eq. (12.12, 12.19) for the PB system in the sector $I = 3/2$, $S = 0$.

	$\bar{D}\Sigma_c$	$\bar{D}\Lambda_c^+$	$\eta_c N$	πN	ηN	$\eta' N$	$K\Sigma$	$K\Lambda$
$\bar{D}\Sigma_c$	-1	0	$-\sqrt{3/2}$	$-1/2$	$-1/\sqrt{2}$	$1/2$	1	0
$\bar{D}\Lambda_c^+$		1	$\sqrt{3/2}$	$-3/2$	$1/\sqrt{2}$	$-1/2$	0	1

Table F.2: Coefficients C_{ab} in the Eq. (12.12, 12.19, 12.20) for the PB system in the sector $I = 1/2$, $S = 0$.

	$\bar{D}_s\Xi_c'$	$\bar{D}_s\Xi_c$	$\bar{D}\Omega_c$	$\pi\Xi$	$\bar{K}\Sigma$	$\eta\Xi$	$\eta'\Xi$	$\bar{K}\Lambda$
$\bar{D}_s\Xi_c'$	1	0	$\sqrt{2}$	0	$\sqrt{3}/2$	$1/\sqrt{6}$	$1/\sqrt{3}$	$-\sqrt{3}/2$
$\bar{D}_s\Xi_c$		1	0	0	$-3/2$	$1/\sqrt{2}$	1	$1/2$
$\bar{D}\Omega_c$			0	$\sqrt{3/2}$	0	$-1/\sqrt{3}$	$1/\sqrt{6}$	0

Table F.3: Coefficients C_{ab} in the Eq. (12.12, 12.19) for the PB system in the sector $I = 1/2$, $S = -2$.

	$\bar{D}_s\Sigma_c$	$\bar{D}\Xi_c'$	$\bar{D}\Xi_c$	$\pi\Sigma$	$\pi\Lambda$	$\eta\Sigma$	$\eta'\Sigma$	$\bar{K}N$	K Ξ
$\bar{D}_s\Sigma_c$	0	$\sqrt{2}$	0	0	0	$-1/\sqrt{3}$	$\sqrt{2/3}$	-1	0
$\bar{D}\Xi_c'$		1	0	$1/\sqrt{2}$	$-\sqrt{3}/2$	$1/\sqrt{6}$	$1/2\sqrt{3}$	0	$1/\sqrt{2}$
$\bar{D}\Xi_c$			1	$-\sqrt{3/2}$	$1/2$	$-1/\sqrt{2}$	$-1/2$	0	$\sqrt{3/2}$

Table F.4: Coefficients C_{ab} in the Eq. (12.12, 12.19) for the PB system in the sector $I = 1$, $S = -1$.

	$\bar{D}_s\Lambda_c^+$	$\bar{D}\Xi_c$	$\bar{D}\Xi_c'$	$\eta_c\Lambda$	$\pi\Sigma$	$\eta\Lambda$	$\eta'\Lambda$	$\bar{K}N$	K Ξ
$\bar{D}_s\Lambda_c^+$	0	$-\sqrt{2}$	0	1	0	$1/\sqrt{3}$	$\sqrt{2/3}$	$-\sqrt{3}$	0
$\bar{D}\Xi_c$		-1	0	$1/\sqrt{2}$	$-3/2$	$1/\sqrt{6}$	$-1/2\sqrt{3}$	0	$\sqrt{3/2}$
$\bar{D}\Xi_c'$			-1	$-\sqrt{3/2}$	$\sqrt{3}/2$	$-1/\sqrt{2}$	$1/2$	0	$1/\sqrt{2}$
$\eta_c\Lambda$				0	0	0	0	0	0

Table F.5: Coefficients C_{ab} in the Eq. (12.12, 12.19, 12.20) for the PB system in the sector $I = 0$, $S = -1$.

	$\bar{D}_s\Sigma_c$	$\bar{K}\Xi$
$\bar{D}_s\Sigma_c$	2	$\sqrt{2}$

Table F.6: Coefficients C_{ab} in the Eq. (12.12, 12.19) for the PB system in the sector $I = 0$, $S = -3$.

	$\bar{D}^*\Sigma_c$	ρN	$K^*\Sigma$
$\bar{D}^*\Sigma_c$	2	-1	1

Table F.7: Coefficients C_{ab} in the Eq. (12.13, 12.19) for the VB system in the sector $I = 3/2$, $S = 0$.

	$\bar{D}^*\Sigma_c$	$\bar{D}^*\Lambda_c^+$	ρN	ωN	ϕN	$K^*\Sigma$	$K^*\Lambda$
$\bar{D}^*\Sigma_c$	-1	0	$-1/2$	$\sqrt{3}/2$	0	1	0
$\bar{D}^*\Lambda_c^+$		1	$-3/2$	$-\sqrt{3}/2$	0	0	1

Table F.8: Coefficients C_{ab} in the Eq. (12.13, 12.19) for the VB system in the sector $I = 1/2$, $S = 0$.

	$\bar{D}_s^*\Xi_c'$	$\bar{D}_s^*\Xi_c$	$\bar{D}^*\Omega_c$	$\rho\Xi$	$\bar{K}^*\Sigma$	$\omega\Xi$	$\phi\Xi$	$\bar{K}^*\Lambda$
$\bar{D}_s^*\Xi_c'$	1	0	$\sqrt{2}$	0	$\sqrt{3}/2$	0	$-1/\sqrt{2}$	$-\sqrt{3}/2$
$\bar{D}_s^*\Xi_c$		1	0	0	$-3/2$	0	$-\sqrt{3/2}$	$1/2$
$\bar{D}^*\Omega_c$			0	$\sqrt{3/2}$	0	$\sqrt{3}/2$	0	0

Table F.9: Coefficients C_{ab} in the Eq. (12.13, 12.19) for the VB system in the sector $I = 1/2$, $S = -2$.

	$\bar{D}_s^*\Sigma_c$	$\bar{D}^*\Xi_c'$	$\bar{D}^*\Xi_c$	$\rho\Sigma$	$\rho\Lambda$	$\omega\Sigma$	$\phi\Sigma$	$\bar{K}^*N$	$K^*\Xi$
$\bar{D}_s^*\Sigma_c$	0	$\sqrt{2}$	0	0	0	0	-1	-1	0
$\bar{D}^*\Xi_c'$		1	0	$1/\sqrt{2}$	$-\sqrt{3}/2$	$-1/2$	0	0	$1/\sqrt{2}$
$\bar{D}^*\Xi_c$			1	$-\sqrt{3/2}$	$1/2$	$\sqrt{3}/2$	0	0	$\sqrt{3/2}$

Table F.10: Coefficients C_{ab} in the Eq. (12.13, 12.19) for the VB system in the sector $I = 1$, $S = -1$.

	$\bar{D}_s^*\Lambda_c^+$	$\bar{D}^*\Xi_c$	$\bar{D}^*\Xi_c'$	$\rho\Sigma$	$\omega\Lambda$	$\phi\Lambda$	$\bar{K}^*N$	$K^*\Xi$
$\bar{D}_s^*\Lambda_c^+$	0	$-\sqrt{2}$	0	0	0	-1	$-\sqrt{3}$	0
$\bar{D}^*\Xi_c$		-1	0	$-3/2$	$-1/2$	0	0	$\sqrt{3/2}$
$\bar{D}^*\Xi_c'$			-1	$\sqrt{3}/2$	$\sqrt{3}/2$	0	0	$1/\sqrt{2}$

Table F.11: Coefficients C_{ab} in the Eq. (12.13, 12.19) for the VB system in the sector $I = 0$, $S = -1$.

	$\bar{D}_s^*\Sigma_c$	$\bar{K}^*\Xi$
$\bar{D}_s^*\Sigma_c$	2	$\sqrt{2}$

Table F.12: Coefficients C_{ab} in the Eq. (12.13, 12.19) for the VB system in the sector $I = 0$, $S = -3$.

Bibliography

[1] M. B. Voloshin, L. B. Okun, JETP Lett. **23**, 333 (1976) [Pisma Zh. Eksp. Teor. Fiz. **23**, 369 (1976)].

[2] A. De Rujula, H. Georgi, S.L. Glashow, Phys. Rev. Lett. **38**, 317 (1976)

[3] E. S. Swanson, Phys. Rept. **429**, 243 (2006)

[4] N. A. Tornqvist , Z. Phys. C **61**, 525 (1994)

[5] T. E. O. Ericson, G. Karl, Phys. Lett. B **309**, 426 (1993)

[6] L. Maiani, F. Piccinini, A. D. Polosa, V. Riquer, Phys. Rev. D **71** 014028 (2004)

[7] T-W. Chiu, T. H. Hsieh, Phys. Rev. D **73**, 111503(R) (2006)

[8] N. A. Tornqvist, Annals Phys. **123**, 1 (1979).

[9] T. Barnes, E. S. Swanson, Phys. Rev. **C77**, 055206 (2008).

[10] F. E. Close, C. E. Thomas, Phys. Rev. **C79**, 045201 (2009).

[11] F.-K. Guo, C. Hanhart, U.-G. Meißner, Phys. Rev. Lett. **102**, 242004 (2009).

[12] F.-K. Guo, C. Hanhart, U.-G. Meißner, Phys. Lett. B **665**, 26 (2008).

[13] U. G. Meissner, Phys. Rept. **161**, 213 (1988).

[14] G. Ecker, J. Gasser, A. Pich and E. de Rafael, Nucl. Phys. B **321**, 311 (1989).

[15] M. C. Birse, Z. Phys. A **355**, 231 (1996)

[16] J. Gasser and H. Leutwyler, Annals Phys. **158**, 142 (1984).

[17] J.J. Sakurai, *Currents and mesons* (University of Chicago Press, Chicago, 1969)

[18] V. de Alfaro, S. Fubini, G. Furlan and C. Rossetti, *Currents in hadron physics* (North Holland, Amsterdam, 1973)

[19] S. Gasiorowicz and D. A. Geffen, Rev. Mod. Phys. **41**, 531 (1969).

[20] O. Kaymakcalan, S. Rajeev and J. Schechter, Phys. Rev. D **30**, 594 (1984).

[21] M. Bando, T. Kugo and K. Yamawaki, Phys. Rept. **164**, 217 (1988).

[22] S. Weinberg, Phys. Rev. **166**, 1568 (1968).

[23] S. R. Coleman, J. Wess and B. Zumino, Phys. Rev. **177**, 2239 (1969).

[24] C. G. . Callan, S. R. Coleman, J. Wess and B. Zumino, Phys. Rev. **177**, 2247 (1969).

[25] G. Ecker, J. Gasser, H. Leutwyler, A. Pich and E. de Rafael, Phys. Lett. B **223**, 425 (1989).

[26] J. Bijnens and E. Pallante, Mod. Phys. Lett. A **11**, 1069 (1996)

[27] B. Borasoy and U. G. Meissner, Int. J. Mod. Phys. A **11**, 5183 (1996)

[28] Y. Brihaye, N. Pak and P. Rossi, Nucl. Phys. B **254**, 71 (1985).

[29] J. Bijnens, C. Bruno and E. de Rafael, Nucl. Phys. B **390**, 501 (1993)

[30] J. Bijnens, arXiv:hep-ph/9502393.

[31] H. Georgi, Phys. Rev. Lett. **63**, 1917 (1989).

[32] K. Kawarabayashi and M. Suzuki, Phys. Rev. Lett. **16**, 255 (1966).

[33] Riazuddin and Fayyazuddin, Phys. Rev. **147**, 1071 (1966).

[34] M. Bando, T. Kugo, S. Uehara, K. Yamawaki and T. Yanagida, Phys. Rev. Lett. **54**, 1215 (1985).

[35] S. Weinberg, Physica A **96**, 327 (1979).

[36] J. Gasser and H. Leutwyler, Nucl. Phys. B **250**, 465 (1985).

[37] V. Bernard, N. Kaiser and U. G. Meissner, Nucl. Phys. A **615**, 483 (1997)

[38] N. Kaiser, Eur. Phys. J. A **3**, 307 (1998).

[39] V. Bernard, N. Kaiser and U. G. Meissner, Nucl. Phys. A **619**, 261 (1997)

[40] J. A. Oller, E. Oset and A. Ramos, Prog. Part. Nucl. Phys. **45**, 157 (2000)

[41] U. G. Meissner and J. A. Oller, Nucl. Phys. A **673**, 311 (2000)

[42] T. Inoue, E. Oset and M. J. Vicente Vacas, Phys. Rev. C **65**, 035204 (2002)

[43] J. A. Oller and U. G. Meissner, Phys. Lett. B **500**, 263 (2001)

[44] E. Oset and A. Ramos, Nucl. Phys. A **635**, 99 (1998)

[45] C. Garcia-Recio, J. Nieves, E. Ruiz Arriola and M. J. Vicente Vacas, Phys. Rev. D **67**, 076009 (2003)

[46] C. Garcia-Recio, M. F. M. Lutz and J. Nieves, Phys. Lett. B **582**, 49 (2004)

[47] T. Hyodo, S. I. Nam, D. Jido and A. Hosaka, Phys. Rev. C **68**, 018201 (2003)

[48] T. Hyodo and W. Weise, Phys. Rev. C **77**, 035204 (2008)

[49] D. Jido, M. Oka and A. Hosaka, Prog. Theor. Phys. **106**, 873 (2001)

[50] D. Jido, J. A. Oller, E. Oset, A. Ramos and U. G. Meissner, Nucl. Phys. A **725**, 181 (2003)

[51] J. A. Oller and E. Oset, Nucl. Phys. A **620**, 438 (1997) [Erratum-ibid. A **652**, 407 (1999)]

[52] J. A. Oller and E. Oset, Phys. Rev. D **60**, 074023 (1999)

[53] J. A. Oller, E. Oset and J. R. Pelaez, Phys. Rev. D **59**, 074001 (1999) [Erratum-ibid. D **60**, 099906 (1999)]

[54] M. F. M. Lutz and E. E. Kolomeitsev, Nucl. Phys. A **730**, 392 (2004)

[55] L. Roca, E. Oset and J. Singh, Phys. Rev. D **72**, 014002 (2005)

[56] D. Jido, J. A. Oller, E. Oset, A. Ramos and U. G. Meissner, Nucl. Phys. A **755**, 669 (2005)

[57] L. Roca, S. Sarkar, V. K. Magas and E. Oset, Phys. Rev. C **73**, 045208 (2006)

[58] A. Dobado and J. R. Pelaez, Phys. Rev. D **56**, 3057 (1997)

[59] N. Kaiser, T. Waas and W. Weise, Nucl. Phys. A **612**, 297 (1997)

[60] E. Oset, Nucl. Phys. A **721**, 58 (2003)

[61] J. Nieves and E. Ruiz Arriola, Phys. Lett. B **455**, 30 (1999)

[62] N. Kaiser, Eur. Phys. J. A **3**, 307 (1998).

[63] V. E. Markushin, Eur. Phys. J. A **8**, 389 (2000)

[64] N. Kaiser, P. B. Siegel and W. Weise, Phys. Lett. B **362**, 23 (1995)

[65] J. C. Nacher, A. Parreno, E. Oset, A. Ramos, A. Hosaka and M. Oka, Nucl. Phys. A **678**, 187 (2000)

[66] S. Sarkar, E. Oset and M. J. Vicente Vacas, Nucl. Phys. A **750**, 294 (2005) [Erratum-ibid. A **780**, 78] (2006)

[67] E. E. Kolomeitsev and M. F. M. Lutz, Phys. Lett. B **585**, 243 (2004)

[68] J. R. Pelaez, Phys. Rev. Lett. **92**, 102001 (2004)

[69] J. R. Pelaez, Mod. Phys. Lett. A **19**, 2879 (2004)

[70] A. V. Anisovich, V. V. Anisovich and V. A. Nikonov, Eur. Phys. J. A **12**, 103 (2001)

[71] A. Dobado and J. R. Pelaez, Phys. Rev. D **65**, 077502 (2002)

[72] A. H. Fariborz, Phys. Rev. D **74**, 054030 (2006)

[73] T. Umekawa, K. Naito, M. Oka and M. Takizawa, Phys. Rev. C **70**, 055205 (2004)

[74] S. Rodriguez and M. Napsuciale, Phys. Rev. D **71**, 074008 (2005)

[75] F. Kleefeld, E. van Beveren, G. Rupp and M. D. Scadron, Phys. Rev. D **66**, 034007 (2002)

[76] F. E. Close, Nucl. Phys. Proc. Suppl. **56A**, 248 (1997)

[77] J. Nieves and E. Ruiz Arriola, Nucl. Phys. A **679**, 57 (2000)

[78] C. Amsler *et al.* [Particle Data Group], Phys. Lett. B **667**, 1 (2008).

[79] A. I. Titov, B. Kampfer and B. L. Reznik, Eur. Phys. J. A **7**, 543 (2000)

[80] A. I. Titov, B. Kampfer and B. L. Reznik, Phys. Rev. C **65**, 065202 (2002)

[81] H. Nagahiro, L. Roca, A. Hosaka and E. Oset, Phys. Rev. D **79**, 014015 (2009)

[82] D. V. Bugg, Eur. Phys. J. C **52**, 55 (2007)

[83] S. Uehara *et al.* [for the Belle Collaboration and for the Belle Collaboration], Phys. Rev. D **78**, 052004 (2008)

[84] M. Albaladejo and J. A. Oller, arXiv:0801.4929 [hep-ph].

[85] R. Molina, D. Nicmorus and E. Oset, Phys. Rev. D **78**, 114018 (2008)

[86] L. S. Geng and E. Oset, Phys. Rev. D **79**, 074009 (2009)

[87] H. Nagahiro, J. Yamagata-Sekihara, E. Oset, S. Hirenzaki and R. Molina, Phys. Rev. D **79**, 114023 (2009)

[88] E. Klempt and A. Zaitsev, Phys. Rept. **454**, 1 (2007)

[89] V. Crede and C. A. Meyer, Prog. Part. Nucl. Phys. **63**, 74 (2009).

[90] C. Amsler, Phys. Lett. B **541**, 22 (2002).

[91] M. Doring, Nucl. Phys. A **786**, 164 (2007)

[92] T. Branz, T. Gutsche and V. E. Lyubovitskij, Phys. Rev. D **78**, 114004 (2008)

[93] Y. Dong, A. Faessler, T. Gutsche, S. Kovalenko and V. E. Lyubovitskij, Phys. Rev. D **79**, 094013 (2009)

[94] T. Branz, T. Gutsche and V. E. Lyubovitskij, arXiv:1005.3168 [hep-ph].

[95] Y. Dong, A. Faessler, T. Gutsche, S. Kumano and V. E. Lyubovitskij, Phys. Rev. D **82**, 034035 (2010)

[96] T. Branz, T. Gutsche and V. E. Lyubovitskij, arXiv:1007.4311 [hep-ph].

[97] X. Liu and H. W. Ke, Phys. Rev. D **80**, 034009 (2009)

[98] D. M. Li, H. Yu and Q. X. Shen, J. Phys. G **27**, 807 (2001).

[99] S. Godfrey and N. Isgur, Phys. Rev. D **32**, 189 (1985).

[100] T. Barnes, F. E. Close, P. R. Page and E. S. Swanson, Phys. Rev. D **55**, 4157 (1997).

[101] T. Barnes, N. Black and P. R. Page, Phys. Rev. D **68**, 054014 (2003).

[102] A. V. Anisovich, V. V. Anisovich, M. A. Matveev and V. A. Nikonov, Phys. Atom. Nucl. **66**, 914 (2003) [Yad. Fiz. **66**, 946 (2003)].

[103] E. Pallante and R. Petronzio, Nucl. Phys. B **396**, 205 (1993).

[104] H. Nagahiro, L. Roca and E. Oset, Eur. Phys. J. A **36**, 73 (2008)

[105] R. Molina, H. Nagahiro, A. Hosaka and E. Oset, Phys. Rev. D **83**, 094030 (2011)

[106] A. Bramon, A. Grau and G. Pancheri, Phys. Lett. B **283**, 416 (1992).

[107] E. Oset, J. R. Pelaez and L. Roca, Phys. Rev. D **67**, 073013 (2003)

[108] D. Gamermann, E. Oset, D. Strottman and M. J. Vicente Vacas, Phys. Rev. D **76**, 074016 (2007)

[109] D. Gamermann and E. Oset, Eur. Phys. J. A **33**, 119 (2007)

[110] R. Molina, D. Gamermann, E. Oset and L. Tolos, Eur. Phys. J. A **42**, 31 (2009)

[111] A. Faessler, T. Gutsche, V. E. Lyubovitskij and Y. L. Ma, Phys. Rev. D **76**, 014005 (2007)

[112] E. E. Kolomeitsev and M. F. M. Lutz, Phys. Lett. B **582**, 39 (2004)

[113] F. K. Guo, P. N. Shen, H. C. Chiang and R. G. Ping, Phys. Lett. B **641**, 278 (2006)

[114] F. K. Guo, P. N. Shen and H. C. Chiang, Phys. Lett. B **647**, 133 (2007)

[115] A. Faessler, T. Gutsche, V. E. Lyubovitskij and Y. L. Ma, Phys. Rev. D **76**, 114008 (2007)

[116] R. Molina, H. Nagahiro, A. Hosaka and E. Oset, Phys. Rev. D **80**, 014025 (2009)

[117] M. B. Wise, Phys. Rev. D **45**, 2188 (1992).

[118] T. Hyodo, D. Jido and A. Hosaka, Phys. Rev. D **75**, 034002 (2007)

[119] T. Hyodo, D. Jido and A. Hosaka, Phys. Rev. Lett. **97**, 192002 (2006)

[120] S. Ahmed *et al.* [CLEO Collaboration], Phys. Rev. Lett. **87**, 251801 (2001)

[121] V. M. Belyaev, V. M. Braun, A. Khodjamirian and R. Ruckl, Phys. Rev. D **51**, 6177 (1995)

[122] P. Colangelo, G. Nardulli, A. Deandrea, N. Di Bartolomeo, R. Gatto and F. Feruglio, Phys. Lett. B **339**, 151 (1994)

[123] F. S. Navarra, M. Nielsen and M. E. Bracco, Phys. Rev. D **65** 037502 (2002)

[124] S. Godfrey and S. L. Olsen, Ann. Rev. Nucl. Part. Sci. **58**, 51 (2008)

[125] E. S. Swanson, Phys. Lett. B **588**, 189 (2004)

[126] E. Braaten and M. Kusunoki, Phys. Rev. D **72**, 054022 (2005)

[127] M. B. Voloshin, Phys. Lett. B **579**, 316 (2004)

[128] F. E. Close and P. R. Page, Phys. Lett. B **578**, 119 (2004)

[129] D. Gamermann and E. Oset, arXiv:0905.0402 [hep-ph].

[130] T. Barnes, S. Godfrey and E. S. Swanson, Phys. Rev. D **72**, 054026 (2005)

[131] S. L. Olsen, arXiv:0901.2371 [hep-ex].

[132] Bai-Qing Li and Kuang-Ta Chao Phys. Rev. D **79**,094004 (2009)

[133] X. Liu and Shi-Lin Zhu, Phys. Rev. D **80**, 017502 (2009)

[134] T. Branz, T. Gutsche and V. E. Lyubovitskij, Phys. Rev. D **80**, 054019 (2009)

[135] E. van Beveren, G. Rupp [arXiv:0906.2278v1 [hep-ph]]

[136] R. Molina and E. Oset, Phys. Rev. D **80**, 114013 (2009)

[137] J. F. Sun, D. S. Du and Y. L. Yang, Eur. Phys. J. C **60**, 107 (2009)

[138] T. F. Carames, A. Valcarce, J. Vijande, Phys. Rev. **D82**, 054032 (2010).

[139] T. Branz, R. Molina and E. Oset, Phys. Rev. D **83**, 114015 (2011)

[140] W. H. Liang, R. Molina and E. Oset, Eur. Phys. J. A **44**, 479 (2010)

[141] T. Branz, L. S. Geng and E. Oset, Phys. Rev. D **81**, 054037 (2010)

[142] S. Uehara *et al.* [Belle Collaboration], Phys. Rev. Lett. **104**, 092001 (2010)

[143] B. Aubert *et al.* [BaBar Collaboration], Phys. Rev. Lett. **101**, 082001 (2008)

[144] H. Nagahiro, L. Roca, E. Oset, Phys. Rev. **D77**, 034017 (2008).

[145] H. Nagahiro, K. Nawa, S. Ozaki *et al.*, [arXiv:1101.3623 [hep-ph]].

[146] T. Aaltonen et al. (The CDF collaboration) [arXiv:0903.2229 [hep-ph]]

[147] S. Godfrey and R. Kokoski, Phys. Rev. D **43**, 1679 (1991).

[148] M. Di Pierro and E. Eichten, Phys. Rev. D **64**, 114004 (2001)

[149] E. van Beveren and G. Rupp, Phys. Rev. Lett. **91**, 012003 (2003)

[150] D. S. Hwang and D. W. Kim, Phys. Lett. B **601**, 137 (2004)

[151] Yu. A. Simonov and J. A. Tjon, Phys. Rev. D **70**, 114013 (2004)

[152] D. Becirevic, S. Fajfer and S. Prelovsek, Phys. Lett. B **599**, 55 (2004)

[153] *in Proceedings of the 3rd International Workshop on Heavy Quarkonium, October 12-15, 2004 (IHEP, Beijing, 2004).* ArXiv:hep-ph/0412158.

[154] G. Rupp, F. Kleefeld, and E. van Beveren, AIP Conf. Proc. **756**, 360 (2005).

[155] R. Molina, T. Branz and E. Oset, Phys. Rev. D **82**, 014010 (2010)

[156] T. F. Carames, A. Valcarce, J. Vijande, Phys. Lett. **B699**, 291-295 (2011).

[157] M. Kaskulov, E. Hernandez and E. Oset, Eur. Phys. J. A **31**, 245 (2007)

[158] M. Kotulla *et al.* [CBELSA/TAPS Collaboration], Phys. Rev. Lett. **100**, 192302 (2008)

[159] G. Wolf, B. Friman and M. Soyeur, Nucl. Phys. A **640**, 129 (1998)

[160] W. Broniowski, W. Florkowski and B. Hiller, Acta Phys. Polon. B **30**, 1079 (1999)

[161] V. Bernard, U. G. Meissner and I. Zahed, Phys. Rev. Lett. **59**, 966 (1987)

[162] T. Hatsuda, T. Kunihiro and H. Shimizu, Phys. Rev. Lett. **82**, 2840 (1999)

[163] D. Jido, T. Hatsuda and T. Kunihiro, Phys. Rev. D **63**, 011901 (2001)

[164] P. Schuck, W. Norenberg and G. Chanfray, Z. Phys. A **330**, 119 (1988); R. Rapp, J. W. Durso and J. Wambach, Nucl. Phys. A **596**, 436 (1996); Z. Aouissat, R. Rapp, G. Chanfray, P. Schuck and J. Wambach, Nucl. Phys. A **581**, 471 (1995); H. C. Chiang, E. Oset and M. J. Vicente-Vacas, Nucl. Phys. A **644**,77 (1998); Z. Aouissat, G. Chanfray, P. Schuck and J. Wambach, Phys. Rev. C **61**, 012202 (2000); D. Davesne, Y. J. Zhang and G. Chanfray, Phys. Rev. C **62**, 024604 (2000)

[165] F. Bonutti *et al.* [CHAOS Collaboration], Phys. Rev. Lett. **77**, 603 (1996); F. Bonutti *et al.* [CHAOS Collaboration], Nucl. Phys. A **638**, 729(1998); P. Camerini, N. Grion, R. Rui and D. Vetterli, Nucl. Phys. A **552**, 451 (1993) [Erratum-ibid. A **572**, 791 (1993)]; F. Bonutti *et al.* [CHAOS Collaboration], Phys. Rev. C **60**, 018201 (1999) ; A. Starostin *et al.* [Crystal Ball Collaboration], Phys. Rev. Lett. **85**, 5539 (2000)

[166] J. G. Messchendorp *et al.*, Phys. Rev. Lett. **89**, 222302 (2002)

[167] M. J. Vicente Vacas and E. Oset, Phys. Rev. C **60**, 064621 (1999)

[168] L. Roca, E. Oset and M. J. Vicente Vacas, Phys. Lett. B **541**, 77 (2002)

[169] P. Muhlich, L. Alvarez-Ruso, O. Buss and U. Mosel, Phys. Lett. B **595**, 216 (2004)

[170] H. Walliser, Nucl. Phys. A **548**, 649 (1992)

[171] D. Gamermann, E. Oset and B. S. Zou, arXiv:0805.0499 [hep-ph]. Eur. Phys. J. A in print.

[172] T. Mizutani and A. Ramos, Phys. Rev. C **74** (2006) 065201

[173] L. Tolos, A. Ramos and T. Mizutani, Phys. Rev. C **77**, 015207 (2008)

[174] G. Ecker, Prog. Part. Nucl. Phys. **35**, 1 (1995)

[175] V. Bernard, N. Kaiser and U. G. Meissner, Int. J. Mod. Phys. E **4**, 193 (1995)

[176] B. Borasoy, P. C. Bruns, U. G. Meissner and R. Nissler, Eur. Phys. J. A **34**, 161 (2007)

[177] F. E. Close and R. G. Roberts, Phys. Lett. B **316**, 165 (1993)

[178] B. Borasoy, Phys. Rev. D **59**, 054021 (1999)

[179] E. M. Haacke, J. W. Moffat and P. Savaria, J. Math. Phys. **17**, 2041 (1976)

[180] E. Oset and A. Ramos, Nucl. Phys. A **679**, 616 (2001)

[181] R. Machleidt, K. Holinde and C. Elster, Phys. Rept. **149**, 1 (1987)

[182] G. Chanfray, D. Davesne, M. Ericson and M. Martini, Eur. Phys. J. A **27**, 191 (2006)

[183] E. Oset, H. Toki, M. Mizobe and T. T. Takahashi, Prog. Theor. Phys. **103**, 351 (2000)

[184] W. Broniowski, W. Florkowski and B. Hiller, Phys. Rev. C **68**, 034911 (2003)

[185] R. Rapp, Nucl. Phys. A **782**, 275 (2007)

[186] O. Lakhina and E. S. SwLanson, Phys. Lett. B **650**, 159 (2007)

[187] E. van Beveren, J. E. G. Costa, F. Kleefeld and G. Rupp, Phys. Rev. D **74**, 037501 (2006)

[188] E. van Beveren, F. Kleefeld and G. Rupp, AIP Conf. Proc. **814**, 143 (2006)

[189] T. Ishikawa *et al.*, Phys. Lett. B **608**, 215 (2005)

[190] L. Tolos, R. Molina, E. Oset and A. Ramos, Phys. Rev. C **82**, 045210 (2010)

[191] E. Hernandez and E. Oset, Z. Phys. A **341**, 201 (1992).

[192] G. E. Brown and M. Rho, Phys. Rev. Lett. **66**, 2720 (1991).

[193] R. Rapp, G. Chanfray and J. Wambach, Nucl. Phys. A **617**, 472 (1997)

[194] W. Peters, M. Post, H. Lenske, S. Leupold and U. Mosel, Nucl. Phys. A **632**, 109 (1998)

[195] M. Urban, M. Buballa and J. Wambach, Nucl. Phys. A **673**, 357 (2000)

[196] D. Cabrera, E. Oset and M. J. Vicente Vacas, Nucl. Phys. A **705**, 90 (2002)

[197] M. Post, S. Leupold and U. Mosel, Nucl. Phys. A **741**, 81 (2004)

[198] D. Cabrera and M. J. Vicente Vacas, Phys. Rev. C **67**, 045203 (2003)

[199] R. Muto *et al.* [KEK-PS-E325 Collaboration], Phys. Rev. Lett. **98**, 042501 (2007)

[200] M. Naruki *et al.*, Phys. Rev. Lett. **96**, 092301 (2006)

[201] M. H. Wood *et al.* [CLAS Collaboration], Phys. Rev. C **78**, 015201 (2008)

[202] J. C. Caillon and J. Labarsouque, J. Phys. G **21**, 905 (1995).

[203] K. Saito, K. Tsushima, D. H. Lu and A. W. Thomas, Phys. Rev. C **59**, 1203 (1999)

[204] M. F. M. Lutz, G. Wolf and B. Friman, Nucl. Phys. A **706**, 431 (2002) [Erratum-ibid. A **765**, 431 (2006)]

[205] P. Muehlich, V. Shklyar, S. Leupold, U. Mosel and M. Post, Nucl. Phys. A **780**, 187 (2006)

[206] M. Kaskulov, H. Nagahiro, S. Hirenzaki and E. Oset, Phys. Rev. C **75**, 064616 (2007)

[207] D. Trnka *et al.* [CBELSA/TAPS Collaboration], Phys. Rev. Lett. **94**, 192303 (2005)

[208] M. Nanova *et al.* [TAPS Collaboration], arXiv:1005.5694 [nucl-ex].

[209] C. Garcia-Recio, J. Nieves, and L. L. Salcedo, Phys. Rev. D **74**, 034025 (2006).

[210] S. Sarkar, B. X. Sun, E. Oset and M. J. V. Vacas, Eur. Phys. J. A **44**, 431 (2010)

[211] E. Oset and A. Ramos, Eur. Phys. J. A **44**, 445 (2010)

[212] E. Oset, E. J. Garzon, J. J. Xie, P. Gonzalez, A. Ramos and A. M. Torres, arXiv:1103.0807 [nucl-th].

[213] M. Lutz, Phys. Lett. B **426**, 12 (1998)

[214] J. Schaffner-Bielich, V. Koch and M. Effenberger, Nucl. Phys. A **669**, 153 (2000)

[215] A. Cieply, E. Friedman, A. Gal and J. Mares, Nucl. Phys. A **696**, 173 (2001)

[216] A. Ramos, E. Oset and L. L. Salcedo, Phys. Rev. C **50**, 2314 (1994).

[217] M. Herrmann, B. L. Friman and W. Norenberg, Nucl. Phys. A **560**, 411 (1993).

[218] G. Chanfray and P. Schuck, Nucl. Phys. A **555**, 329 (1993).

[219] E. Oset and A. Ramos, Nucl. Phys. A **679**, 616 (2001)

[220] L. Tolos, C. Garcia-Recio and J. Nieves, Phys. Rev. C **80**, 065202 (2009)

[221] A. Ramos and E. Oset, Nucl. Phys. A **671**, 481 (2000)

[222] L. Tolos, A. Ramos, A. Polls and T. T. S. Kuo, Nucl. Phys. A **690**, 547 (2001)

[223] L. Tolos, A. Ramos and A. Polls, Phys. Rev. C **65**, 054907 (2002)

[224] L. Tolos, A. Ramos and E. Oset, Phys. Rev. C **74**, 015203 (2006)

[225] R. Arnaldi *et al.* [NA60 Collaboration], Phys. Rev. Lett. **96**, 162302 (2006)

[226] V. K. Magas, L. Roca and E. Oset, Phys. Rev. C **71** (2005) 065202

[227] P. Muhlich and U. Mosel, Nucl. Phys. A **765**, 188 (2006)

[228] M. Kaskulov, L. Roca and E. Oset, Eur. Phys. J. A **28**, 139 (2006) Phys. Rev. C **73**, 045213 (2006)

[229] P. Muhlich and U. Mosel, Nucl. Phys. A **773** (2006) 156.

[230] J. Nieves and E. Ruiz Arriola, Phys. Rev. D **64**, 116008 (2001)

[231] B. C. Liu and B. S. Zou, Phys. Rev. Lett. **96**, 042002 (2006)

[232] L. S. Geng, E. Oset, B. S. Zou and M. Doring, Phys. Rev. C **79**, 025203 (2009)

[233] N. Kaiser, P. B. Siegel and W. Weise, Nucl. Phys. A **594**, 325 (1995)

[234] J. J. Wu, R. Molina, E. Oset and B. S. Zou, Phys. Rev. Lett. **105**, 232001 (2010)

[235] J. J. Wu, R. Molina, E. Oset and B. S. Zou, arXiv:1011.2399 [nucl-th].

[236] http://www.gsi.de/fair/index.html

[237] R. Arnaldi *et al.* [NA60 Collaboration], Eur. Phys. J. C **59**, 607 (2009)

[238] C. Djalali, M. H. Wood, R. Nasseripour and D. P. Weygand [CLAS Collaboration], J. Phys. G **35**, 104035 (2008).

[239] C. Djalali, private communication.

[240] S. J. Brodsky and G. F. de Teramond, Phys. Rev. Lett. **60**, 1924 (1988).

[241] B. Gong, X. Q. Li and J. X. Wang, Phys. Lett. B **673**, 197 (2009).